Unveiling stellar-mass black holes in globular clusters with dynamical models

University of Surrey

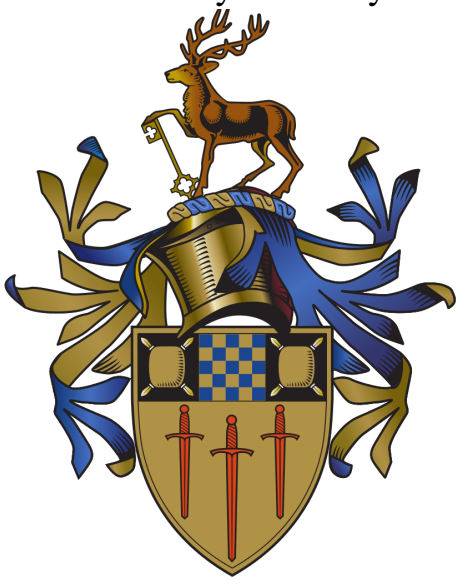

Miklos Peuten

First Supervisor: Mark Gieles
Second Supervisor: Alessia Gualandris

September 28, 2018

Abstract

The recent discovery of a gravitational wave produced by two merging stellar-mass black holes started a search for environments where two stellar mass black holes can become a binary and merge. One favourable environment could be globular clusters, but the evolution of black holes in them is still widely debated.

In this thesis, I present a method, based on isotropic lowered isothermal multimass models with which stellar mass black hole populations in globular clusters can be dynamically inferred and the main properties of the cluster can be estimated. In the models, I am using an improved stellar evolution code from Balbinot and Gieles (2018) to which I added black hole evolution. Before applying the multimass models to data, I made a detailed comparison between the properties of multimass models and collisional N-body simulations. I find that all dynamical stages are well described by the models and that a stellar mass black hole population reduces mass segregation.

For the Milky Way globular cluster NGC 6101, I run three N-body simulations to show that the observed lack of observable mass segregation could be explained by a stellar mass black hole population. To differentiate this explanation from others, I create different multimass models and find that measuring the cluster's velocity dispersion could help to prove the black hole population.

In the final chapter I follow-up on this prediction, and present new line-of-sight velocities of NGC 6101's velocities with the ESO *MUSE* instrument, I find, applying my method, that the cluster has 86^{+30}_{-23} black holes, which could explain its currently observed lack of mass segregation. This thesis in concluded by a discussion on how improve dynamical detections of BH populations with future observations and models.

Dedication

I want to dedicate this PhH thesis to my wife Angelika, for always supporting me throughout these four years, and also to my wonderful daughters Hannah and Sarah, for leaving school and friends behind to accompany me on this abroad adventure. I think your initial reluctance soon gave room to new and happy experiences, and I hope you cherish this time as much as I do.

I also want to dedicate this PhH thesis to my father,

Dr. Dr. Matthias Peuten
($\star$ 02/02/41 - † 20/04/18)

whom I would have loved to invite to my graduation celebration.

Declaration

'I confirm that the submitted work is my own work and that I have clearly identified and fully acknowledged all material that is entitled to be attributed to others (whether published or unpublished) using the referencing system set out in the programme handbook. I agree that the University may submit my work to means of checking this, such as the plagiarism detection service Turnitin UK. I confirm that I understand that assessed work that has been shown to have been plagiarised will be penalised.'

Aspects of this work have appeared in, or are due to appear in the following publications:

- Peuten, M., Zocchi, A., Gieles, M., Gualandris, A., and Henault-Brunet, V. (2016), MNRAS, 462, 2333–2342, *A stellar-mass black hole population in the globular cluster NGC 6101?*
- Peuten, M., Zocchi, A., Gieles, M., and Henault-Brunet, V. (2017), MNRAS, 470, 2736–2761, *Testing lowered isothermal models with direct N-body simulations of globular clusters - II. Multimass models.*
- Peuten, M., Husser, T.-O., Gieles, M., Balbinot, E., de Boer, T., Hénault-Brunet, V., Lapenna, E., Kamann, S., Zocchi, A. and Dalessandro, E. (in prep.) *Dynamical inference of a stellar-mass black hole population in the Galactic globular cluster NGC 6101*

Acknowledgements

I would like to thank the following people/organisations who have helped me throughout my P.h.D. and/or have made this work possible:

- My supervisor Mark Gieles for making this PhD thesis possible, for help with words and deeds over the course of the four years and for the exercise of patience in the many long meetings we had;
- My co-supervisor, Alessia Gualandris for her helpful suggestions, advice and not to forget her well-intentioned reminders;
- the European Research Council for funding my position and offering young researchers the possibility to thrive in their subject;
- Alice Zocchi, for her colourful suggestions and her deep knowledge that she has always liked to share
- Eduardo Balbinot, for his fresh insights and needed opinions from an observer's perspective;
- Vincent Henault-Brunet, for sharing his his extensive knowledge with me
- Thomas de Boer for interesting discussions and very helpful advice and comments
- Tim-Oliver Husser and Sebastian Kamann, for quick and uncomplicated help on short notice, when problems with the reduction and velocity extraction of the *MUSE* observations lead to a dead-end
- Past and present office colleagues for the many completely off-topic discussions which help to keep sane and for some good advice which more than once saved my day
- Simon F. Portegies Zwart and Justin I. Read for taking the time to read my PhD thesis and conduct my viva examination
- The University of Surrey computing facilities for maintaining the different computing nodes used for this PhD Thesis and for not suspending my account six days prior to submission.
- Last but not least my wife, Angelika Hornbach, for successfully hunting down all the "witches" which tried to hide in all of my publications

Contents

List of Figures

List of Tables

Chapter 1

Introduction

Sometimes called the final frontier, the Universe has always fascinated mankind throughout its existence. One of the earliest records is the 16500 years old ancient mural painting in the caves of Lascaux in France which is nowadays believed to depict the Pleiades (Rappenglück 1997). Also known as Seven Sisters or M45, they are one of the nearest and brightest open star clusters, which can be observed with the naked eye. Since then, mankind has increasingly evolved and with us the instruments and knowledge we gained about the Universe, without it losing any of its fascination. Quite to the contrary, each new finding fuels the fascination further than before: The recent detection of gravitational waves emitted by two colliding black holes (Abbott et al. 2016d) has significantly spurred the general interest in this new area of physics, which before was only of theoretical nature. The already strong interest of the general population in black holes has also grown further which is reflected by the multiplicity of popular articles being published since detection of the gravitational waves.

With all the modern gravitational wave detectors, space-based telescopes and artificial intelligence powering astronomy, it is still stunning how little we know about the Universe. There is no recent observation that does not bring up new questions - if it can answer, at all, the question it was carried out for. We still lack satisfying answers even to many of the fundamental questions. One of those rather simple questions is about the location of black holes, as it is believed that in our Universe, one out of every thousand stars will turn, or has already turned, into a black hole. With the Milky Way having roughly 100 billion stars, this implies that there are about 100 million black holes hiding. If we knew where the black holes are located, we could better study and understand how and when two of them merge, creating the observed gravitational waves. In turn, we could be using the data gathered from these mergers to also better understand these regions. The observation of black holes could also help to gain further insight into fundamental physical processes in the field of nuclear physics (Hessels et al. 2015), gravitational physics and general relativity (Benacquista and Downing 2013). For example, the theory of the Hawking Radiation (Hawking 1975) is one of the interesting cases where general relativity and quantum mechanics both play an important role. Observing it could help to gain further insight into both theories and their probable interactions.

In this PhD thesis, I try to contribute a little piece to the big puzzle, by searching for signatures of stellar-mass black holes in globular clusters using dynamical models. First, I will introduce what globular clusters, stellar-mass back holes and the dynamical models

are, and how they relate to each other.

1.1 Globular clusters

The first discovered Milky Way globular cluster, called M22, was found by the German amateur astronomer Abraham Ihle in the year 1665 (Monaco et al. 2004). Up to today, roughly ~ 160 globular clusters have been found in the Milky Way, with research suggesting that up to 20 are still undiscovered (Ashman and Zepf 1992). Globular clusters have been found in virtually every larger galaxy and some smaller galaxies (Harris 1991). So far, the galaxy with the most globular clusters found is M87, hosting over 13.000 of them (McLaughlin et al. 1994).

The simplest definition of a globular cluster is a self-gravitating spherical collection of $10^4 - 10^7$ stars orbiting a galactic centre. There are also more stringent definitions which limit them to certain mass and/or ages ranges or the existence of multiple populations (Gratton et al. 2012, discussed below), but so far none of those criteria are satisfied by all generally accepted globular clusters (Meylan and Heggie 1997). The important properties of all the objects which are considered globular clusters in the Milky Way are listed in the Harris (1996) catalogue: the absolute visual magnitude of all Milky Way globular clusters is found to be in the range between -10 to 0 with a median at -7.2. The distances from the Milky Way centre vary between $0.5\,\mathrm{kpc}$ up to $125\,\mathrm{kpc}$ with a median distance of $5.1\,\mathrm{kpc}$. The half light radius, which is the radius from which half of the total light of the globular cluster is radiated, is of the order of a few arc-minutes which translates to a range between $\sim 1\,\mathrm{pc}$ up to $\sim 25\,\mathrm{pc}$ with a median at $\sim 3\,\mathrm{pc}$. With ages between $8\,\mathrm{Gyr}$ to $13\,\mathrm{Gyr}$, they are the oldest known components in the Milky Way. In some galaxies, besides the population of old globular clusters, also young massive clusters are found (Portegies Zwart et al. 2010).

Given their high stellar densities (surpassing $\rho \geq 10^4\,\mathrm{M}_\odot\,\mathrm{pc}^{-3}$ in their core), which is several orders of magnitude higher than for example the density in the galactic plane, globular clusters are the ideal target for studies of stellar collisions and interactions as well as gravity itself (Sigurdsson and Phinney 1993, 1995). Globular clusters are interesting regions to observe when one searches for exotic objects (Hessels et al. 2015). This is especially true when looking for objects which can only form from dynamical interactions such as millisecond pulsars (Hessels et al. 2006), cataclysmic variables, binary X-ray sources, blue stragglers or exotic combinations such as a binary consisting of two neutron stars (Prince et al. 1991). For the search of stellar-mass black holes (Strader et al. 2012; Chomiuk et al. 2013; Miller-Jones et al. 2015; Bahramian et al. 2017; Giesers et al. 2018), globular clusters have also proven to be an interesting target as I will discuss below (Section 1.3).

The formation process of globular clusters is still not fully understood, but the general idea is that they form out of regions in galaxies which have interstellar medium densities higher than in regular star-forming regions, such as found in star-burst regions or where two galaxies are interacting (Elmegreen and Efremov 1997). Early analysis of the stellar population seemed to indicate that globular clusters have a simple stellar population (Bruzual 2010), i.e. that all stars where created with the same initial condition at around the same time and with the same iron abundance ([Fe/H]), the only difference being their initial mass. With the estimated average Milky Way globular cluster age of around 12

Gyrs, their stars are expected to be quite evolved, making globular clusters an ideal place for astronomers to study stellar evolution at different stages of their life (Renzini and Fusi Pecci 1988). More detailed studies have found that the stellar population of globular clusters is far more complex, showing the existence of multiple populations (Bedin et al. 2004; Piotto 2010), in the sense that abundance of light elements varies between the different populations. Various mechanisms, such as self-enrichment, have been proposed so far but none of them is fully conclusive yet (Bastian and Lardo 2017). This even further raised the interests of stellar population research in globular clusters.

Furthermore, a dichotomy in the Milky Way globular cluster population was found by Dutch astronomer Oosterhoff (Oosterhoff 1939; van Albada and Baker 1973) in 1939: He found that, when looking at the average period of the *ab*-type RR Lyrae stars, the Milky Way globular cluster population could be divided into two groups. Later it was found (Kinman 1959), that one differentiating propriety between those two groups was the metallicity of the clusters, with one group having on average stronger metal lines than the other. Nowadays it is confirmed that globular clusters can be divided into two groups, with the metallicity being the differentiating criterion: One group of globular clusters are considered "metal-rich" ($[\mathrm{Fe/H}] > -0.8$) which are mainly located in the Milky Way bulge, and the other one which is considered "metal-poor" ($[\mathrm{Fe/H}] < -0.8$) where the globular clusters are associated with the Milky Way halo (Zinn 1985). It is nowadays believed that the "metal-rich" group of globular clusters where formed in-situ while the "metal-poor" group is made out of globular clusters that where accreted from satellite galaxies, hence their different composition (Côté et al. 1998). The Milky Way globular cluster Omega Centauri is even suspected to be the remnant core of such a disrupted satellite dwarf galaxy (Freeman 1993; Bekki and Freeman 2003; Meza et al. 2005). This conjecture questions the current assumption that there is no significant amount of cold dark matter in globular clusters (Baumgardt et al. 2010; Ibata et al. 2013), although if a globular cluster forms in a dark matter halo, the dark matter is pushed to the outer parts by relaxation effects (Baumgardt and Mieske 2008).

Not only the composition of globular clusters is of interest, but also the interplay with their host galaxy: globular clusters are used to study the structure (Shapley 1918), potential (Koposov et al. 2010; Bonaca et al. 2014), formation and evolution (Friel 1995; Freeman and Bland-Hawthorn 2002) of the Milky Way. In dwarf galaxies, globular clusters are used as probes for dark matter densities of the host system (Goerdt et al. 2006; Sánchez-Salcedo et al. 2006; Contenta et al. 2018). Also globular clusters are used to determine the distance of the host galaxy, owing to the fact that peak of the luminosity function of the globular clusters seems to be around $M_{\mathrm{V}} \sim -7.5 \pm 0.2$ independent of the galaxy observed (Rejkuba 2012).

Being the oldest known and still existing objects in the Milky Way, globular clusters are often seen as the "building blocks" of galaxies, so that studies of their initial condition, their evolution and their current properties directly reflects the evolution of their host galaxies. In summary, globular clusters have proven to be an interesting laboratory to study several astrophysical questions.

Throughout the thesis, several properties of globular clusters will be used recurrently. Most of them, such as the total cluster mass (M_{cl}), are obvious and do not need further introduction. Others, however, need an explanation, such as the half-light radius, sometimes also called effective radius, which is the radius containing half of the total light.

The half-mass radius ($r_{\rm h}$) is a related property which is more commonly used when describing simulations of globular clusters, as it can be calculated directly from them. This is the radius within which half of the mass is concentrated. If a globular cluster is mass segregated (see Section 1.2) these two quantities are not necessarily the same.

There are two more radii which are commonly used when discussing globular clusters: One is the so called core radius $r_{\rm c}$ which represents the size of the central region, and for which different definition exists: the commonly adopted one (Heggie and Hut 2003) is

$$r_c = \sqrt{\frac{3v_c^2}{4\pi G\rho_c}} \tag{1.1.1}$$

where v_c^2 is the central mean square velocity, ρ_c the central density and G the gravitational constant. In isothermal models (see Section 1.4) the core radius $r_{\rm c}$ is the distance at which the space density drops to one third of the central value. In projection, this is equivalent to the radius where the projected (surface) density is half the value at the centre.

The other radius is the tidal radius $r_{\rm t}$ which is the radius at which the attraction from the host galaxy starts to dominate, i.e. stars observed further away than this are generally considered to be not bound to the cluster and lost to the galactic potential. The tidal radius thus defines the size of a globular cluster, but given that this is generally hard to observe, the half-light radius is the preferred quantity when discussing globular cluster sizes. A related quantities is $c = \log_{10}(r_{\rm t}/r_{\rm c})$ which is a measure of how concentrated a cluster is. The median concentration of Milky Way globular clusters is ~ 1.5.

Besides the radial scale, there are two time scales which give information about the dynamical evolution of a globular cluster: The crossing time $\tau_{\rm cr}$, sometimes also called the dynamical time, is the time it takes for a star to cross its star cluster (Spitzer and Hart 1971):

$$\tau_{\rm cr} = \frac{R}{\bar{v}} \tag{1.1.2}$$

where R is the size of the system and $\bar{v}$ the typical velocity of a star. The crossing time for a stars at the half-mass radius is proportional to:

$$\tau_{\rm cr} \propto \frac{r_{\rm h}^{3/2}}{(GM)^{1/2}} \tag{1.1.3}$$

with M the total cluster mass. The last steps assumes the cluster to be in virial equilibrium, which means that the virial equation is approximately satisfied:

$$2T + V = 0 \tag{1.1.4}$$

with T being the total kinetic energy and V the total potential energy of all objects in the cluster. Typical crossing times at the half-mass radius for Milky Way globular clusters are a few Myr and therefore relatively short compared to their ages.

The most important time scale is the relaxation time: As a star passes trough a cluster, it will interact with other cluster members (also described in the next section), and thereby slowly loses its initial state. The time required for an ensemble of stars in a cluster to lose all information of their initial state is the relaxation time scale. Assuming a Maxwellian velocity distribution, Spitzer and Hart (1971) define the relaxation time as:

$$\tau_{\rm r} = \frac{0.065v^3}{G^2m^2n\ln\Lambda} \tag{1.1.5}$$

with v the root mean square velocity, n the number density of the stars and $\Lambda = \gamma N$ the argument of the Coulomb logarithm, with γ having values between 0.02 and 0.4 depending on the stellar mass function (Giersz and Heggie 1994, 1996). It is obvious that the value of $\tau_{\rm r}$ is dependent on the position, as for example in the core, the number density is higher, therefore more interactions can happen in the same time, thereby a star loses its initial state faster there than at the cluster's outer regions. It has become common practise (Spitzer 1987) to calculate $\tau_{\rm r}$ for average quantities inside the half-mass radius, the so-called half-mass relaxation time (Spitzer and Hart 1971):

$$\tau_{\rm rh} = \frac{0.138 N^{1/2} r_h^{3/2}}{(Gm)^{1/2} \ln \Lambda} \tag{1.1.6}$$

In theoretical studies, often the initial half-mass relaxation time ($\tau_{\rm rh,0}$) this is the half-mass relaxation time at the creation of the cluster is used to compare time-scales of dynamically different globular cluster models.

For Milky Way globular clusters, this time scale is of the order of $\sim 1.2\,{\rm Gyr}$, much longer than $\tau_{\rm cr}$. From this it follows that stars in globular clusters experience many orbits without or with only a few interactions, meaning that the mean free path of these stars exceeds the size of the globular cluster greatly. Nevertheless the average age of globular clusters is still higher than the average value of $\tau_{\rm rh}$ and the effect of the many two-body encounters should have destroyed the memory of the initial state for most Milky Way globular cluster stars. Therefore, the half-mass relaxation time is a quantity used to compare and analyse the dynamical state of a globular cluster, which is the next topic.

1.2 Mass segregation

The aspect of globular cluster evolution which is of most interest throughout this thesis is mass segregation: We assume that a newly formed globular cluster can be approximated as a dense collection of stars (all gas dissipated) in virial equilibrium, with mass being the only property differentiating them. In the inevitable two-body encounters, two stars will exchange energy and momentum and following the equipartition theorem, the flow of energy will be on average such that the kinetic energy of the two members try to equalize. This means that the heavier star will lose velocity, while the lighter star will gain velocity, on average. Given the densities found in globular clusters, each star will endure many such encounters in a few $\tau_{\rm rh}$. This means that, at a given location, the heaviest stars have the lowest average velocities which in turn means that they will sink to the cluster centre. While for the lightest stars it means that they will have on average the highest velocity and are thereby being pushed into the clusters halo. If the velocity is high enough, they can even escape from the globular cluster. This whole process of heavy stars falling into the cluster center and lighter stars being pushed into the cluster's outskirts is known as mass segregation. Given that the globular clusters are older than their respective $\tau_{\rm rh}$, it is expected to find mass segregation in Milky Way globular clusters, which is also found in several globular clusters, so far (King et al. 1995; Sollima et al. 2014). Theoretical studies found that clusters older than $5\tau_{\rm rh,0}$ should be fully mass segregated (Gill et al. 2008). Studies (Baumgardt et al. 2008; Zonoozi et al. 2017) have indicated that some globular clusters might have formed with primordial mass segregation, i.e. that those globular clusters had already some degree of mass segregation, right at their formation.

The process of mass segregation tries to drive the cluster into full energy equipartition, which it never reaches as the lowest mass stars have energies high enough to leave the cluster (Merritt 1981; Miocchi 2006; Gieles and Zocchi 2015; Bianchini et al. 2016). Recently Bianchini et al. (2016) studied this effect and found that only partial equipartition is achieved in clusters and that there is a limiting mass above which stars are in energy equipartition while below they are not. They found that the limiting mass is dependent on the concentration, lower concentrated clusters having a higher limiting mass, and on the range of the mass spectrum, mass spectra with higher mass stars having also a higher limiting mass.

Another dynamical effect impacting cluster evolution is the so called "core collapse": In two-body encounters, stars in the cluster core transfer kinetic energy to the stars located in the outer regions, thereby falling into lower energy orbits where their kinetic energy increases again as the result of the negative heat capacity of self gravitating systems (Lynden-Bell and Wood 1968). Over time, this repeated process leads to an increase in core density and to an overall cluster expansion as the energy is diffused throughout the cluster. This effect is seen in cluster simulations regardless whether it has a mass spectrum or not, but when there is a mass spectrum, mass segregation reinforces this effect. This leads to the heaviest stars getting pushed further into the cluster core, which increases the core's density, while the lowest mass stars get pushed into the outskirts. This collapse is delayed or even halted by interaction with binaries which release energy by decreasing their semi-major axis (Vesperini and Chernoff 1994). If the most heaviest objects expel themselves from the cluster, due to strong interactions with each other (see also discussion for black holes below), another core collapse can occur, until it is stopped again. This is why globular clusters can be modelled as gas having a negative heat capacity: When the core loses heat, the core contracts further towards core collapse, thereby "heating" the core further up (Heggie and Hut 2003). If the heaviest object in a globular cluster are observable stars, a core collapse is observed as a power-law cusp in the globular cluster's surface brightness profile, which is observed in several Milky Way globular clusters (Djorgovski and King 1986).

Besides these, stellar evolution also drives the globular cluster's evolution, turning heavy stars into lighter remnants and thereby removing mass from the globular cluster, which leads to the cluster expanding (Gieles et al. 2010). This expansion is stopped as soon as the cluster fills its Roche-volume, which is the volume within which all objects are gravitationally bound to the globular cluster. From then on, the cluster will lose stars to its host galaxy, and with it mass, which in turn reduces the clusters Roche-volume. This leads to the cluster shrinking, until dissolution (Hénon 1961; Gieles et al. 2011).

1.3 Stellar-mass black holes

A black hole is a spacetime region which has such strong gravitational effects that nothing, not even light, can escape from it. According to the theory of general relativity, to deform spacetime in such a way that it creates a black hole, a sufficiently compact mass is needed. So far two types of black holes are known to exist: stellar-mass black holes with masses up to $100\,\mathrm{M}_\odot$ and which form when massive stars ($\gtrsim 16\,\mathrm{M}_\odot$) end their short life in a gravitational collapse. And second, super massive black holes (SMBH) which have masses in excess of $10^5\,\mathrm{M}_\odot$ and which are found in the centre of galaxies (Antonucci 1993; Urry

and Padovani 1995). For these, different formation theories exist, ranging from primordial black holes, which where formed after the Big Bang, to black holes which grew by accretion: But none of them were verified so far. In the mass range between $100\,\mathrm{M}_\odot$ and $10^5\,\mathrm{M}_\odot$, the so called intermediate mass black holes are suspected. So far there is no unambiguous detection for such a black hole, but it is assumed that they might exist in ultraluminous X-ray sources or in low-luminosity active galactic nuclei(Patruno et al. 2006). Several globular clusters were also suspected to harbour an intermediate mass black hole, but so far searches for signals of accretion onto an intermediate mass black holes were inconclusive (Tremou et al. 2018b) as where dynamical studies of individual globular clusters (Zocchi et al. 2018; Gieles et al. 2018). Therefore, in the context of globular clusters, we are interested in stellar-mass black holes only.

The recent surge in interests in stellar-mass black holes comes from several recent findings: First and foremost, the detection of a gravitational wave produced by two merging stellar-mass black holes (Abbott et al. 2016d). Not only did this confirm Einstein's Theory of general relativity in the very strong field limit and in particular his Theory of gravitational waves (Einstein 1916), it is also the first direct proof for the existence of black holes and a dynamical indication that two black holes do merge within a Hubble time (Abbott et al. 2016a). Also this new eye into the Universe found that the masses of stellar-mass black holes are higher than anticipated from X-ray binary measurements (Abbott et al. 2016a), giving rise to improved models of black hole and binary black hole formation (Belczynski et al. 2016). Up to today six such events were detected out of which five were binary black holes mergers (Abbott et al. 2016d,b, 2017a,b,c) and one is a binary neutron star merging into a black hole (Abbott et al. 2017d). So far the exact location of those initial black holes within their galaxies could not be determined, but simulations show that globular clusters could be a good candidate to harbour them (Abbott et al. 2016a).

Like with black holes in general, their evolution in globular clusters is also full of unsolved questions and speculations: Assuming a Kroupa (2001) initial mass function with a mass range between $0.1\,\mathrm{M}_\odot$ and $100\,\mathrm{M}_\odot$, we expect around 0.18% to 0.22% (depending on the clusters metallicity) of stars to turn into black holes at the end of their lifetime. In the process of their formation, they receive a natal kick following the same physics as the natal kick received when neutron stars form. While the kick velocity distribution of neutron stars is known (Hut et al. 1991; Drukier 1996a; Hansen and Phinney 1997; Davies and Hansen 1998; Pfahl et al. 2002; Ivanova et al. 2005; Podsiadlowski et al. 2005; Ivanova et al. 2008a), the kick velocity distribution or even magnitude of black holes is still highly debated (Belczynski et al. 2002, 2010; Repetto et al. 2012; Fryer et al. 2012; Janka 2013; Mandel 2016; Repetto et al. 2017; O'Shaughnessy et al. 2017): if they were higher than the cluster's escape velocity, then not many would be initially retained in them; which is the case for neutron stars where only around 10% are retained in globular clusters. For heavier black holes, there are formation scenarios with a failed supernova, i.e. the stars collapse directly into a black hole and no or a low kick is received (Fryer and Kalogera 2001; Fryer et al. 2012).

If the globular clusters had been able to initially keep some black holes, then for many years, the assumption (Kulkarni et al. 1993; Sigurdsson and Hernquist 1993) was that they would sink into the cluster centre, due to mass segregation (see above) and then form, a sub-system that is dynamically decoupled from the rest of the globular cluster (Spitzer

1969). In this subsystem the black holes interact with one another and kick each other out and within a few Myr, only one, two or none of them would be left. Therefore, globular clusters with an age over a few Gyr were generally considered black hole free. In recent years, this picture has changed due to improved theoretical studies and observations: Using different theoretical and numerical approaches, several studies (Mackey et al. 2008; Morscher et al. 2013; Breen and Heggie 2013a,b; Sippel and Hurley 2013; Heggie and Giersz 2014; Morscher et al. 2015; Wang et al. 2016; Webb et al. 2018; Banerjee 2018, see also Chapter 3) have shown that if a population of black holes are initially retained in a globular cluster, then they could survive several Gyr in the cluster, and some of them could survive there for a Hubble time or longer, if the two-body relaxation time of the hosting globular cluster is long enough (Morscher et al. 2015; Webb et al. 2018). Apparently the black hole core subsystem is not decoupled, and it has been shown that the evolution of this subsystem is governed by the hosting globular clusters energy demands (Breen and Heggie 2013a,b). Observationally (see Chapter 3), in clusters with a black hole population, one would expect to see a cored low-density central region. This is due to the black holes sinking into the cluster centre, as mass segregation is acting, pushing the observable stars out. These inflated profiles are observed in some halo Milky Way globular clusters and in dwarf galaxy globular clusters. For the latter this was already associated as indication for a black hole population (Merritt et al. 2004; Mackey et al. 2008). In the context of the above discussed results from Bianchini et al. (2016) that there is a limiting mass below which stars are not in full energy equipartition, I show in Chapter 2 that for clusters with black holes, that this limiting mass is above most observable stars. Hence, the observed mass segregation is reduced for clusters with black holes.

The first indication for black holes in Milky Way globular clusters was found in M22 (Strader et al. 2012), where two black hole candidates were found using radio and X-ray observations, hinting that there could be up to 100 more black holes in this cluster. Using the same method, a black hole candidate was also found in the globular cluster M63 (Chomiuk et al. 2013). The X-ray source X9 in the globular cluster 47 Tuc was identified as another quiescent black hole candidate when analysing observations in radio and X-ray (Miller-Jones et al. 2015; Bahramian et al. 2017). Looking for microlensing events, Minniti et al. (2015) identified another possible black hole candidate in the Milky Way globular cluster NGC 6553. Recently, Giesers et al. (2018) studied a binary in the Milky Way globular cluster NGC 3201 and found that the unobserved secondary had a minimal mass of at least $4.36 \pm 0.41\,\mathrm{M}_{\odot}$, which in the current understanding can only be a stellar-mass black hole. Also, in Extragalactic globular clusters, several indications for black holes were found (Mackey et al. 2008; Maccarone et al. 2007; Barnard et al. 2008; Barnard and Kolb 2009; Roberts et al. 2012). Apparently, not all globular clusters are black hole free as previously anticipated.

1.4 Lowered isothermal multimass models

When dealing with highly complex systems in physics, such as a globular cluster, there is the need to find a simplified model, which describes the observable properties using known physical assumptions and laws. Models are always generalisations of the true underlying physics, but are an essential tool to better understand, analyse and compare otherwise complex systems.

For Milky Way globular clusters, one of the first such models was introduced by Plummer (1911) to fit surface brightness profiles. These models are nowadays known as the Plummer model and are a polytrope of index $n = 5$. A polytrope is a solution of the Lane–Emden equation, a dimensionless form of Poisson's equation, where the pressure depends upon the density, such that its equation of state is:

$$P = K\rho^{1+1/n} \tag{1.4.1}$$

where P is the pressure, ρ is the density, K is a constant and n is the polytrope index (sometimes also given in the form of the polytrope exponent $\gamma = 1 + 1/n$). Polytropes are also used in other areas of astrophysics, such as for the modelling of neutron stars ($n = 0.5 - 1$), stars ($n \sim 1.5$) or white dwarfs ($n \sim 3$).

The distribution function (f) is a common way of describing a star cluster (Meylan and Heggie 1997), it gives the mass density of stars with a given mass at a given position with a given velocity. The mean number of stars in an infinitely small phase-space and mass range region can be deduced from $f d^3\mathbf{r} d^3\mathbf{v} dm$ and therefore the density can be calculated as:

$$\rho = \int f d^3\mathbf{r} d^3\mathbf{v} dm \tag{1.4.2}$$

The distribution function can also be used in the Boltzmann equation giving an equation for the dynamical evolution of a star cluster:

$$\frac{\partial f}{\partial t} + \mathbf{v}\frac{\partial f}{\partial \mathbf{x}} - \frac{\partial \phi}{\partial \mathbf{r}}\frac{\partial f}{\partial \mathbf{v}} = \Gamma(f) \tag{1.4.3}$$

with ϕ the potential per unit mass, also known as the specific potential, and $\Gamma(f)$ the collision term, describing the effect of two-body interactions. This equation can be simplified due to the fact that the first term vanishes as the crossing times in star clusters are so short that the stars' distribution can be assumed to be stationary after a few orbits (Meylan and Heggie 1997). Also, the effect of two-body interactions is generally considered negligible, due to the long time-scales involved. The simplified version of Equation (1.4.3) is therefore:

$$\mathbf{v}\frac{\partial f}{\partial \mathbf{x}} - \frac{\partial \phi}{\partial \mathbf{r}}\frac{\partial f}{\partial \mathbf{v}} = 0 \tag{1.4.4}$$

This equation is known under different names such as the collisionless Boltzmann equation, the Vlasov equation or Liouville's equation. A general solution for simple cases is given by the Jeans' theorem, which states that the distribution function must be a function of the constants of the integrals of motion for a star in the given potential. For a self-consistent solution the density must correspond to the distribution function and the potential can be found from the Poisson's equation for gravity as:

$$\nabla^2\phi = 4\pi G\rho = 4\pi G \int f d^3\mathbf{r} d^3\mathbf{v} dm \tag{1.4.5}$$

For the Plummer model the distribution function is (Dejonghe 1987):

$$f(E) = \frac{3}{4\pi}(2E)^{7/2} \tag{1.4.6}$$

where $E = v^2/2 + \phi(r)$ is the specific energy, i.e. the energy per unit mass of a star with velocity v and at a the position r in a star cluster potential described by the specific potential $\phi(r)$.

Many important properties of the Plummer model can be calculated analytically, which is why it is widely used for the initial set-up of star cluster simulations (see next section). But the model has one important drawback: the model cluster has an infinite radius. Furthermore, deeper observations of Milky Way globular clusters showed that the Plummer model fails to describe them sufficiently.

To overcome this problem, better models to describe the observed density profiles were introduced: One of the first was introduced by Woolley (1954) who used an isothermal model as starting point. Assuming that the cluster is isothermal and that the velocity distribution is a Maxwellian distribution everywhere in the cluster, the distribution function of such an isothermal model is:

$$f\left(E\right) = A \exp\left(-\frac{E}{s^2}\right) \tag{1.4.7}$$

for $E \leq 0$ and $f(E) = 0$ otherwise. A and s are two constants: the first is related to the total cluster mass and the latter is the one-dimensional velocity dispersion in the cluster. Like the Plummer model, this model has an infinite size but also an infinite mass. To overcome this, Woolley (1954) introduced a constant by which the energy is lowered:

$$f\left(E\right) = A \exp\left(-\frac{E - \phi\left(r_t\right)}{s^2}\right) \tag{1.4.8}$$

The idea here is to recreate the tidal effects of the host galaxy on the globular cluster: By reducing the energy by the value of $\phi\left(r_t\right)$ the effect of the galactic potential is imitated and the resulting model has now finite size and mass and is almost isothermal in the core. These kind of models are generally known as "lowered" isothermal models, because the energy of the models are artificially lowered to reflect the observed tidal truncation.

The most commonly known lowered isothermal model is the one presented by King (1966), which is generally know as King model. Compared to the Woolley (1954) model, where the distribution function is discontinuous at $E = \phi\left(r_\mathrm{t}\right)$, the King models subtract an additional constant from the distribution function, thus making it continuous at $E = \phi\left(r_\mathrm{t}\right)$. The distribution function of the King model reads:

$$f\left(E\right) = A \left(\exp\left(-\frac{E - \phi\left(r_t\right)}{s^2}\right) - 1\right) \tag{1.4.9}$$

It must be noted, that in theses models s is no longer the one-dimensional velocity dispersion but a velocity scale which only for very concentrated models approaches the one-dimensional velocity dispersion. It is nowadays attributed that King's clear and simple presentation of the theoretical and observational findings leads to the success of these models (Meylan and Heggie 1997). Furthermore, it turned out that the King distribution function is a good approximation to a steady state solution of the Fokker-Planck equation (Heggie and Hut 2003). Even today, more than fifty years later, the King model is the standard model of choice for globular cluster studies.

To describe elliptical galaxies, Wilson (1975) presented another version of a lowered isothermal model, where the distribution function of the isotropic and non-rotating version

of the model reads as:

$$f(E) = A\left(\exp\left(-\frac{E-\phi(r_t)}{s^2}\right) - 1 + \frac{E-\phi(r_t)}{s^2}\right) \tag{1.4.10}$$

The difference to the King distribution function is that the additional energy term makes also the derivative of the distribution function continuous at $E = \phi(r_\mathrm{t})$. Being made to describe elliptical galaxies, the original formulation of the Wilson (1975) model had also a description for rotation and anisotropy. McLaughlin and van der Marel (2005) showed that many Milky Way and extragalactic globular clusters are better described by the isotropic and non-rotating Wilson (1975) models than by King (1966) models, showing that these models are also relevant in the context of globular clusters.

Davoust (1977) found that all three models, (Woolley 1954, King 1966 and Wilson 1975) could be described by one distribution function in which the series expansion of the exponential function in energy is reduced by the leading order. Recently Gomez-Leyton and Velazquez (2014) presented a further generalisation, where the parameter can become continuous and not only the three known models can be reproduced by this description but also models lying in-between those models. Their presented distribution function reads:

$$f(E) = AE_\gamma\left(g, -\frac{E-\phi(r_\mathrm{t})}{s^2}\right), \tag{1.4.11}$$

where g is a model parameter and E_γ is defined as

$$E_\gamma(a,x) = \begin{cases} \exp(x) & a = 0 \\ \exp(x)\,P(a,x) & a > 0 \end{cases} \tag{1.4.12}$$

with $P(a,x) \equiv \gamma(a,x)/\Gamma(a)$, the regularised lower incomplete gamma function. By either setting $g = 0, 1, 2$, one can recover the Woolley (1954), King (1966) and Wilson (1975) models respectively. We will refer to g as the truncation parameter, as it describes the polytropic part near the escape energy and is related to the polytropic index as $n = g + 1.5$. From this it follows that for values above $g = 3.5$, the models have a polytropic index of 5 and above, and therefore, as already mentioned above, become infinite in radius (Gieles and Zocchi 2015).

All these models assume the velocity distribution to be isotropic, i.e. there are no preferred orbits within the cluster, therefore their distribution functions only depend on the energy. To analyse clusters with radial anisotropy, i.e. where radial orbits are dominating at least in a part of the cluster, Michie (1963) presented a description using the same approach as King (1966) adding the description for radial anisotropy for isothermal models as presented by Eddington (1915). The distribution function for these models are:

$$f(E) = A\exp\left(-\frac{J^2}{2r_a^2 s^2}\right)\left(\exp\left(-\frac{E-\phi(r_t)}{s^2}\right) - 1\right) \tag{1.4.13}$$

where r_a is the anisotropy radius and $J = |r \times v|$ the specific angular momentum. The radial anisotropy of these models is such that in the core of the models, i.e. $r < r_\mathrm{a}$, it is isotropic, beyond r_a it becomes radially anisotropic and then it becomes isotropic again at the tidal radius. It is noteworthy that the more famous King (1966) models were

introduced three years later and are the isotropic version of the Michie (1963) models, which is why some authors refer to both models as the Michie-King models.

Another extension to the lowered isothermal models was introduced by Da Costa and Freeman (1976) when they failed to fit King (1966) models to density profiles of the Milky Way globular cluster M3: In all of the above models, all stars were assumed to be of equal mass, one of the many simplifications made to reduce complexity, but Da Costa and Freeman (1976) relaxed this assumption by including a binned mass spectrum. For each mass bin, they created a separate King model representing that mass group within the globular cluster, and the distribution function of this multimass model is simply the sum of each individual distribution function:

$$f\left(E\right) = \sum_j f_j\left(E\right) = \sum_j A_j \left(\exp\left(-\frac{E - \phi\left(r_t\right)}{s_j^2} \right) - 1 \right) \tag{1.4.14}$$

where the constant A_j is related to the total mass in mass bin j. Da Costa and Freeman (1976) assumed the model to be in full equipartition of energy, i.e.

$$m_i \sigma_i^2 = m_j \sigma_j^2 \; \forall i, j \tag{1.4.15}$$

From this follows that the other constant s_j, which is the velocity scale of mass bin j, in equation (1.4.14) is connected to a global value of the velocity scale s such as

$$s_j = s \mu_j^{-\delta} \tag{1.4.16}$$

where $\delta = 0.5$ stands for a fully mass segregated cluster, $\mu_j = m_j / \bar{m}$ is the dimensionless mean mass of stars in the j-th mass component and $\bar{m}$ a reference mass which originally is the central density weighted mean-mass. As already discussed for the single-mass King model is the relation between s_j and 1d velocity dispersion for mass bin j at the centre ($\sigma^2_{1d,j,0}$) such, that they only become equal for the case of a cluster with infinite dense core, which for all clusters studied here is never the case and therefore $\sigma_{1d,j0} < s_j$. This in turn means that the multimass models are never in a state of energy equipartition despite being fully mass segregated (Merritt 1981; Miocchi 2006; Gieles and Zocchi 2015; Bianchini et al. 2016), as already discussed above and something I am going to discuss further in Chapter 2. Another interesting aspect of these models is that due to the "lowering" of the Maxwellian velocity distribution, the velocity distribution of the lowest mass bins becomes almost independent of their mean mass (Meylan and Heggie 1997).

Having measured velocities for the same globular cluster as Da Costa and Freeman (1976), M3, Gunn and Griffin (1979) included the radial velocity anisotropy formulation from Michie (1963) into the multimass model from Da Costa and Freeman (1976) to improve on the globular clusters modelling. Michie (1963) included the anisotropy such that it is independent of mass and therefore the anisotropy radius is the same for all mass bins.

Recently, Gieles and Zocchi (2015) presented their LIMEPY (Lowered Isothermal Model Explorer in PYthon) software which can reproduce all of the above discussed versions of the lowered isothermal models using only one distribution function:

$$f_j\left(E, J^2\right) = A_j \exp\left(-\frac{J^2}{2 r_{\mathrm{a},j}^2 s_j^2} \right) E_\gamma\left(g, -\frac{E - \phi\left(r_\mathrm{t}\right)}{s_j^2} \right) \tag{1.4.17}$$

Multimass models can be generated as well, using the same approach as presented in Da Costa and Freeman (1976), albeit with some improvements: The previous assumption of full mass segregation was relaxed by introducing the possibility to change parameter δ in equation (1.4.18). For $\delta = 0.5$, full mass segregation is assumed, while for $\delta = 0$, no mass segregation is assumed. Also, the relation of the anisotropy radius was changed for multimass models: While previously it was independent of mass, Gieles and Zocchi (2015) introduced a parameter η such as:

$$r_{a,j} = r_a \mu_j^{\eta} \tag{1.4.18}$$

Despite the great success of multimass lowered isothermal models in observational (see for example Illingworth and King 1977; Pryor et al. 1986; Lupton et al. 1987; Meylan 1987; Richer and Fahlman 1989; Meylan and Mayor 1991; Meylan et al. 1995; Sosin 1997; Piotto and Zoccali 1999; Richer et al. 2004; Paust et al. 2010; Beccari et al. 2010; Sollima et al. 2012; Beccari et al. 2015; Sollima et al. 2017, to name a few) and theoretical (Takahashi and Lee 2000; Sollima et al. 2015) studies over the last 40 years since their introduction, there are still several aspects and assumptions made in the construction of the multimass models for which they are criticized (McLaughlin 2003; Meylan and Heggie 1997). One obvious issue is the high number of parameters: in LIMEPY, a multimass model has $2N_{\rm MB}+7$ parameters, with $N_{\rm MB}$ being the number of mass bins, compared to a single mass LIMEPY model which always has only 5 parameters. According to McLaughlin (2003), it is therefore easier for multimass models to fit physically different models to the same dataset than it is for a single-mass model. Another point of criticism is the selection of the right mass function and the number of mass bins to use. Meylan and Heggie (1997) describe the approach normally found in observational studies as "compromise between convenience and realism". Another assumption for which multimass models have been criticized is the assumption of equipartition of energy (McLaughlin 2003; Trenti and van der Marel 2013), which as already discussed is not the case: multimass models only achieve partial equipartition, which is also found in simulations of globular clusters.

Several aspects of multimass models were already tested and analysed with the help of star clusters computer simulations: Takahashi and Lee (2000) used Fokker-Planck simulations and Sollima et al. (2015) compared multimass models to projected quantities from N-body simulations. But so far no completed analysis for multimass models exists, making the use of such models unfavourable.

1.5 N-body simulations

As discussed above, star clusters can be approximated as an accumulation of N stars without any residual gas left, and the dominating force acting between those stars is the gravitational force. Therefore, if one wants to analyse the dynamical evolution of the cluster, one has to solve for each individual star, the following second order linear differential equation, which comes out of Newton's famous *Philosophiae Naturalis Principia Mathematica* (Newton 1687):

$$\ddot{\mathbf{x}}_i = \sum_{i \neq j}^{N} \frac{m_j}{|\mathbf{x}_i - \mathbf{x}_j|^2} \mathbf{e}_{i,j} \; i = 1, \ldots, N \tag{1.5.1}$$

with $\mathbf{x}_i$ the 3-d position of the star i in the cluster, m_i its mass, $\mathbf{e}_{i,j}$ the unit vector directed from position of star i to star j. This problem is generally known as the N-body problem and is despite its simplicity still an area of active research. Assuming that one of the stars is fixed, Johann Bernoulli presented in 1710 a complete solution for the case of $N = 2$ (Bernoulli 1742). The N-body problem has ten integrals of motion (these are integrals that remain constant over time), which are: the 3-dimensional position of the centre of mass, the 3-dimensional linear momentum vector, the 3-dimensional angular momentum vector and the total energy of the N-body system (Bruns 1887). Jacobi (1843) found that with the help of symmetries in the N-body problem, two more integrals of motion can be found, giving a total of 12 integrals of motion. The dimensionality of an N-body problem is calculated as $6N$, as each star has six variables, three for the position and three for the velocity. From this, it is obvious why the two-body problem can be solved analytically: the total degree of freedom for this problem is zero, as it has 12 dimensions but also 12 integrals of motion. Poincaré (1892) showed using these results in an award winning paper, that there is no general closed-form analytic solution using integrals which can solve the N-body problem with more than two particles. However, for certain restricted N-body models with more than two particles, there are analytic solutions using integrals, and the search for those is still a topic of active research (Šuvakov and Dmitrašinović 2013).

That there is an analytical solution for the N-body problem with three stars was shown by Sundman (1913), who constructed a series solution to the power of $t^{1/3}$. He showed that these series converges for all non-negative values of the time t as long as the initial angular momentum is not zero. To overcome the problem of a singularity due to close encounters, he already included, regularization which through a transformation replaces the ill-conditioned problem into a well-conditioned problem. The power series solution for more than three stars was finally found by Wang (1991). Unfortunately, the solution found by Wang (1991) converges very slowly, which is why it is not used for studying star clusters nowadays.

Instead, nowadays numerical approaches are favoured, where the first such experiment was done by Holmberg (1941) who replaced the gravitational force with another $1/r^2$ dependent force, the intensity of light: replacing the different stars with light bulbs, the gravitational force could be determined by measuring the direction-depended light intensity at any given point, from which the acceleration for each star/bulb could be calculated. This approximation was unfortunately very slow and prone to errors and can nowadays be seen as example of creativity needed to solve physical problems before the advent of fully programmable automatic digital computers which interestingly were invented in the same year. The first use of computers to solve the numerical N-body problem was done by von Hoerner (1960) on a Siemens & Halske 2002 transistor computer which had a clock speed of only 200 kHz ($\sim$ 800 FLOPs). Using $N = 16$ and later $N = 25$ (von Hoerner 1963), von Hoerner (1960) already studied fundamental questions concerning the set-up and operation of such simulation as well as the behaviour of star clusters: von Hoerner identified the conservation of energy as an ideal quantity to check for the quality of the simulation. Also he already faced the problem of close encounters, which heavily increased the runtime of a simulation and he already discussed different solutions to the problem.

The name mostly associated with N-body simulations of star clusters is that of Sverre

Aarseth who in 1963 (Aarseth 1963) presented the first N-body simulation with 100 stars and since then has developed a series of NBODY software which nowadays is considered the de-facto standard. Over the course of more than five decades, all kind of improvements of physical, mathematical and computational nature were added to the code (Aarseth 2003): the latest incarnation NBODY6 uses a fourth-order Hermite integrator (Makino 1991; Makino and Aarseth 1992; Aarseth 1999) with an Ahmad and Cohen (1973) neighbour scheme; close encounters and binaries are treated with a Kustaanheimo–Stiefel regularization (Stiefel and Kustaanheimo 1965; Mikkola and Aarseth 1998) while higher order multiple systems are calculated using a chain regularization method (Mikkola and Aarseth 1990, 1993, 1996). Implementing the stellar evolution and binary stellar evolution code from Hurley et al. (2000, 2002), NBODY6 can reproduce all stages of a star life including the formation of black holes. Improvements on the computational side are also included such as the support for GPUs (Nitadori and Aarseth 2012) and multiple computers (Spurzem 1999; Wang et al. 2015) working together. Nevertheless, simulating realistic globular clusters still takes time: Heggie (2014) simulated the Milky Way globular cluster M4 with 484710 initial stars and it took 2 years and 8 month of computing time to reach the clusters current age of $12\,\mathrm{Gyr}$. Recently Wang et al. (2016) was able to run an N-body simulation of a globular cluster with 10^5 initial stars for a simulated time of $12\,\mathrm{Gyr}$ for the first time in only six month computation time, using an improved parallel version of NBODY6.

1.6 This thesis

From the above presentation, it is clear that some globular clusters might harbour a black hole population in their centre. The obvious question is: how can we detect it? Unfortunately, most techniques that have been used to detect black holes so far are only able to detect one or at most two black holes or can only give qualitative results. We still lack a proven method to measure the bulk of the black holes in globular clusters. As discussed above, a globular cluster with black holes should show certain characteristics such as an inflated profile and the lack of mass segregation, which could be used to probe for black holes in globular clusters.

In this PhD thesis, I present with the help of lowered isothermal multimass models and observations of the velocity and position of the globular clusters stars, a method to measure the black hole population of globular clusters. I then apply this method to the Milky Way globular cluster NGC 6101, to determine the clusters black hole population. This method can contribute to answer the question where in the Milky Way black holes are hiding.

First, I have to verify whether the assumptions made in the construction of the lowered isothermal multimass models are valid, because as already mentioned above they have never been fully verified. So far there have been only a few studies of multimass models (Takahashi and Lee 2000; Trenti and van der Marel 2013; Sollima et al. 2015), but these mostly focussed on specific aspects of them and never attempted a complete test of the models. Therefore, I first test if the multimass models indeed produce realistic models of globular clusters. This is the topic of Chapter 2 where I fit multimass models as provided by the LIMEPY software (Gieles and Zocchi 2015) to a set of N-body simulations, with varying initial black hole retention fractions. Not only do I test the models to see whether

they can reproduce the N-body data, but I also consider the evolution of some parameters which cannot be calculated directly. In particular, the newly introduced parameters δ and η in the new definition of the multimass distribution function from Gieles and Zocchi (2015), see equation (1.4.17), are of interests. In the context of stellar-mass black holes evolution in globular clusters, the development of the mass segregation parameter δ is especially interesting, as both could be related. I also consider the common problem of choosing the right number of mass bins for the mass function and how to do the binning for it.

After having shown that multimass models indeed are a viable tool to study globular clusters, in Chapter 3, I focus my attention on the Milky Way globular cluster NGC 6101, an unimpressive metal poor-star cluster located 11.2 kpc (Harris 1996) away from the Galactic Centre. Dalessandro et al. (2015) found for this $13\,\mathrm{Gyr}$ old globular cluster a lack of mass segregation. Together with the cluster's inflated profile with a low central density, the cluster shows signs of harbouring a stellar-mass black hole population. Creating three N-body simulations of NGC 6101, I show in this chapter that indeed a black hole population could reproduce the observed lack of mass segregation as well as the inflated profile. As it often happens in astronomy, alternative explanations exist which could explain some or all aspects observed. Using multimass models, I analyse this problem and propose an observational test, which could help differentiate the proposed explanations: by measuring the velocity dispersion profile, one should be able to test for a black hole population in NGC 6101.

I was able to secure observation time at the Very Large Telescope operated by the European Southern Observatory on Cerro Paranal in the Atacama Desert to measure the velocities of NGC 6101 stars using the Multi Unit Spectroscopic Explorer (*MUSE*) instrument. *MUSE* is an integral-field spectrograph with a field of view of 1 x 1 $arcmin$ and a spatial pixel scale of $0.2arcsec/pixel$. For each of these pixels, *MUSE* produces a full spectrum in the range from 465 nm to 930 nm with an average resolution of R = 3000. In Chapter 4, I first present the reduction and extraction of the velocities from 1108 stars in NGC 6101, using the recently developed technique for extracting stellar spectra from crowded field observations by Kamann et al. (2013). Applying the knowledge we gained so far on multimass models, I present, in the second half, the modelling of NGC 6101. For this, I additionally use all available *Hubble Space Telescope* data of NGC 6101 as well as the newly released data of this globular clusters from the $Gaia$ (Gaia Collaboration et al. 2016a,b) satellite. For the creation of the needed mass function I use an improved version of the mass function generation code from Balbinot and Gieles (2018) which I present in Appendix A. I find that NGC 6101 most likely retained $2 \pm 1\%$ of its assumed initial black holes, which corresponds to 86^{+30}_{-23} black holes with a total mass of $291^{+144}_{-84}\,\mathrm{M}_\odot$ mass.

In the final Chapter 5, I give a conclusion, highlighting the most important results from this PhD Thesis and discussing their impact in the general context. Finally, I will give an outlook on future projects which might profit from my work.

Chapter 2

Testing lowered isothermal models with direct N-body simulations of globular clusters - II: Multimass models

Abstract

Lowered isothermal models, such as the multimass Michie-King models, have been successful in describing observational data of globular clusters. In this study, I assess whether such models are able to describe the phase space properties of evolutionary N-body models. I compare the multimass models as implemented in LIMEPY (Gieles & Zocchi) to N-body models of star clusters with different retention fractions for the black holes and neutron stars evolving in a tidal field. I find that multimass models successfully reproduce the density and velocity dispersion profiles of the different mass components in all evolutionary phases and for different remnants retention. I further use these results to study the evolution of global model parameters. I find that over the lifetime of clusters, radial anisotropy gradually evolves from the low- to the high-mass components and I identify features in the properties of observable stars that are indicative of the presence of stellar-mass black holes. I find that the model velocity scale depends on mass as $m^{-\delta}$, with $\delta \simeq 0.5$ for almost all models, but the dependence of central velocity dispersion on m can be shallower, depending on the dark remnant content, and agrees well with that of the N-body models. The reported model parameters, and correlations amongst them, can be used as theoretical priors when fitting these types of mass models to observational data.

This Chapter was published in Monthly Notices of the Royal Astronomical Society (MNRAS), Volume 470, Issue 3, p.2736-2761 (Peuten et al. 2017).

2.1 Introduction

The amount of available data from observations of globular clusters (GCs) is steadily increasing. With the arrival of the ESA–Gaia data (Gaia Collaboration et al. 2016c), we are entering the era of high-precision kinematics, allowing us to study properties of GCs with unprecedented detail. This calls for adequate methods of analysing and describing them in an equally detailed way. Despite the fact that GCs are thought to be free of dark matter (Baumgardt et al. 2010; Ibata et al. 2013; Baumgardt 2017), and to have evolved to spherical and isotropic configurations as the result of two-body relaxation, GCs are complex systems to model. They consist of stars and stellar remnants with different masses and luminosities and primordial and dynamically processed binary stars (Heggie 1975; Goodman and Hut 1989; Hut et al. 1992; Heggie et al. 2006; Trenti et al. 2007). The mass and luminosity functions depend on the stellar initial mass function (IMF), age and metallicity. GC stellar populations display chemical anomalies (Gratton et al. 2004) and broadened main sequences (MS), possibly the result of variations in the helium abundance (Milone et al. 2014). Furthermore GCs evolve in a galactic tidal field that influences their evolution and present-day properties (Chernoff and Weinberg 1990; Johnston et al. 1999; Takahashi and Portegies Zwart 2000; Baumgardt and Makino 2003; Küpper et al. 2010; Rieder et al. 2013; Renaud et al. 2017).

Modelling GCs on a star-by-star basis using direct N-body models has only become possible recently: Hurley et al. (2005) presented the first N-body simulation of an open cluster, Zonoozi et al. (2011) modelled a low-mass GC and finally Heggie (2014) and Wang et al. (2016) presented the first N-body simulations of GCs with $N \sim 10^6$. The faster Monte Carlo method allows to explore the parameter of the initial conditions to some extent (Heggie and Giersz 2008; Giersz et al. 2013). To infer properties for a large number of GCs with models with several degrees of freedom, static models that are fast to calculate are required. By using relatively simple models, that are motivated by the underlying physical processes that drive their evolution, differences between models and observations can be used to increase our understanding (Binney and McMillan 2011).

In the context of GCs, the King (1966) models are often compared to observations, although they cannot describe all GCs successfully. For example, McLaughlin and van der Marel (2005) find that the more extended Wilson (1975) models are better in describing the surface brightness profiles of some Galactic GCs. In addition, both King and Wilson models have isothermal cores, which are not able to describe the late stages of core collapse (Lynden-Bell and Eggleton 1980; Cohn 1980). The models I am going to test and discuss in the context of GCs are multimass, anisotropic and spherical models (hereafter multimass models), which describe the properties of GCs considering their stellar mass function (MF) in the form of mass bins. This formulation allows for different behaviour of the different components. These models are defined by a distribution function (DF) which is a solution of the collisionless Boltzmann equation assuming a Maxwellian velocity distribution that is 'lowered' to mimic the effect of a negative escape energy as the result of the galactic tides. The multimass formulation of a King model was first introduced by Da Costa and Freeman (1976, I note that a formulation of a multimass model was already presented in Oort and van Herk 1959). Gunn and Griffin (1979) extended these models including radial anisotropy as formulated by Eddington (1915) for isothermal models (see also Michie 1963).

Since their introduction, multimass models have been successfully used in a multitude of studies such as in Illingworth and King (1977), Pryor et al. (1986), Lupton et al. (1987), Meylan (1987), Richer and Fahlman (1989), Meylan and Mayor (1991), Meylan et al. (1995), Sosin (1997), Piotto and Zoccali (1999) and Richer et al. (2004) to name a few. More recently, they have been used in observational studies, such as those by Paust et al. (2010), Beccari et al. (2010), Sollima et al. (2012), Beccari et al. (2015) and Sollima et al. (2017), as well as in theoretical studies (Takahashi and Lee 2000; Sollima et al. 2015).

Davoust (1977) realized that the DFs of the Woolley (1954), King (1966) and Wilson (1975) models can be written as a single DF with one additional integer parameter. Gomez-Leyton and Velazquez (2014) further generalized this formulation, allowing to calculate models in between the three classical models. (Gieles and Zocchi 2015) (hereafter GZ15) took up these formulation and added radial anisotropy as defined in the Michie–King models (Michie 1963) and multiple mass components as in Gunn and Griffin (1979). GZ15 introduced a power-law dependence between mass and anisotropy radius for each mass bin, while Gunn and Griffin (1979) argued that was not necessary because most events that influence the anisotropy are mass independent or not very important. GZ15 also implemented the possibility to change the degree of mass segregation with an additional parameter δ that describes the relation between the velocity scale and mass, which in most models is assumed to be equal to $1/2$.

Despite their success in describing observational data, multimass models have been criticized for several assumptions made in their construction (see McLaughlin 2003 and Meylan and Heggie 1997). One such aspect is that multimass models have more parameters than single-mass models: in the formulation by GZ15, there are $2N_{\rm MB} + 5$ parameters and 2 scales, with $N_{\rm MB}$ being the number of mass bins, compared to 3 parameters and 2 scales for the single-mass model. It is therefore easier to fit multimass models to the data because they have more degrees of freedom (McLaughlin 2003). Not only the selection of the right number of mass bins, but also how they are defined is criticized as a 'usual compromise between convenience and realism', as Meylan and Heggie (1997) put it. Given the numerous studies successfully using multimass models, this problem does not seem to be too much of a concern, but I nevertheless explored it in my study. Another assumption for which multimass models have been criticized is the assumption of equipartition of energy (McLaughlin 2003; Trenti and van der Marel 2013). Indeed the velocity scale is usually assumed to scale with the mass as $m^{-1/2}$, but I note that evolutionary multimass models only achieve partial equipartition (Merritt 1981; Miocchi 2006; GZ15; Bianchini et al. 2016) as the result of the escape velocity.

Several aspects of multimass models were already analysed with the help of Fokker–Planck (Takahashi and Lee 2000) and N-body simulations (Sollima et al. 2015). The goal of this study is to compare the multimass models in the formulation by GZ15 to a set of N-body models to assess the quality of the former and to analyse whether some of the above mentioned criticism is justified. In this comparison I do not include any source of uncertainties, such as observational biases, to see how good the models are under ideal conditions. Hence, I determine the MF of the multimass models directly from the N-body data.

The comparison is done by fitting the multimass models to snapshots from different N-body models using a Markov Chain Monte Carlo (MCMC) method. Additionally, I study the new parameters which are now available in the extended formulation of the

models by GZ15. In particular, the continuous truncation parameter as introduced by Gomez-Leyton and Velazquez (2014) and the parameter that controls the mass dependence of the anisotropy for each mass bin. Furthermore, I study the behaviour of the mass segregation parameter δ, which in previous studies was fixed to $\delta = 1/2$. By letting this parameter free, I can test whether this assumption is justified. By varying the amount of stellar-mass black holes (BHs) and neutron stars (NSs) retained in the different N-body models, I also study their impact on the cluster as well as on the different parameters of the best-fitting models.

In Zocchi et al. (2016), a similar analysis was presented for single-mass models. This comparison showed that the single-mass models are successful in describing the different phases of the dynamical evolution. Zocchi et al. (2016) studied the development of radial anisotropy in GCs and found that the models can be used to put limits on the expected amount of radial anisotropy.

This paper is structured as follows: in the next section, I give a brief overview of the multimass models. Then in Section 2.3, I discuss how the N-body models were generated and I discuss their properties. In Section 2.4, I present the method used for the analysis and the challenges I encountered. The radial profiles of density, velocity dispersion and anisotropy are discussed in Section 2.5. In Section 2.6, I discuss the values of the best-fitting model parameters and scales, and their implications. Finally, in Section 2.7, I discuss my results and present my conclusions.

2.2 The LIMEPY Models

The multimass models used in this study are provided by the LIMEPY (Lowered Isothermal Model Explorer in PYTHON)[1] software package (GZ15). A model has different components, each representing stars in a mass range, characterized by a mean and total mass. The DF of the jth mass component is given by

$$f_j\left(E, J^2\right) = A_j \exp\left(-\frac{J^2}{2r_{\mathrm{a},j}^2 s_j^2}\right) E_\gamma\left(g, -\frac{E-\phi\left(r_\mathrm{t}\right)}{s_j^2}\right), \tag{2.2.1}$$

for $E < \phi(r_\mathrm{t})$ and 0 otherwise. The specific energy $E = v^2/2 + \phi(r)$ is one of the two integrals of motion, where v is the velocity and $\phi(r)$ the specific potential at a distance r from the centre. The energy E is lowered by the potential at the truncation radius $\phi(r_\mathrm{t})$. The function E_γ is defined as

$$E_\gamma\left(a, x\right) = \begin{cases} \exp\left(x\right) & a = 0 \\ \exp\left(x\right) P\left(a, x\right) & a > 0 \end{cases} \tag{2.2.2}$$

with $P\left(a, x\right) \equiv \gamma\left(a, x\right) / \Gamma\left(a\right)$ the regularized lower incomplete gamma function. The other integral of motion is the specific angular momentum $J = r v_\mathrm{t}$, where v_t is the tangential component of the velocity vector.

The anisotropy radius r_a is a parameter that controls how anisotropic the model is. The system is isotropic in the centre, radially anisotropic in the intermediate part and near r_t it is isotropic again. For small values of r_a, the models are strongly anisotropic and for

[1] https://github.com/mgieles/limepy

values of r_a lager than r_t, the models are completely isotropic. GZ15 include a power-law dependence between mass and anisotropy radius:

$$r_{\mathrm{a},j} = r_\mathrm{a}\mu_j^\eta \tag{2.2.3}$$

with μ_j the dimensionless mean mass of stars in the jth mass component, defined as:

$$\mu_j = \frac{m_j}{\bar{m}} \tag{2.2.4}$$

where m_j is the mean mass of stars in the jth component and $\bar{m}$ a reference mass which I set equal to the global mean mass. If η is set to zero the anisotropy radius is independent of the mass as in Gunn and Griffin (1979). LIMEPY expects r_a to be input in units of the King radius (r_0), $\hat{r}_\mathrm{a} = r_\mathrm{a}/r_0$, hence $\hat{r}_\mathrm{a}$ is the parameter I vary.

The truncation parameter g was introduced by Gomez-Leyton and Velazquez (2014) and describes the polytropic part near the escape energy. The polytropic index n relates to g as $n = g + 3/2$ and this formulation allows to calculate models in-between the classical models: for $g = 0$ and $r_\mathrm{a} \gg r_\mathrm{t}$, the DF is identical to the one from the Woolley model (Woolley 1954). A Michie–King (Michie 1963; King 1966) model is reproduced for $g = 1$ and for $g = 2$ one gets the non-rotating Wilson model (Wilson 1975). The range of possible values for the model parameter are $0 \leq g \leq 3.5$ because as discussed in Gomez-Leyton and Velazquez (2014) and GZ15, there are no finite models above $g = 3.5$. The final parameter needed to define the models is the dimensionless central potential W_0 (King 1966, $\hat{\phi}_0$ in GZ15) which specifies how centrally concentrated the model is. It is a boundary condition for solving Poisson's equation.

Besides these parameters, there are also two constants which define the physical scales of the model: one is the global velocity scale s and the other is the normalization constant A which sets the phase space density. Instead of these scales, the code needs as input the total cluster mass M_Cl and a radial scale r_scale (which can be r_0, the half-mass radius r_h, the viral radius r_v or r_t), which are internally converted to A and s.

The velocity scale s_j is deduced from s as:

$$s_j = s\mu_j^{-\delta} \tag{2.2.5}$$

It is usually assumed that $\delta = 1/2$, but in this study I determine the value of this parameter from the fits to the N-body models.

The constants s_j and A_j are connected to the mass in each component (M_j), which the user provides together with m_j. It must be noted that M_Cl is a required input parameter, independent from the M_j parameters, because the latter are only used to compute the relative masses in each component. Only after the model is solved, $\sum_j M_j = M_\mathrm{Cl}$.

Given these five parameters (g, W_0, δ, r_a and η) and two scales (M_Cl, r_scale) together with the description of the mass bins (M_j, m_j) LIMEPY first calculates the density for each mass bin via:

$$\rho_j = \int f_j\left(E, J^2\right) d^3v \tag{2.2.6}$$

Then, the dimensionless Poisson equation is solved

$$\nabla^2\hat{\phi} = -9\sum_j \alpha_j\hat{\rho}_j \tag{2.2.7}$$

with $\alpha_j = \rho_{j,0}/\rho_0$, $\hat{\rho}_j = \rho_j/\rho_{j,0}$ and the dimensionless positive potential $\hat{\phi} = (\phi(r_\mathrm{t}) - \phi)/s^2$, is iteratively solved by varying α_j until the calculated M_j converges to the input values. After the model is solved, it is scaled to M_Cl and r_scale. I can then find the likelihood for any phase space coordinate using the DF (equation 2.2.1).

In equation (2.2.4), I set $\bar{m}$ to the mean mass of the cluster. In the formulation by Da Costa and Freeman (1976), Gunn and Griffin (1979) and GZ15, $\bar{m}$ is the central density weighted mean mass. After performing several comparisons, I found that models calculated by the two different formulations give the same results within the numerical uncertainties. Furthermore I found that using the global mean mass instead speeds up the calculation, especially for models with BHs. When using the global $\bar{m}$ the meaning of two model parameters is modified compared to Da Costa and Freeman (1976), Gunn and Griffin (1979) and GZ15: W_0 and r_a both represent their value for a hypothetical mass group with a mass of $\bar{m}$. Besides computational improvement, this change from the original formulation also allows us to compare the multimass W_0 value with the single-mass W_0 value, as both represent the W_0 value for the mean mass group.

One can easily translate the values given in one $\bar{m}$ definition (W_0, $\hat{r}_\mathrm{a}$) to another $\bar{m}^*$ definition (W_0^*, $\hat{r}_\mathrm{a}^*$) by applying the following two equations:

$$W_0^* = W_0 \left(\frac{\bar{m}^*}{\bar{m}} \right)^{2\delta} \tag{2.2.8}$$

$$\hat{r}_\mathrm{a}^* = \hat{r}_\mathrm{a} \left(\frac{\bar{m}^*}{\bar{m}} \right)^{(\eta+\delta)} \tag{2.2.9}$$

The δ term in equation (2.2.9) comes from the r_0 dependence of $\hat{r}_\mathrm{a}$.

As further improvement to the original formulation of the LIMEPY models I found that radially anisotropic models can be constructed faster if one first calculates the M_j array of the corresponding isotropic model and then uses this model as starting point to solve the anisotropic model. As with the previous improvement, the differences are only of numerical nature. This procedure is now implemented in the current distribution of LIMEPY.

2.3 Description of the N-body models

For the computation of the N-body data, I use the approach presented in Trenti et al. (2010): the stellar evolution is done first and separately from the dynamical evolution. I do this because Galactic GCs have different dynamical ages but have all roughly the same physical age of around $12\,\mathrm{Gyr}$. I consider models with different retention fractions of NSs and BHs and analyse them at various dynamical ages. Temporal units are always expressed in units of the initial half-mass relaxation time ($\tau_{\mathrm{rh},0}$) of the N-body model.

2.3.1 Set-up of the N-body models

For this analysis, I run four N-body models, with different amounts of NSs and BHs, which where kindly simulated for me by Dr. Alice Zocchi. Each N-body model was set up as a cluster with $N = 10^5$ stars initially following the Hénon isochrone model (Hénon

1959) with $r_{\rm h} = 2.25\,{\rm pc}$. As IMF, I adopted a Kroupa IMF (Kroupa 2001) in the mass range between $0.1\,{\rm M}_\odot$ and $100\,{\rm M}_\odot$ without any primordial binaries. Then, by using the fitting formula by Hurley et al. (2000) and assuming a metallicity of $[{\rm Fe/H}] = -2$, the stars were evolved to an age of about $12\,{\rm Gyr}$.

The effect of supernova kick velocity was mimicked by removing a certain fraction of NSs and BHs from the initial conditions described above. The retention fraction of NSs and BHs after supernova kicks is highly uncertain (Repetto et al. 2012; Mandel 2016). To bracket all possible cases, four different values for the fraction of remnants that are retain in the cluster, were consider : 100 per cent (all the remnants are retained, simulation N1), 33 per cent (simulation N0.3), 10 per cent (simulation N0.1) and 0 per cent (all the remnants are removed, simulation N0). The initial half-mass relaxation time for all four clusters was $\tau_{\rm rh,0} = 350\,{\rm Myr}$ before the stellar evolution and the removal of the dark remnants, after these steps the $\tau_{\rm rh,0}$ values are $412\,{\rm Myr}$ for N1, $426\,{\rm Myr}$ for N0.3, $427\,{\rm Myr}$ for N0.1 and $428\,{\rm Myr}$ for N0.

The clusters are evolved on a circular orbit with a circular velocity of $V_{\rm c} = 220\,{\rm kms}^{-1}$ at a distance of $R_{\rm G} = 4\,{\rm kpc}$, in a singular isothermal galactic potential to mimic a galaxy. The equation of motion is solved in an inertial reference frame centred on the cluster.

These four stellar systems were then dynamically evolved with the state-of-the art N-body integrator NBODY6 (Aarseth 2003), in the variant with GPU support (Nitadori and Aarseth 2012), until total dissolution of each cluster, i.e. until less than 100 objects are left in the cluster. Every object reaching a distance greater than twice the Jacobi radius ($r_{\rm J}$) is considered lost and is removed from the N-body model. As the stellar evolution is done before the actual N-body simulation, binaries which formed in the course of the simulations were also only evolved dynamically.

A snapshot of each cluster is taken every ${\rm Gyr}$, resulting in 48 snapshots[2] (11 for model N1, 13 for model N0.3, 12 for model N0.1 and 12 for model N0) which I fit the multimass models to (Section 2.4).

2.3.2 Selecting bound objects

Because multimass models describe bound objects in a cluster, I removed any unbound object from the N-body models. I discuss here how I selected the unbound objects for each N-body snapshot.

First, I determine the Jacobi radius

$$r_{\rm J} = \left(\frac{GM_{\rm Cl}}{2\Omega^2}\right)^{1/3} \tag{2.3.1}$$

in which $M_{\rm Cl}$ is the total mass within $r_{\rm J}$ and $\Omega = V_{\rm c}/R_{\rm G}$ is the orbital angular velocity. As a first guess, I set $M_{\rm Cl}$ equal to the total mass of all stars in the snapshot and then determine $r_{\rm J}$ through an iterative approach.

With $r_{\rm J}$ determined I am now able to calculate the specific critical energy which is equal to the potential at $r_{\rm J}$

$$E_{\rm crit} = \phi\left(r_{\rm J}\right) = -\frac{GM_{\rm Cl}}{r_{\rm J}} \tag{2.3.2}$$

[2]The snapshots can be retrieved from `http://astrowiki.ph.surrey.ac.uk/dokuwiki/doku.php?id=tests:collision:mock_data:challenge_2`

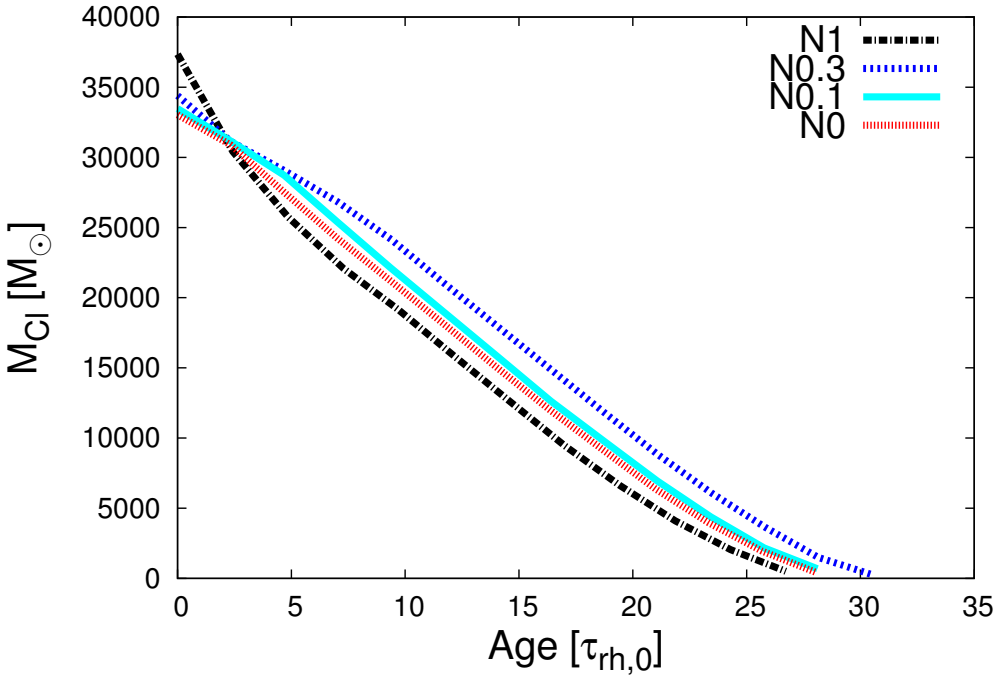

Figure 2.1: Evolution of the cluster mass $M_{\rm Cl}$ for the four N-body models. Age is given in units of their $\tau_{\rm rh,0}$.

The true critical energy is different as equation (2.3.2) neglects the tides. I adopted this definition nevertheless to be consistent with the multimass models, which also do not account for the changed potential due to tidal effects. I considered an object bound if it is within $r_{\rm J}$ and for its energy it holds $E_i < E_{\rm crit}$, and I only used these bound objects in the rest of this analysis.

2.3.3 Properties of the N-body models

Fig. 2.1 shows how $M_{\rm Cl}$ for the four different N-body models evolves over the course of the simulation. It is apparent that the cluster with 100 per cent initial BH and NS retention (simulation N1) has the highest initial mass loss, but there seems to be no direct correlation between the number of BHs and NSs and initial mass loss as can be seen from the other three N-body models. Over the course of evolution the four models seem to have aligned their mass-loss rate which is in accordance with the findings of Lee and Ostriker (1987) and Gieles et al. (2011) that the escape rate of clusters with the same mass mainly depends on the tidal field, which is the same for all four models.

In Fig. 2.2, I have plotted the evolution of $r_{\rm h}$ for the four different N-body models. As can be seen in the figure, increasing the retention fraction of the BHs leads to an expansion of the cluster: simulation N1, with 100 per cent NS and BH retention has an $r_{\rm h}$ which is on average twice as large as the $r_{\rm h}$ from simulation N0 with no NS and BH retention. The cluster in simulation N0.3 loses all of its BHs at around $7\tau_{\rm rh,0}$ and for the rest of the simulation its $r_{\rm h}$ resembles that of N0. The effect of stellar-mass BHs on the radius evolution was also described by Mackey et al. (2008). The global evolution of $r_{\rm h}$ however is essentially the same, independent of BHs and NSs retained, and follows the description

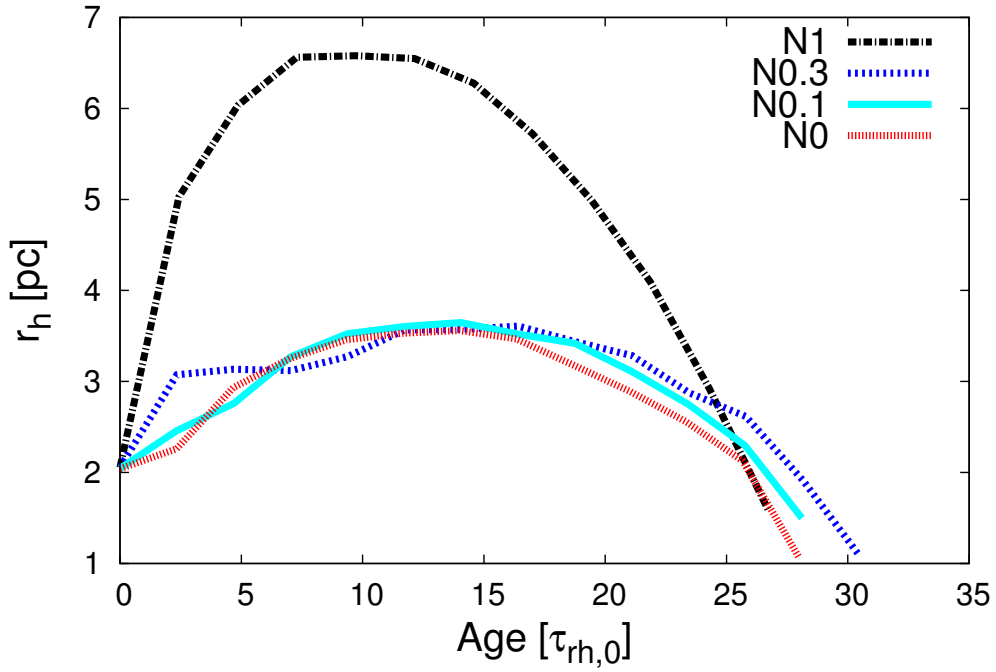

Figure 2.2: Evolution of the cluster half-mass radius $r_{\rm h}$ for the four N-body models. Age is given in units of their $\tau_{\rm rh,0}$.

in Gieles et al. (2011). In the first half of their lifetime, the clusters are in the expansion-dominated phase while in the second half the clusters are in the evaporation-dominated phase during which $r_{\rm h}$ decreases again until total dissolution.

Fig. 2.3 shows the relative number evolution for the BHs and NSs in the simulation N1, N0.3 and N0.1. As can be seen in the bottom figure, the cluster from N-body simulation N1 with 100 per cent initial BHs and NSs retention is the only cluster that retains its BHs almost until to the end of its lifetime, while the cluster from N-body simulation N0.3 loses all its BHs at around $7\tau_{\rm rh,0}$ and the one from simulation N0.1 already at $2\tau_{\rm rh,0}$. Looking at the NSs in the top of Fig. 2.3, I see their initial loss is not as strong as for the BHs. But as soon as all BHs have left the cluster, the NSs escape rate increases such that the cluster N0.1 loses all its NS at around $\sim 21\tau_{\rm rh,0}$. Only the cluster from N-body simulation N1 has a population of NS left at the end of its lifetime. After all BHs are lost, NSs, then being the most massive objects in the cluster, segregate to the centre and are then ejected from the cluster due to interactions they experience with each other.

Tables B.1-B.4 list various properties of the different snapshots, such as the dynamical age, the bound mass and the number of NSs and BHs.

2.3.4 Mean mass at different radii

As I will also discuss in Sec. 3.3.2 (Peuten et al. 2016), I find that the mean mass profile is independent of the remnant retention fraction. In Fig. 2.4, I plot this for all four N-body models at four different times in their evolution: $2.3\tau_{\rm rh,0}$, $7.1\tau_{\rm rh,0}$, $16.5\tau_{\rm rh,0}$ and $26\tau_{\rm rh,0}$. Looking at the different times I see that the overall behaviour is the same for all models independent of their dark remnant population. Some divergences between the different

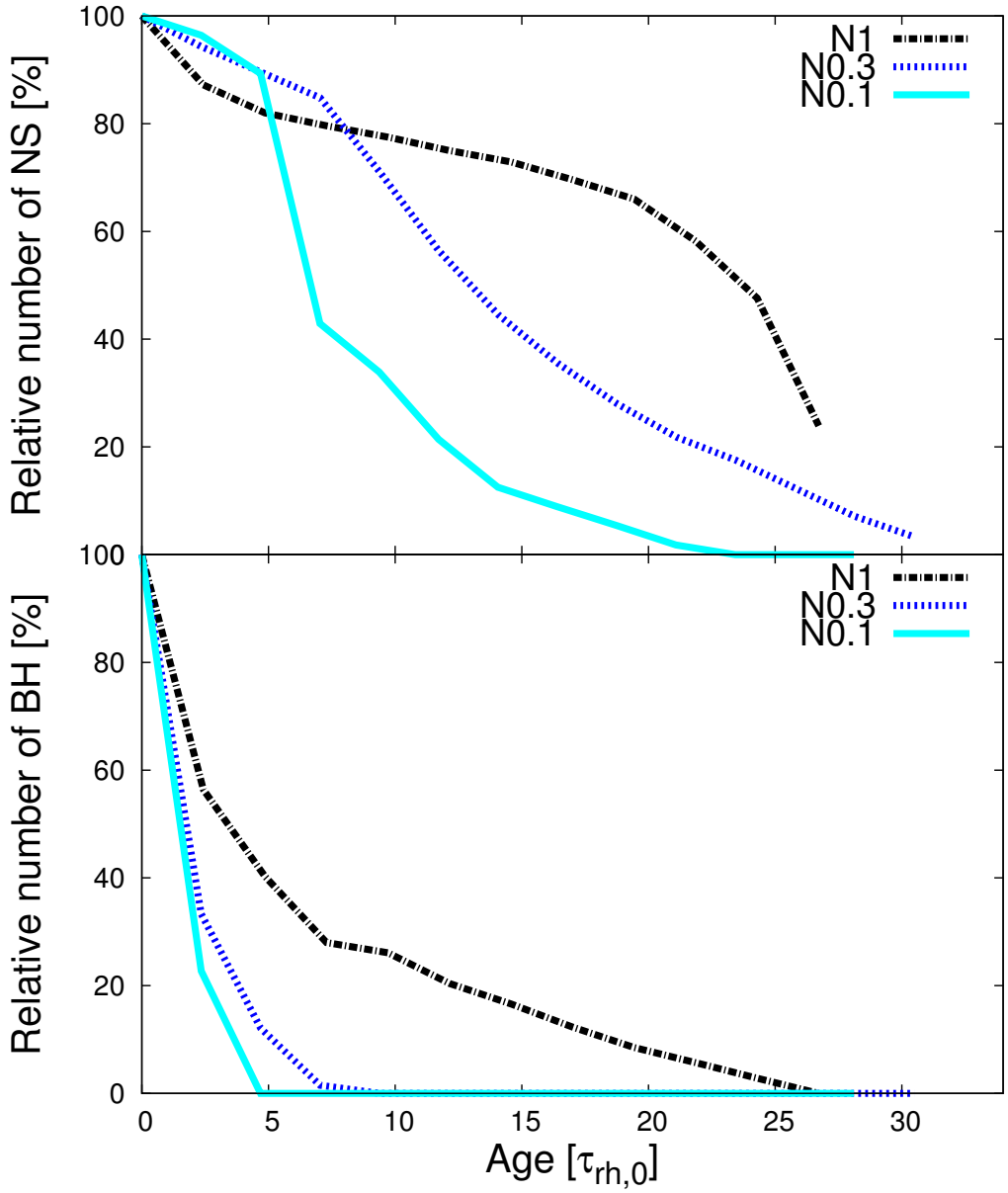

Figure 2.3: Evolution of the relative number of NS (top) and BH (bottom) as function of time in units of $\tau_{\rm rh,0}$ for the three models which initially retained BHs and NSs.

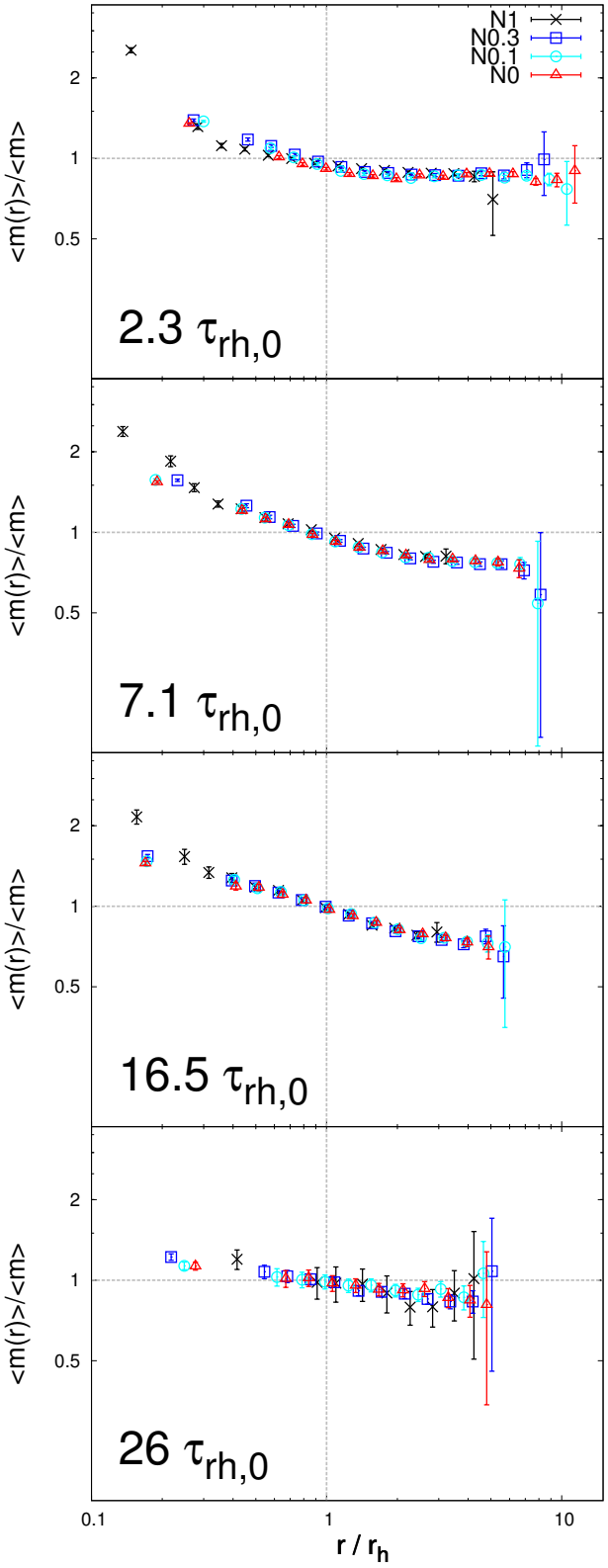

Figure 2.4: Relative mean mass (i.e. mean mass of stars in radial bins divided by the total mean mass) as a function of the distance from the cluster centre in units of $r_{\rm h}$, for all simulations at four different times: $2.3\tau_{\rm rh,0}$, $7.1\tau_{\rm rh,0}$, $16.5\tau_{\rm rh,0}$ and $26\tau_{\rm rh,0}$. Triangles (red), circles (cyan), boxes (blue) and stars (black) refer to simulation N0, N0.1, N0.3 and N1, respectively. Error bars denote 1σ uncertainties.

N-body models can be seen in the first snapshot at $2.3\tau_{\rm rh,0}$ but over the course of evolution these differences diminish. The profiles get flatter over time. This is comparable to the behaviour found for a set of N-body models where the dynamical and stellar evolution were done concurrently in Chapter 3 (Peuten et al. 2016). Here, the evolution over time is less strong because the stellar evolution was done before the dynamical evolution. I am not aware of a theory providing an explanation for this attractor solution of $\bar{m}(r)$, but for single-mass system it is known that after several relaxation times the evolution becomes self-similar (Hénon 1961, 1965). Also it had been shown that the evolution of radii and mass of the multimass systems is comparable to those of single-mass systems (Lee and Goodman 1995; Gieles et al. 2010) but faster. Furthermore Giersz and Heggie (1996, 1997) showed in multimass N-body models that after some time the mean mass in Lagrangian shells stops evolving and, to a first approximation, stays constant. Although I do not explore this here, this result could be used as a theoretical prior when comparing multimass models to data.

2.4 Method

To determine the best-fitting multimass models for each snapshot I use the MCMC software package EMCEE (Foreman-Mackey et al. 2013), which is a pure-PYTHON implementation of the Goodman & Weare's Affine Invariant MCMC Ensemble sampler (Goodman and Weare 2010). The PYTHON implementation makes it straightforward to couple it with LIMEPY. Furthermore, I benefit from the fact that I created a distributed grid computing version of PYTHON's *map()* function, thereby dynamically distributing efficiently the workload from several MCMC runs over all available CPU cores at the University of Surrey Astrophysics computing facilities.

The fitting process consists of computing a multimass model based on the input parameters provided by the MCMC walker position in parameter space and the current mass bin description (see the next section). Then the likelihood for each star in all mass bins is calculated using the DF (see equation 2.4.3) and the phase space position of the star from the N-body snapshot. By randomly varying the walker positions in parameter space, the MCMC algorithm tries to find those parameters which maximize the product of these individual likelihoods. The best-fitting value of each parameter is estimated as the median of the marginalized posterior distribution using all walker positions from all chains after removing the initial burn-in phase. This generally coincides with the value of the parameter providing the largest likelihood. For the 1σ errors, I use the values from the 16th and 84th percentiles.

2.4.1 Determining the mass bins

As mentioned in Section 2.1, the mass bin selection for multimass models is in most cases a choice of convenience (Meylan and Heggie 1997) as throughout the literature there is no general rule on how to select the best. This can be partially explained by the fact that most publications consider different data for their analyses, and have different research targets, leading to different approaches on how to set up the MF. However, I do know everything about my N-body models, and this allows us to test the mass bin selection for multimass

models. In particular, I want to understand what the minimum number of mass bins is to get a stable result and how to choose the bins.

For this analysis I use the N-body snapshot of simulation N1 at the time of $2.9\,\tau_{\rm rh,0}$. As I wanted to trace the overall evolution of the different star types, I opted against mixing them and therefore I give every star type at least one bin. This means that I have at least five mass bins, one each for the MS stars, the evolved stars[3] (ES), the white dwarfs (WD), NSs and BHs. Looking at the BHs, NSs and ESs I decided to not further split them into several bins given the fact that they have either a rather small range of possible masses and/or are to low in number to justify the split. This leaves us with MS stars and WDs which are both numerous and do have a large mass range: $0.1 - 0.83\,{\rm M}_\odot$ for the MS stars and $0.55 - 1.44\,{\rm M}_\odot$ for the WDs in my N-body snapshots.

First, I determine how the bin selection influences the results of the analysis. For this, I choose four different binning methods: a logarithmic binning, a linear binning, a binning where in each mass bin there is an equal number of stars and a binning where there is the same amount of mass in each mass bin. I fixed the number of WD mass bins to one and then for each bin type I calculated the multimass model repeatedly with increasing number of MS star bins. The general idea here is that with increasing number of mass bins, the overall parameters like $M_{\rm Cl}$, $r_{\rm h}$, etc., should converge to the value one would get for the ideal case, where each star has its own mass bin. I find that the results are almost independent of the way one chooses the binning: the number of MS mass bins needed to converge is the same and the difference between the different models are for all properties generally less than 5 per cent. I therefore choose for the further analysis the logarithmic binning.

Then I determine the minimum number of bins needed to get stable results, as increasing the number of bins also increases the computation time of the models. I varied the number of mass bins of the MS stars and the WDs independently from each other. Here again, I see that with increasing number of mass bins the different quantities converge. I find that I need at least two WDs mass bins and at least four MS stars mass bins for the different quantities to converge. Increasing the number of bins any further does not improve the results (values are comparable within 5 per cent). For my further analysis, I opt to use five MS stars mass bins and three WDs mass bins. Therefore, in total I consider eleven mass bins (MS: 5; ES: 1; WD: 3; NS: 1; BH: 1) to set up my multimass models. Tables B.5-B.8 list the mass bins for all N-body snapshots used.

2.4.2 Artificial background population

Before I present the results, I discuss a particularity which I encountered in my analysis. The potential of LIMEPY models is spherical, however, the true potential of the cluster is triaxial because of the effect of tides. Also the Lagrange points of the cluster, through which stars can escape (Fukushige and Heggie 2000; Baumgardt 2001; Küpper et al. 2010; Claydon et al. 2017), are not accounted for in the multimass model. Therefore, the models are not able to describe the objects near the critical energy correctly. From this, it follows that some of the objects which are unbound in the true potential are still found bound in my definition and cannot be described by the model correctly. These objects pose a problem because they drive the fit to unrealistic parameter values.

[3] In this work, every post MS star which is not a remnant is called an ES.

To cope with this problem, I introduced an artificial background population with a constant likelihood (i.e. uniform distribution) in phase space. I added the artificial background population with a total mass of around 1 per cent of the original cluster mass to the N-body snapshot. This background population has the same MF as the cluster. The upper limit for the maximal distance and velocity are chosen to be twice the maximal values from the original snapshot ($r_{\rm max}$ and $v_{\rm max}$).

I describe the likelihood function of the background model as

$$\mathfrak{L}_B = \frac{M_{\rm Back}}{V\, M_{\rm tot}} \tag{2.4.1}$$

where $M_{\rm tot}$ is the total mass of the snapshot including the artificial background and $M_{\rm Back}$ is the mass of the background only. The phase space volume V is defined as

$$V = \frac{4}{3}\pi\,(2r_{\rm max})^3 \times \frac{4}{3}\pi\,(2v_{\rm max})^3 \tag{2.4.2}$$

The total likelihood of an object for a given model is calculated as

$$\mathfrak{L} = \frac{f(E,J^2)}{M_{\rm tot}} + \frac{M_{\rm Back}}{V\, M_{\rm tot}} \tag{2.4.3}$$

When integrated over the whole phase space volume within $2v_{\rm max}$ and $2r_{\rm max}$ the first term equals to $M_{\rm Cl}/\,M_{\rm tot}$ and the second to $M_{\rm Back}/\,M_{\rm tot}$, giving a total likelihood of unity, as required.

2.4.3 MCMC results

I initiate the MCMC walkers in a randomly chosen sphere in parameter space. For some snapshots, I run several fits with different initial conditions to test for any divergence. I chose flat priors restricted mainly by currently observed values for the parameters and/or by the range in which they are considered physically valid. For the MCMC fitting, I started out with around 500 walkers and found good fits for the N-body model N0 without BHs and NSs. For the other models, prominently those with BHs, converging fits were only achieved with at least 2000 walkers. On average, each MCMC chain was run for 1000 iterations and convergence was reached after around 300 iterations, which I trimmed from the MCMC chains for the calculation of the best-fitting parameters. The MCMC chain took on average longer to converge in snapshots with BHs than in snapshots without. In some cases, I also had to adjust the EMCEE scale parameter a, which is generally set to 2, to increase the acceptance rates (for details on how this affects the MCMC algorithm see the discussion in Foreman-Mackey et al. 2013, their equation 2).

In Figs 2.5 and 2.6, I show the marginalized posterior probability distribution for each parameter as well as the 2D projections of the posterior probability distribution representing the covariance between the different fitting parameters for two MCMC runs. Figs 2.5 and 2.6 show the results of the fitting to the N-body model N0 at $2.3\tau_{\rm rh,0}$, and to the N-body model N1 at $17.0\tau_{\rm rh,0}$, respectively. The obvious difference between the two models is that for model N1 there are two parameters, namely $r_{\rm a}$ and η that do not converge to a single value. The stellar system in this particular N-body snapshot is isotropic: values of

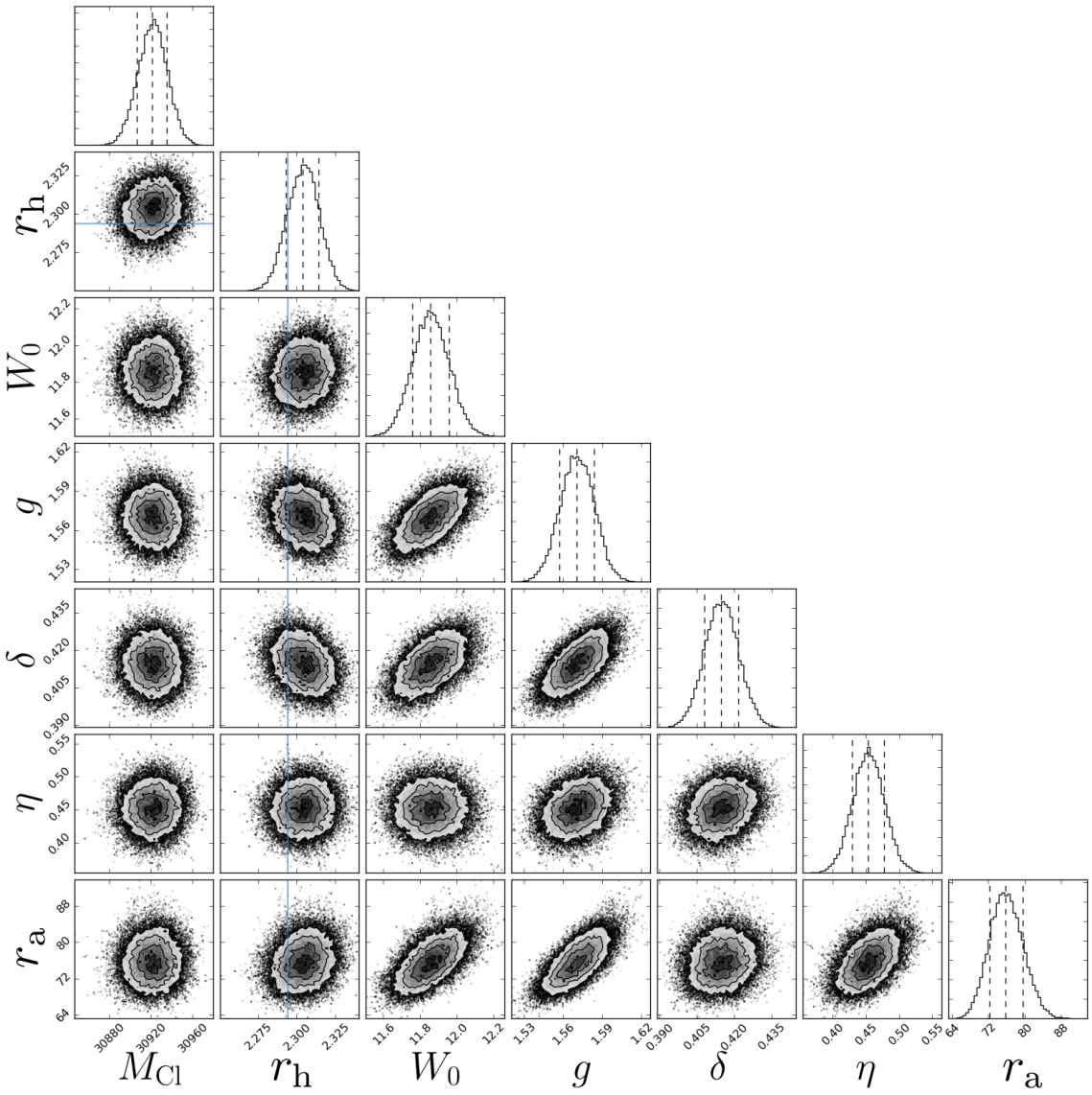

Figure 2.5: Marginalized posterior probability distribution and 2D projections of the posterior probability distribution for the model parameters and scales. This figure shows the results of the MCMC fitting to the N-body model N0 at $2.4\tau_{\rm rh,0}$. The dashed lines in the marginalized posterior probability distribution indicate the 16th, 50th and 84th percentiles.

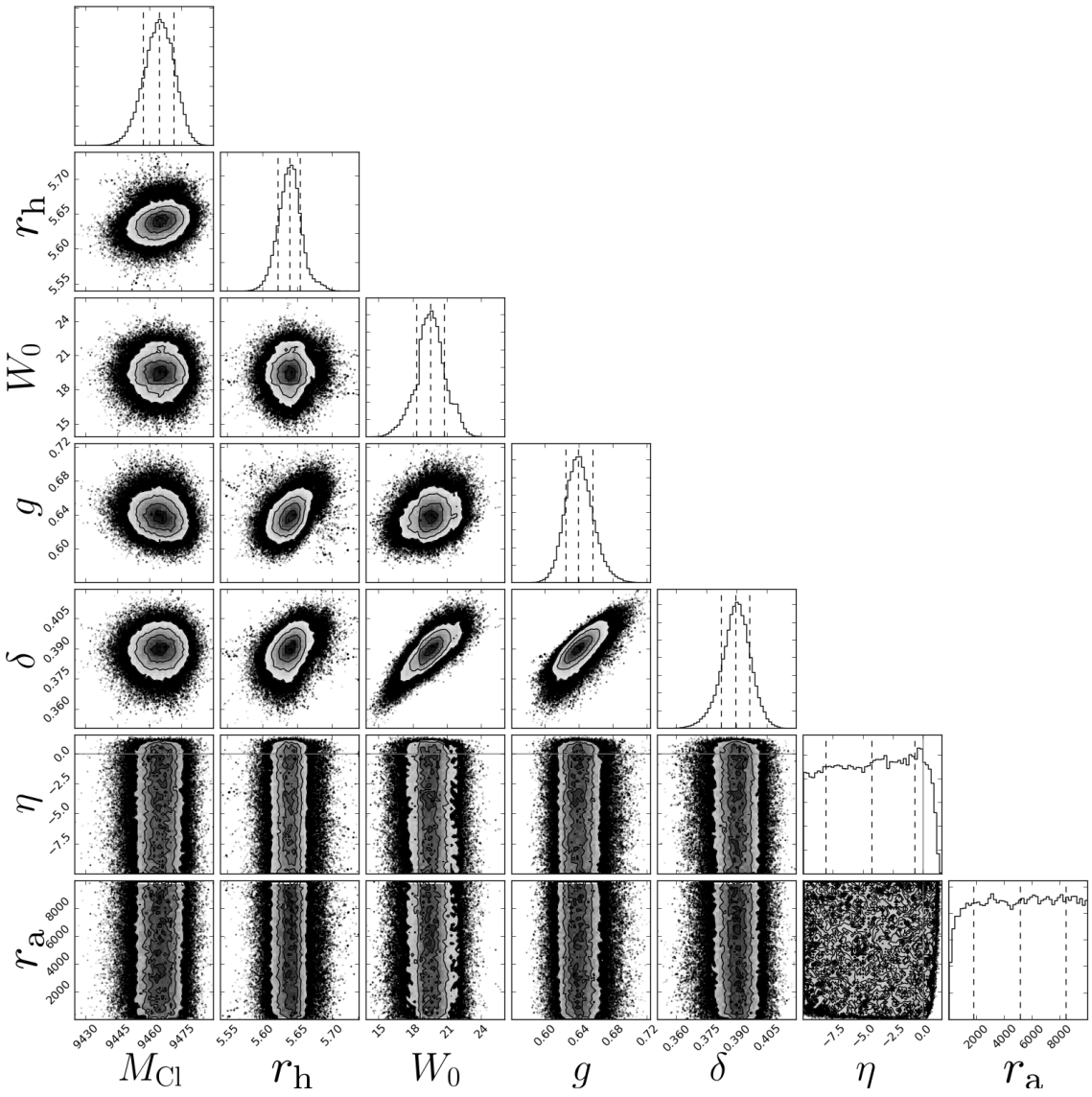

Figure 2.6: Marginalized posterior probability distribution and 2D projections of the posterior probability distribution for the model parameters and scales. This figure shows the results of the MCMC fitting to the N-body model N1 at $17.0\tau_{\rm rh,0}$. The dashed lines in the marginalized posterior probability distribution indicate the 16th, 50th and 84th percentiles. The best-fitting values of η and $r_{\rm a}$ are unconstrained because this stellar system is not radially anisotropic.

$r_{\rm a}$ larger than $r_{\rm t}$ generate isotropic models, equally likely to reproduce the data, and for this reason, the values of $r_{\rm a}$, and consequently of η, cannot be constrained.

Looking at the 2D projections of the posterior probability distribution in Figs 2.5 and 2.6, one can see that they are nearly circular for most of the parameter pairs. This shows that when using the full phase space information of each star, degeneracies between the different parameters can be alleviated.

Tables B.9-B.12 list the best-fitting parameters for all the N-body snapshots I considered.

2.5 Comparison of multimass models and N-body models

In the first part of my analysis, I compare the best-fitting multimass models with the results directly computed from the N-body snapshots for each model at all times.

2.5.1 Mass density profile

First, I compare the mass density profiles of the best-fitting multimass models and the N-body models. For this, I binned each mass bin of the N-body data such that in each radial bin there are at least 30 objects and each radial bin has a minimal radial width of $0.15\,\mathrm{pc}$. I assumed Poisson errors for the uncertainties of the binned data and define the position uncertainty by the 16th and 84th percentiles of the distribution of the positions of the objects in each bin. In Fig. 2.7, I compare the mass density profiles for the three models N1, N0.3 and N0 at four different times: $2.3\tau_{\rm rh,0}$ which is the first snapshot for each N-body model, $7.1\tau_{\rm rh,0}$, $16.5\tau_{\rm rh,0}$ and $26\tau_{\rm rh,0}$ the snapshot at the end of the clusters lifetime. For clarity I only show one mass bin per stellar type. I did not include the results of model N0.1, since they are similar to the results of model N0. Together with the best-fitting result from the multimass models, I also plot the results from the walker positions at the last iteration of the MCMC routine, reflecting the uncertainties of the results.

As can be seen from Fig. 2.7, the best-fitting multimass models reproduce the mass density profiles of the different mass components. Differences are only found in the outermost regions and innermost regions as well as for cases where the number of objects in a mass bin is low. For the outer regions, a difference is expected: as already discussed in Section 2.4.2, the models assume that the cluster is spherically symmetric, which is not the case in the N-body models as the clusters are slightly elongated due to tidal forces.

For the differences in the most central parts one sees that the mass density is underestimated for the heavier mass bins while for the lighter mass bins it is overestimated. This could be explained by the fact that these models are post core collapse, therefore their density profiles are slightly different from isothermal models (Lynden-Bell and Eggleton 1980). Given that the differences in the centre are small, one can see that multimass models are able to describe post-collapse models.

The overall agreement between multimass and N-body models for the density profiles is consistent with the findings of Sollima et al. (2017) who fitted Michie–King models to observational data of NGC 5466, NGC 6218 and NGC 6981: for all three GCs, the multimass models reproduce the observed mass density profiles (see their fig. 6). Differences are only found in the outer regions, most likely for the same reasons as discussed above.

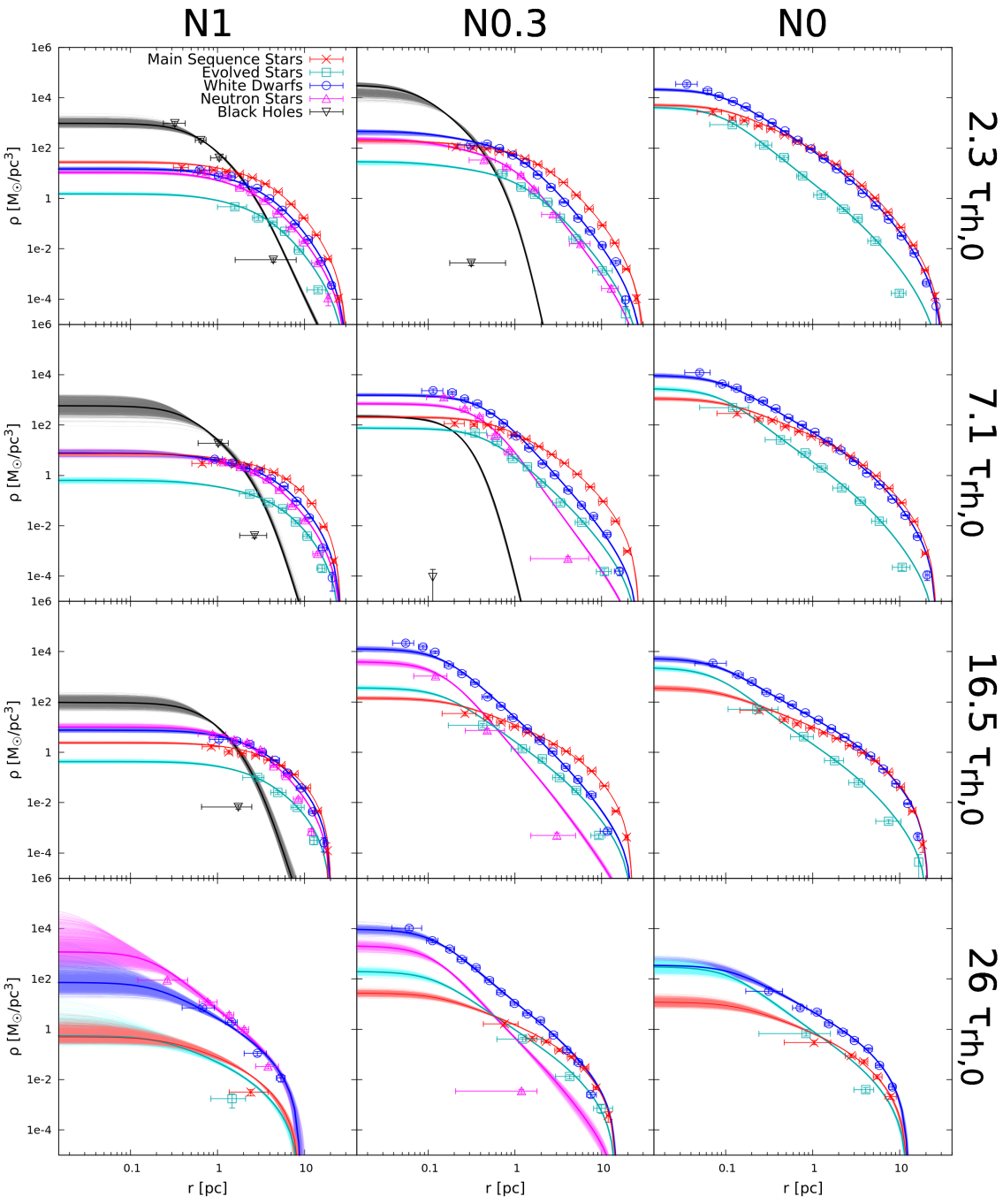

Figure 2.7: Comparison of the mass density profiles for models N1, N0.3 and N0 at four different ages: $2.3\tau_{\rm rh,0}$, $7.1\tau_{\rm rh,0}$, $16.5\tau_{\rm rh,0}$ and $26\tau_{\rm rh,0}$. The points represent the binned N-body data, the thick lines represent the best-fitting multimass models profiles and the thin lines represent the results from the walker positions at the last iteration. Red represents the MS stars, cyan – ESs, blue – WDs, pink – NSs and black – BHs. Error bars denote 1σ uncertainties.

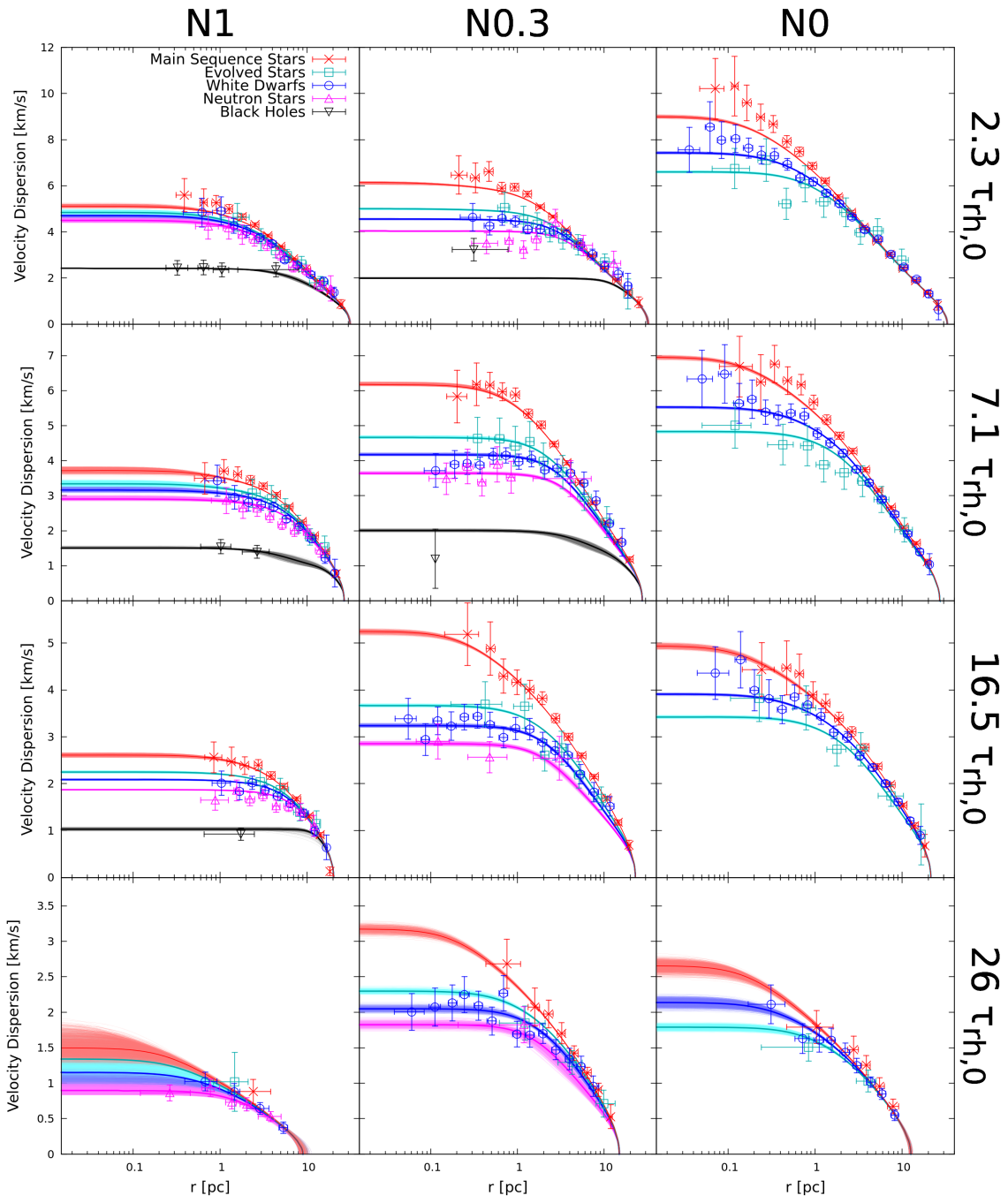

Figure 2.8: Comparison of the velocity dispersion profiles for models N1, N0.3 and N0 at four different ages: $2.3\tau_{\rm rh,0}$, $7.1\tau_{\rm rh,0}$, $16.5\tau_{\rm rh,0}$ and $26\tau_{\rm rh,0}$. The points represent the binned N-body data, the thick lines represent the best-fitting multimass models profiles and the thin lines represent the results from the walker positions at the last iteration. Red represents the MS stars, cyan – ESs, blue – WDs, pink – NSs and black – BHs. Error bars denote 1σ uncertainties.

When one compares the different models in Fig. 2.7 at the same dynamical ages it can be seen that models without BHs are denser and the stars are found far more concentrated than in models with BHs. The BHs in the centre 'push' the lower mass stars out of the core, which results in a large core radius ($r_{\rm c}$) as well as a larger $r_{\rm h}$, an effect further studied in Chapter 3 (Peuten et al. 2016) for the cluster NGC 6101. In the evolution of model N0.3, one can see how the cluster changes when all BHs have been lost: the central regions get efficiently populated by the next lighter objects and the resulting mass density profile of the cluster looks as concentrated as the one from model N0 at that same dynamical age, leaving no clue about its diminished BH population.

2.5.2 Velocity dispersion

For the comparison of the velocity dispersion profiles in Fig. 2.8, I used the same snapshots as for the mass density profiles. For the calculations of the velocity dispersions, I am using a mass-weighted approach to make the values comparable to the values from the multimass model as they are calculated for the mean mass of each mass bin. The velocity dispersion is therefore calculated as:

$$\sigma_k^2 = \frac{\sum_i^N m_i \left[v_{k,i} - \langle v_k \rangle\right]^2}{\sum_i^N m_i} \qquad k = r, \theta, \phi \tag{2.5.1}$$

with

$$\langle v_k \rangle = \frac{\sum_i^N m_i v_{k,i}}{\sum_i^N m_i} \qquad k = r, \theta, \phi \tag{2.5.2}$$

the mass-weighted mean velocity for each component. The calculation of the uncertainties of the binned N-body data was done using the description from Pryor and Meylan (1993) using their equation (12). Again, the results from the best-fitting multimass models are in agreement with the data from the N-body models. As with the mass density profiles, small difference can be seen in the outermost regions. In the plot of model N0.3 at $7.1\tau_{\rm rh,0}$, there is no value from the N-body snapshot for the BHs as there is only one BH left, in which case σ is undefined.

When comparing the different models at the same dynamical age I find that in clusters with BHs, the velocity dispersions for the different mass bins are smaller than in clusters without BHs (see discussion in Section 2.6.5). As the cluster is losing its BH population (see for example the evolution of model N0.3), the velocity dispersions of the different mass bins increase to the values seen in model N0 which had all its BHs removed before the actual N-body evolution, again leaving no hint of the lost BH population. In Section 2.6.5, I will look again at this relation and discuss an explanation for this behaviour.

2.5.3 Radial anisotropy

In this section, I consider the anisotropy of the velocities. In Section 2.5.3, I consider the anisotropy profile within the cluster and in Section 2.5.3 I consider the global anisotropy of the cluster as a whole.

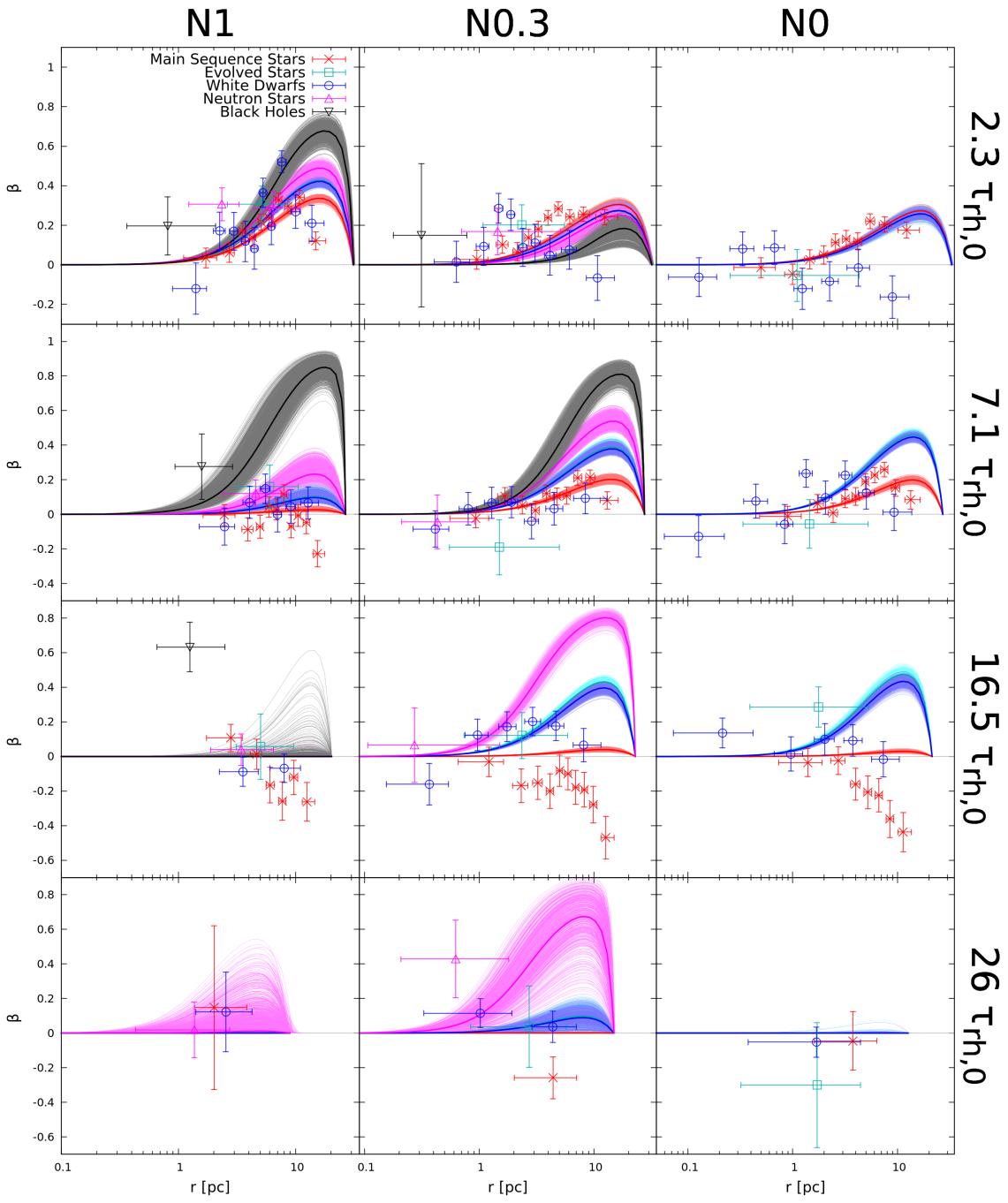

Figure 2.9: Comparison of the anisotropy profiles for models N1, N0.3 and N0 at four different ages: $2.3\tau_{\rm rh,0}$, $7.1\tau_{\rm rh,0}$, $16.5\tau_{\rm rh,0}$ and $26\tau_{\rm rh,0}$. The points represent the binned N-body data, the thick lines represent the best-fitting multimass models profiles and the thin lines represent the results from the walker positions at the last iteration. Red represents the MS stars, cyan – ESs, blue – WDs, pink – NSs and black – BHs. Error bars denote 1σ uncertainties.

Anisotropy profiles

The anisotropy parameter β is defined as (Binney and Tremaine 1987):

$$\beta \equiv 1 - \frac{\sigma_{\rm t}^2}{2\sigma_{\rm r}^2} \tag{2.5.3}$$

with $\sigma_{\rm r}$ the radial velocity dispersion and $\sigma_{\rm t}$ the tangential velocity dispersion. For $\beta < 0$, the orbits are tangentially biased, for $\beta = 0$ they are isotropic, for $0 < \beta < 1$ they are radially biased and for $\beta = 1$ they are radial.

In Fig. 2.9, I compare the anisotropy profiles from the best-fitting multimass models for a selection of mass bins to the anisotropy profiles from the N-body snapshots. As the β parameter is more affected by random scatter, I had to bin the data from the N-body snapshots differently than in the previous two plots. I varied the number of objects per bin, such that the average uncertainty in β is ≤ 0.1 and there are no more than 10 radial bins per mass bin to not overcrowd the plots. For the ESs and the BHs, the average β uncertainty was always well above 0.1 which is why I only show one radial bin for each in all snapshots.

Comparing the predictions from the best-fitting multimass model with the results from the N-body data, I find that when the snapshot has some degree of radial anisotropy the multimass models qualitatively reproduce them. This can be seen best with the mass bins from the MS stars. Also differences between the best-fitting multimass prediction and the binned data can be seen at the outer regions of the cluster. When some of the mass bins are tangentially anisotropic the best-fitting model is isotropic as my multimass models cannot describe any other kind of anisotropy.

Looking at the data from the snapshots itself, I see that the heaviest mass bins become more radially anisotropic, while the low-mass bins become first isotropic and then tangential anisotropic. I will discuss the evolution of the anisotropy further in Section 2.6.7 when I analyse the best-fitting η parameter.

Global anisotropy

To quantify the global anisotropy I use the parameter κ, that was introduced by Polyachenko and Shukhman (1981) and is defined as

$$\kappa = \frac{2K_{\rm r}}{K_{\rm t}} \tag{2.5.4}$$

where $K_{\rm r} = 0.5 \sum_i m_i v_{{\rm r},i}^2$ is the radial component of the kinetic energy and $K_{\rm t} = 0.5 \sum_i m_i v_{{\rm t},i}^2$ the tangential component. For $\kappa = 1$, the models are isotropic, for $\kappa > 1$ they are radially anisotropic and for $\kappa < 1$ they are tangentially anisotropic.

In Fig. 2.10, I compare the values of κ obtained for the best-fitting multimass models and for the N-body snapshots. For the uncertainties of the N-body data, I used Poisson statistics. The best-fitting multimass models are able to qualitatively reproduce the overall behaviour of the κ parameter. It can be seen that at later times, the low-mass stars are tangentially anisotropic, which cannot be reproduced by LIMEPY. This also explains why the best-fitting value of κ (and β) from the multimass models does not converge to unity immediately (or $\beta \simeq 0$): there are still radial orbits left and the tangential orbits are treated

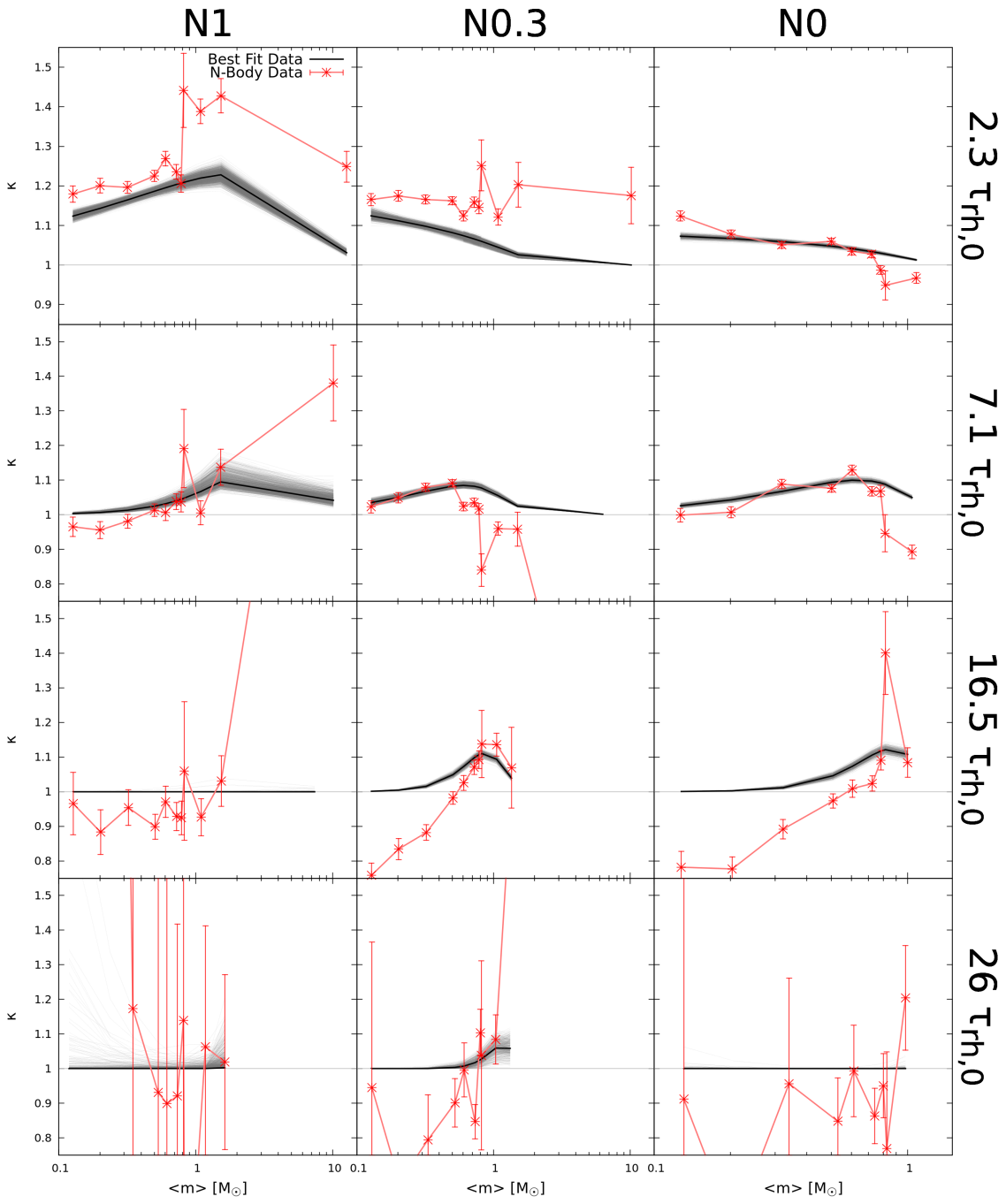

Figure 2.10: Comparison of the values of the global anisotropy parameter κ as a function of mass of the different components for models N1, N0.3 and N0 at four different ages: $2.3\tau_{\mathrm{rh},0}$, $7.1\tau_{\mathrm{rh},0}$, $16.5\tau_{\mathrm{rh},0}$ and $26\tau_{\mathrm{rh},0}$. The red points represent the N-body data, the thick black lines represent the best-fitting multimass models values and the thin grey lines represent the results from the walker positions at the last iteration. Error bars denote 1σ uncertainties.

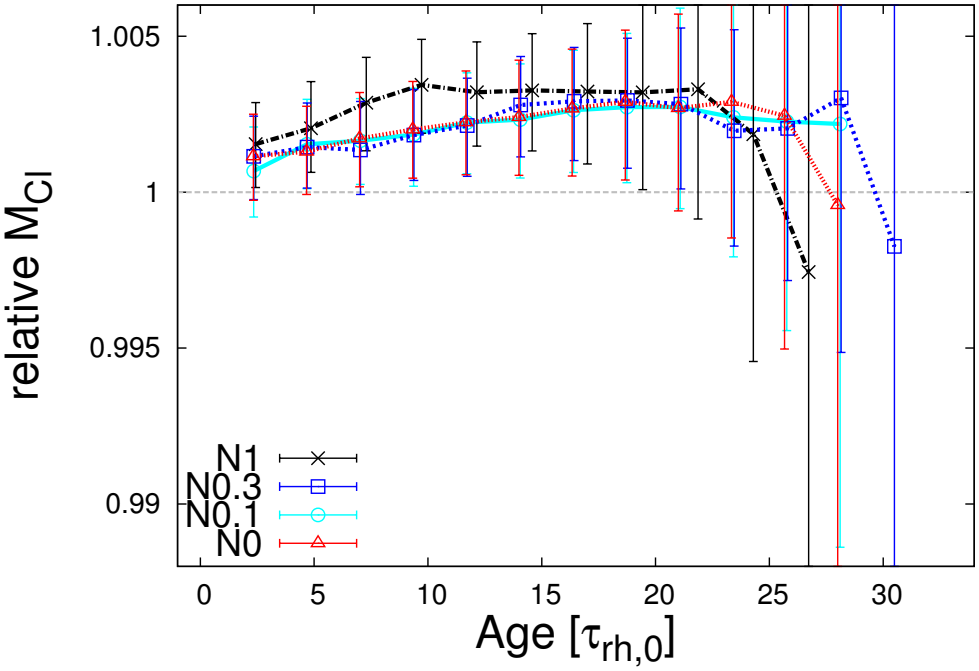

Figure 2.11: Best-fitting value of the total mass of the cluster, $M_{\rm Cl}$, divided by the true mass calculated from the N-body snapshots as a function of time in units of $\tau_{\rm rh,0}$. The multimass models reproduce the true masses within 1%. Error bars denote 1σ uncertainties.

as isotropic, so the best-fitting results for κ (and β) still indicate some radial anisotropy, resulting in a smoother transition from radial anisotropy to isotropy with respect to what is observed in the N-body data. Clusters that are dominated by tangential orbits are therefore, by construction, not well reproduced by the multimass models used in my study (see also Sollima et al. 2015).

Looking at the N-body data, I see that κ of the lowest mass bins typically goes down with time, while κ of the heaviest mass bins goes up. For model N1 with BHs, this change is faster than for model N0 with no BHs and NSs. I refer the reader to Section 2.6.7 for a further analysis.

2.6 Analysis of model parameters

I focus here on the best-fitting parameters resulting from my fitting procedure. The two model scale parameters can be computed directly from the N-body data, therefore I use them to assess the quality of the multimass models. For the other five model parameters, I am analysing their evolution to see whether they can give us some further insights into the clusters. Furthermore, I also discuss the evolution of two additional quantities ($r_{\rm t}$ and κ) to assess the quality of the models.

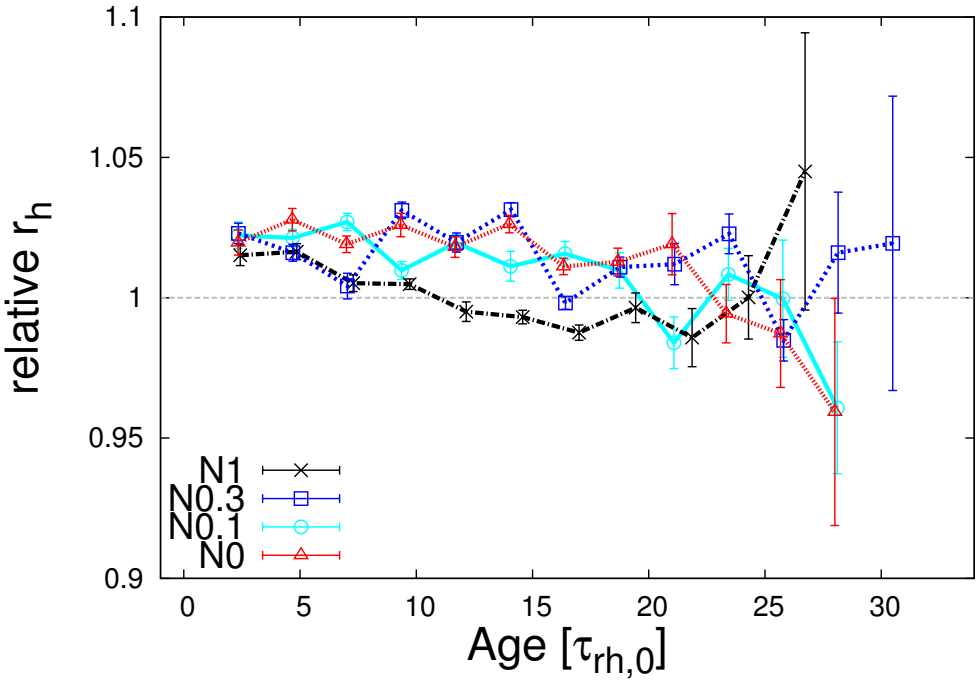

Figure 2.12: Best-fitting half-mass radius $r_{\rm h}$ divided by the true value calculated from the N-body snapshots as a function of time in units of $\tau_{\rm rh,0}$. The multimass models reproduce the true half-mass radii within 5%. Error bars denote 1σ uncertainties.

2.6.1 Total cluster mass

In Fig. 2.11, I plot the $M_{\rm CL}$ from the best-fitting multimass model divided by the true cluster mass as measured in the N-body model for all four N-body models throughout their cluster lifetime. As can be seen in this figure, the best-fitting value is always within 1% of the N-body value but almost none of these are consistent within the 1σ uncertainties: there is some systematic error in the multimass models which is not accounted for yet. However, given that the difference is always smaller than 1% this effect is negligible. The results are comparable to the single-mass results from Zocchi et al. (2016) where an accordance within 5% of the true values was found.

Sollima et al. (2015) found that single-mass models underestimated the mass of an N-body system by 50%, depending on its dynamical state. There are several differences between their study and ours which could lead to such different results. They are using simulated observations as input for their analysis, which affects the recovery of the MF. Shanahan and Gieles (2015) found that approximating mass-segregated clusters by single-component models leads to an underestimation of the mass by a factor of two or three, especially for metal-rich GCs. Also the models used in Sollima et al. (2015) have less parameters than the ones used here, as for example they do not incorporate the variable truncation parameter g. Zocchi et al. (2016) showed for single-mass models that the total mass is better recovered when allowing g to be free. I discuss the effect of g in Section 2.6.4.

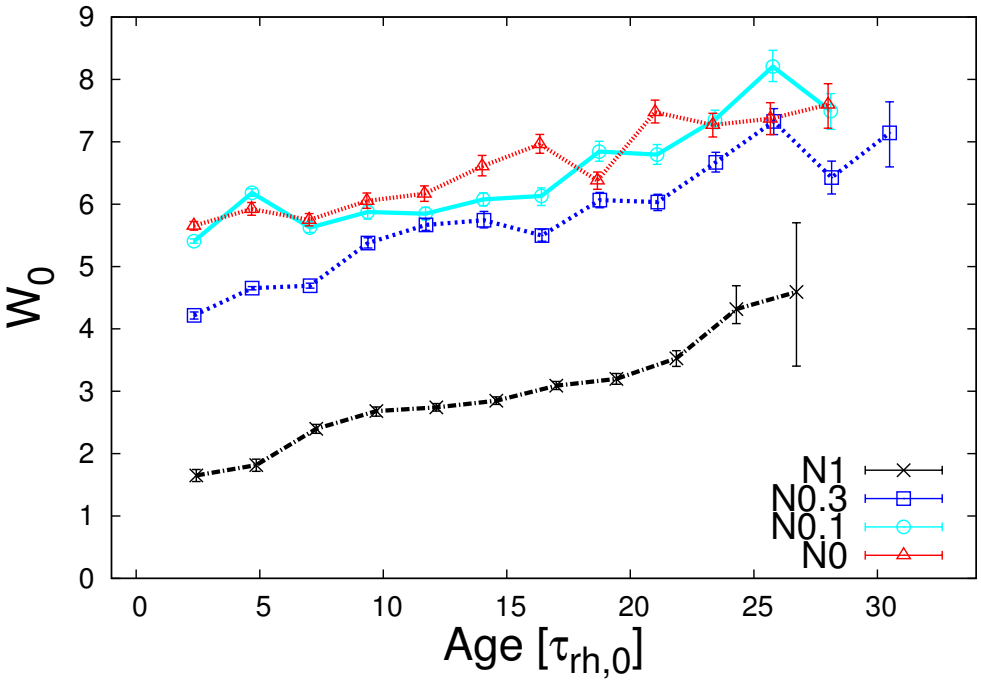

Figure 2.13: Best-fitting value of the central dimensionless potential, W_0, obtained for all four N-body models, as a function of time in units of $\tau_{\rm rh,0}$. Error bars denote 1σ uncertainties.

2.6.2 Half-mass radius

The second scale parameter that can be computed from the N-body models is $r_{\rm h}$: In Fig. 2.12, I plot $r_{\rm h}$ from the best-fitting multimass models divided by the true value as computed from the N-body data, for all four clusters throughout their lifetime. Again I find good agreement, within a few percent. As with $M_{\rm Cl}$, only a few of the data points show agreement within 1σ uncertainties. These results are comparable to the result for the single-mass case by Zocchi et al. (2016) who found an agreement within 7%.

2.6.3 Dimensionless central potential

Now that I have shown that multimass models can reproduce the most important cluster properties, I focus on analysing the other fitting parameters. First, I look at the dimensionless central potential W_0 for which the evolution over the whole lifetime for the four N-body models is plotted in Fig. 2.13. As discussed in Section 2.2, the W_0 value in multimass models represents the dimensionless central potential of a hypothetical mass group with a mass equal to the global mean mass. As the global mean mass increases from $(0.36 \pm 0.01)\,{\rm M}_\odot$ to $(0.8 \pm 0.2)\,{\rm M}_\odot$ during the evolution of the four N-body models, the W_0 values do not refer to the same stellar population and this needs to be kept in mind when comparing W_0 values of different N-body models and/or at different times. Using the central density weighted mean mass instead of the global mean mass has other issues, as can be seen for example in the snapshots of model N0.3 at $4.7\tau_{\rm rh,0}$ or in model N1 at $26.7\tau_{\rm rh,0}$ in Fig. 2.14. In both cases, the number of BHs decreases to (almost) zero reduc-

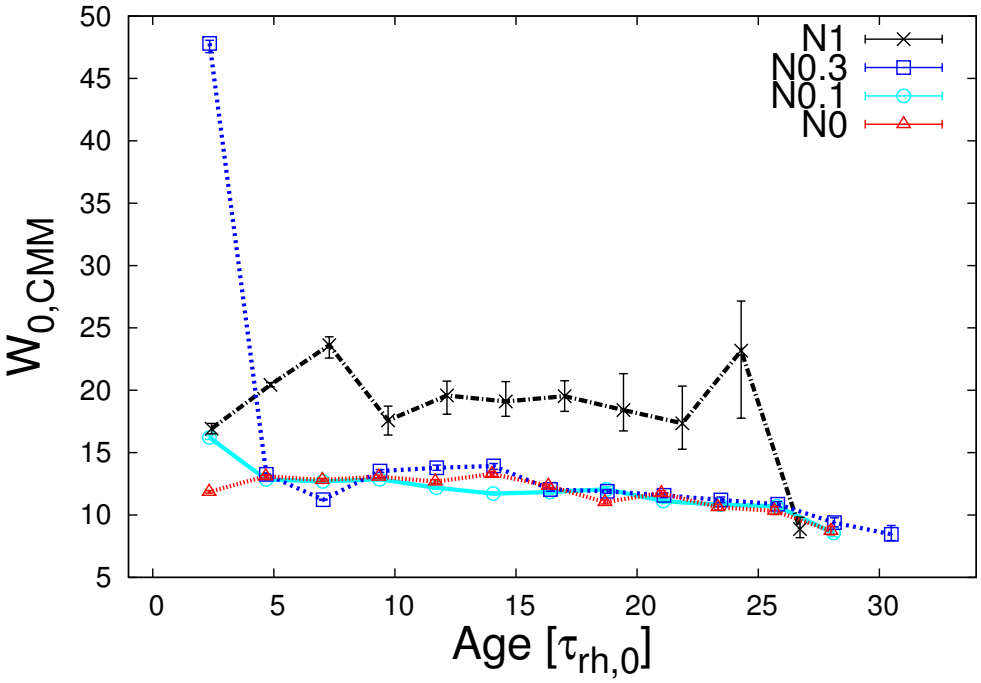

Figure 2.14: Central dimensionless potential obtained for the best-fitting multimass models when considering the central density weighted mean mass as the reference mass $\bar{m}$ for the four N-body models over time in units of $\tau_{\rm rh,0}$. Error bars denote 1σ uncertainties.

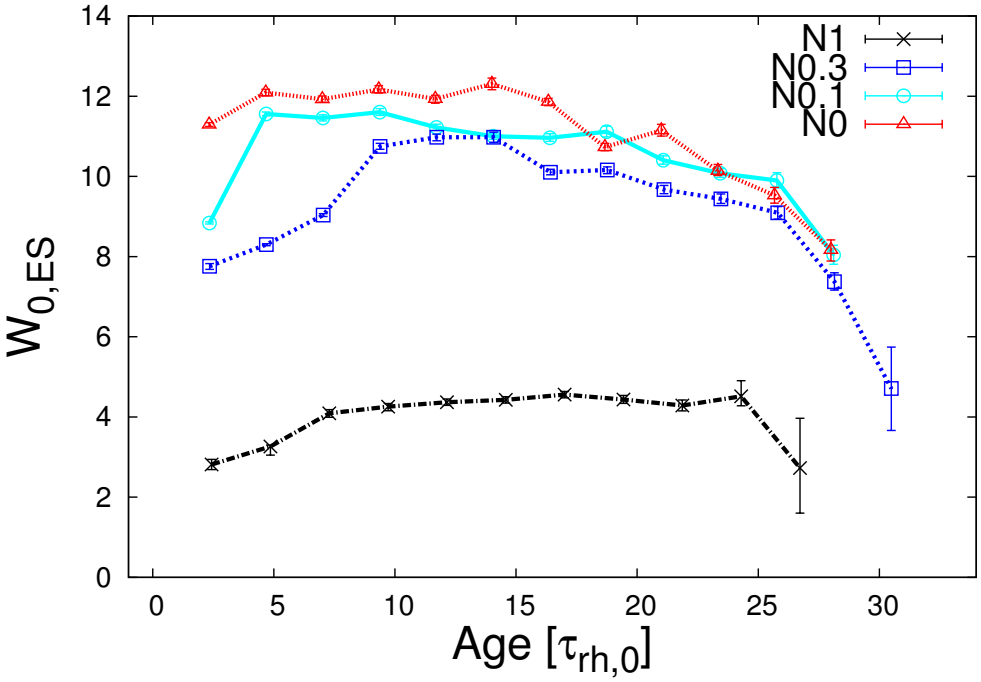

Figure 2.15: Central dimensionless potential of the ESs for the four N-body models over time in units of $\tau_{\rm rh,0}$. Error bars denote 1σ uncertainties.

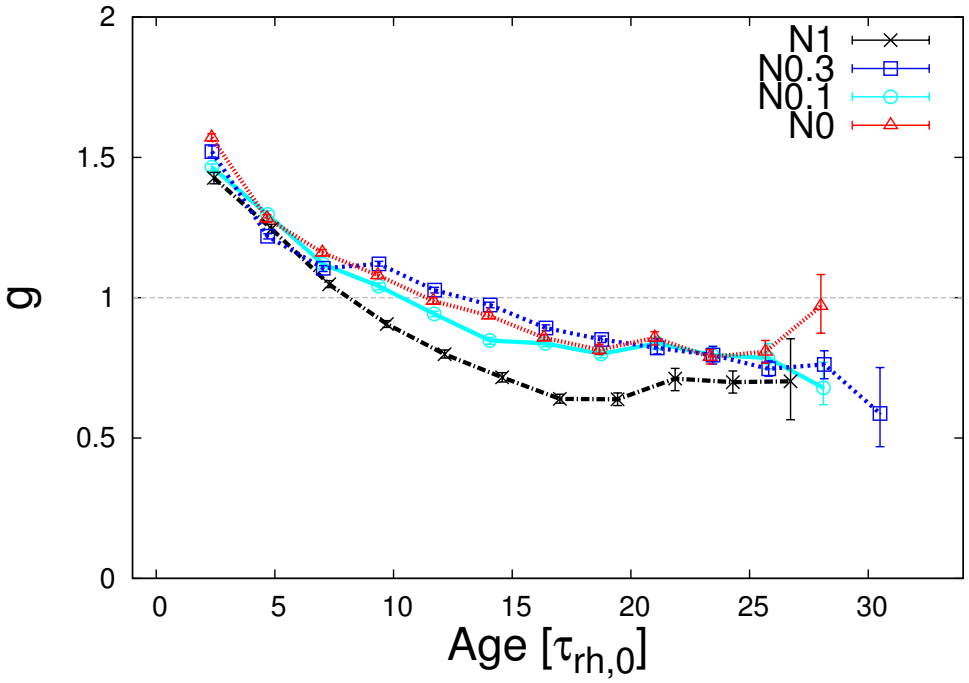

Figure 2.16: Best-fitting values of the truncation parameter g obtained for the four N-body models over time in units of $\tau_{\rm rh,0}$. Error bars denote 1σ uncertainties.

ing the central density weighted mean mass more than the global mean mass, explaining the more significant change of the W_0 values in this figure.

It is also possible to use the values of W_0 obtained for different mass bins for a comparison. As an example I consider the ESs mass bin, because not only does the average mass of the ESs not vary in my models [$\bar{m}_{\rm ES} = (0.821 \pm 0.006)\,{\rm M}_\odot$], but it also represents the objects that are easiest to observe. In Fig. 2.15, I plot the evolution of the W_0 values of the ESs for all four N-body models over their entire lifetime. The uncertainties are estimated by calculating the W_0 values of the ESs for the last 10 iterations of all the walkers and then using the values from the 16th and 84th percentiles as 1σ uncertainties.

Looking at Figs 2.13 and 2.15, one can see the effect of BHs as discussed in Section 2.5.1: in clusters with BHs, the other stars are pushed outwards and the cluster appears less concentrated with a low value of W_0 for the mean mass stars and ESs. While clusters without BHs instead appear much more concentrated as the normal stars can occupy the centre and therefore have a higher W_0 value for the mean mass stars and for the ESs. Therefore, clusters with low W_0 value for the observable stars are much more likely to be hosting a BH population than clusters with a high W_0 value (Merritt et al. 2004; Mackey et al. 2008; Peuten et al. 2016, see also Chapter 3).

2.6.4 Truncation parameter

The truncation parameter g provides an indication of the effect of external tides on the stellar system. In Fig. 2.16, I plot the evolution of g for the four clusters over their lifetime. The evolution is similar for all four N-body models: at the beginning g is around 1.5 which represents a model in between a Wilson (1975) model ($g = 2$) and a

King (1966) model ($g = 1$). As the clusters fill their Roche volume, the tides interact with the clusters, stripping their outermost stars and thereby making the truncation in energy space steeper. This evolution is reflected in the truncation parameter g decreasing as the cluster evolves, converging at the end of the lifetime to a value of around $g \approx 0.73$ which represent a model between a King (1966) and a Woolley (1954) model ($g = 0$).

The results are comparable to the single-mass model findings of Zocchi et al. (2016), though they start with a higher truncation parameter, due to the fact that they start with a smaller initial $r_\mathrm{h}/r_\mathrm{J}$ ratio ($= 0.01$) than I do ($r_\mathrm{h}/r_\mathrm{J} = 0.7$). I must note that I only use bound objects in my analysis, which might lead to smaller values of the truncation parameter as in the outer regions of the clusters ($0.8r_\mathrm{J} - r_\mathrm{J}$) most objects are energetically unbound (Claydon et al. 2017).

As before, I see a difference between the model with BHs (N1) and the models which are mostly BH free (N0, N0.1 and N0.3): at the beginning the value of g decreases faster for model N1 than for the other three models and therefore also converges quicker to its final value. This behaviour in the first half of evolution is not too surprising given that r_h of that model is roughly twice as large as the others, thereby the impact on the steepness of the truncation is stronger (see Section 2.3.3).

McLaughlin and van der Marel (2005) found that Wilson models are equally good or better in describing a sample of Galactic and extragalactic clusters than King models. With my results of the evolution of g, one can interpret McLaughlin and van der Marel (2005) findings that clusters with large g are still dynamically expanding towards filling the Roche volume (see also Carballo-Bello et al. 2012).

2.6.5 Mass segregation

In Fig. 2.17, I plot the evolution of the best-fitting value for δ during the whole lifetime of the four N-body models. In the initial stages of their evolution, all four N-body models are still in the process of segregation, as they were set up without any primordial mass segregation. Over the course of evolution of the clusters, the value converges to around $\delta = 0.5$. This is in accordance with findings of Sollima et al. (2017), who study mass segregation in observations of GCs. At late stages, there are some snapshots for which the best-fitting value is $\delta \gtrsim 0.5$, however the results are compatible with 0.5 within 3σ. Sollima et al. (2015) found that for some of their late N-body snapshots, the multimass models underestimate the amount mass segregation. The same is also found for the best-fitting multimass model to the observations of NGC 6218 in Sollima et al. (2017). However, I do not find this in these models.

To further analyse the behaviour of δ over the course of the cluster evolution, I additionally plot in Fig. 2.18 the central velocity dispersion for the different mass bins from the N-body data together with the predicted central velocity dispersion from the best-fitting multimass model (see also Fig. 2.8). Given the results from Section 2.5.2, it is no surprise that the best-fitting multimass models are able to reproduce the true values.

Despite the fact that the best-fitting models have $\delta \approx 0.5$, this does not mean that the multimass models are in a state of energy equipartition, as can be seen in Fig. 2.18. This was already pointed out by Merritt (1981) and Miocchi (2006) as well as by GZ15. In a mass-segregated multimass model the following relation

$$m_j s_j^2 = m_i s_i^2 \; \forall j, i \; j \neq i \tag{2.6.1}$$

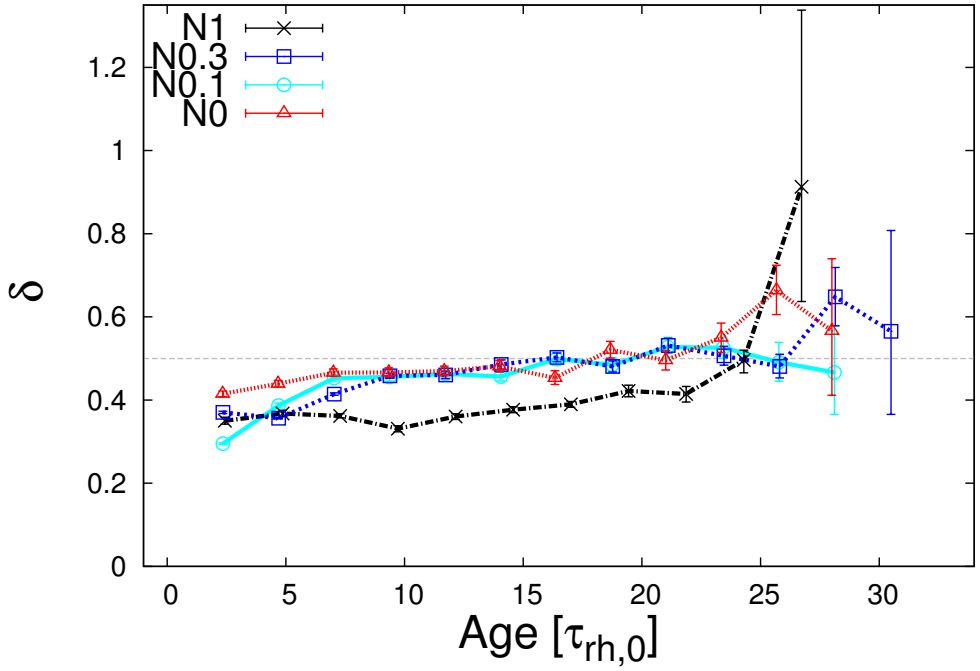

Figure 2.17: Best-fitting values of mass segregation parameter δ for all four N-body models over time in units of $\tau_{\rm rh,0}$. Error bars denote 1σ uncertainties.

holds true with s_j and s_i being the velocity scale of two different mass bins. For the 1D velocity dispersion at the centre the relation:

$$m_j s_j^2 = m_j \sigma_{1d,j0}^2 \; \forall j \tag{2.6.2}$$

only holds true for $W_0 \rightarrow \infty$. In the N-body models, I am studying here $W_0 \ll \infty$ and therefore $\sigma_{1d,j0} < s_j$, which means that my multimass models are never in a state of energy equipartition despite having $\delta = 0.5$.

Furthermore Bianchini et al. (2016) showed, using Monte Carlo simulations, that in clusters only objects above a certain critical mass $m_{\rm eq}$ can be in energy equipartition. The value of $m_{\rm eq}$ depends on the mass spectrum of the cluster, and is larger for cluster with a wider mass spectrum, i.e. when BHs are retained. This trend can also be seen in Fig. 2.18, where the number of mass bins following the $\sigma_{1d}(0) \propto m_j^{-1/2}$ relation, which are therefore in energy equipartition, is only greater than one for the models without BHs. For models with BHs, only the BHs can be in energy equipartition as they are the only ones which have a mass greater than $m_{\rm eq}$. This leads to the largest part of the other objects in these clusters having a smaller spread in the velocity dispersions, which is the reason for the reduced mass segregation in the observable stars in clusters with BHs.

Looking at the results in Fig. 2.17, I can conclude that setting the mass segregation parameter to a fixed value of $\delta = 0.5$ as in its initial formulation of the multimass models by Da Costa and Freeman (1976) is indeed justified to model all but the youngest clusters. As those are not yet fully mass segregated, the value of δ must therefore be smaller, something also found by Sollima et al. (2015, 2017) for young clusters.

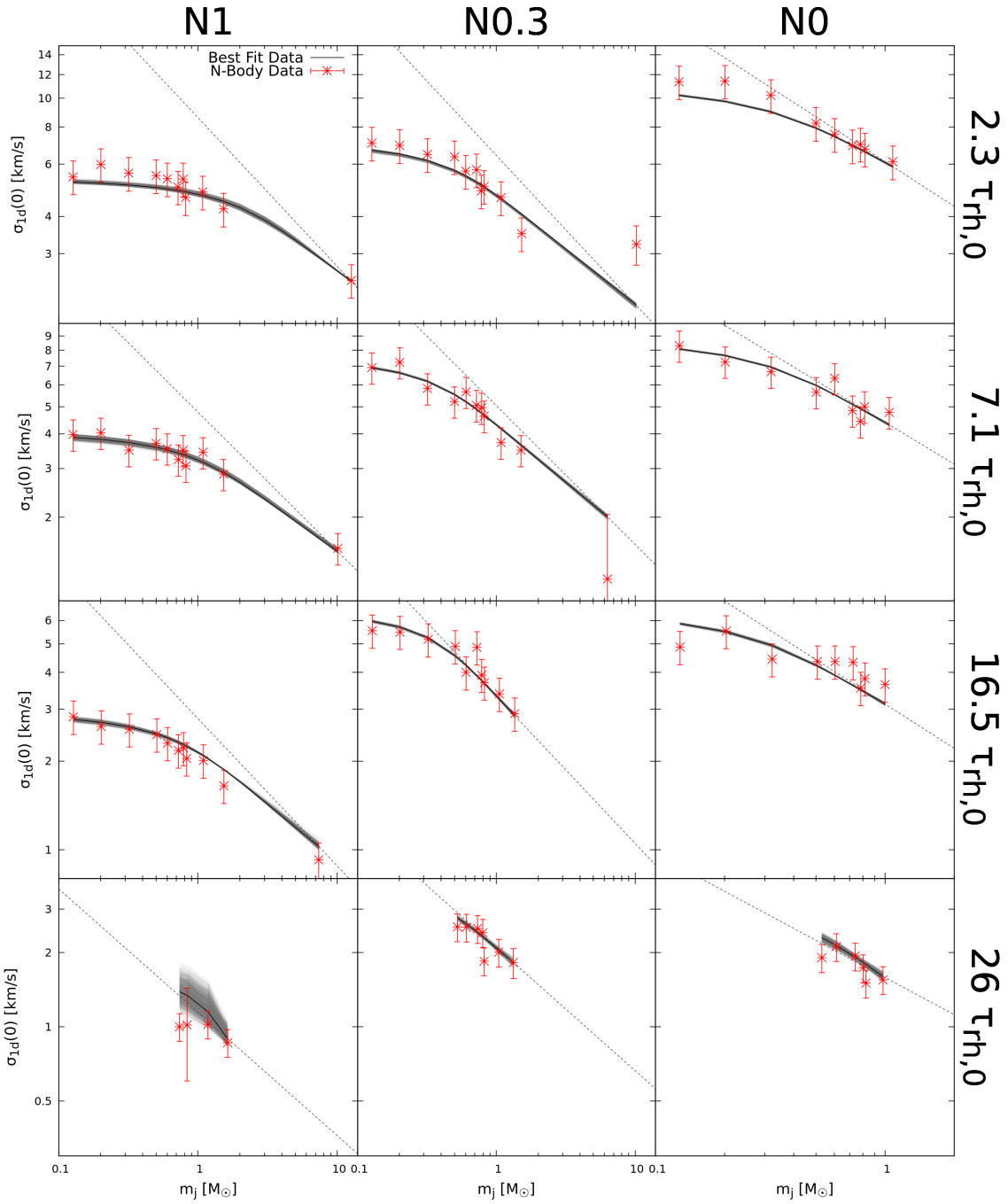

Figure 2.18: Comparison of the central velocity dispersion for the different mass bins for Models N1, N0.3 and N0 at four different dynamical ages: $2.3\tau_{\rm rh,0}$, $7.1\tau_{\rm rh,0}$, $16.5\tau_{\rm rh,0}$ and $26\tau_{\rm rh,0}$. The red points represent the binned N-body data, the black lines represent the best-fitting multimass models central velocity dispersion and the thin grey lines represent the results from the walker positions at the last iteration. The dashed black line shows a $\sigma_{1d}(0) \propto m_j^{-1/2}$ reference line. For the snapshots with a BH population several additional mass bins in the high-mass end were included to better show the relation. Error bars denote 1σ uncertainties.

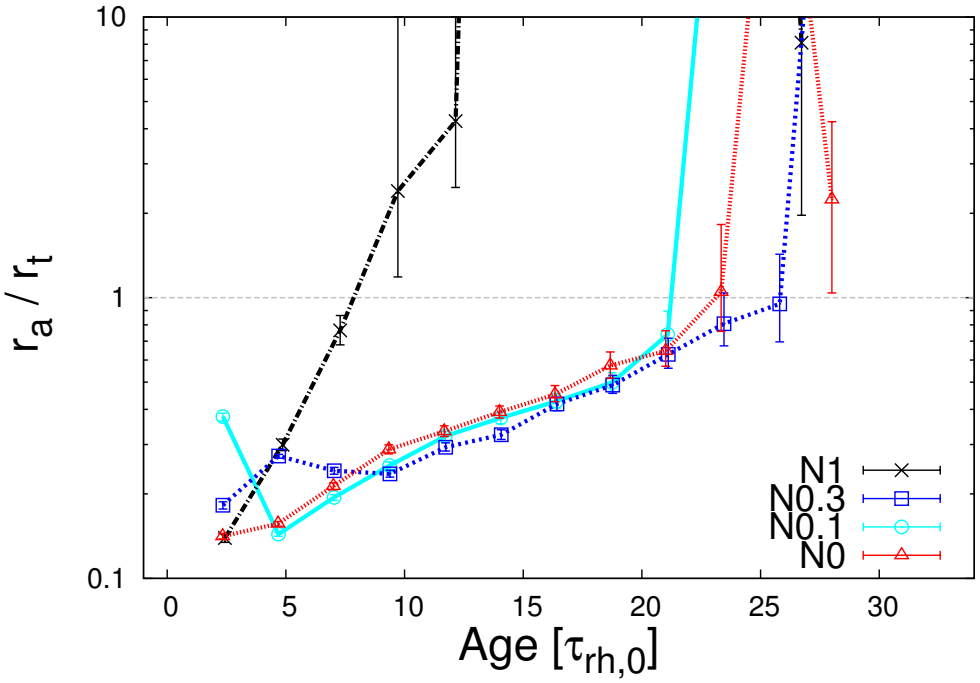

Figure 2.19: Anisotropy radius $r_{\rm a}$ in units of the truncation radius $r_{\rm t}$ as obtained for the best-fitting multimass models for all four N-body models over time in units of $\tau_{\rm rh,0}$. Error bars denote 1σ uncertainties.

2.6.6 Anisotropy radius

The last two fitting parameters are coupled together as they both determine $r_{{\rm a},j}$ for each mass bin as can be seen in equation (2.2.3).

First I focus on $r_{\rm a}$. In Fig. 2.19 I plot $r_{\rm a}/r_{\rm t}$ of the best-fitting model, for all four N-body models during their lifetime. If $r_{\rm a}/r_{\rm t} \gtrsim 1$, the cluster is isotropic (see Section 2.2). Considering the definition of $r_{{\rm a},j}$ (equation 2.2.3), it follows that even if $r_{\rm a}$ is well above $r_{\rm t}$ for some mass bins $r_{{\rm a},j}$ can still be below $r_{\rm t}$ and therefore these mass bins still show some degree of radial anisotropy.

Looking at Fig. 2.19, one can see that the model which retained all its BHs (N1) behaves differently from the other models. Model N1 is only radially anisotropic at the beginning of the lifetime and quickly becomes isotropic. The model without BHs (N0) loses its radial anisotropy more slowly and only at the end of its lifetime it becomes isotropic/tangentially anisotropic. The two models in between (N0.3 and N0.1) behave at the beginning differently: as long as they still have some BHs left their $r_{\rm a}$ value evolves independently, but after all BHs are lost their $r_{\rm a}$ value drops to the $r_{\rm a}$ value of N0 at the same dynamical age and from then on essentially follows the $r_{\rm a}$ evolution of model N0.

These results obtained for the BH-free clusters are comparable, albeit with smaller magnitude, to the results found for the single-mass case by Zocchi et al. (2016). They showed that the anisotropy radius is monotonically decreasing till the cluster reaches core collapse after which it is monotonically increasing, and it eventually becomes so large that the corresponding model is isotropic.

Before I discuss the possible physical reasons behind the evolution of $r_{\rm a}$, I first have a

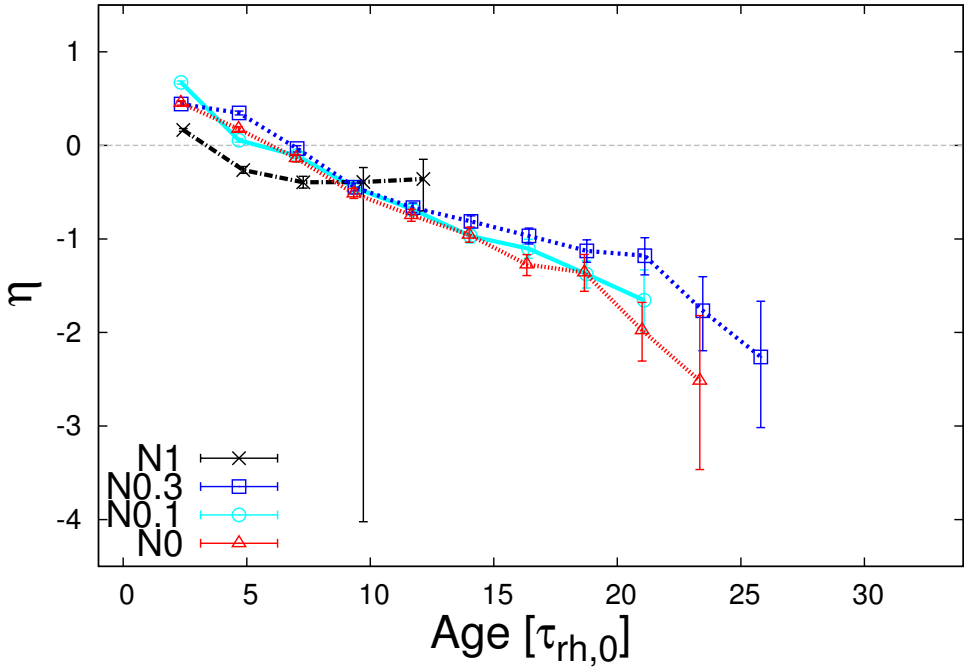

Figure 2.20: Best-fitting anisotropy parameter η for all four N-body models over time in units of $\tau_{\rm rh,0}$. Error bars denote 1σ uncertainties.

look at the fitting parameter η, which is needed to include a dependence of the anisotropy radius on the mass.

2.6.7 Mass-dependent anisotropy

The anisotropy parameter η is a novel fitting parameter in multimass models. In Fig. 2.20, I plot the values of η for the four clusters over time. I only plot this for the snapshots showing some degree of anisotropy. The most important feature is that η evolves for all clusters from a value of $\eta \approx 0.5$ at the beginning of the clusters lifetime to a value of ≈ -2.5 at the end of their lifetime. The model which retains BHs throughout its lifetime (N1) stops the evolution earlier with a value of $\eta \approx -0.5$.

The evolution of η is not surprising given what I already saw in Section 2.5.3, where I showed that the amount of radial anisotropy is decreasing in the low-mass bins and is increasing in the high-mass bins. This is reflected in the development of η changing from a positive value to a negative one over time. This trend is comparable to what Sollima et al. (2015) found in their analysis of the *W5rh1R8.5* N-body model from Baumgardt and Makino (2003): they found that the low-mass stars, which are preferentially located in the cluster outer regions due to mass segregation, become tangentially anisotropic. The reason for this behaviour is that interactions occurring in the cluster centre kick stars into the cluster halo on to radial orbits (Lynden-Bell and Wood 1968; Spitzer and Shull 1975). As stars on radial orbits reach the cluster boundary with positive velocity, they can escape the cluster more efficiently, thereby depleting the low-mass population from stars with radial orbits, leaving only the stars with tangential orbits in the cluster.

To test the relevance of η, I rerun fits to model N0 but this time fixing $\eta = 0$ compara-

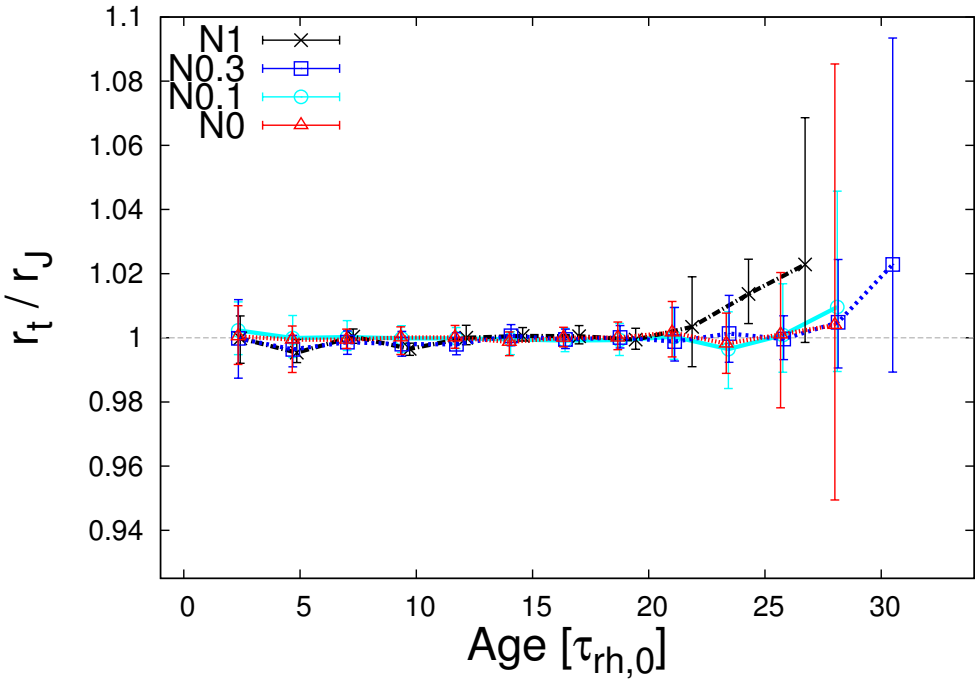

Figure 2.21: Ratio of the truncation radius $r_{\rm t}$ obtained for the best-fitting models to the Jacobi radius $r_{\rm J}$ determined from the N-body snapshots for all four models as a function of time in units of $\tau_{\rm rh,0}$. Error bars denote 1σ uncertainties.

ble to the original formulation by Gunn and Griffin (1979). In these fits, the most obvious difference is that with increasing time, and therefore also with a higher absolute value of η, the uncertainties of $r_{\rm a}$ increase up to five times the value recovered in the fits with a non-fixed η value. Therefore, the introduction of η improves the ability to describe the data.

2.6.8 Truncation radius

At the end of my comparison, I look at two quantities on which I do not fit but which get computed by the multimass models and which can be calculated for the N-body models. In Fig. 2.21, I plot $r_{\rm t}$ divided by $r_{\rm J}$ as determined in Section 2.3.2 for the four N-body models over their whole lifetime. The values of $r_{\rm t}$ and their uncertainties were computed using all the walker positions of the last ten iterations of the MCMC runs. This figure shows that $r_{\rm t}$ stays within 3% of the computed $r_{\rm J}$ and in all but two cases the results are consistent within their 1σ uncertainties. The largest discrepancies can be seen at the end of the lifetime of the clusters. Compared to the single-mass models in Zocchi et al. (2016) which showed divergence of a factor of two, the multimass models are able to reproduce $r_{\rm t}$ accurately.

2.6.9 Global anisotropy parameter

In Fig. 2.22, I look at the evolution of the global value of κ. Here, I have plotted the comparison between the best-fitting value inferred using the walker positions of the last 10

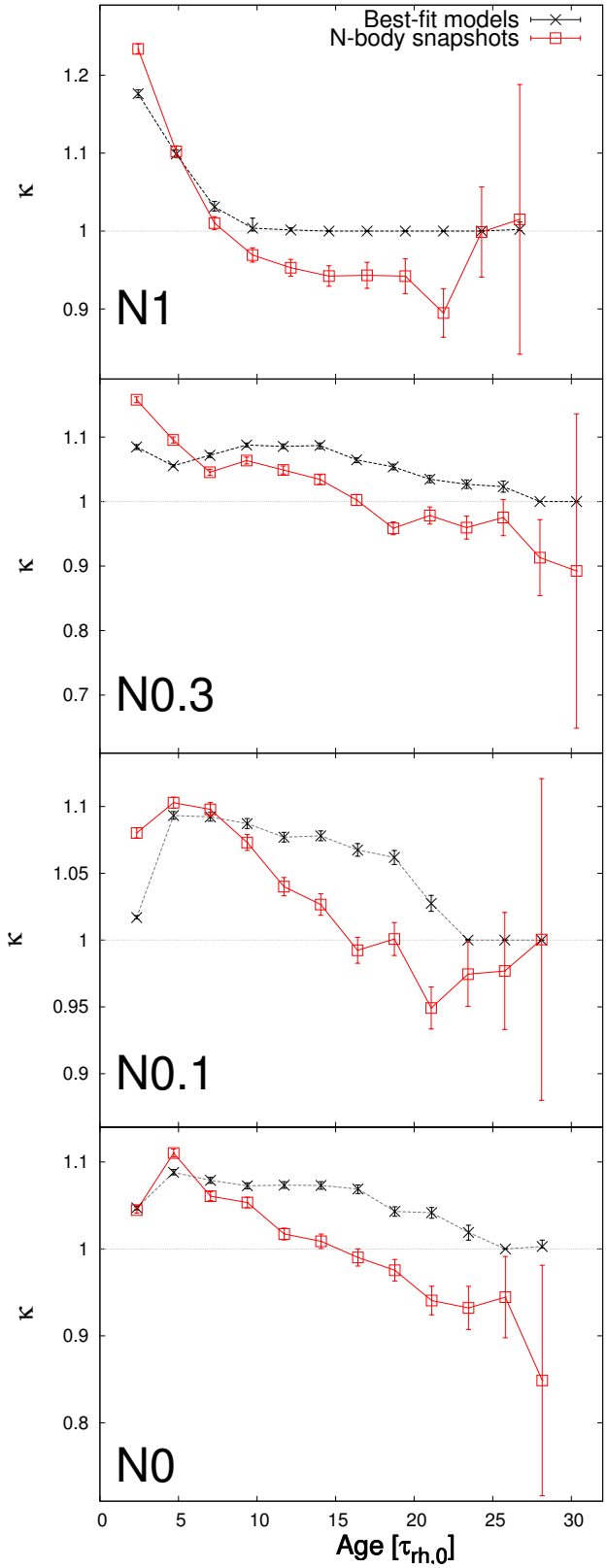

Figure 2.22: Comparison of the values of the global anisotropy parameter κ for the four different N-body models over their whole lifetime. The black dashed lines represent the best-fitting multimass estimate, and the red solid lines represent the true values directly calculated from the N-body snapshots.

iterations of the MCMC runs from each snapshots to the one calculated from the N-body snapshots directly. These are calculated applying equation (2.5.4) to all objects in the N-body model. For the uncertainties of the N-body data, I used Poisson statistics. As before the best-fitting multimass models qualitatively reproduce the overall trend as long as the N-body model is radially anisotropic. When the N-body snapshots becomes tangentially anisotropic, the best-fitting multimass models are isotropic. Hence, the multimass κ values still shows some radial anisotropy where the true cluster is already dominated by tangentially anisotropic orbits. For all models $\kappa < 1.7 \pm 0.25$, from which it follows that all models are stable against radial orbit instability as discussed in Polyachenko and Shukhman (1981).

2.7 Discussion and conclusion

In this study, I assessed the validity of the multimass anisotropic models provided by the LIMEPY software (GZ15) fitting them to N-body models. I find that the N-body models are well described by multimass models, a result which is fortunate given the long list of observational studies using multimass models to analyse GCs (see Section 2.1). Zocchi et al. (2016) showed for the single-mass case that the LIMEPY models are able to describe clusters at all evolutionary phases. Although the agreement is not perfect, the systematic differences are negligible for most applications and parameters of interest (see also the discussion in Section 2.6.1).

My comparison shows that the best-fitting total cluster masses are off by no more than 1% from the true value as computed from the N-body snapshots. The best-fitting cluster half-mass radius is reproduced within 5% and the truncation radius is reproduced within 3%.

I find that the mass density and velocity dispersion profiles of the different mass bins are well reproduced by the multimass models. If the N-body snapshot is radially anisotropic then the multimass models are generally able to reproduce it.

I show that in the N-body models, regardless of initial BHs and NSs retention, the truncation parameter g evolves from roughly 1.5 to about 0.7. The general trend can be explained by the tidal effects stripping the loosely bound stars. I find that the best-fitting mass segregation parameter δ converges to a value close to 0.5 for my N-body models, which is the value used in the original formulation by Da Costa and Freeman (1976). Only for young clusters which are not yet mass segregated is the best-fitting value smaller and for models with BHs it is ~ 0.4.

The newly introduced η parameter shows that the anisotropy radius is mass dependent and that this mass dependence changes in my N-body models over time from $\eta = 0.5$ where the lighter stars are more radially anisotropic to $\eta = -2.5$ ($\eta = -0.5$ for the model which initially retained all its BHs) where the heavy objects are more radially anisotropic. I find in this study that the effects which influence the anisotropy radius are more mass dependent than initially thought and therefore η is another relevant parameter when analysing radial anisotropy with multimass models. Furthermore, I find that clusters with a BH population can be tangentially anisotropic for most of their lifetime.

The W_0 parameter for the observable ESs is lower for the clusters with BHs than for the clusters without BHs. Therefore, clusters which still harbour a stellar-mass BH population should appear less dense when looking at the observable stars. N-body simulation

N0.1, which loses its BHs within its first $\tau_{\rm rh,0}$, does not show any strong differences to simulation N0, despite having a population of NSs. The influence of the NSs on a cluster is therefore negligible, compared to the impact stellar-mass BHs have on a cluster.

I conclude that the LIMEPY multimass models are an adequate tool to study the global properties of GCs, as the results from the comparison with N-body models show a good agreement with their properties inferred from multimass models.

Chapter 3

A stellar-mass black hole population in the globular cluster NGC 6101?

Abstract

Dalessandro et al. observed a similar distribution for blue straggler stars and main-sequence turn-off stars in the Galactic globular cluster NGC 6101, and interpreted this feature as an indication that this cluster is not mass-segregated. Using direct N-body simulations, I find that a significant amount of mass segregation is expected for a cluster with the mass, radius and age of NGC 6101. Therefore, the absence of mass segregation cannot be explained by the argument that the cluster is not yet dynamically evolved. By varying the retention fraction of stellar-mass black holes, I show that segregation is not observable in clusters with a high black hole retention fraction ($> 50\%$ after supernova kicks and $> 50\%$ after dynamical evolution). Yet all model clusters have the same amount of mass segregation in terms of the decline of the mean mass of stars and remnants with distance to the centre. I also discuss how kinematics can be used to further constrain the presence of a stellar-mass black hole population and distinguish it from the effect of an intermediate-mass black hole. My results imply that the kick velocities of black holes are lower than those of neutron stars. The large retention fraction during its dynamical evolution can be explained if NGC 6101 formed with a large initial radius in a Milky Way satellite.

This Chapter was published in Monthly Notices of the Royal Astronomical Society (MNRAS), Volume 462, Issue 3, p.2333-2342 (Peuten et al. 2016)[1].

[1] A video was produced, highlighting the most important aspects of this chapter for the general audience: `https://www.youtube.com/watch?v=-fmWeYcAksQ`

3.1 Introduction

Globular clusters (GCs) are old stellar systems ($\sim 10 - 13\,\mathrm{Gyr}$) with masses ($\sim$ few $10^5\,\mathrm{M}_\odot$) and densities ($\sim$ few $1000\,\mathrm{M}_\odot\,\mathrm{pc}^3$) resulting in two-body relaxation time-scales shorter than their age. In two-body encounters, the lighter stars generally gain velocity while the heavier stars lose velocity. After many subsequent encounters, the low-mass stars gain velocity with respect to the high-mass stars, which in turn means that in GCs, light stars are found further away from the centre than high-mass stars (King et al. 1995). This effect is generally referred to as mass segregation. Because GCs are older than their respective half-mass relaxation time ($\tau_{\rm rh}$) (Hénon 1961; Gieles et al. 2011), we expect the stars and remnants of different masses to have different distributions in phase space. This effect has been confirmed observationally (King et al. 1995; Sollima et al. 2014).

There are different ways to study mass segregation in GCs. The one I will mostly refer to in this study is the use of cumulative radial distributions of stars with different masses: in a mass-segregated cluster, we expect the stars with high mass, such as blue straggler stars (BSSs) to be more centrally concentrated than main-sequence turn-off stars (MSTO). If the cluster is not mass-segregated, then the cumulative radial distributions are the same. Gill et al. (2008) showed that the presence of an intermediate-mass black hole (IMBH) reduces the amount of mass segregation among observable stars, and they suggest that this could be used as an observable indication of the presence of an IMBH.

Dalessandro et al. (2015) (hereafter D15) recently studied different properties of the GC NGC 6101, such as the radial distribution of the BSSs, the radial variation of the binary fraction and the radial variation of the luminosity and mass function (MF). From their analyses, they conclude that this cluster is not mass-segregated. They also found a large core radius relative to the half-light radius (effective radius) for the GC ($R_{\rm c}/R_{\rm eff} \approx 0.4$).

NGC 6101 is a metal-poor cluster with $[\mathrm{Fe/H}] = -1.98$ (Carretta et al. 2009) located at a distance of 14.6 kpc (D15) from the Sun and 11.2 kpc (Harris 1996) from the Galactic Centre. When fitting a King (1966) model to the observed number density profile, D15 obtained a concentration $c = \log(r_{\rm t}/r_{\rm c}) = 1.3$ and a projected effective radius of $R_{\rm eff} = 128.2$ arcsec. These values are larger than the values listed in the Harris (1996) catalogue and those given by McLaughlin and van der Marel (2005). D15 attribute the larger radii to their improved method of background subtraction. D15 estimate that NGC 6101 has an half-mass relaxation time-scale of $\tau_{\rm rh} \sim 5.4 - 6.3$ Gyr.

The value of the initial half-mass relaxation time ($\tau_{\rm rh,0}$) for NGC 6101 should be smaller than the one we measure today for this cluster, because in roughly the first half of the evolution of tidally limited GCs, the half-mass relaxation time increases due to stellar mass-loss and two-body relaxation-driven expansion (Gieles et al. 2010). In Section 3.2, I estimate $\tau_{\rm rh,0}$ to be $\sim 2.8\,\mathrm{Gyr}$. Gill et al. (2008) found that a cluster needs to be $\sim 5\tau_{\rm rh,0}$ old to appear fully mass-segregated. Given the estimated age of $13\,\mathrm{Gyr}$ (Dotter et al. 2010), we expect NGC 6101 to show signs of mass segregation.

The objective of this study is to understand this contradiction: on one hand, the cluster appears to be not mass-segregated, on the other hand mass segregation is expected based on the age and estimated $\tau_{\rm rh,0}$. It has been shown (Mackey and Gilmore 2004; Merritt et al. 2004; Lützgendorf et al. 2013) that a population of heavy remnants can result in a large core radius ($r_{\rm c}$) over half-mass radius ($r_{\rm h}$), as observed for NGC 6101. Because black

hole (BH) candidates have recently been observed in several GCs (Strader et al. 2012; Chomiuk et al. 2013), I investigate the effect of a population of remnants on the apparent mass segregation for the case of NGC 6101. To do this, I use a set of N-body simulations with different retention fractions of BHs, and I compare them to the observations. I also use dynamical equilibrium models to formulate predictions on other observable quantities.

This paper is organized as follows: in Section 3.2, I present the N-body models used in this analysis. In Section 3.3, I discuss the results of the analysis of my N-body models and I show the effects produced by a population of stellar-mass BHs on the observations. In Section 3.4, I propose a method to observationally distinguish the scenario I introduce here from other possible explanations, by looking at the kinematics of the cluster. In Section 3.5, I discuss my results in the context of other scenarios and present my conclusions.

3.2 Description of the N-body models

I run three numerical simulations with the N-body integrator NBODY6 (Aarseth 2003), in the variant with GPU support (Nitadori and Aarseth 2012). In the following, I describe the steps I carried out to set up the initial conditions for the simulations and I illustrate their basic properties.

The current properties of NGC 6101 as measured by D15 are presented in the first line of Table 3.1. I adopted a mass-to-light ratio of $\Upsilon_{\rm V} = 1.9\ {\rm M}_\odot/\,{\rm L}_\odot$ (McLaughlin and van der Marel 2005). Combined with the V-band luminosity of $L_{\rm V} = 5.7 \times 10^4\,{\rm L}_\odot$, I find a present-day mass of $M_{\rm cl} = 1.1 \times 10^5\,{\rm M}_\odot$. I then determined the current number of objects in NGC 6101 to be $N = 2.71 \times 10^5$ by assuming an average mass of $\bar{m} = 0.4\,{\rm M}_\odot$.

3.2.1 Estimating the initial conditions of NGC 6101

To estimate the initial conditions of NGC 6101, I used the fast star cluster evolution code EMACSS (Evolve Me A Cluster of StarS; Alexander et al. 2014). By applying Hénon's predictions (Hénon 1961, 1965) that in a state of balanced evolution, the flow of energy within a cluster is independent of the actual energy source in the core, EMACSS calculates the evolution of some of its fundamental properties, such as mass, half-mass radius and mean mass.

I approximate the Milky Way potential by a singular isothermal sphere with $V_{\rm circ} = 220\,{\rm km/s}$. I assume a circular orbit at NGC 6101 current Galactocentric radius of $R_{\rm G} = 11.2\,{\rm kpc}$. For the cluster itself, I assumed a Kroupa (2001) initial mass function (IMF) between 0.1 and $100\,{\rm M}_\odot$.

I ran EMACSS for a grid of different initial values for the total number of objects N and the half-mass radius. Each cluster is evolved to $13\,{\rm Gyr}$ and the half-mass radius and the total mass of the cluster at this age are compared to the current properties of NGC 6101. The initial half-mass radius and total mass of the cluster that provide the best match to the present day properties are chosen as initial conditions of the N-body simulations and are given in the second line of Table 3.1.

Table 3.1: Properties of the globular cluster NGC 6101. The first line lists the current properties of the cluster, the second line the initial properties as determined with EMACSS and the third line the scaled initial properties that I use as initial conditions to set up my simulation. Columns from 2 to 10 list, respectively, the total V-band luminosity $L_{\rm V}$ of the cluster in solar units, the total mass of the cluster $M_{\rm cl}$ in solar masses, the number of stars N, the average mass of stars in solar masses, the half-mass radius $r_{\rm h}$ in pc, the effective radius $R_{\rm eff}$ in pc, the Galactocentric distance $R_{\rm G}$ in kpc, the metallicity $[{\rm Fe/H}]$ in solar units and the half-mass relaxation time $\tau_{\rm rh}$ in Gyr. The references for the values listed in the first line are indicated in the notes.

	$L_{\rm V}$	$M_{\rm cl}$	N	$\bar{m}$	$r_{\rm h}$	$R_{\rm eff}$	$R_{\rm G}$	$[{\rm Fe/H}]$	$\tau_{\rm rh}$
Current properties	$5.7\times10^{4\star}$	1.1×10^{5}	2.7×10^{5}	0.40	$12.3^{\dagger}$	$9.2^{\dagger}$	$11.2^{\star}$	$-1.98^{\ddagger}$	$5.4-6.3^{\dagger}$
Initial unscaled properties	–	2.0×10^{5}	3.1×10^{5}	0.64	5.8	4.4	11.2	-1.98	2.8
Initial scaled properties	–	6.4×10^{4}	1.0×10^{5}	0.64	7.6	5.7	30.0	-1.98	2.8

References: * Harris (1996), † Dalessandro et al. (2015) and ‡ Carretta et al. (2009).

Table 3.2: Initial and final properties of the three N-body models, as indicated in the first column. I list the values of the scaled number of bound stars N^*, the total mass of bound stars M in $\mathrm{M}_{\odot}$, the scaled half-mass radius $r_{\rm h}^*$ in pc, the number of black holes contained in the cluster $N_{\rm BH}$ and their total mass $M_{\rm BH}$ in $\mathrm{M}_{\odot}$: the values provided for these quantities in the first part of the table refer to the initial properties of the clusters, the ones in the second part to the properties they have at an age of 13 Gyr. Moreover, I also provide the total number of black holes contained in the clusters before taking into account the effect of the kick velocity, $N_{\rm BH,created}$.

N-body	Initial properties						Final properties				
model	N^*	M	$r_{\rm h}^*$	$N_{\rm BH}$	$M_{\rm BH}$	$N_{\rm BH,created}$	N	M	$r_{\rm h}$	$N_{\rm BH}$	$M_{\rm BH}$
N0	10^5	5.4×10^4	7.6	0	0	176	8.8×10^4	3.2×10^4	13.6	0	0
N0.5	10^5	6.3×10^4	7.6	105	1442	177	8.5×10^4	3.1×10^4	14.1	64	486.6
N1	10^5	6.3×10^4	7.6	176	2024	176	8.3×10^4	3.1×10^4	20.0	120	840.3

I point out that the set of initial properties that I identified in this way correspond to a cluster with an initial half-mass relaxation time of $\tau_{\rm rh,0} = 2.8\,{\rm Gyr}$, implying that NGC 6101 is about $\approx 4.6\tau_{\rm rh,0}$ old.

3.2.2 Model scaling

Although it is feasible to model NGC 6101 with a direct N-body model (see Heggie 2014 and Wang et al. 2016), I decide to model NGC 6101 with scaled N-body models in order to explore several scenarios for the retention of the stellar-mass BHs. I used the approach from Heggie and Giersz (2008), where the scaled model has the same half-mass relaxation time as the real cluster, accounting for the fact that much of the cluster dynamics is dominated by two-body relaxation. If the number of stars in the scaled model is N^*, then I can find the half-mass radius of the scaled model, $r_{\rm h}^*$, in terms of N and $r_{\rm h}$ from the expression of $\tau_{\rm rh}$ (Spitzer and Hart 1971, eq. 5):

$$\frac{r_{\rm h}^*}{r_{\rm h}} = \left(\frac{N}{N^*}\right)^{1/3} \left(\frac{\log \gamma N^*}{\log \gamma N}\right)^{2/3} . \tag{3.2.1}$$

Here I set $\gamma = 0.02$ (Giersz and Heggie 1996).

The scaling for the Jacobi radius ($r_{\rm J}$) is the same as for $r_{\rm h}$. Because I want to simulate the cluster in the same tidal field strength as for the EMACSS runs (as mentioned in Section 3.2.1), I need to scale $R_{\rm G}$. The Jacobi radius can be estimated as (King 1962):

$$r_{\rm J} = \left(\frac{GM_{\rm cl}}{2\Omega^2}\right)^{1/3} , \tag{3.2.2}$$

where $\Omega = V_{\rm circ}/R_{\rm G}$ is the local angular velocity. I can now express the scaling relation for $R_{\rm G}$ as

$$\frac{R_{\rm G}^*}{R_{\rm G}} = \left(\frac{N}{N^*}\right)^{1/2} \left(\frac{r_{\rm h}^*}{r_{\rm h}}\right)^{3/2} . \tag{3.2.3}$$

When making use of scaled N-body models, one needs to be aware that processes that have a different N-dependence as the relaxation time, are not modelled correctly. I am mostly concerned about the behaviour of the BH population. Breen and Heggie (2013a,b) showed that the escape rate of BHs in GCs is set by $\tau_{\rm rh}$ of the cluster as a whole, i.e. not by the time-scale of the BH sub-cluster itself. The fraction of BHs that is retained at an age of 13 Gyr after dynamical evolution should therefore not be affected by the scaling.

For my simulations, I set the number of initial stars to $N^* = 10^5$ and scaled the other properties accordingly (see third line of Table 3.1).

3.2.3 N-body simulations

Because previous works (see discussion in Section 3.1) have shown that a population of stellar-mass BHs could give rise to a large (observed) core radius, I set up three N-body simulations, each of which is characterized by a different fraction of BHs retained with respect to their initial number: in model N1, all the BHs are retained in the cluster, in model N0.5, only 50% of BHs are retained and in model N0, no BHs are retained.

As initial condition for the three simulations, I consider a set of stars distributed according to the Plummer model (Plummer 1911). I do not include primordial binaries, primarily to speed up the computations (see the discussion in Wang et al. 2015). Excluding them may affect the efficiency of BH binary formation and ejection (see Chatterjee et al. 2017; Rodriguez et al. 2016a), but because I am mainly interested in studying the difference between clusters with and without BHs, my approach is justified. I adopt the same stellar IMF as for the EMACSS models (Section 3.2.1) and I control the removal of the BHs created in the cluster by varying their initial supernova kick velocity. For simulation N1, I set the initial kick velocity to zero, so that all the BHs are kept in the cluster. In the case of simulation N0.5, I want to retain 50% of the BHs: to do this, for each BH, I draw a random number from a flat distribution in the range $(0, 1)$, and I assign a kick velocity greater than the escape velocity to the BH only if the drawn value is above 0.5. This procedure allows us to retain, on average, 50% of the BHs, without the need of knowing their total number. For simulation N0, I assign a kick velocity greater than the escape velocity to all BHs so that none of them are retained in the cluster.

The cluster is moving on a circular orbit in the $(x, y)-$plane with orbital velocity of $V_{\rm circ} = 220\,{\rm km/s}$. The stars are evolved with the stellar evolution prescription of Hurley et al. (2000) for a metallicity of $[{\rm Fe/H}] = -1.98$. I summarize the initial and final (after 13 Gyr) properties of the simulations in Table 3.2.[2]

3.3 Results

With the N-body models of NGC 6101 in place, I perform the same analysis as carried out by D15. I compare the cumulative radial distribution for the different star types in my numerical simulations to the one presented in D15. Next, I analyse the MF slope of my N-body models and again compare them to results presented by D15 for NGC 6101. I could, in principle, also analyse the radial distribution of the binary stars, but the models were created without primordial binaries, and the binaries that formed in the course of the simulation are too few to give a meaningful result.

3.3.1 Cumulative radial distribution

In their Fig. 7, D15 show the cumulative radial distribution of four different groups of stars observed in NGC 6101: BSSs, horizontal branch stars, red giant branch stars (RGBs) and MSTO stars. They point out that the four groups have the same distribution in the cluster. Here I consider the same quantities in my simulations, and compare them with their finding.

I focus my analysis on the distribution of BSS and MSTO stars, because they have the largest mass difference among the star types analysed by D15 and, if the cluster is mass-segregated, should therefore have the largest difference in spatial distribution. I label stars in the mass range $0.79 - 0.81\,{\rm M}_\odot$ as MSTO stars.

No BSSs were created in my simulations, because I did not include primordial binaries in my simulations: it has been shown in observational studies (Sollima et al. 2008; Knigge

[2]A flight trough cluster N1 and N0 at the end of the simulation can be viewed at `https://www.youtube.com/watch?v=SN9PuvW0oV4`

et al. 2009) as well as in simulations (Chatterjee et al. 2013; Sills et al. 2013) that the efficiency of BSS formation is positively correlated with the binary fraction. The number of binaries has not only an influence on the BSSs created by mass transfer in a binary but also an important influence on the BSSs created by collisions, as the majority of these collisions are binary-mediated. So the number of primordial binaries directly affects the creation of BSSs.

I therefore need a proxy for the BSSs and since the only relevant property for this analysis is the mass of the stars and not their type, I use white dwarfs (WDs) as a proxy for BSSs. WDs are the only abundant objects for which the mass range reaches values high enough to be comparable to BSSs. Red giants, for example, which are the evolved stars[3] with the highest mass in my simulations only reach slightly above the MSTO mass after $13\,\mathrm{Gyr}$ of evolution and are therefore not a good BSS proxy candidate.

The estimated mass range for BSSs in GCs ranges from 0.6 to $3.74\,\mathrm{M}_\odot$ (Shara et al. 1997; Gilliland et al. 1998; De Marco et al. 2005; Lovisi et al. 2012; Fiorentino et al. 2014) with average mass in the range between 1.0 and $1.3\,\mathrm{M}_\odot$ (De Marco et al. 2005; Lovisi et al. 2012). With particular reference to the GC NGC 6101, the only available information on the mass of its BSSs is that for all of them, it holds that $M_{\mathrm{BSS}} \leq 2\,M_{\mathrm{MSTO}} \approx 1.6\,\mathrm{M}_\odot$ (Marconi et al. 2001). Because the determination of masses of BSSs is very uncertain, I decide to consider two different mass ranges for the BSS proxies in my simulations: the first sample is formed by WDs with masses in the range of $1.0 - 1.5\,\mathrm{M}_\odot$ and an average mass of $1.1\,\mathrm{M}_\odot$, the second sample by WDs with masses in the range of $1.187 - 1.5\,\mathrm{M}_\odot$ and an average mass of $1.3\,\mathrm{M}_\odot$. I note here that the largest mass for a WD in my simulations is $1.5\,\mathrm{M}_\odot$.

Using WDs as a proxy for BSSs may overestimate the degree of central concentration. This is because WDs were more massive in the recent past and therefore could still be migrating outwards towards their relaxed position (for an observational study of this process, see Richer et al. 2013). Some of the BSSs (in particular, the ones that are formed from the merger of stars induced by collisions) on the other hand could still be migrating inwards because they were less massive in the recent past. The amount of mass segregation that is inferred from the comparison of the distribution of WD and MSTO stars in my simulations is therefore overestimated with respect to the one that could be obtained when considering BSSs.

In Fig. 3.1, I show the cumulative distribution of projected distances for the MSTO stars, the BHs and the two BSS-proxies samples for the three simulations. In all cases, the cluster is projected along the z-axis (I carefully checked that the results do not depend on the choice of the selected projection axis). The result of D15 for NGC 6101 is presented in the right-hand panel of Fig. 3.1. With an increasing number of BHs retained in the cluster, the differences in radial distribution of MSTO stars and BSS-proxies diminish. The different amount of mass segregation observed in this way is surprising at first sight because all three models have evolved for the same amount of dynamical time. In the next sections, to further understand this issue, I proceed by analysing the mass distribution of all the objects, including the remnants [WDs, neutron stars (NSs) and BHs].

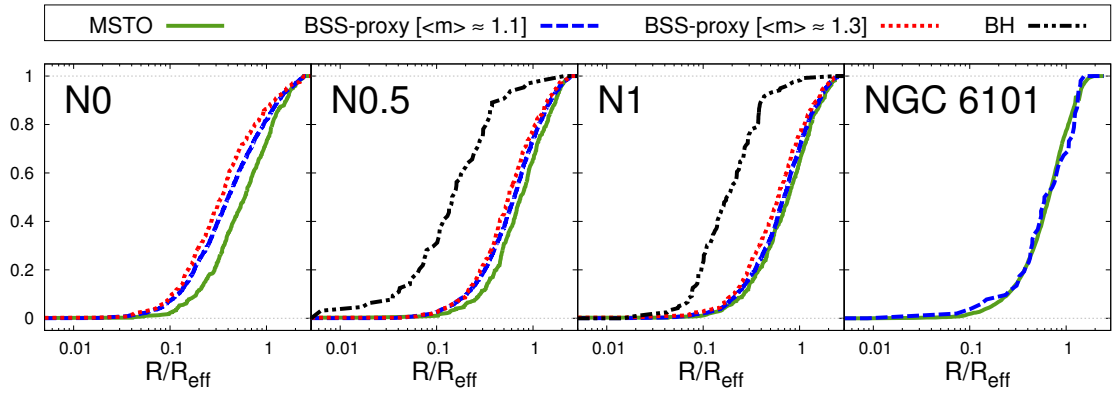

Figure 3.1: Cumulative radial distribution of different groups of stars. In the first three panels, I show the distributions of the MSTO stars (solid green lines), of the two samples of BSS-proxy stars (the one with average mass of $\langle m \rangle = 1.1\,\mathrm{M}_{\odot}$ is represented with dashed blue lines, the one with $\langle m \rangle = 1.3\,\mathrm{M}_{\odot}$ with dotted red lines), and the black holes (double dot−dashed black lines) as a function of the projected distance from the centre, in units of the projected effective radius $R_{\rm eff}$. Each panel corresponds to the $13\,\mathrm{Gyr}$ snapshot of a different simulation, as indicated by the labels. For comparison, in the last panel on the right, I provide a copy of Fig. 7 of D15 with the measured cumulative radial distributions of BSSs and MSTO stars in NGC 6101.

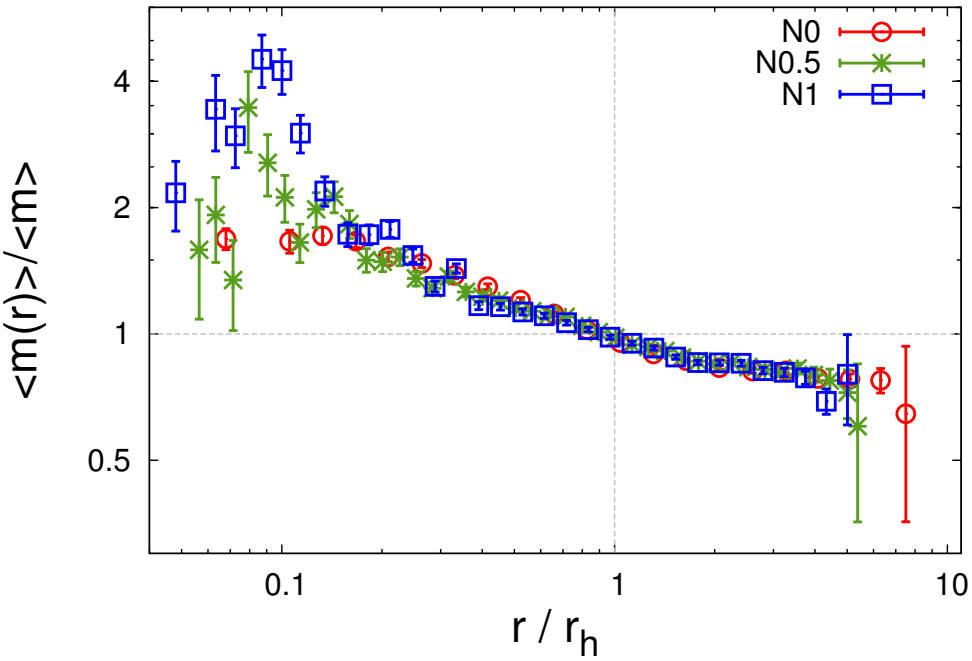

Figure 3.2: Relative mean mass as a function of the distance from the cluster centre in units of $r_{\rm h}$. The relative mean mass corresponds to the ratio of the mean mass of stars in radial bins divided by the total mean mass. Circles (red), stars (green) and boxes (blue) refer to simulation N0, N0.5 and N1, respectively. Error bars denote 1σ uncertainties.

3.3.2 Mean mass at different radii

In Fig. 3.2, I show the relative mean mass, i.e. the mean mass of all objects in radial bins divided by the global mean mass, as a function of the distance from the cluster centre in units of the half-mass radius, for my three simulations at $13\,\mathrm{Gyr}$. By comparing the relative mean mass of the three clusters, I see that they show the same behaviour. The main difference is found in the innermost region ($r/r_\mathrm{h} \lesssim 0.1$) where, in the snapshots with BHs, the scatter around the common mean value is greater than in the snapshot without BHs.

I analyse the radial dependence of the relative mean mass at different times, and I find that it has the same overall behaviour independently of the presence of BHs. Only in the inner regions ($r/r_\mathrm{h} \lesssim 0.1$), there is a difference between the profiles of different simulations at different times, with the mean mass in the centre increasing faster in the models with BHs. In Fig. 3.3, I show the relative mean mass for the three simulations at four different times in their evolution (2.6, 5.3, 7.9 and $10.5\,\mathrm{Gyr}$). A change in the slope of this quantity is observed for all the simulations: outside the half-mass radius, it becomes steeper in time. For single-mass systems, it is well understood that after several relaxation times the evolution is self-similar (Hénon 1961, 1965). No studies regarding the evolution of the structure of multimass systems exist yet, but it has been shown that the evolution of mass and radii of multimass models is comparable to the single-mass case (Lee and Goodman 1995; Gieles et al. 2010), but faster in time. These N-body results suggest that there also exists self-similarity in terms of the mean mass profile.

I find that the regions where the BSS-proxies are located are significantly smaller in the cases with BHs, and are less central than in the case without BHs, as show in Fig. 3.1. When BHs are present in the system, I find that the rest of the stars are pushed outwards, and their distributions are more similar to one another. Multimass collisional systems will try to reach equipartition, but the lowest mass stars never reach equipartition because they are in the regime near the truncation energy (Merritt 1981; Miocchi 2006; Gieles and Zocchi 2015; Bianchini et al. 2016). Bianchini et al. (2016) use Monte Carlo simulations to show that clusters only achieve partial equipartition, and that stars with masses below m_eq have similar velocity dispersions, independent of mass, while stars with $m >> m_\mathrm{eq}$ achieve equipartition ($\sigma \sim m^{-1/2}$). These authors show that m_eq is larger for low-concentration models. For models with a wide mass spectrum, m_eq is also higher (comparable to the density-weighted mean mass in the core), and for clusters containing BHs, this could be above the turn-off mass. This implies that the absence of mass segregation among visible stars can be a signal that m_eq is much higher than the turn-off mass: at the age of GCs, this can only be due to BHs.

3.3.3 MF slope

Another indication that NGC 6101 lacks mass segregation is the observation that the cluster MF slope is independent of the distance to the cluster centre (D15). In a mass-segregated cluster, one expects a radius-dependent MF slope (e.g. Webb et al. 2014); I therefore need to also study whether a stellar-mass BH population can reproduce a radius-independent constant MF slope as seen in NGC 6101 to further confirm my theory.

[3] In this work, every post-main-sequence (MS) star which is not a remnant is regarded as an evolved star.

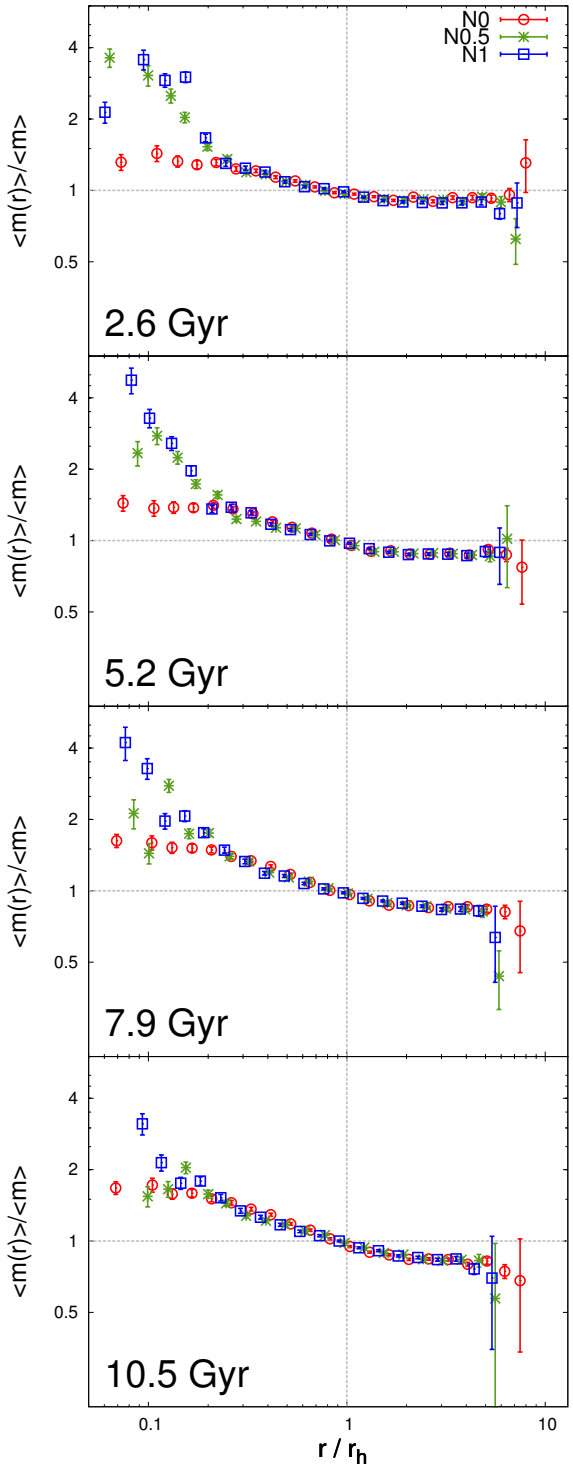

Figure 3.3: Relative mean mass (i.e. mean mass of stars in radial bins divided by the total mean mass) as a function of the distance from the cluster centre in units of $r_{\rm h}$, for all simulations at four different times: 2.6, 5.3, 7.9 and 10.5 Gyr. Circles (red), stars (green) and boxes (blue) refer to simulation N0, N0.5 and N1, respectively. Errorbars denote 1σ uncertainties.

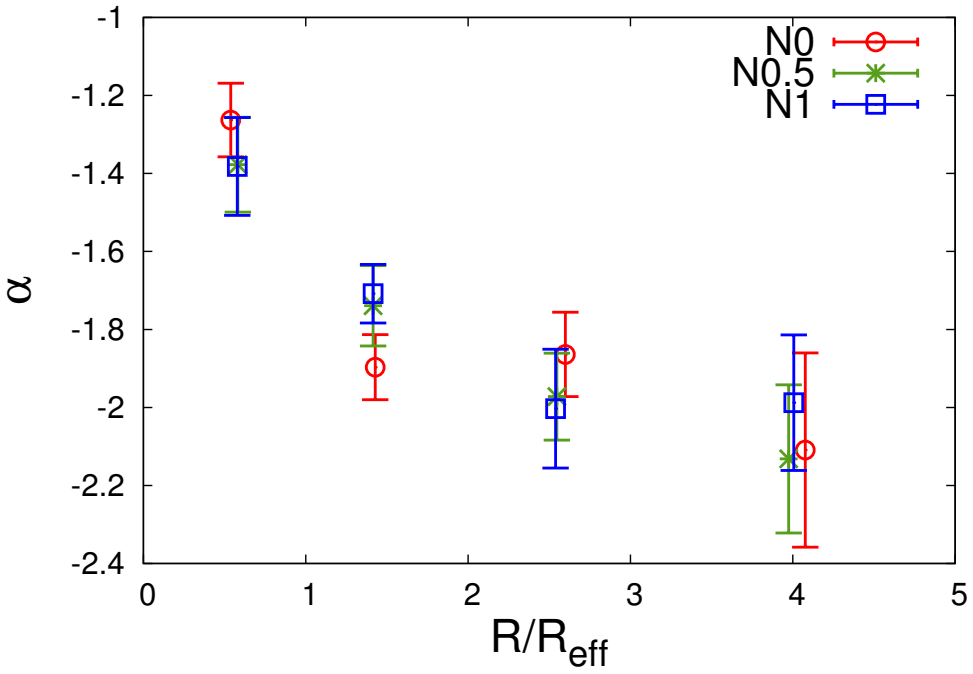

Figure 3.4: Mass function slope (α) as a function of the projected distance from the centre in units of $R_{\rm eff}$ for all three simulations at $13\,{\rm Gyr}$. Circles (red), stars (green) and boxes (blue) refer to simulation N0, N0.5 and N1, respectively. Error bars denote 1σ uncertainties.

To study the slope of the MF, I used a procedure similar to the one used by D15. First, I project the N-body data from each model at $13\,{\rm Gyr}$ along the z-axis and then I select the MS and the evolved stars in the mass range $0.35 - 0.7\,{\rm M}_{\odot}$, which corresponds to the mass range of stars in the FORS2 data set used by D15. Next, I divide the stars in four concentric annuli ($0.0 - 1.0\,R_{\rm eff}$, $1.0 - 2.0\,R_{\rm eff}$, $2.0 - 3.5\,R_{\rm eff}$ and $3.5 - 5.0\,R_{\rm eff}$) and further separate them in 10 mass bins. Finally, for each annulus, I fit a power law of the form ${\rm d}N/{\rm d}m \sim m^{\alpha}$, to the mass bins and determine the MF slope.

In Fig. 3.4, I show the MF slope of my simulations as a function of projected radius. For the simulation without BHs, I see a decrease of the MF slope with increasing distance from the cluster centre. With increasing amount of initially retained BHs, the MF slope becomes flatter. The MF of the N1 simulation varies negligibly with radius and therefore I can reproduce the radius-independent MF slope as found in NGC 6101 with my N-body model which initially retained all BHs.

3.4 Prediction for the expected kinematics

The observable properties that are often used to quantify the amount of mass segregation in GCs are the cumulative radial distribution of their observable stars, or the MF slope at different radii. In Section 3.3, I showed that, by using these observations, it is impossible to distinguish between a cluster that is not mass-segregated, and a mass-segregated cluster containing a population of stellar-mass BHs. Moreover, a cluster containing an IMBH

would also show no sign of mass segregation as the IMBH halts the mass segregation process (Gill et al. 2008). It is therefore necessary to identify an additional observational property to discriminate between these three options.

In addition, I note that the two N-body models with BHs can reproduce the large core and the missing observable mass segregation, while the one without BHs is not able to reproduce either. From these models, it is therefore not possible to conclude whether the absence of observable mass segregation is due to the BHs, or due to the large core. Bianchini et al. (2016) found that $m_{\rm eq}$ (i.e. the mass below which stars have similar distributions, see discussion in Section 3.3.2) depends on the concentration of the cluster. To make sure that the absence of mass segregation is not due to the large core, which could be the result of other physics that was not included in my N-body models (i.e. a high primordial binary fraction; Vesperini and Chernoff 1994, Giersz and Heggie 2011, or an even larger core at formation), I consider equilibrium models that are able to include different mass components (so-called multimass models) and the effect of mass segregation. In these models, I can vary the stellar MF, and adjust the central concentration to match the observed number density profile of NGC 6101, to take advantage of their predictive power.

I use the models which are provided by the software package LIMEPY[4] (Lowered Isothermal Model Explorer in Python; Gieles and Zocchi 2015). This package allows the user to compute models including multiple mass components, and a variable amount of radial anisotropy. These models are a solution to the collisionless Boltzmann equation assuming a Maxwellian velocity distribution that is 'lowered' to mimic the effect of an escape energy due to the Galactic tides. LIMEPY models include the well-known single-mass King model (King 1966) as well as its multimass extension by Da Costa and Freeman (1976). The models include the truncation prescription by Gomez-Leyton and Velazquez (2014) with a continuous truncation parameter allowing us to model clusters in between the three classically known Woolley (1954), King (1966) and Wilson (1975) models. The LIMEPY models accurately describe the phase-space density of N-body models of single-mass systems (Zocchi et al. 2016) and multimass systems (See Chapter 2 / Peuten et al. 2016).

I consider four different dynamical models, to take into account the different scenarios introduced above:

- a single-mass model, representing a cluster with no mass-segregation; in the following, I refer to this as model SM.
- a multimass model representing a mass segregated cluster containing no BHs. Since it is comparable to N-body simulation N0, I name it M0.
- a multimass model, identified as model M0.5, representing a mass-segregated cluster containing 36% of its initial population of BHs, corresponding to the number of BHs retained in model N0.5 after $13\,\mathrm{Gyr}$.
- a multimass model, called M1, representing a mass-segregated cluster containing 68% of its initial population of BHs, corresponding to the number of BHs retained in model N1 after $13\,\mathrm{Gyr}$.

[4] LIMEPY can be found at: `https://github.com/mgieles/limepy`

Table 3.3: Main properties of the single-mass model SM, and of the multimass models M0, M0.5 and M1, as listed in the first column. I provide the total mass of the system M, the total mass of black holes $M_{\rm BH}$ and the mean mass of black holes $\langle m_{\rm BH}\rangle$, all expressed in $\mathrm{M}_\odot$, the half-mass radius $r_{\rm h}$, the projected effective radius $R_{\rm eff}$ and the assumed Jacobi radius $r_{\rm J}$ in pc and the central line-of-sight velocity dispersion σ_0 in km/s. The last two columns of the table refer to the structural parameters of the models that were determined through the fitting procedure (errors are also listed), namely the concentration parameter W_0 and the truncation parameter g.

Model	M	$M_{\rm BH}$	$\langle m_{\rm BH}\rangle$	$r_{\rm h}$	$R_{\rm eff}$	$r_{\rm J}$	σ_0	W_0	g
SM	1.08×10^5	0	0	12.4	9.3	84.6	2.7	$6.0^{+0.8}_{-0.9}$	$1.0^{+0.5}_{-0.4}$
M0	1.08×10^5	0	0	16.8	12.6	84.6	2.2	$7.5^{+1.1}_{-1.4}$	$0.8^{+0.41}_{-0.39}$
M0.5	1.14×10^5	1770	7.6	11.6	8.7	86.0	3.0	$28^{+8.4}_{-12}$	$2.08^{+0.09}_{-0.07}$
M1	1.20×10^5	3225	7.0	11.4	8.6	87.4	3.2	$22^{+9.2}_{-9.1}$	$2.13^{+0.07}_{-0.06}$

To calculate the multimass models M0, M0.5 and M1, it is necessary to provide an MF. Here I use the MF determined from the N-body models, by considering five mass bins for the MS stars, three mass bins for the WDs and one bin each for the evolved stars, NSs and BHs (for a discussion about the selection of mass bins, I refer the reader to Chapter 2.4.1 / Peuten et al. 2017).

I summarize the properties of all models in Table 3.3. For all models, the luminosity of the cluster is set to the value given in the first line of Table 3.1. The mass is determined by assuming the same mass-to-light ratio as in Section 3.2 with value of $\Upsilon_{\rm V} = 1.9\ \mathrm{M}_\odot/\,\mathrm{L}_\odot$ for models SM and M0. To account for the mass of the BHs that do not contribute to the luminosity of the cluster, I changed the mass-to-light ratio to $\Upsilon_{\rm V} = 2.0\ \mathrm{M}_\odot/\,\mathrm{L}_\odot$ for M0.5 and $\Upsilon_{\rm V} = 2.1\ \mathrm{M}_\odot/\,\mathrm{L}_\odot$ for M1 to calculate their respective mass. For each model, I calculated the expected Jacobi radius using equation (3.2.2) with the same assumptions as in Section 3.2 and the above estimated mass. With these choices, I set the scales of the models, and I am only left with two structural parameters and a scale to fit on: W_0, which determines the concentration of the models, g, the truncation parameter and an additional normalization parameter which accounts for the unknown number of total stars used in the number density profile by D15 and which has no physical meaning to the results.

I carry out the fits by means of the EMCEE (Foreman-Mackey et al. 2013) software, which is a pure-PYTHON implementation of the Goodman & Weare's Affine Invariant Markov chain Monte Carlo Ensemble sampler (Goodman and Weare 2010). For the case of the multimass models, I fit on the number density of the evolved stars as these are the stars for which it is possible to obtain measurements. The best-fitting parameters obtained with this fitting procedure are provided in Table 3.3.

For the analysis of the case with an IMBH, I considered the family of dynamical models[5] presented by Miocchi (2007), which describe a single-mass cluster with an IMBH in the centre. Within this family, I selected the model characterized by $W_0 = 7.75$ and $M_{\rm IMBH}/M = 0.01$. I chose this model because it resembles the number density profile of NGC 6101, and its IMBH mass is comparable to the total mass of the BH population in model M0.5. To scale this model, I use the same scales I assumed for model M0.5.

[5]Several pre-tabulated models from this family are available for download at: `http://www.cosmic-lab.eu/bhking/`

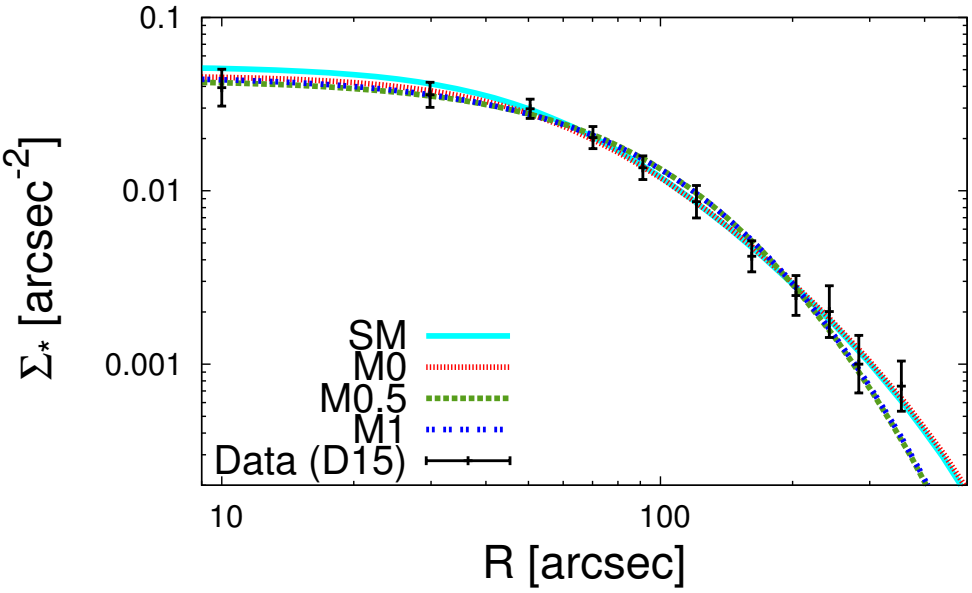

Figure 3.5: Number density profile of the globular cluster NGC 6101. Black points with error bars indicate the measurements from D15. Solid (cyan), fine dotted (red), thick dotted (green) and double dotted (blue) lines represent the profiles of the best-fitting models SM, M0, M0.5 and M1, respectively. Error bars denote 1σ uncertainties.

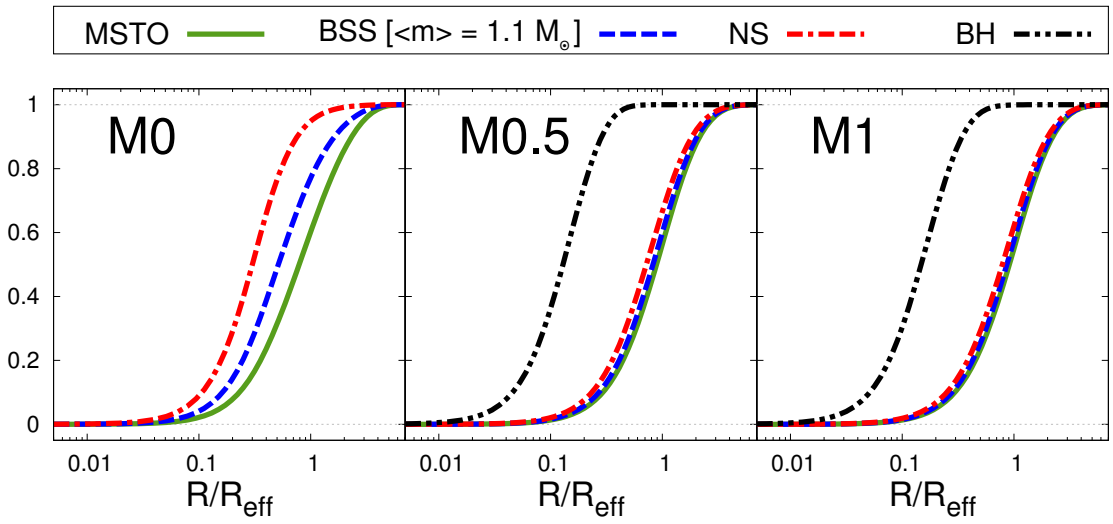

Figure 3.6: Cumulative radial distribution of different groups of stars. I show the distributions of the MSTO stars (solid green lines), of the BSS-proxy stars (dashed blue lines), of the NSs (double dash−dotted red lines) and of black holes (double dot−dashed black lines) as a function of the projected distance from the centre, in units of the projected effective radius $R_{\rm eff}$. Each panel corresponds to one of the multimass models I considered, as indicated by the labels. The average mass for the MSTO stars is $0.8\,{\rm M}_{\odot}$, for the NSs $1.4\,{\rm M}_{\odot}$ and for the BSS-proxy stars $1.1\,{\rm M}_{\odot}$. For the BHs, the average mass is $7.6\,{\rm M}_{\odot}$ for M0.5 and $7.0\,{\rm M}_{\odot}$ for M1.

In Fig. 3.5, I show the number density profiles of the four best-fitting dynamical models together with the observed values from D15. All the models appear to describe the observed data well. A slight disagreement is only seen at large radii, where the two dynamical models including BHs slightly underestimate the outermost point. For the three multimass models, I also calculated the cumulative radial distributions of MSTO stars, BSSs, NSs and BHs. As proxy for the BSSs, I chose the WD mass bin with an average mass of $1.1\,\mathrm{M}_{\odot}$ and as MSTO stars, I chose the mass bin with an average mass of $0.8\,\mathrm{M}_{\odot}$. Fig. 3.6 shows the same behaviour already found for the numerical simulations, and shown in Fig. 3.1: when considering a larger number of BHs in the cluster, the distributions of the other types of stars become more similar.

As a way to distinguish between the different proposed explanations for the missing signatures of mass segregation, I consider the line-of-sight velocity dispersion profiles predicted by the models and shown in Fig. 3.7. For the models with mass segregation, I used again only the evolved stars for the calculation of the line-of-sight velocity dispersion, as these are the stars for which it is possible to obtain measurements. In the N-body models, these stars have luminosities in the range of $\log\left(\mathrm{L}/\mathrm{L}_{\odot}\right) = 0.7 - 3.3$. For the models without mass segregation, a selection of stars is irrelevant as the line-of-sight velocity dispersion is the same for all stars. The values of the central line-of-sight velocity dispersion obtained for models M0.5 and M1, representing mass-segregated clusters with BHs, are respectively 0.3 and $0.5\,\mathrm{km\,s^{-1}}$ larger than the one obtained for model SM (no mass segregation, no BHs), which is, in turn, $0.5\,\mathrm{km\,s^{-1}}$ larger than that predicted for model M0 (mass-segregated cluster without BHs). The line-of-sight velocity dispersion profile for the IMBH model follows the SM profile. It only differs in the central $10\,\mathrm{arcsec}$, where a cusp in the velocity profile is found. I note that the number density profile does not resolve this area, and therefore the central rise expected when an IMBH is present cannot be detected. The central line-of-sight velocity dispersion for the IMBH model is $2.4\,\mathrm{km\,s^{-1}}$ larger than the one of model SM: this means that a measurement of the line-of-sight velocity dispersion within the inner $10\,\mathrm{arcsec}$ could distinguish between the scenarios.

3.5 Discussion and conclusion

Recently, D15 observed that BSS and MSTO stars have the same radial distribution in the GC NGC 6101, and they argue that the cluster is not mass-segregated and not dynamically evolved. Sarajedini and Da Costa (1991) and Marconi et al. (2001), who also studied the radial distribution of the BSSs in this cluster, found indications for mass segregation. The reason for this discrepancy is that each of these papers analyse a different sample of BSS stars. Sarajedini and Da Costa (1991) were the first ones to study BSSs in this cluster and they found 28 BSSs. Marconi et al. (2001) found and studied 73 BSSs in NGC 6101. D15, however, reduced the sample of BSSs in NGC 6101 to 52 objects, after identifying and removing sources which are contaminated and/or blended by other MS stars or evolved stars. Given these and other improvements by D15, I adopt their interpretation that NGC 6101 does not show any observable signs of mass segregation.

By carrying out three numerical N-body simulations containing a different amount of BHs, I showed that the same behaviour is found in a mass-segregated cluster containing a population of stellar-mass BHs. Indeed, even if they are not directly observable, BHs have

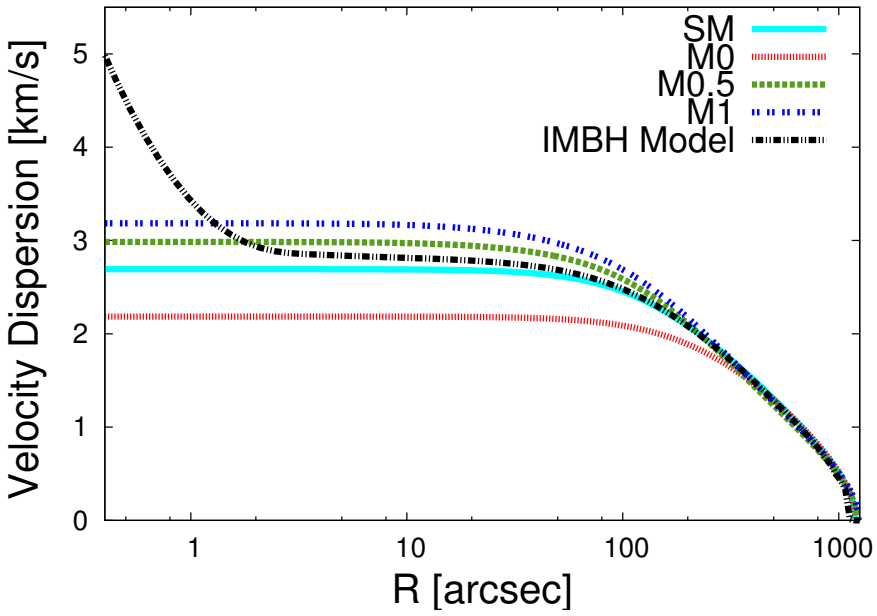

Figure 3.7: Line-of-sight velocity dispersion profiles predicted by the models. Solid (cyan), fine dotted (red), thick dotted (green), double dotted (blue) and dot−dashed (black) lines show the profiles predicted from the SM, M0, M0.5, M1 and IMBH model, respectively. In the case of multimass models, I show here the profiles relative to the mass bin representing evolved stars, which are the ones for which is possible to obtain measurements.

an effect on the overall distribution of stars in the mass range available for observations ($0.7 - 1.6\,\mathrm{M}_{\odot}$) that appear to have the same distribution, as shown in Fig. 3.1.

We also see from my simulation without BHs (N0) that the age and present-day mass and half-mass radius suggest that NGC 6101 is dynamically evolved, and is expected to be mass-segregated. Model N0 shows clear evidence for observable mass segregation. The scenario of a non-mass-segregated cluster could then only be explained if some of my assumptions, such as the age of the cluster, its stellar evolution or its IMF, were significantly different from what I assumed here, which I consider unlikely. I therefore favour the explanation that NGC 6101 contains a stellar-mass BH population.

Stellar-mass BH candidates were recently found in M22 and M63 by Strader et al. (2012) and Chomiuk et al. (2013), respectively. Several studies have shown that, if the initial supernova kicks are not large enough to eject the BHs from the cluster at creation, then a significant fraction of BHs can be retained for more than $12\,\mathrm{Gyr}$ (Breen and Heggie 2013a,b; Sippel and Hurley 2013; Morscher et al. 2015); in particular, this happens when clusters have large initial radii (Morscher et al. 2015; Rodriguez et al. 2016b). Moreover, Mackey et al. (2008) showed that the large cores of GCs in the Magellanic Clouds can be explained by the presence of a population of stellar-mass BHs in the systems. The fact that NGC 6101 is on a retrograde orbit is seen as an indication for an extragalactic origin (Geisler et al. 1995). More recently, it has been suggested that NGC 6101 was accreted into the Milky Way (Mackey and Gilmore 2004) and could originally come from the Canis Major dwarf galaxy (Martin et al. 2004). One of the arguments used by Mackey and Gilmore (2004) to support the claim that NGC 6101 is accreted is the observation that

the large core radius of the cluster is more comparable to the core radii of GCs in dwarf galaxies than to those of clusters in the Milky Way. This raises the question why GCs that form in dwarf galaxies contain more BHs than GCs that form *in situ*. There are no reasons to expect that the initial stellar MF is significantly different in dwarf galaxies (although, see Geha et al. 2013), nor that the supernova kicks are different in dwarf galaxies. One idea is that all GCs retain a large fraction of their BHs after supernova kicks (i.e. BH kicks are low), and that GCs in dwarf galaxies form with lower densities (e.g. Elmegreen 2008). A low-density implies a long $\tau_{\rm rh}$ (for a given mass), such that fewer BHs are dynamically ejected.

An alternative explanation for the observed properties of NGC 6101 could be the presence of an IMBH. This central object would cause, in many respects, effects similar to those of a population of stellar-mass BHs, such as the formation of a large core and a large ratio of core radius to half-mass radius (Trenti et al. 2007; Lützgendorf et al. 2013). In addition, an IMBH can quench mass segregation among the visible stars: Gill et al. (2008) show that this effect is due to close encounters between stars and the IMBH, resulting in slingshot ejections to large distances, thereby reversing mass segregation. Moreover, the IMBH is likely to acquire a companion, either a star or a remnant, which makes stellar ejections particularly common. Gill et al. (2008) also measured mass segregation by looking at the variation with radius of the average mean mass of MS stars with mass in the range $0.2-0.8\,{\rm M}_{\odot}$. They showed that an IMBH with mass equal to 1% of the cluster mass generates a small variation of this quantity between the centre and the half-mass radius, and they conclude that if such variation is smaller than $\sim 0.07\,{\rm M}_{\odot}$, the cluster is likely to be hosting an IMBH. As a comparison, in both my N-body simulations containing a population of BHs, the variation of the average mass between the centre and the half-mass radius is also smaller than $0.07\,{\rm M}_{\odot}$ (for N0.5, I find a variation of $0.03\,{\rm M}_{\odot}$, for N1 of $0.04\,{\rm M}_{\odot}$), when considering MS stars. Gill et al. (2008) also discuss the possibility that a BH population could create the same observable effect, but they assume that BHs will leave the GC rather quickly and their impact on the observed mass segregation should therefore be rather small.

Another possible alternative explanation could be the presence of binaries alone: it is known that binaries inflate the core (Vesperini and Chernoff 1994; Giersz and Heggie 2011) and could therefore also explain the large core of NGC 6101. With my current results, I cannot quantify the degree of expected mass segregation due to binaries. A qualitative result can be drawn if one assumes that the binaries have a mass distribution comparable to the one of the NSs: the first panel of Fig. 3.6, relative to model M1, shows that the NSs alone have a negligible effect on the apparent observational mass segregation and therefore the expected effect due to binaries alone should also be rather low.

Due to recent confirmation of the existence of gravitational waves by a binary BH merger (Abbott et al. 2016d), it is worth mentioning that GCs with a sizeable BH population, such as NGC 6101, could be a cradle of gravitational wave sources (Portegies Zwart and McMillan 2000; Aarseth 2012): not only do recent studies show that a significant fraction of BHs can be retained for more than $12\,{\rm Gyr}$ but they also predict a high binary fraction among the BHs in the core (Morscher et al. 2015).

Finally, I propose an observational test to distinguish the various possible scenarios for the cluster. From a comparison of distribution function-based models to the number density profile of NGC 6101, I show that a mass-segregated cluster with stellar-mass BHs

is expected to have a central line-of-sight velocity dispersion $\sim 0.5\,\mathrm{km\,s^{-1}}$ larger than a non-segregated cluster without BHs. When considering the presence of an IMBH in the centre of the cluster, the predicted central line-of-sight velocity dispersion should be even larger, assuming a value up to $\sim 5.1\,\mathrm{km\,s^{-1}}$. Looking at the star counts by D15 for NGC 6101, one can see that approximately 100 RGB stars (or 20% of D15 sample), with a V-band magnitude between 13.5 and 18.7, are located within the core radius, with around 7 of them located within the inner 10 arcsec. By obtaining an accurate measure of the velocity dispersion of NGC 6101 within the core radius, it should be possible to discriminate between the proposed scenarios, and to determine the dynamical state of this cluster.

Chapter 4

Dynamical inference of a stellar-mass black hole population in the Galactic globular cluster NGC 6101

Abstract

The Galactic globular cluster (GC) NGC 6101 is a candidate GC to host a stellar-mass black hole population. I present kinematics of NGC 6101 of 1108 stars obtained with the *MUSE* integral field spectrograph. I model the cluster using lowered isothermal multimass models together with a model for the mass function of stars and remnants, including the effect of stellar evolution and dynamical ejection and a statistical treatment of binaries. I complement the kinematics with data from *HST* and *Gaia* and find that the cluster is best described by a model where $291^{+144}_{-84}\,\mathrm{M}_{\odot}$ of the primordial BH population is still retained. I find a total cluster mass of $1.71^{+0.14}_{-0.12} \times 10^5\,\mathrm{M}_{\odot}$ and a half-mass radius of $17.6^{+0.2}_{-0.2}\,\mathrm{pc}$. Finally, I find that roughly half of the cluster's mass consists of non-luminous stellar remnants. This paper presents the first dynamical detection of a stellar-mass black hole population in a GC. I discuss limitations in my modelling approach and provide a discussion on how future observations can improve the significance of this detection in NGC 6101 and in other GCs.

This Chapter will be submitted for publication in Monthly Notices of the Royal Astronomical Society (MNRAS), and will be published as Peuten et al., (in prep).

Sec. 4.4.1 was written together with Dr. Edurado Balbino and Sec. 4.4.2 was written together with Dr. Thomas de Boer. The analysis described in Sec. 4.3.2 was carried out together with Dr. Tim-Oliver Husser, the description itself was fully written by myself.

4.1 Introduction

With the recent detections of gravitational waves emitted by two colliding stellar mass black holes (BH) (Abbott et al. 2016a,c,d), not only was Einsteins theory of gravitational waves (Einstein 1916) confirmed, but also the existence of stellar-mass BH and the fact that two BHs can merge within a Hubble time (Abbott et al. 2016a) has been proven true. As with any astronomical discovery, this created more questions than it answered: One of these questions is in which environment two stellar-mass BHs can become a binary and merge. Various scenarios have been put forward, involving massive binary star physics and dynamical formation in dense stellar systems such as globular clusters (GCs) (Abbott et al. 2016a). The answer to this question could help to further refine studies to better understand BHs and their physics (Benacquista and Downing 2013; Hessels et al. 2015).

From stellar evolution models I find that around $\sim 0.2\%$ of stars in a GC (or $\sim 10\%$ of the mass) turn into a stellar-mass BHs at the end of their lifetime. However, there is an ongoing debate whether the natal kick of these stellar-mass BHs is low enough to keep them in the cluster (Belczynski et al. 2002, 2010; Repetto et al. 2012; Fryer et al. 2012; Janka 2013; Mandel 2016; Repetto et al. 2017; O'Shaughnessy et al. 2017; Pavlík et al. 2018). Yet there are BH formation scenarios in which stellar-mass BHs do not receive a significant natal kick at all (Fryer and Kalogera 2001; Fryer et al. 2012). Recent studies found that if the natal kick is so low that a stellar-mass BH population is kept in a GC, then a significant fraction can be retained up to the current lifetime of Galactic GCs, especially for clusters with large initial radii (Mackey et al. 2008; Morscher et al. 2013; Breen and Heggie 2013a,b; Sippel and Hurley 2013; Heggie and Giersz 2014; Morscher et al. 2015; Wang et al. 2016; Banerjee 2018; Webb et al. 2018). This is different from the previously dominating understanding that BHs would sink into the GC's centre where they would start to kick each other out until only one, two or none of them remain (Kulkarni et al. 1993; Sigurdsson and Hernquist 1993).

There are several recent observations hinting at stellar-mass BHs in GCs. In M22, two stellar-mass BH candidates were found (Strader et al. 2012) using radio and X-ray observations, hinting that there could be up to 100 stellar-mass BHs in this cluster. Using the same technique, a stellar-mass BH candidate in the GC M63 (Chomiuk et al. 2013) was detected. In the GC 47 Tuc, the X-ray source X9 was identified as another quiescent stellar-mass BH candidate (Miller-Jones et al. 2015; Bahramian et al. 2017). Another possible BH candidate was identified in the Milky Way GC NGC 6553 using microlensing events (Minniti et al. 2015). Using *MUSE* observations, Giesers et al. (2018) recently found a stellar-mass BH candidate in a binary system in the GC NGC 3201. In extragalactic GCs, several indications for stellar-mass BHs were also found (Mackey et al. 2008; Barnard et al. 2008; Barnard and Kolb 2009; Roberts et al. 2012).

These results indicate that some GCs might still harbour a BH population, which could be cradles for further gravitational wave events (Portegies Zwart and McMillan 2000; Aarseth 2012). So far, the methods used to successfully identify BHs in GCs are only able to detect individual BHs. Therefore, to detect BH populations in GCs, new methods are needed. Arca Sedda et al. (2018) used a set of Monte Carlo GC simulations with stellar-mass BH populations and found a correlation between the average GC surface brightness inside the projected half-light radius and the mass density of the stellar-mass BH population. Askar et al. (2018) used this relation to estimate the properties of possible

BH populations in 29 Milky Way GCs. Predictions from such relatively simple relations understandably call for confirmation using more elaborated methods and observations.

One of the GCs for which Askar et al. (2018) predicted a BH population is the Milky Way GC NGC 6101: it is located in the constellation Apus (Dunlop 1828) at a distance of 14.6 kpc (Dalessandro et al. 2015) from the Sun and 11.2 kpc (Harris 1996) from the Galactic Centre. With an estimated age of $13\,\mathrm{Gyr}$ (Dotter et al. 2010) and a metallicity of $[\mathrm{Fe/H}] = -1.98$ (Carretta et al. 2009), NGC 6101 is generally considered a metal-poor old halo GC. Compared to most other halo GCs, its properties are unusual, especially as its large core radius should have made it comparatively hard to survive its suspected $13\,\mathrm{Gyr}$ at its current distance to the Galactic Centre (Mackey and Gilmore 2004). Martin et al. (2004) showed that its current characteristics are consistent with being accreted from the Canis Major dwarf galaxy. This is further supported by its retrograde orbit with a mean radial velocity of $364.3 \pm 1.9\mathrm{km/s}$ (Geisler et al. 1995; Sohn et al. 2018). Furthermore, Mackey and Gilmore (2004) showed that some of the properties of NGC 6101, such as the large core radius, are more comparable to the properties of GCs found in dwarf galaxies than to those of GCs in the Milky Way.

The recent interest in NGC 6101 comes from the debate about its dynamical state: when Sarajedini and Da Costa (1991) found the centrally concentrated blue straggler stars (BSS) in NGC 6101, they assumed the cluster to be mass-segregated. Using *Hubble Space Telescope* (*HST*) and ground observations of NGC 6101, Marconi et al. (2001) studied the radial distribution of different star types in NGC 6101 and also found the heavier BSSs to be more centrally concentrated than the lighter main-sequence turn-off stars (MSTO), hence they also concluded the cluster to be mass-segregated. Using the same observations and adding further ground-based observations, Dalessandro et al. (2015) revisited the GC and found the opposite: using an improved BSS selection mechanism which is able to detect and remove sources which are contaminated and/or blended by other stars, they find that the radial distributions of BSS, MSTO, horizontal branch (HB) stars and red giant branch (RGB) stars are not indistinguishable from one another, hence the cluster lacks any sign of observable mass segregation. Furthermore, they also studied the radial-dependent binary fraction within the main sequence (MS) stars, as well as the radial variation of the stellar mass function (MF), and found in both a lack of mass segregation.

In Chapter 3 (Peuten et al. 2016), I presented an explanation for the observed lack of mass segregation in NGC 6101 as presented in Dalessandro et al. (2015): using different N-body simulations of NGC 6101 with different amounts of initially retained BHs, I found that, if the cluster had retained most of its stellar-mass BH population, then one should measure a reduced level of mass segregation when looking at the observable stars only. Given that many properties of NGC 6101 are more comparable to GCs in dwarf galaxies (Mackey and Gilmore 2004) and regarding its possible extragalactic origins, in Sec. 3.5 I discuss the possibility that the BH evolution in GCs in dwarf galaxies might be different from that in the Milky Way: assuming that the physics behind the BH natal kicks is the same, the longer half-mass relaxation times (t_{h}) due to lower densities in dwarf galaxies (Elmegreen 2008) could lead to fewer stellar-mass BHs being dynamically ejected (Breen and Heggie 2013a).

Recently, Sollima and Baumgardt (2017) re-analyzed the *HST* observations of NGC 6101 in order to determine the MF. Using these results, Baumgardt and Sollima (2017) found a radially dependent variation in the MF, which is a sign for mass segregation

in NGC 6101. Webb et al. (2017) revisited the observations used in Dalessandro et al. (2015) and they come to a comparable conclusion: NGC 6101 does show signs of mass segregation although the degree of mass segregation is lower than one would expect for a cluster of that dynamical age.

I also discussed other theoretical explanations for the apparently reduced mass segregation in Chapter 3, such as the presences of an intermediate-mass black hole (IMBH) in the core of NGC 6101. Also, an IMBH could explain the observed large core and the large ratio of core radius over half-mass radius (Trenti et al. 2007; Lützgendorf et al. 2013). However, the existence of IMBH is fiercely debated, as almost every dynamical detection of an IMBHs has been rebutted by alternative interpretations or improved data (Zocchi et al. 2018; Gieles et al. 2018) and recent searches for signals of accretion onto an IMBH in several Milky Way GCs are also inconclusive (Tremou et al. 2018a). An other explanation for the current properties of NGC 6101 could be binaries, as they are also known to inflate the cores of GCs (Vesperini and Chernoff 1994; Giersz and Heggie 1996). Unfortunately, with the currently available observations, it is not possible to distinguish between the different proposed explanations for NGC 6101's reduced mass-segregation.

Using lowered isothermal multimass models, I showed in Sec. 3.4 that a measurement of NGC 6101's line-of-sight velocity dispersion should differentiate between those discussed solutions, and in the case of a stellar-mass BH population, those measurements should also help to further constrain the BH population. This is the target of this study: using *MUSE* observations, I determine the velocity dispersion of NGC 6101 within its half-light radius. Together with other observable data of NGC 6101 at hand, I model the GC, using lowered isothermal multimass models (Gieles and Zocchi 2015), to quantify the putative BH population of this cluster dynamically.

This paper is organized as follows: in Sec. 4.2, I present the *MUSE* observations of NGC 6101 and their reduction. In Sec. 4.3, I present the different steps needed to extract the velocity dispersion from the observations. In Sec. 4.4 I present the additional observations also used in this study. Next, in Sec. 4.5, I explain the modelling approach used in this study to analyse NGC 6101 and the tests I performed to check it. Also in this section I present and discuss my results from the modelling of NGC 6101. And finally, in Section 4.6, I present my conclusion.

4.2 Observation and reduction

The observations used in this study were obtained on six nights between May and June 2017 using the *MUSE* (Bacon et al. 2014) panoramic integral field spectrograph at the ESO/VLT (Prop ID: 099.D-0824, PI:Peuten). The observational run consisted of eight observation blocks (OBs) covering different regions between NGC 6101's centre and its half-light radius. Each observation used the Wide Field Mode of the *MUSE* instrument which covers an area of $1' \times 1'$ on the sky. The observations were planned such that each observation is overlapped by at least another one. To average out any systematic effects between the individual spectrograph and to better reject cosmics, I applied a 4-point dither pattern with small $0.5''$ offsets and 90 degrees derotator rotation between each exposure. Each such exposure was taken in nominal mode without adaptive optics, which covers a wavelengths range from 480 nm to 930 nm with a resolving power of 1770 to 3590

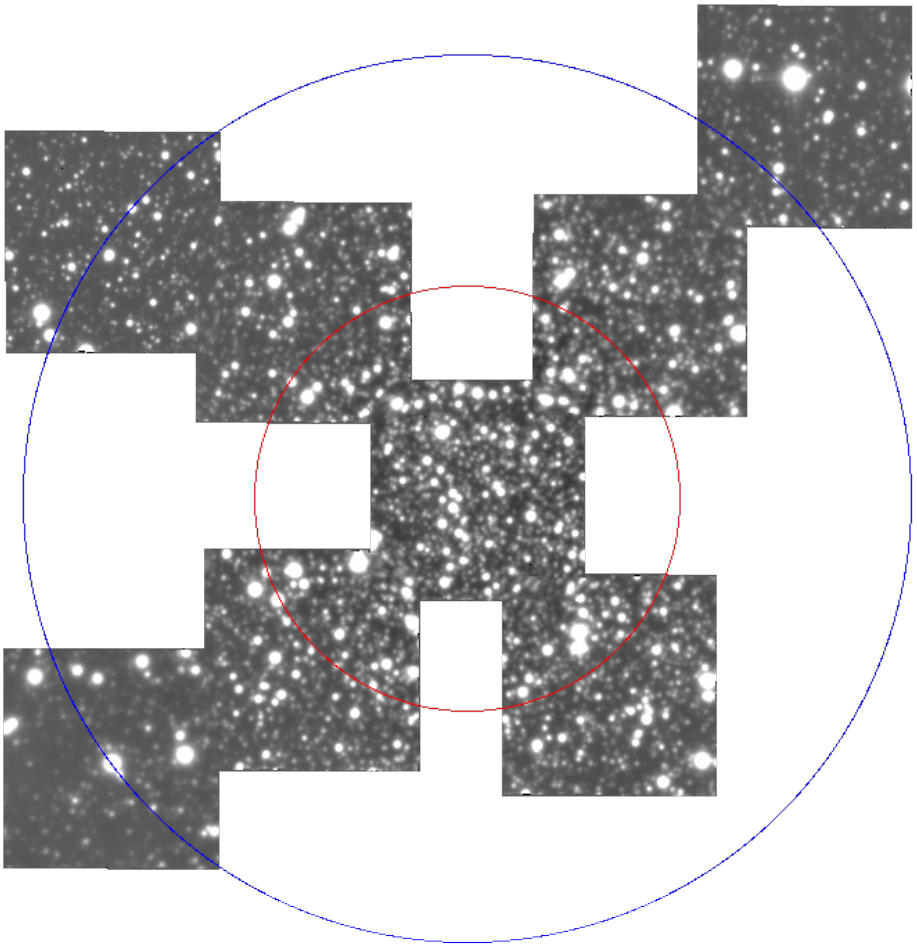

Figure 4.1: White light image of the combined observed *MUSE* data used in this publication. Superimposed are the core radius (red, inner circle) as well as the half-light radius (blue, outer circle).

respectably. Additionally, in each observation one sky exposure was taken at the end. The overall seeing was between $1.41''$ and $1.05''$ with a median of $1.175''$.

For the reduction of the observations, I used the official *MUSE* pipeline (Weilbacher et al. 2014) version 2.0.1. For the data from each of the 24 integrated field units (IFU) of the *MUSE* instrument, the basic reduction steps were performed separately: First, the bias, the flat, the wavelength calibration, the line spread function and the illumination corrections were computed for each of the IFU images. Then, using these information, any instrumental signature was removed from those exposures. In the next step, using observations from standard stars, which were observed in the same night, a response curve was created which was later used for the flux calibration. Using the sky observations, a model for the sky spectrum was also created. The last step of the actual reduction consisted of removing any sky contributions, applying flux calibration and astrometric calibration and finally merging the data of the 24 IFUs into one data-cube. Before I could progress, I combined the different exposures of the same regions, so that I was left with one data-cube for each of the 8 different regions observed. Fig. 4.1 shows a combined white light picture of all 8 OBs.

4.3 Data analysis

For the data analysis of my observations, I mainly followed the analysis presented in Husser et al. (2016) and Kamann et al. (2016, 2018), as they also observe GCs using the *MUSE* instrument in a comparable configuration and they also determine among others the velocity dispersion profile of their GCs.

4.3.1 Stellar spectrum extraction

One of the many reasons why GCs are interesting objects to observe is the fact that they have stellar densities which are several orders of magnitude higher than for example those found in the galactic plane. On the other hand, this means that observations of GCs suffer from heavy blending: due to the finite angular resolution, I observe the superposition of the light of different stars convolved by the system-dependent point-spread function (PSF). The observation of NGC 6101 presented here is no exclusion from this problem. I therefore have to disentangle the signals from different stars, before I can extract the individual spectra from the datacubes. For this task, I use the software PAMPELMUSE (Kamann et al. 2013) (version 0.94.0.3) which was purposely build to extract stellar spectra from crowded field observations made with the *MUSE* instrument. PAMPELMUSE needs a reference catalogue with a higher spatial resolution than the *MUSE* instrument, in a band also covered by the instrument. It then uses this data and some initial assumptions of the PSF to create a mock image to cross-correlate it to the observed one. From this comparison coordinate transformation between the catalogue and the observation, were determined as well as candidates for spectra extraction are selected. Next, using one wavelength slice of the datacube, the different previously selected sources are first fit using the current estimates for PSF and coordinate transformation. Then, all but few of the bright isolated sources are removed from the data and the PSF and the coordinate transformation is fit using only the remaining sources. After several iteration of this approach, the different parameters of the PSF and coordinate transformation converge. This approach is

than applied to all wavelength slices of the datacube, resulting in a wavelength-dependent model for the different parameters of the PSF and coordinate transformation. To even out random jumps in between the different wavelength slices, polynomial fits are then applied to these parameters, resulting in a smooth wavelengths-dependent description of the individual parameters. Using this parametrisation of the PSF and coordinate transformations, PAMPELMUSE is finally able to extract the spectra from the different sources out of the *MUSE* datacube.

For the NGC 6101 observation presented here, I can use the data from "*The ACS Globular Cluster Survey*" (Sarajedini et al. 2007; Anderson et al. 2008) as reference catalogue for the PAMPELMUSE extraction. Only some small patches at the edge of the observations are not covered by this catalogue. For these regions I use, as reference catalogue, the data presented in Marconi et al. (2001) which is based on observations made with $1.54\ \mathrm{m}$ Danish telescope at ESO/La Silla. Using these two catalogues, I extracted 2042 spectra from 1990 individual stars with a S/N ≥ 10, with V band magnitude ranging from 13.31 to 26.54 and a median of 19.87. I therefore have spectra covering the whole region of the evolved stars as well as for the high mass end of the main sequence stars in NGC 6101.

4.3.2 Radial velocity

The steps described in this section were carried out together with Dr. Tim-Oliver Hussler, the description was written by myself.

For the measurement of the radial velocities, we used a template-based method which uses the full spectrum rather than fitting on individual strong absorption features. For this, we used a method similar to the one presented in Husser et al. (2016) which itself is based on the method presented in Koleva et al. (2009): the idea is that the different transformations are applied to the reference spectrum until it matches the observed spectrum, which stays therefore untouched. In this study, we used the Göttingen Spectral Library (Husser et al. 2013) which has the following three parameters: the effective temperature of the star T_{eff}, the metallicity $[\mathrm{M/H}]$ and the surface gravity $\log g$. To create models inbetween the reference models, cubic splines are used and it is assumed that the wavelengths are independent from one another.

First we determined the mean line spread function (LSF) of the *MUSE* data, with which we convolved the currently selected model spectrum. This spectrum then had the same resolution as the *MUSE* data. Then, we applied a Doppler shift to the model spectrum to mimic the expected shift due to the stars velocity (v_{sys}).

Besides using a model star spectrum, we also fit a selection of telluric absorption lines (Husser and Ulbrich 2014): using the FASCODE-based (Clough et al. 1992, 2005) Line-By-Line Radiative Transfer Model[1] and assuming varying abundances, we computed a set of model spectra for the molecules with absorption lines in the *MUSE* observation wavelength. From these, we created data absorption spectra $T_n(X_n)$ for the different molecules, using a simple polynomial to interpolate for their different abundances (X_n) in the air. As with the model spectra, we then convolved these spectra with the mean *MUSE* LSF, and to compensate the inaccuracy in the wavelength calibration, we applied another Doppler shift (v_{Tel}). In Sec. 4.3.3, I am going to use the results of those telluric components to check and correct these wavelength calibration inaccuracies.

[1] `http://rtweb.aer.com/lblrtm_frame.html`

In each fitting step, we first calculated the model spectrum and then applied the velocity Doppler shift, and did the same for the telurric absorption models. Next, we combined both spectra, and then we multiplied the spectrum with a Legendre polynomial (P_n) to reproduce the observed fluxes. The order n of the polynomial was selected such that the lines in the spectrum are never misinterpreted as continuum fluxes. Finally, we summed up the difference between model spectra and observed spectra for each wavelength bin. We used a Levenberg-Marquardt optimisation to find those parameters of the model star spectrum ($T_{\rm eff}$, $[{\rm M/H}]$, $\log g$), the telluric absorption spectra ($T_n(X_n)$), the two doppler-shifts ($v_{\rm sys}$, $v_{\rm Tel}$) and the Legendre polynomial (P_n) that described the observed spectrum best.

We chose random initial conditions, which gave questionable results for the parameters $T_{\rm eff}$ and $\log g$ of the model star spectrum. Therefore, the results for the best-fit value for $[{\rm M/H}]$ should also be treated with caution, although the median value of -1.75 looks reasonable taking into account the previously measured metallicity of $[{\rm Fe/H}] = -1.98$ (Carretta et al. 2009). The reader must note that the model fits on the overall metal abundance and not on the iron abundance and that GCs are usually over-abundant in alpha elements hence the higher value for metal abundance. Improving the best-fit values of the model star spectrum should not improve the measured radial velocities of the stars. As this is the only value we were interested in, we opted against trying to improve the best-fit values.

In total, we could measure the radial velocity in 2004 spectra from 1952 different stars, which means that for 52 of them, we have two measurements of their radial velocity.

4.3.3 Telluric correction

When using observations to determine the radial velocities of the stars which span over a month, such as in my case, it is important to make sure that they are all measured in the same reference frame: even a small variation in the wavelength calibration can introduce artificial signals which can lead to an overestimation of the radial velocity dispersion. This is especially problematic as the expected velocity dispersion in NGC 6101 is rather low and therefore this effect could have a significant impact.

To therefore check for variations of the wavelength calibration, I used the measured velocities of the telluric components as discussed above. Before I could do this, I first had to undo the barycentric correction applied to the data by the *MUSE* reduction pipeline. Next, for all spectra with an S/N > 30, I calculated for each night the average velocity of the telluric component as depicted in Fig. 4.2: the night-to-night variation has a relatively low maximal difference of $0.75\,{\rm km\,s^{-1}}$ and the variation within one night is with $0.07\,{\rm km\,s^{-1}}$ negligible. The average standard deviation for the telluric components is $1.42\,{\rm km\,s^{-1}}$.

I use the average value of the telluric velocity from each night as absolute velocity offset and subtract it from all stellar velocities observed in the same night. The standard deviation of the telluric velocities is also quadratically added to the uncertainties of the stellar radial velocities, as I use it as a measure for the accuracy of the wavelength solution.

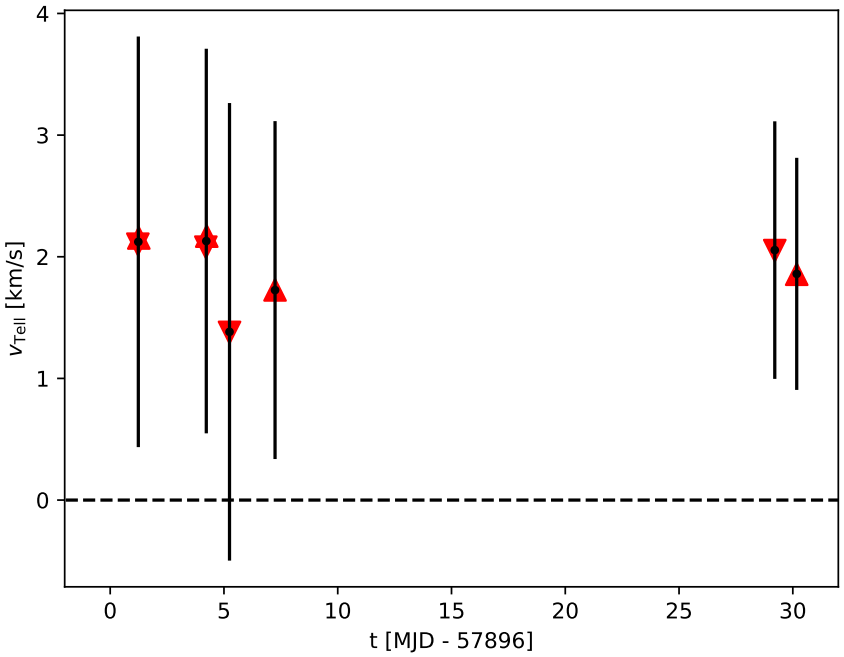

Figure 4.2: Average velocity of the telluric components for the different observed nights and OBs: The black points are the average value for each night with errorbars representing its standard deviation. Red triangles represent the average for the different OBs.

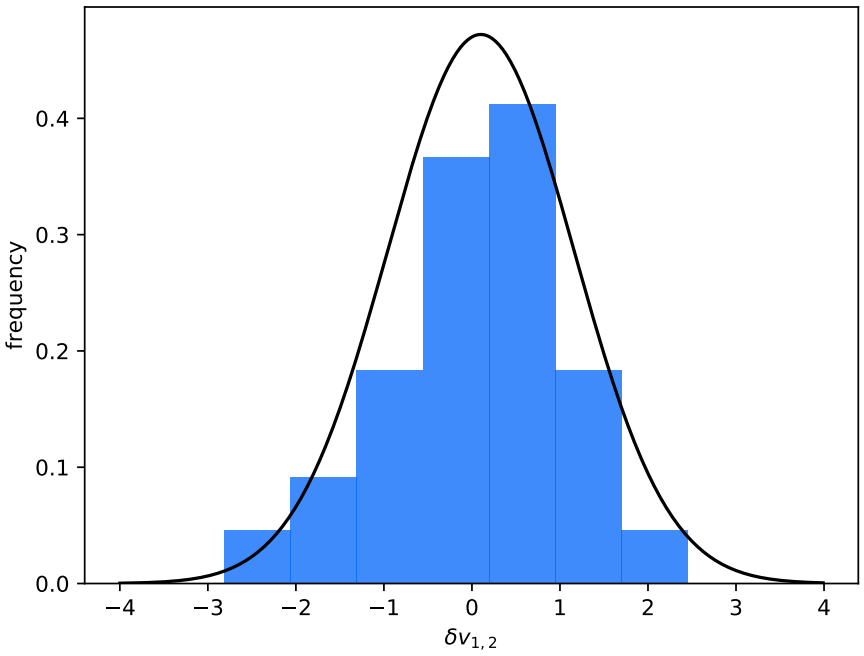

Figure 4.3: Histogram of the radial velocity difference for those stars which were observed twice. The black line represents the best fit Gaussian with $\sigma = 1.06$.

4.3.4 Uncertainties

Next, I had to carefully analyse the uncertainties, as wrong uncertainties can lead to wrong estimates of the velocity dispersion (van de Ven et al. 2006). To do this, I used those spectra from stars that were observed more than once. From the 52 stars where I have two spectra, I selected those pairs for which the S/N ratio agrees within 25%, and then for each of them, I calculated the quantity:

$$\delta v = \frac{v_2 - v_1}{\sqrt{\epsilon_1^2 + \epsilon_2^2}} \tag{4.3.1}$$

where v_i is the measured velocity of star i and ϵ_i its corresponding uncertainty. If the uncertainties are correct and have negligible uncertainties themselves, then the values for δv should come from a Gaussian distribution centred at the origin with a standard deviation of unity. If the standard deviation is greater than unity, the uncertainties are underestimated; if it is smaller than unity, they are overestimated.

The drawback of this method is that undetected radial velocity (RV) variable stars will systematically broaden the distribution and thereby artificially increase the recovered uncertainties. With my dataset, I have no means to identify RV variable stars, as several observations of the same region are needed to detect RV stars. To handle the broadening introduced by binaries, I later use a statistical approach which I will present in Sec. 4.3.8.

The results can be seen in Fig. 4.3: I find that the uncertainties are underestimated by a factor of 1.06 and I therefore multiply the uncertainties by that given factor and rerun the fit to confirm that now the uncertainties are more realistic.

4.3.5 Cluster membership

For the selection of cluster membership i opted for a simple 3σ clipping in velocity space, as the expected radial velocity for NGC 6101 of $364.3 \pm 1.9\mathrm{km/s}$ (Geisler et al. 1995) is high compared to the expected velocities of the Milky Way stars in that region. I could have also included $[\mathrm{M/H}]$ as additional selection constrain, but as already discussed in Sec. 4.3.2, the results of $[\mathrm{M/H}]$ should be handled with care. In Fig. 4.4, i have plotted the measured radial velocity against the measured value of $[\mathrm{M/H}]$ for all stars. Also indicated are the stars I consider cluster members and the stars which I consider non-members, as well as the region in velocity space which divides both groups. I identify 1758 stars as cluster members and 194 ($\sim 10\%$) as non-members.

The non-members can be further subdivided into a group of Milky-Way foreground stars and stars which might belong to NGC 6101 but their measured velocity is too different from the expected radial velocity for NGC 6101. All of the spectra belonging to those stars have a S/N lower than 18.5 and a measured velocity uncertainty greater than $7.5km/s$, except for three stars: these three stars have a S/N hight than 27 and a measured velocity uncertainty smaller than $4.2km/s$, one even has a S/N as high as 96.4 and a measured velocity uncertainty of only $1.5km/s$. Still those three stars have measured velocities which are more than 3σ away from the expected cluster radial velocity, as can be seen in Fig. 4.5. Together with the low uncertainty, this suggests that these three stars might be in a binary configuration. In Fig. 4.4 and Fig. 4.5, these three stars are marked as blue stars, and in Tab. 4.1, I list their properties, as further observations of these stars might help to constrain their binary nature further.

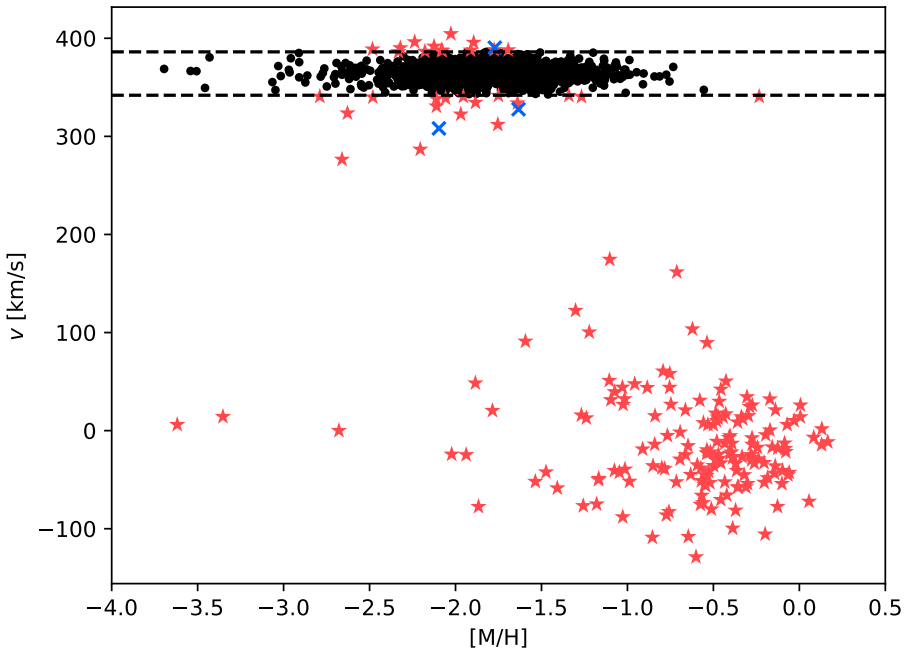

Figure 4.4: Measured velocity for the different stars plotted against their metalicity. Black dots represent stars which I considered as cluster member, red stars those stars which I do not consider as cluster members and the three blue crosses are stars which I consider as binary candidates in the cluster. The two black dash lines represent the 3σ selection criteria. As discussed in the text should the values for metallicity be treated with caution: The appender spread is explainable trough the high uncertainties recovered, which are not shown in this plot for a clearer view. I also omitted the uncertainties of the velocities for a better understanding.

Table 4.1: Properties of the three binary candidates found in my sample: First the ID number as given to them in the "*The ACS Globular Cluster Survey*" (Sarajedini et al. 2007; Anderson et al. 2008) catalogue, followed by their sky positions. Next their S/N in my *MUSE* observation and finally their measured velocities with the accompanying uncertainty in km/s.

ID	RA	DEC	SNR	v km/s
1618	$16:26:12.272$	$-72:12:59.91$	96.4	327.7 ± 1.5
10482	$16:25:45.421$	$-72:13:16.23$	27.3	308.1 ± 4.2
24324	$16:25:53.135$	$-72:12:41.76$	34.2	390.4 ± 3.0

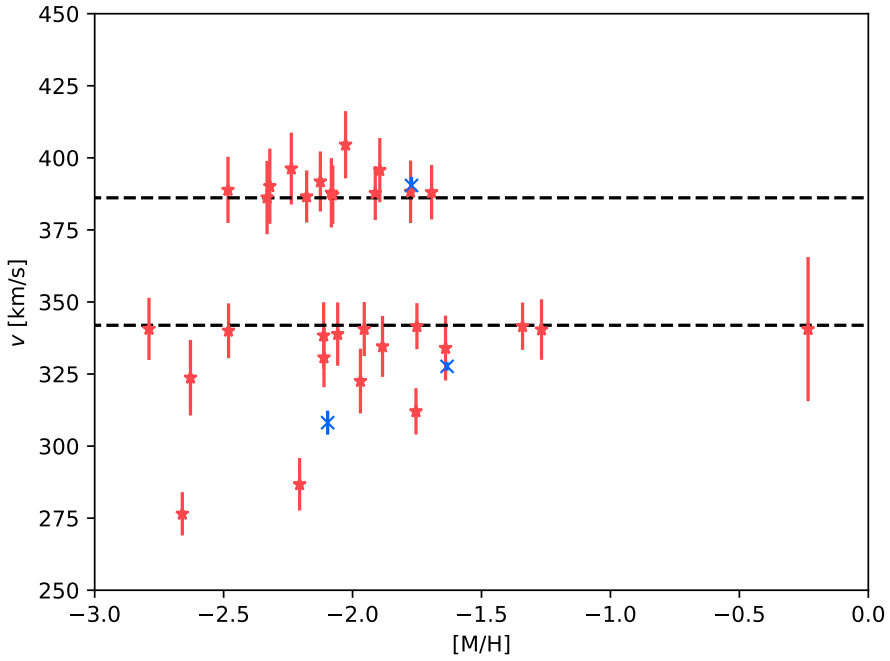

Figure 4.5: Selection from Fig. 4.4 showing only the stars which are considered cluster members but fall out of the selection criteria (red). This time with their velocity uncertainty. The blue crosses represent the three binary candidates, which have a distinctive lower uncertainty than the rest of the objects. The two black dash lines represent the 3σ selection criteria.

4.3.6 Final selection

In studies like the one presented here, there is always the trade-off between including as much data as possible and excluding as many suspected faulty data as possible. As mentioned before, I am only using spectra with a S/N ≥ 10 to remove spectra which are faulty due to cosmic-ray hits or residuals from saturated neighbours. To further reduce the effect the measured radial velocity uncertainties have on my analysis, I decided to remove all velocities with an uncertainty $> 8.0\,\mathrm{km\,s^{-1}}$ from my analysis. This removes 650 (37%) stars from the set and leaves us with 1108 stars to work on.

Removing stars with a high uncertainty in the radial velocity preferably removes the less luminous and therefore less massive stars from my data: due to the fact that these stars have on average a lower S/N value and therefore also a higher uncertainty for the radial velocity. This can be seen in Fig. 4.6 where I have plotted the uncertainty of the measured velocity against the S/N. Colour-coded is the V-band luminosity of each star. But for my study, removing the low mass stars is not a problem as I are primarily interested in the velocity dispersion of the brighter giants and main-sequence turn of stars.

In Fig. 4.7, a histogram of the measured velocities of all stars I use for my analysis is shown. From this data, I find that the radial cluster velocity of NGC 6101 is $364.3 \pm 0.16\,\mathrm{km\,s^{-1}}$, which agrees very well with the previous literature value of $364.3 \pm 1.9\mathrm{km/s}$ (Geisler et al. 1995), which is also indicated in the histogram together with its uncertainty.

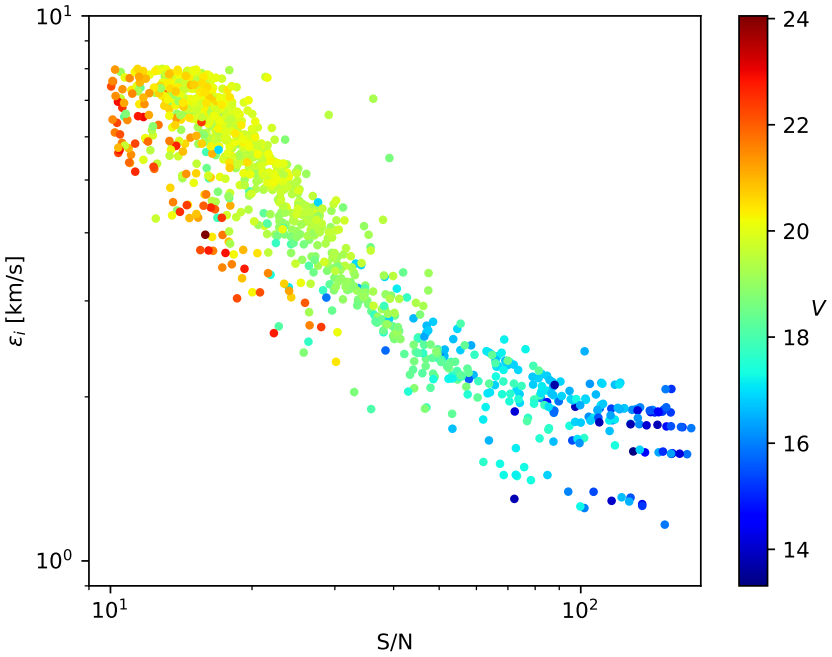

Figure 4.6: Radial velocity uncertainty against S/N for all the stars used for the analysis. Colour-code is the V-band luminosity. As can be seen have the brightest stars the highest S/N and therefore also the lowest uncertainties.

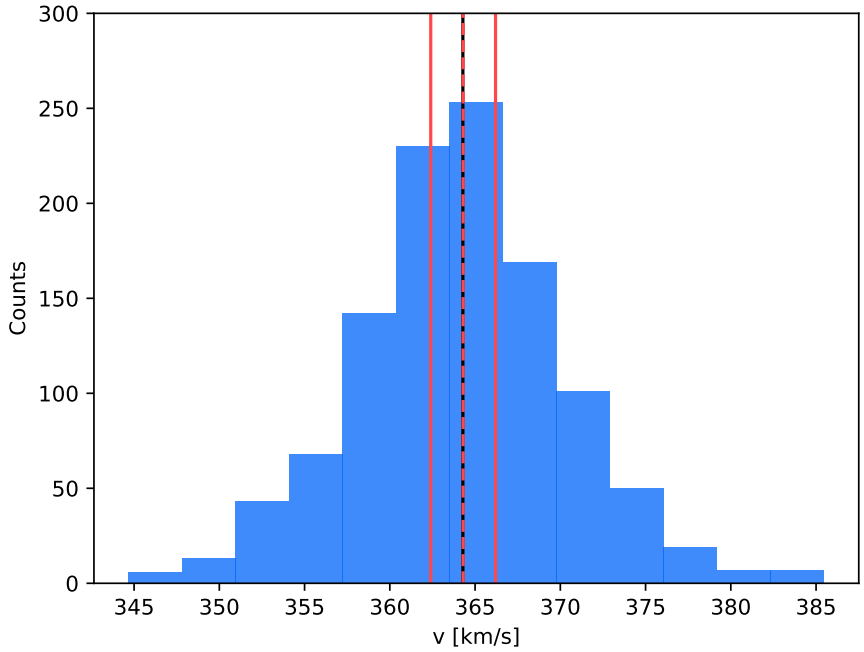

Figure 4.7: Histogram of the velocities from the stars considered bound to the cluster. The average velocity of $364.3 \pm 0.16\,\mathrm{km\,s^{-1}}$ (black line) is equal to the previously founded value (red dashed line, red solid line: 1σ region).

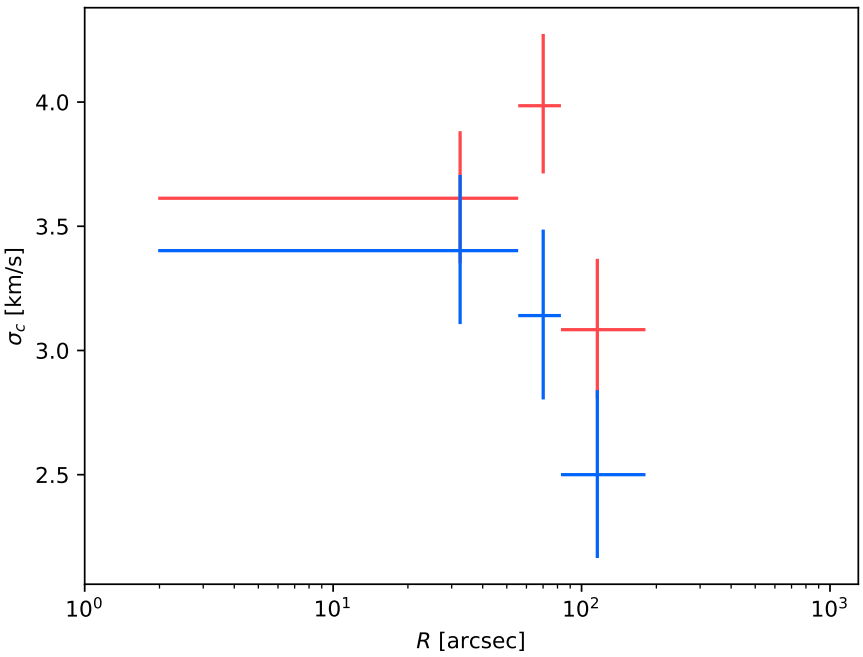

Figure 4.8: Measured velocity dispersion profile using 3 radial bins, the y-errorbars represent the uncertainty of the velocity dispersion while the x-errorbars show the radial range covert. The red points represent the best fit values, ignoring any influences from binaries, while the blue points incorporate the binary effects.

4.3.7 Radial velocity dispersion

With the data finally ready, I can now calculate the radial velocity dispersion of NGC 6101. For this, I apply the approach as presented in Pryor and Meylan (1993): I assume that the velocity of the stars in a cluster are drawn from a Gaussian distribution such that the likelihood of observing a velocity v_i for star i is given by:

$$\mathcal{L}_{\text{single}}\left(v_i|\sigma_{\text{c}}\right) = \frac{1}{\sqrt{2\pi\left(\sigma_c^2+\epsilon_i^2\right)}}\exp\left(-\frac{\left(v_i-\bar{v}\right)^2}{2\left(\sigma_{\text{c}}^2+\epsilon_i^2\right)}\right) \tag{4.3.2}$$

with ϵ_i its uncertainty, $\bar{v}$ the cluster velocity and σ_c its velocity dispersion. To determine the cluster's velocity dispersion, I have to find those values for $\bar{v}$ and σ_c that maximise the likelihood for all measured velocities. For this, I use a Goodman & Weare's Affine Invariant Markov chain Monte Carlo (MCMC) Ensemble sampler (Goodman and Weare 2010) as found in the PYTHON software package EMCEE (Foreman-Mackey et al. 2013).

In the modelling of the cluster, I will present a best-fit velocity dispersion profile, but for the sake of completeness, I present in Fig. 4.8 a velocity dispersion profile (red points) based on the *MUSE* observation only.

4.3.8 Binary influence on the velocity dispersion

As already mentioned in Sec. 4.3.4, binaries broaden the velocity dispersion in a non-Gaussian way. To overcome this influence, one approach is to conduct repeated observations of the same field to identify binaries. Given that I have only a single epoch for the majority of stars, I used a statistical approach instead: in Cottaar et al. (2012) and Cottaar and Hénault-Brunet (2014), the authors present a likelihood function for the binary populations, which allows to determine the underlying true velocity dispersion and binary fraction without the need of locating individual binaries. The likelihood for observing a star with velocity v_i, is then given by the convolution of $\mathcal{L}_{\rm single}$ and the likelihood of observing a velocity as the result of binary orbital motions ($\mathcal{L}_{\rm bin}$)

$$\mathcal{L}_{\rm binary}\left(v_i|\sigma_i,\Theta_{\rm bin}\right)=\int\mathcal{L}_{\rm single}\left(v_i|\sigma_i\right)\mathcal{L}_{\rm bin}\left(v_i-v'|\,\Theta_{\rm bin}\right)dv' \tag{4.3.3}$$

where $\Theta_{\rm bin}$ are the parameters of the binary population, $\mathcal{L}_{\rm single}$ is the likelihood from equation (4.3.2) and $\mathcal{L}_{\rm bin}$ is the likelihood of the velocity offset (v_i-v') being due to orbital motions of binaries. To calculate $\mathcal{L}_{\rm bin}$ from Cottaar et al. (2012), I randomly sampled 10^8 binaries using the Raghavan et al. (2010) log-normal period distribution with a mean at $\log_{10}P=5.03$ and a dispersion of $\sigma_{\log_{10}P}=2.28$ where P is in days. For the binary mass ratio distribution, I used the power-law relation of $\mathrm{d}N/\mathrm{d}q\sim q^{-0.5}$ for $0.1<q<1$ as presented in Reggiani and Meyer (2013) and a flat eccentricity distribution as observed in Raghavan et al. (2010).

The combined likelihood function for determining the radial velocity dispersion including the binary effects is:

$$\mathcal{L}\left(v_i|\sigma_i,\Theta_{\rm bin}\right)=f_{\rm bin}\mathcal{L}_{\rm binary}+\left(1-f_{\rm bin}\right)\mathcal{L}_{\rm single} \tag{4.3.4}$$

where $f_{\rm bin}$ is the binary fraction. Using the above likelihood function, in the form of Cottaar and Hénault-Brunet (2014) VELBIN software, and the radial bins used in the previous section, I rerun the MCMC fit and find the underlying velocity dispersion as depicted by the blue points in Fig. 4.8. Compared to the results from the previous section, the velocity dispersion profile behaves more like one would expect, although the average uncertainty is higher than before.

Assuming the binary fraction to be independent of radius, as found by Dalessandro et al. (2015) for NGC 6101, the best-fit value for the binary fraction is $f_{\rm bin}=14^{+7}_{-5}\%$, which is in agreement with the previously found values by Dalessandro et al. (2015) ($f_{\rm bin}=(14.4\pm0.9)\%$), Milone et al. (2012) ($f_{\rm bin}=(9.6\pm0.6)\%$) and Sollima et al. (2007) ($f_{\rm bin}=(15.6\pm1.3)\%$), albeit with a higher uncertainty. When modelling the cluster, I will present an improved value for the binary fraction, as here the cluster dispersion is fixed to three values, while in the modelling the cluster dispersion can vary with the radius.

To better quantify the effect of binaries on the measured velocity dispersion, I calculated the kurtosis, which is a measure of the "peakness" or "tailedness" of a distribution: for values below 0, the distribution is flat peaked compared to a Gaussian distribution; while for values above 0, the distribution has extended wings and a narrower peak compared to a Gaussian distribution; and for 0, the distribution is a Gaussian distribution. As the binaries should increase the number of stars found with higher velocity difference, one would expect values for the kurtosis above 0, which I find with a value of 0.69 calculated over the whole dataset.

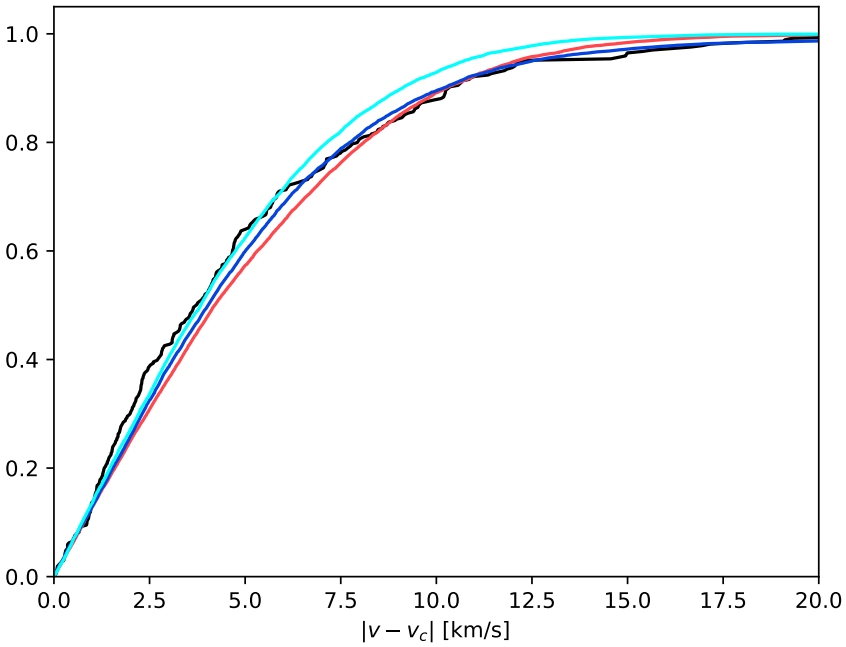

Figure 4.9: Cumulative velocity difference for the data from the middle data point from Fig. 4.8, in black, compared to three different predictions. In red: compared to the best fit Gaussian assuming no binaries. In blue: compared to the best fit model incorporating binaries. In cyan: compared to the underlying Gaussian distribution from the blue line.

Additionally, in Fig. 4.9 I present the cumulative velocity difference, which is the cumulative histogram over the absolute difference between the measured velocity of each star and the mean cluster velocity, for the middle radial bin from Fig. 4.8. The red line represents the best-fit prediction assuming no binaries. The blue line represents the best-fit prediction assuming binaries and the cyan line represents the underlying Gaussian distribution from the best-fit prediction with binaries, i.e. from the blue line. As can be seen, when no binaries are considered, the fit has problems to recover the profile, while when binaries are considered the overall agreement is better. Looking at the underlining Gaussian distribution from the blue line, one can see the pronounced wings at the high velocity difference part, due to the binaries.

While the effect of the binaries can be perceived as subtle at first glance from Fig. 4.9, the effect on my study is not neglectable as can be seen in Fig. 4.8. Therefore, the effects of binaries have to be considered when studying low velocity dispersion regions like GCs.

4.4 Additional data

In this section I present two additional data sets I am going to use: firstly, I use *HST* data for getting the number density profiles of the observable stars in different mass bins, and secondly, I use *Gaia* data to infer the density profile of the cluster out to his tidal radius.

4.4.1 Hubble Space Telescope data

This section was conducted and written together with Dr. Edurado Balbino.

We used ACS/WFC data from proposal IDs 13297 (PI: Piotto) and 10775 (PI: Sarajedini). The former provides data in the inner parts in the F606W and F814W filters, while the latter provides 5 pointings in the outskirts using F475W and F814W filters. The exposure times in F475W, F606W and F814W are approximately 4740s, 5920s, and 8040s.

The photometry was carried out using DOLPHOT (Dolphin 2000). We use the F814W images as reference frames and run the photometry on the non-geometrically corrected images where charge transfer efficiency (CTE) corrections were applied (i.e. images with `_flc` extension). We adopted the recommended DOLPHOT parameters for crowded field photometry. The final catalogue consists of on-sky positions (obtained using the World Coordinate System of the reference frames), vegamag magnitudes and uncertainties, and other goodness-of-the-fit and shape parameters.

We refine our final photometry by adopting a cut in $|\textit{roundness}| < 0.4$ to remove extended sources and other spurious features in the image. Since our central pointing is the same used by Dalessandro et al. (2015), we adopt a magnitude cut in F814W of $m_{F814W} < 24$ which corresponds to a completeness level of $\sim$95% according to the authors. Since the exposure times are similar in the outer ACS fields and crowding is less severe, we adopt the same magnitude cut for the outer fields, assuming a similar completeness level will be reached.

In Fig. 4.10, we show the spatial distribution of the *HST* sources. The cluster centre (Goldsbury et al. 2010) and half-light radius are indicated. The side panels show colour magnitude diagrams (CMDs) for a few selected fields.

4.4.2 *Gaia* data

This section was primarily conducted and written together with Dr. Thomas de Boer.

We make use of data from the *Gaia* mission (Gaia Collaboration et al. 2016a,b; Lindegren et al. 2018) to determine the number density as a function of cluster radius. The recently released Data Release 2 (DR2) data includes proper motions for stars down to $G = 21$ mag along with spectro-photometry in the G, $G_{\rm BP}$ and $G_{\rm RP}$ bands (Riello et al. 2018; Evans et al. 2018; Lindegren et al. 2018). We select our sample of NGC 6101 member stars by first performing a colour-magnitude selection using an isochrone with *Gaia* bandpasses from the Padova library (Marigo et al. 2017). We adopt an age and metallicity as derived in the literature and shift the isochrone to the correct distance (Harris 1996; Marín-Franch et al. 2009). Following this, we select member stars in a conservative region around the isochrone with $(G_{\rm BP} - G_{\rm RP}) - (G_{\rm BP} - G_{\rm RP})_0 < 2 \times \delta(G_{\rm BP} - G_{\rm RP})$ at each G magnitude. A minimum colour error of 0.03 is adopted to avoid arbitrarily small selection windows for the brightest stars.

After the colour selection, we employ *Gaia* proper motions to compute the cluster membership probability. The proper motion cloud is modelled using a Gaussian mixture model with one component for the cluster and another for the Milky Way foreground. An initial guess for the cluster centre is taken from Gaia Collaboration et al. (2018), after which the distribution is fit using the EMCEE MCMC package. Our final cluster sample is composed of all stars with a cut at prob$>$0.5.

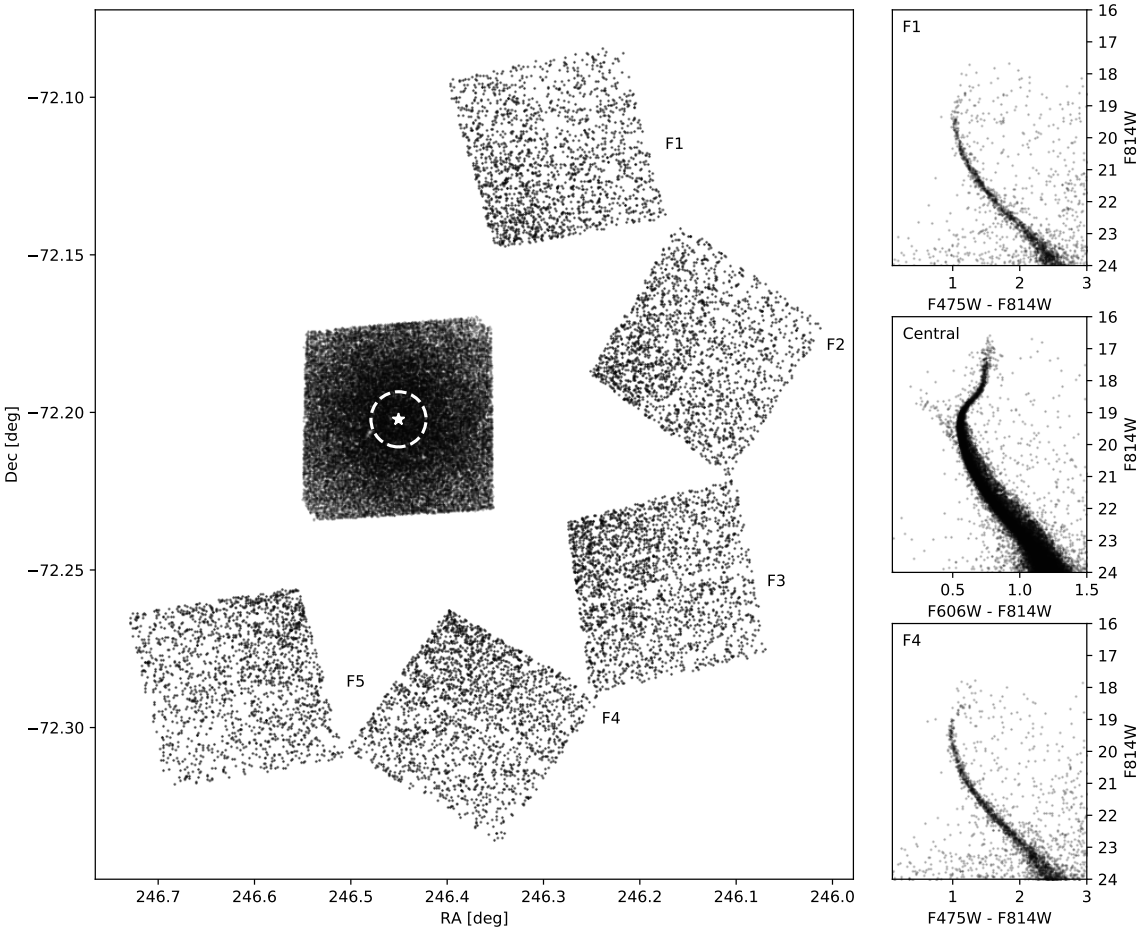

Figure 4.10: Large panel: on-sky distribution of *HST* sources classified as stars and brighter than 24 in F814W. The white star symbol shows the centre of the cluster, the dashed circle shows the half-light radius. Small panels: CMDs for F1 (top), Central (centre), and F4 (bottom) fields.

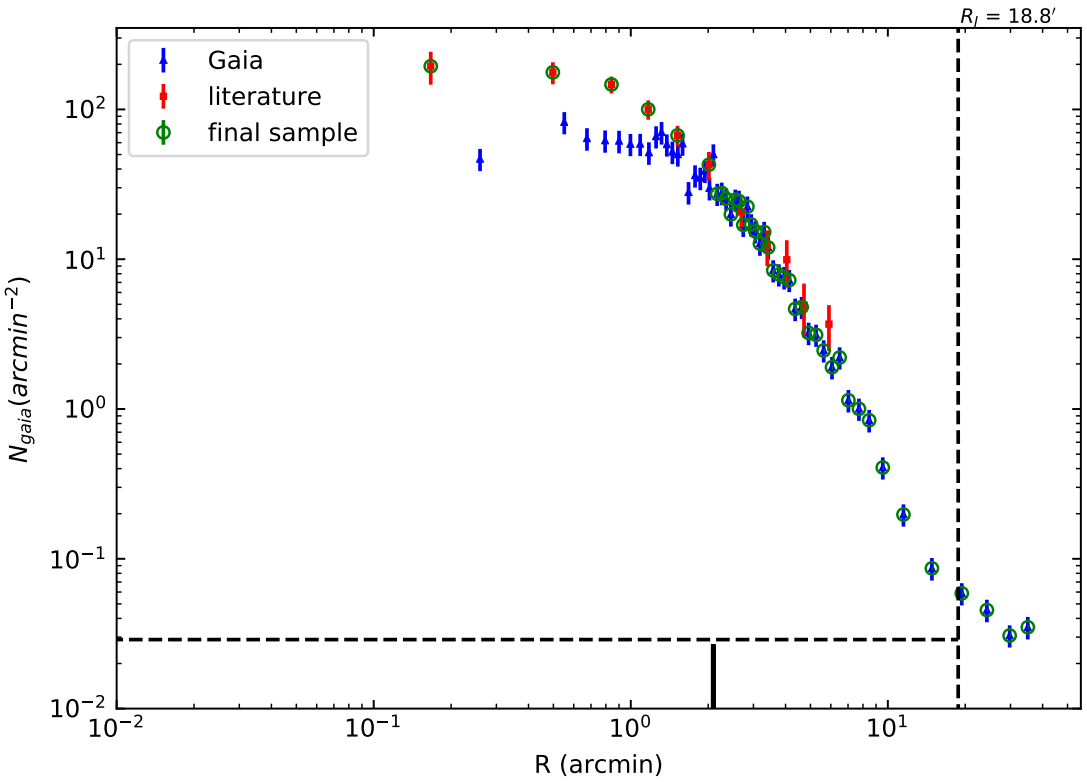

Figure 4.11: The number density profile of NGC 6101. Blue triangles show the profile as obtained from *Gaia* DR2 after the selections for parallax, proper motion and colours described in Sec. 4.4.2. Red squares show the literature number density profile from Dalessandro et al. (2015), scaled to the *Gaia* profile using all points in the overlapping region outside the *Gaia* inner usable radius of ≈2′. Finally, the green circles show our final profile combining both datasets. For reference, the vertical dashed line shows the Jacobi radius while the dashed horizontal line shows the background level estimated using stars between 1.5 and 2 Jacobi radii.

The density profile is constructed by binning the data as a function of distance from the cluster centre. We adopt a fixed number of 50 radial bins, with an equal number of stars in each bin. The resulting *Gaia* profile represents a homogeneous coverage of the GC outskirts that is unmatched in other surveys. However, due to crowding effects towards the cluster centre, the inner parts of the profiles are incomplete. Therefore, we complement the *Gaia* profiles with literature profiles from Dalessandro et al. (2015) which is reliable and complete in the centre. We use the *Gaia* completeness analysis of Arenou et al. (2018) to determine the radius up to which the *Gaia* profile is reliable. Adopting a cut-off density of 10^5 stars/deg^2 at $G = 20$ mag, we find a cut-off radius of 2.83 arcmin. The two profiles are tied together using the overlapping region of both datasets (outside the inner usable *Gaia* radius) to calibrate the literature data to *Gaia* system. Fig. 4.11 shows the density profile as determined from *Gaia* data (in blue triangles), along with the existing literature profile from Dalessandro et al. (2015) as red squares. The *Gaia* profile becomes incomplete in the inner regions, as evidence by the drop in density at a radius of $\approx 2'$. The green circles show the final combined density profile adopted for the cluster.

4.5 Modelling NGC 6101

For the modelling of NGC 6101, I use a MCMC approach to find the parameters of the cluster model that describe the observed properties best. I use the self-consistent multimass lowered isothermal model (hereafter multimass model). For the required stellar MF, I use an improved version of the MF evolution code presented in Balbinot and Gieles (2018). I present the models and their particularities in the Appendix. A. After a dynamical model is created, I have to calculate its likelihood: as I have observations from different instruments at hand, I have to use different approaches to calculate the total likelihood, which I discuss in Sec. 4.5.2. This likelihood is then used by the MCMC routine to find those model parameters which maximise the (log) likelihood. But before I can use my approach on the observations, I first present, in Sec. 4.5.3, the different mock clusters created to fine-tune and prove my modelling approach. And finally, in Sec. 4.5.4 I present the results from the best-fit model to the data of the observations.

4.5.1 Model

I use the multimass models provided by the LIMEPY (Gieles and Zocchi 2015) software. This software takes a set of parameters as well as a MF to compute a multimass model for which it calculates different observable properties such as the line-of-sight velocity dispersion and the mass density profile. LIMEPY calculates these properties for the whole cluster as well as for the different mass species separately. As input parameters LIMEPY expects a value for the central or global dimensionless concentration (also known as King W_0), a value for the truncation parameter (g) which describes the polytropic part near the escape energy (see Gomez-Leyton and Velazquez 2014), a value for the total cluster mass (M), a value of a radial scale such as the half-mass radius ($r_{\rm h}$) and finally a value for the mass segregation (δ), which sets the velocity scale of each component as a function of its mass: $s_j \propto m_j^{-\delta}$, where $\delta = 0$ for a model without mass segregation $\delta = 0.5$ for a fully mass segregated cluster. Furthermore, LIMEPY requires a MF in the form of the average mass (m_j) and the total mass (M_j) for each mass bin. For an in-depth review on

the models, see Gieles and Zocchi (2015) and for a discussion on their performance in the single mass case, see Zocchi et al. (2016). For the multimass case, see Peuten et al. (2017).

To create the MF, I use the approach from Balbinot and Gieles (2018) which was further improved and is fully presented in the Appendix A. As this approach uses mass bins, I first have to decide on the binning and the number of bins to use. Here, I decided to use 28 mass bins which are binned logarithmically. The MF code uses two times 28 bins internally, to keep track of stars and remnants. As the MF evolves, stars are removed because of stellar evolution and ejection. Depending on the age, metallicity and BH retention, the final MF consists of $12 - 14$ mass bins. Only in cases where all BHs are retained, more mass bins are needed. In Sec. 2.4.1, I studied selection strategies for the MF for the use in multimass models, and settled for 11 logarithmically binned mass bins for the study, as increasing the number of mass bins did not improve my results significantly. Therefore using 28 mass bins for the MF can be seen as a safe choice optimum computing time, which increases with the number of mass bins, and accuracy. In Tab. 4.2, I list the resulting mass bin borders from my MF approach, assuming all BHs are retained. Also indicated are which mass bins are covered by the different observational data.

Next, I have to decide on the initial mass function (IMF) as well as on the initial number of stars. As IMF, I use a Kroupa (2001) IMF, which is a broken power law, with a slope of -1.3 between $0.1\,\mathrm{M}_\odot$ and $0.5\,\mathrm{M}_\odot$, and a slope of -2.3 between $0.5\,\mathrm{M}_\odot$ and $100\,\mathrm{M}_\odot$. For the initial number of stars (N_0), I choose 10^7 stars: due to the fact that LIMEPY uses only the relative number of stars per bin for its calculation, I can safely set this value to 10^7 without loss of generality.

For the evolution of the MF, I assumed the cluster's currently observed metallicity of $[\mathrm{Fe/H}] = -1.98$ (Carretta et al. 2009) and evolve the cluster for $12.4\,\mathrm{Gyr}$: while the currently age of NGC 6101 is $13\ \mathrm{Gyr}$ (Dotter et al. 2010), the predicted maximal observed star mass from the MF was below the observed one; I therefore adopted the cluster age which best fits the observed maximal star mass. This is not too surprising, given the simplifications made in the construction of the MF model: the assumption that stars turn directly into white dwarfs (WD) at the end of their lifetime, thereby ignoring the post-main sequence star evolution completely could led to such mismatch. By reducing the evolution time, I am able to describe those stars which have recently left the main-sequence and have not yet turned into a WD.

The MF code can differentiate between pre- and post mass segregated mass ejection, but to reduce the complexity of the model, I opt to only use the latter, as tests have shown that the expected difference is marginal (see Sec. 4.5.3) and has no effect on the recovered BH population.

The first MF parameter I fit is the escape rate of stars per Myr due to tidal forces ($\dot{N}$): LIMEPY requires the shape of the MF, therefore the best fit value of $\dot{N}$ is dependent on the initial number of stars. I therefore fit instead on the escape rate relative to the initial number of stars:

$$K = \dot{N}/N_0 \tag{4.5.1}$$

which is only sensitive to the relative MF. As the values of K are expected to be relatively small, I fit on the relative rate per Gyr.

The next fitting parameter is the initial neutron star (NS) retention which controls how

many NS stay in the cluster after formation. However, tests have shown (see Sec. 4.5.3) that this value cannot be recovered with sufficient accuracy using the approach presented here. But given the fact that this fraction is a well studied quantity (Hut et al. 1991; Drukier 1996b; Hansen and Phinney 1997; Davies and Hansen 1998; Pfahl et al. 2002; Podsiadlowski et al. 2005; Ivanova et al. 2008b), I use the generally accepted fixed value of 10% (Pfahl et al. 2002) for my modelling.

The stellar-mass BH retention is the next model parameter, for which my test have shown that it cannot be recovered with sufficient accuracy either. Furthermore, it is degenerate with the dynamical BH retention ($f_{\rm BH,dyn}$). Different from the NS retention fraction, there is unfortunately no consensus on its value as of today (Belczynski et al. 2002, 2010; Repetto et al. 2012; Fryer et al. 2012; Janka 2013; Mandel 2016; Repetto et al. 2017; O'Shaughnessy et al. 2017; Pavlík et al. 2018), which is why I set this value to unity for simplicity. The dynamical stellar-mass BH retention, however is the parameter in which I am interested, as it controls the number of BHs retained in the cluster: this parameter mimics the effect of the dynamical ejection of BHs from the cluster's core, by removing BHs starting from the massive end. My tests with mock data have shown that this value can be recovered with sufficient accuracy. I therefore use it as one of my fitting parameters.

The last parameter I are going to fit on is the binary fraction $f_{\rm bin}$. As already discussed in Sec. 4.3.8, I assume that it is constant within the cluster.

In Tab. 4.3, I list all eight fitting parameters and their prior distributions. The best-fit value of each parameter is estimated as the median of the marginalized posterior distribution using all walker positions from all chains after removing the initial burn-in phase. This generally coincides with the value of the parameter providing the largest likelihood. For the 1σ errors I use the values from the 16th and 84th percentiles.

4.5.2 Likelihood

The idea is to find those parameters of the multimass and MF models which best describe the velocity dispersion as well as the additional available observations of NGC 6101. To find the best fitting parameters, I again use the MCMC software package EMCEE, which can easily be combined with LIMEPY, the MF generation code and VELBIN as all four codes are PYTHON-based. Furthermore, I can make use of my distributed grid computing version of PYTHON's *map()* function, which can dynamically and efficiently distribute the workload from several MCMC runs over all available CPU cores at the University of Surrey Astrophysics computing facilities.

In each MCMC step, I first create an MF based on the model parameters and then I use this MF and the other fitting parameters to create a multimass LIMEPY model. From this model, different observable properties are inferred and then the likelihood that the observed data is described by this model is calculated. This likelihood is then used by the MCMC routine to find the best fit values.

In the following, I am going to present the different contributions to the likelihood function: for the likelihood of the observed radial velocity dispersion, I use the likelihood from equation (4.3.4) and I use the predicted velocity dispersion from the LIMEPY model at the distance of the star as $\sigma_{\rm c}$. The cluster velocity $\bar{v}$, also needed by equation (4.3.4), is fixed to $364.3\,{\rm km\,s^{-1}}$; and the binary fraction $f_{\rm bin}$ is, as already discussed, one of the

Table 4.2: Mass range used for the individual mass bins in my multimass modelling, as provided by the MF evolution code for a NGC 6101 like cluster assuming all BHs are retained. If no BH are retained, mass bins 14 - 23 are removed. For models with BH retention in between, only certain mass bins are removed, starting from the heaviest one. I indicate the lower and upper bin border in $\mathrm{M}_\odot$ for each mass bin, followed by the star type represented by that the mass bin and by which instrument this mass bin was observed.

Mass bin	$m_{\rm lo}$ $\mathrm{M}_\odot$	$m_{\rm up}$ $\mathrm{M}_\odot$	Stellar type	Instrument
0	0.1	0.12	MS	
1	0.12	0.15	MS	
2	0.15	0.18	MS	
3	0.18	0.22	MS	
4	0.22	0.27	MS	
5	0.27	0.33	MS	
6	0.33	0.41	MS	
7	0.41	0.5	MS	*HST*
8	0.5	0.65	MS	*HST*, *MUSE*
9	0.65	0.78	MS	*HST*, *MUSE*, *Gaia*
10	0.5	0.65	WD	
11	0.65	0.78	WD	
12	0.78	1.11	WD	
13	1.11	1.44	NS	
14	2.45	3.19	BH	
15	3.19	4.16	BH	
16	4.16	5.43	BH	
17	5.43	7.07	BH	
18	7.07	9.22	BH	
19	9.22	12.0	BH	
20	12.0	15.7	BH	
21	15.7	20.4	BH	
22	20.4	26.6	BH	
23	26.6	34.7	BH	

Table 4.3: Fitting parameters of my modelling approach. I list the symbol together with a description as well as the prior used.

Parameter	Description	Prior
W_0	central dimensionless concentration	uniform distribution, with $0 < W_0 \leq 20$
g	truncation parameter	uniform distribution, with $0 \leq g \leq 2$
$r_{\rm h}$	half-mass radius	uniform distribution, with $0 < r_{\rm h} \leq 25$
M	total cluster mass	uniform distribution, with $0 < M \leq 1e7$
δ	mass segregation parameter	uniform distribution, with $0 \leq \delta \leq 0.5$
K	relative escape rate	uniform distribution, with $-7.7 \times 10^5 \leq K < 0$
$f_{\rm BH,dyn}$	dynamical stellar-mass BH retention	uniform distribution, with $0 \leq f_{\rm BH,dyn} \leq 1$
$f_{\rm bin}$	binary fraction	uniform distribution, with $0 \leq f_{\rm bin} \leq 1$

fitting parameters. For the estimate of the star masses, also needed by the VELBIN code, I use the *I*-band magnitude mass relation computed from the *HST* data, as discussed in Sec. 4.4.1.

For the calculation of the likelihood of my model with respect to the observed *HST* data, I first calculated the number density profile ($\Sigma_{*,j}$) for each mass bin: for this I split each mass bin into radial bins (each having 50 stars) and then calculated the number density profiles, taking into account the different observed coverage on sky and assuming that all stars with masses above $0.4\,\mathrm{M}_{\odot}$ were detected. Given the complexity of the observed *HST* fields (see Fig. 4.10), the observed coverage on sky was computed using a Monte-Carlo method. For the uncertainty of the measured number density profile ($\delta\Sigma_{*,j}$), Poisson uncertainties were assumed. The likelihood to measure a given number density with its uncertainty at the position R in the mass bin j with the current model is therefore:

$$\mathcal{L}_{\mathrm{HST},j}\left(\Sigma_{*,j}\left(R\right),\delta\Sigma_{*,j}\left(R\right)|\Sigma_{j}\left(R\right)\right) = \frac{1}{\sqrt{2\pi\left(\delta\Sigma_{*,j}\left(R\right)\right)^{2}}}\exp\left(-\frac{1}{2}\frac{\left(\Sigma_{j}\left(R\right)-\Sigma_{*,j}\left(R\right)\right)^{2}}{\left(\delta\Sigma_{*,j}\left(R\right)\right)^{2}}\right) \tag{4.5.2}$$

where $\Sigma_{j}\left(R\right)$ is the model number density in projection at the distance R in the mass bin j. As LIMEPY does not provide the number density profile, I have to calculate it from the provided mass density: the number density for a mass bin is the mass density of that mass bin divided by the bins mean mass. The total likelihood form the *HST* data is found by summing of the logarithm of $\mathcal{L}_{\mathrm{HST},j}$ for the three mass bins covered by the instrument. Using this approach, I am fitting on two quantities at the same time: the number density profile of each mass bins and therefore also on the total mass in each mass bin, in the observed range. The other is the radial dependent mass function, as each cut in a radial bin can be seen as mass function at that given distance, which helps to estimate the cluster's mass segregation.

Compared to the *MUSE* data and *HST* data, which cover the central parts of the cluster, the *Gaia* data covers the outskirts of the cluster and thus can further improve the fitting process. I use the number density profile in its binned form, as presented in Fig. 4.11, and compare it with the LIMEPY prediction for the heaviest observable mass bin. To overcome any problems due to different offsets in the observed data with respect to the model, I only fit on the shape of the profiles and not on their absolute values. Therefore, assuming Gaussian uncertainties, the likelihood to observe the measured number density $\Sigma_{*}\left(R\right)$ and its uncertainty $\delta\Sigma_{*}\left(R\right)$ at the projected distance R in the most massive stellar mass bin, i.e. in the turn-off mass bin, is:

$$\mathcal{L}_{\mathrm{GAIA}}\left(\Sigma_{*}\left(R\right),\delta\Sigma_{*}\left(R\right)|\,\Sigma_{\mathrm{TO}}\left(R\right)\right) = \frac{1}{\sqrt{2\pi\delta\Sigma_{*}\left(R\right)^{2}}}\exp\left(-\frac{1}{2}\frac{\left(G\Sigma_{\mathrm{TO}}\left(R\right)-\Sigma_{*}\left(R\right)\right)^{2}}{\delta\Sigma_{*}\left(R\right)^{2}}\right) \tag{4.5.3}$$

where $\Sigma_{\mathrm{TO}}\left(R\right)$ is the predicted number density from the model at the distance R in the turn-off mass bin. G is the scaling parameter that is found from maximizing the likelihood for the vertical offset. It is defined as:

$$G = \frac{\sum_{i}\Sigma_{\mathrm{TO}}\left(R_{i}\right)\Sigma_{*}\left(R_{i}\right)}{\sum_{i}\left(\Sigma_{\mathrm{TO}}\left(R_{i}\right)\right)^{2}} \tag{4.5.4}$$

with R_i the list of projected radii from the binned *Gaia* data.

The total likelihood function used for the MCMC algorithm is therefore the sum of the logarithm of the likelihood functions equation (4.3.4), (4.5.2) and (4.5.3) over their respective data sets.

4.5.3 Testing the modelling

To evaluate the expected accuracy of the fitting approach and to fine-tune several steps and parameters, I performed several test fits on mock data. To create this data, I used LIMEPY's and VELBIN's function to sample projected mock data. As input parameter for the model cluster, I am using the currently observed values of NGC 6101 as determined and listed in Tab. 3.1 from Chapter 3. For the model parameters where I have no observable results, I used either the results from the model fitting presented in Tab. 3.3 or an educated guess: I set the central dimensionless concentration to $W_0 = 6$, the truncation parameter to $g = 1.7$, the half-mass radius to $r_h = 12.3\,\mathrm{pc}$ and the total cluster mass to $M = 1.1 \times 10^5\,\mathrm{M}_\odot$. The mass segregation parameter is set to $\delta = 0.35$ in accordance with values found for N-body models with BH in Chapter 2. The MF parameter K is set to $K = -9.7 \times 10^{-3}\,\mathrm{Gyr}^{-1}$. The initial number of NS retained is set to 10% as discussed above. The number of initially retained BH is set to unity and the fraction of dynamically retained BHs is set to 10%. As binary fraction I use for the mock data a value of $f_{\mathrm{bin}} = 13\%$ and for the cluster velocity I use $\bar{v} = 364.3\,\mathrm{km\,s}^{-1}$.

Because LIMEPY works with a binned MF, the resulting mock data is also binned in mass space. To overcome problems associated with this and to create more realistic mock data, I used the algorithm presented in Appendix A.5 to sample discrete masses from the binned data.

In the next step, I tried to recreate the available observed data set, by first generating a set of data covering the same mass range as observed for each instrument used. Next, assuming a distance of $14.6\,\mathrm{kpc}$ for NGC 6101 (Dalessandro et al. 2015), I transformed the position of the stars into observational space and removed those data points in areas which are not covered by the instruments: For the mock *HST* data, I drew for each star a random number in the range between zero and one and removed it from the set, if the value was above the completeness function $f(R)$ at the stars distance. For the *MUSE* data, I randomly selected 1108 stars to mimic the observed selection and then used the VELBIN sample code to add an uncertainty following a Gaussian distribution and randomly add the additional signal due to binaries. The mock *Gaia* data was created by sampling the number density profile for the heaviest mass bin at the same radial distances as observed, and then an uncertainty following a Gaussian distribution was added. Finally, the mock *Gaia* data was normalised to incorporate the effect of the different offsets between observed data and model.

With the mock data at hand, I ran the MCMC fit, until convergence, and then compared the recovered values and uncertainties with the initial parameters. For the selection of the right binning criterion of the *HST* data, I performed several fits, testing different binning approaches and varying their different parameters. After having determined this, I ran several fits with different initial conditions to make sure that the results were always recovered by my approach. Next, I varied the number of MCMC walkers and iterations and found that using 100 walkers for 500 steps after convergence is a safe choice for my

study.

In the following, I present the results of one of the test fits to one of the mock data sets: the posterior distribution of this MCMC fit is presented in Fig. 4.12, and as can be seen, six of the parameters are recovered within 1σ, including the dynamical BH retention, and all are recovered within 2σ. What can also be seen in this plot is that there is a correlation between the central dimensionless concentration (W_0) and the dynamical BH retention: the less concentrated the cluster is, the less BH it needs to have in its central region to reproduce the observed profile. Studying this correlation further, I found that the difference in likelihood between a model with BH (higher W_0) and no BH (lower W_0) is relatively small compared to other influences on the likelihood calculation such as a different binning of the *HST* data or variation in the mass bin borders. This shows that my approach could be able to recover NGC 6101's true parameters with the observed data I have at hand.

In Fig. 4.13, I show the comparison between the mock *Gaia* data and the prediction from the best-fit model and find a good reproduction by the model. Next, in Fig. 4.14, I present the comparison between the mock *HST* data and the best-fit prediction from my approach: again, the prediction is able to reproduce the observed profiles for the three different mass bins well enough. For the mock MUSE data, I present the comparison in two plots: in the first plot, Fig. 4.15, I compare the best-fit velocity dispersion profile with the true one and find good agreement for both mass bins. In the second plot, Fig. 4.16, I take into account that the velocity dispersion profiles of an observed cluster is normally determined using equation (4.3.2) only, i.e. neglecting the effect of binaries. For this, I determined the mock velocity dispersion profile using the approach presented in Sec. 4.3.7; while for the best-fit model prediction, I convolved the true velocity dispersion profile with the profiles due to binaries. Here again, a good agreement is found. For my NGC 6101 *MUSE* data, I will mainly use this comparison to determine the quality of the fit, as no assumptions about the binary population is needed for this.

To also show that the approach is able to detect when no BHs are left in the cluster, I generated additional mock models, where I set the initial number of retained BHs and the number of dynamically retained BH to zero and set the value for the mass segregation equal to $\delta = 0.5$ as is expected for old BH-free clusters (Chapter 2, Peuten et al. 2017). The posteriori distribution of the MCMC fit to one of the BH-less data can be seen in Fig. 4.17: as with the tests before, the model is able to recover the lack of the BH population, while also recovering most of the other parameters with sufficient accuracy.

As already mentioned, I also tested how well different parameters are recovered in the fits: for two of the parameters - the initial NS retention and the initial BH retention - I found that with the uncertainties recovered, virtually every possible value is within 2σ. This can be seen in Fig. 4.18 where I show the posteriori distribution of a fit to the mock data with BH, where both parameters were let free. This is why I decided to fix those two values, as already explained above. Furthermore, one can see in the covariance matrix that, as expected, the initial BH retention and the dynamical BH retention are degenerated, which further justifies the need of fixing the initial BH retention to unity. Obviously, my method cannot distinguish between initially or dynamically ejected BHs, which for the target of my study is not relevant.

Another test I did is to see whether the assumption of only using post mass segregation ejection is a valid one: to test this I created a mock model where the switch from pre-

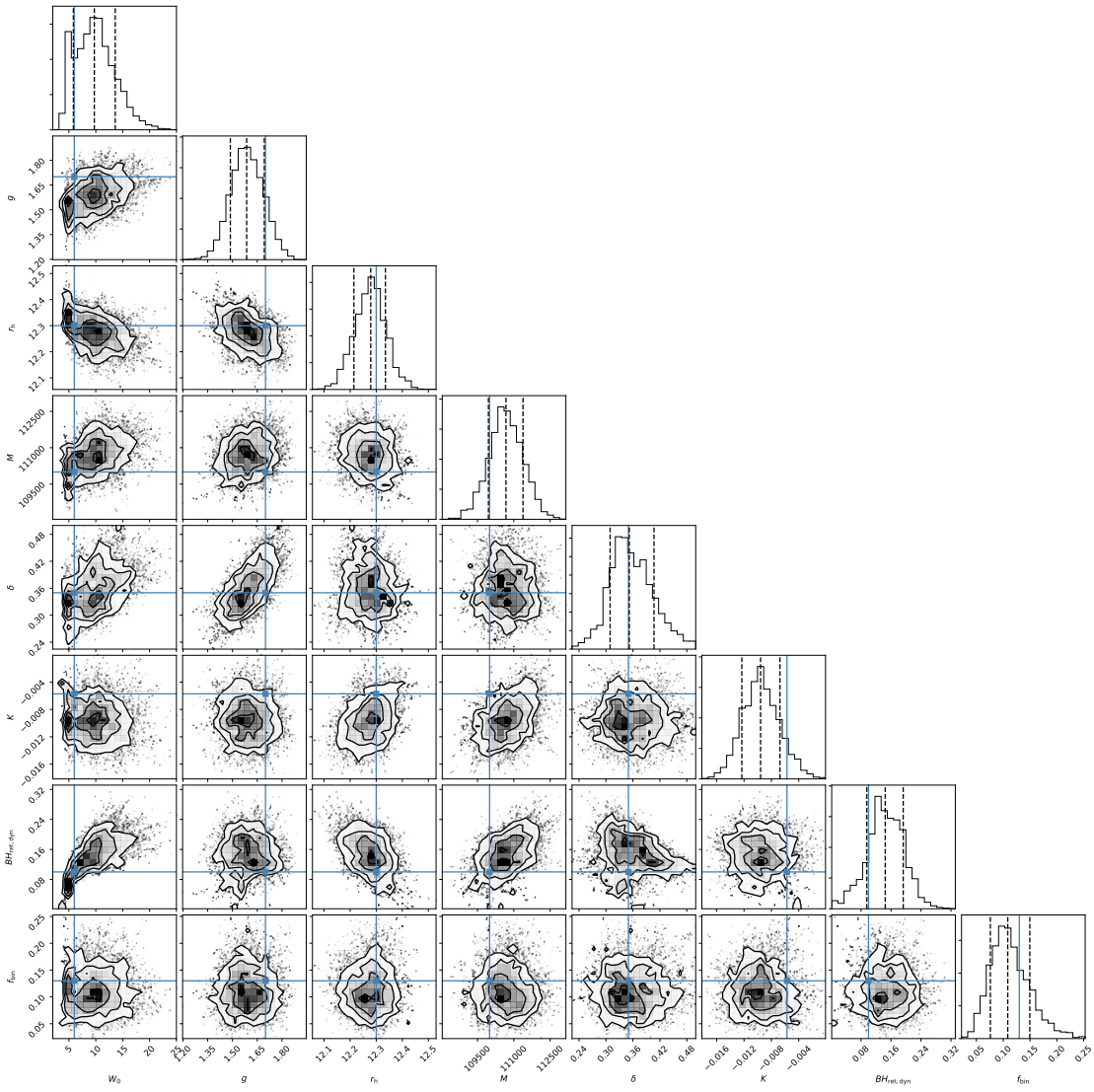

Figure 4.12: Marginalised posterior probability distribution and 2d-projections of the posterior probability distribution of the fitting parameters of a mock data set with a BH population. The black dashed line represent the 16th, 50th and 84th percentiles and the blue solid lines the true value used to create the mock data.

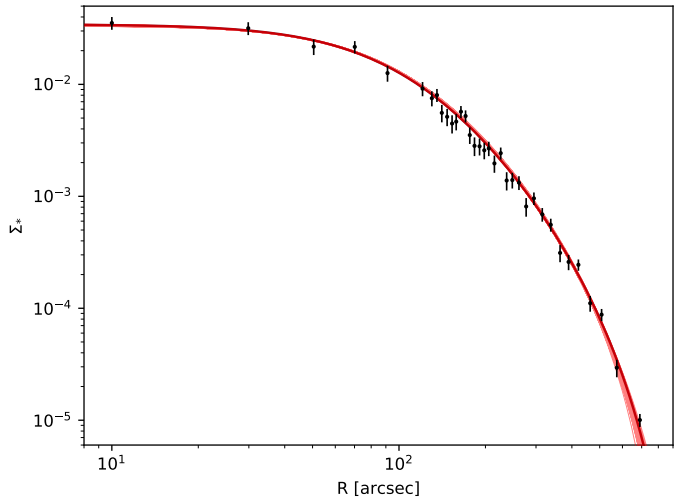

Figure 4.13: Comparison between the mock *Gaia* number density profiles (black dots) and the best-fit modelling prediction (dark red line) for a mock model with BHs. The thin red lines represent the results from the walker positions at the last iteration. As the mock *Gaia* data is normalised, no units are given for the number density.

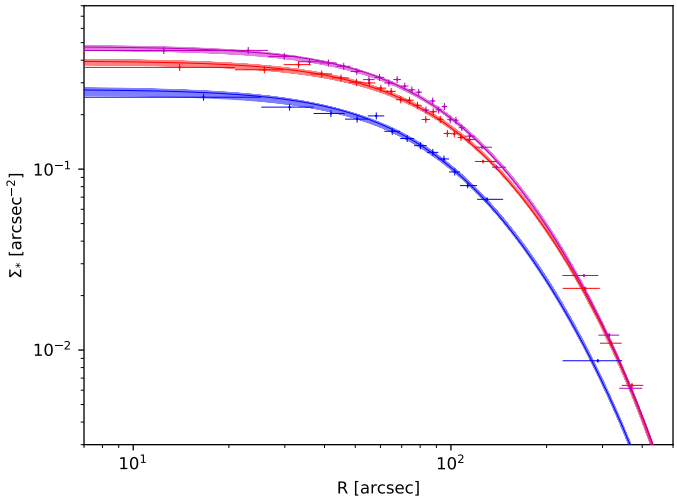

Figure 4.14: Comparison between the mock *HST* number density profiles (dots) and the best-fit modelling prediction (dark lines) for a mock model with BHs. The red lines/dots represent the 7th mass bin as listed in Tab. 4.2, the magenta lines/dots the 8th and the blue lines/dots the 9th. The x-bars for the mock *HST* data represent the radial range covered by that bin and the y-errorbar denote 1σ uncertainties. The thin lines represent the results from the walker positions at the last iteration. Note: For clarity I increased the number of stars per bin to 500 and limited the x-range scale.

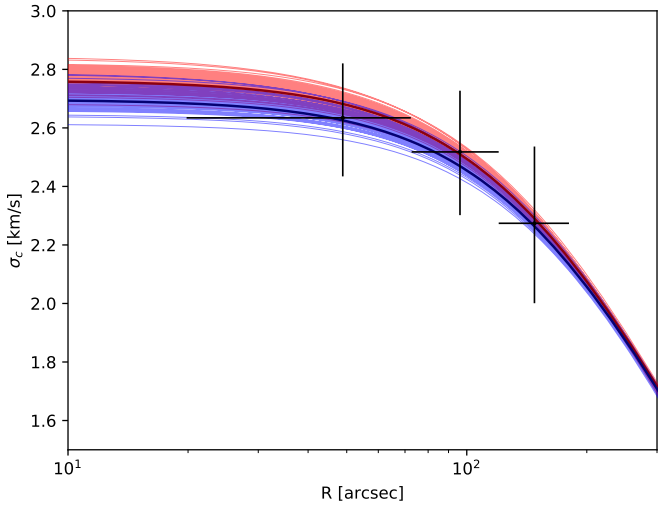

Figure 4.15: Comparison between the mock *MUSE* velocity dispersion profiles (dots) and the best-fit modelling prediction (dark lines) for a mock model with BHs. The red lines represent the 8th mass bin as listed in Tab. 4.2, the blue lines the 9th. The x-bars for the mock *MUSE* data represent the radial range covered by that bin and the y-errorbar denote 1σ uncertainties. The thin lines represent the results from the walker positions at the last iteration.

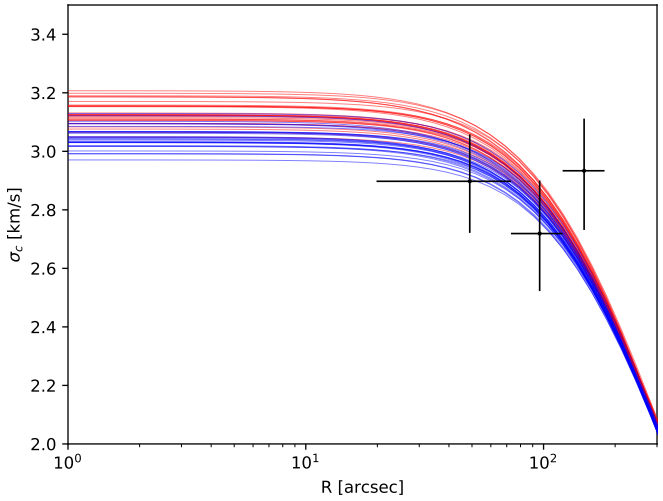

Figure 4.16: Comparison between the mock *MUSE* velocity dispersion profiles (dots), determined without applying any corrections for binaries, compared to best-fit modelling prediction (dark lines) where the velocity dispersion was convolved with the profiles due to binaries, for a mock model with BHs. The red lines represent the 8th mass bin as listed in Tab. 4.2, the blue lines the 9th. The x-bars for the mock *MUSE* data represent the radial range covered by that bin and the y-errorbar denote 1σ uncertainties. The thin lines represent the results from the walker positions at the last iteration.

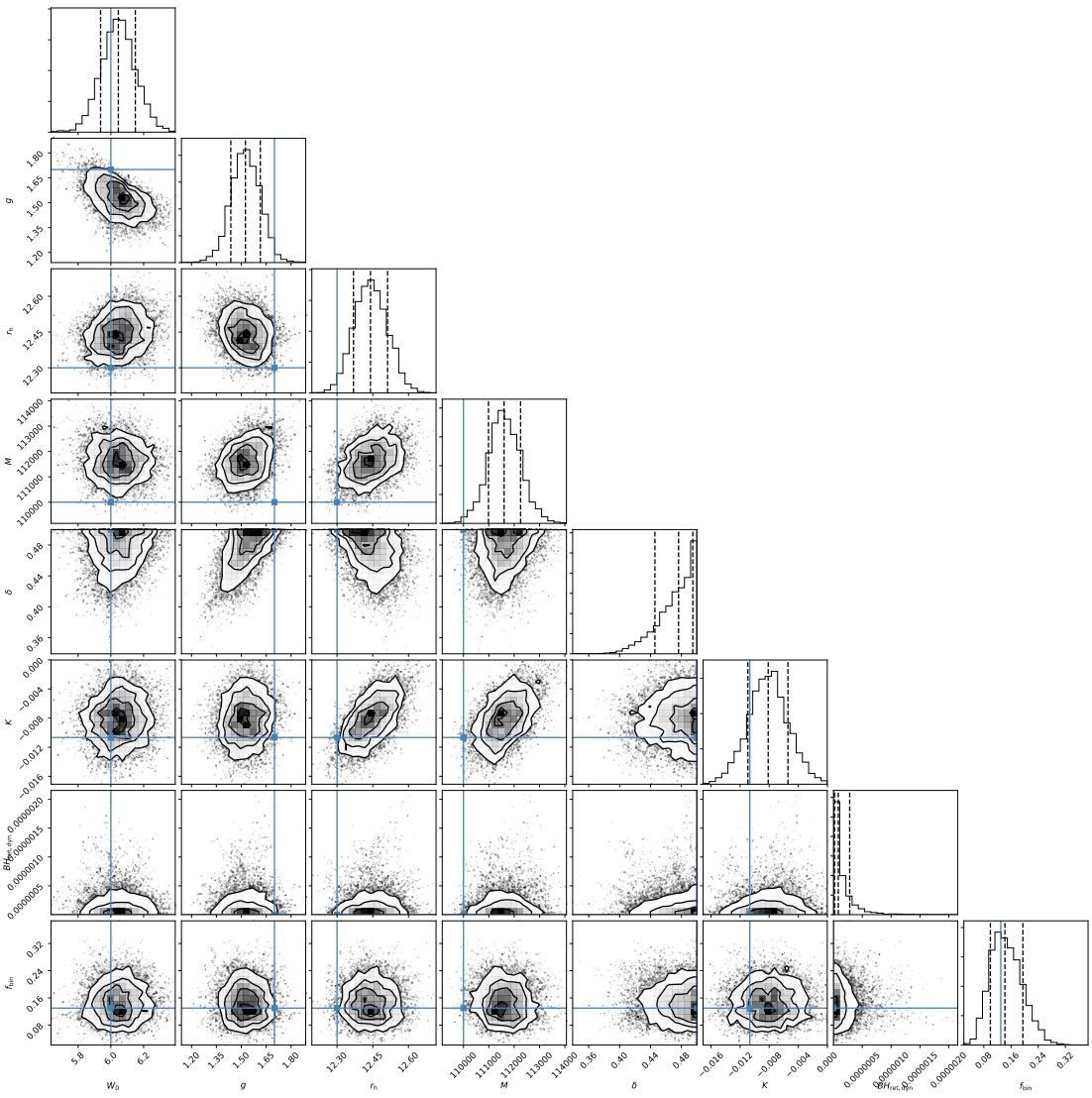

Figure 4.17: Marginalised posterior probability distribution and 2d-projections of the posterior probability distribution of the fitting parameters of a mock data set without a BH population. The black dashed line represent the 16th, 50th and 84th percentiles and the blue solid lines the true value used to create the mock data. As can be seen is my approach able to detect that no BHs are in this mock data set.

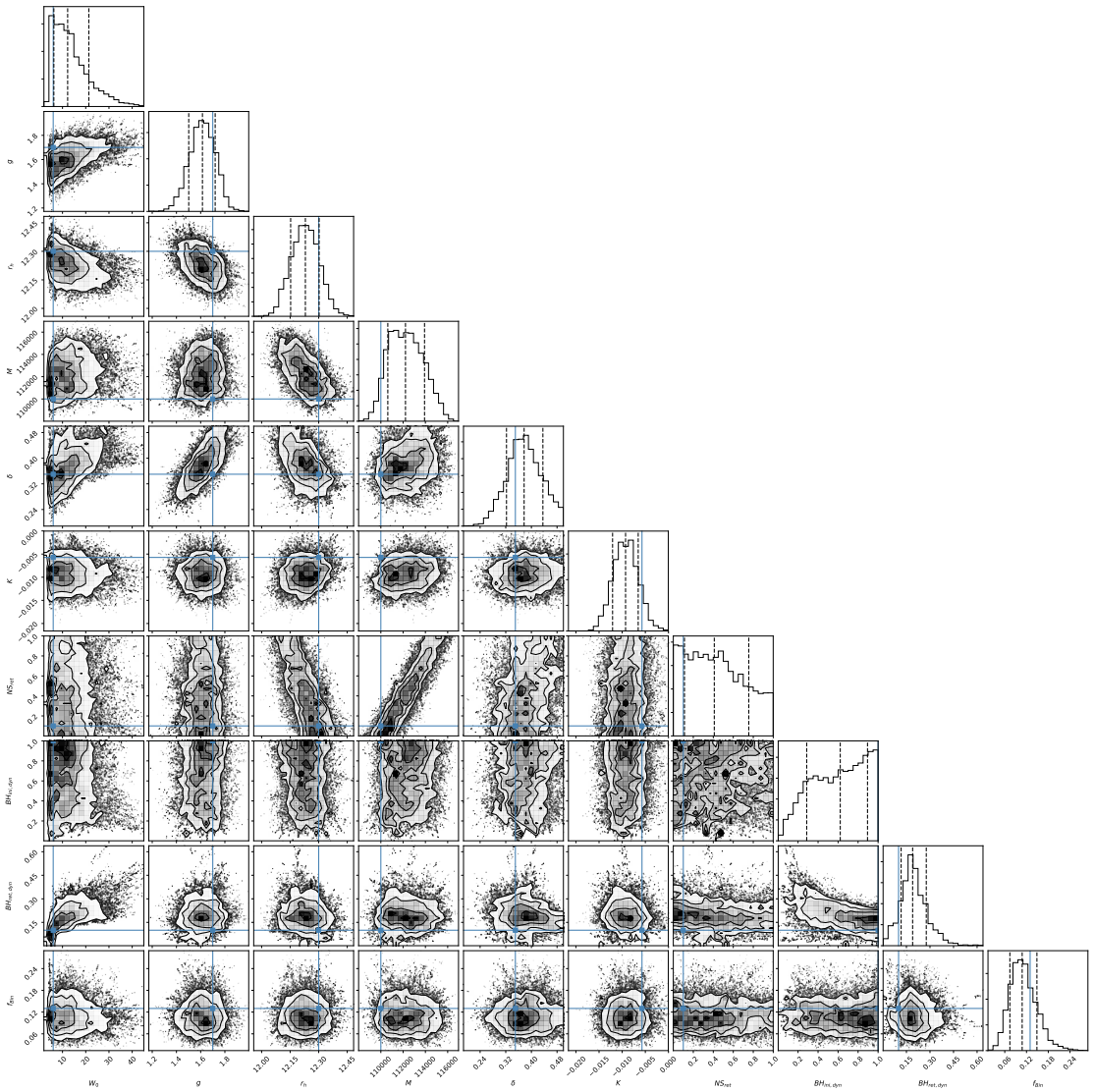

Figure 4.18: Marginalised posterior probability distribution and 2d-projections of the posterior probability distribution of the fitting parameters of the same mock as in Fig. 4.12 but this time also fitting on the initial NS and on the initial BH retention. The black dashed line represent the 16th, 50th and 84th percentiles and the blue solid lines the true value used to create the mock data. Both additional parameters cannot be recovered by the model, furthermore the initial BH retention is degenerate with the dynamical BH retention.

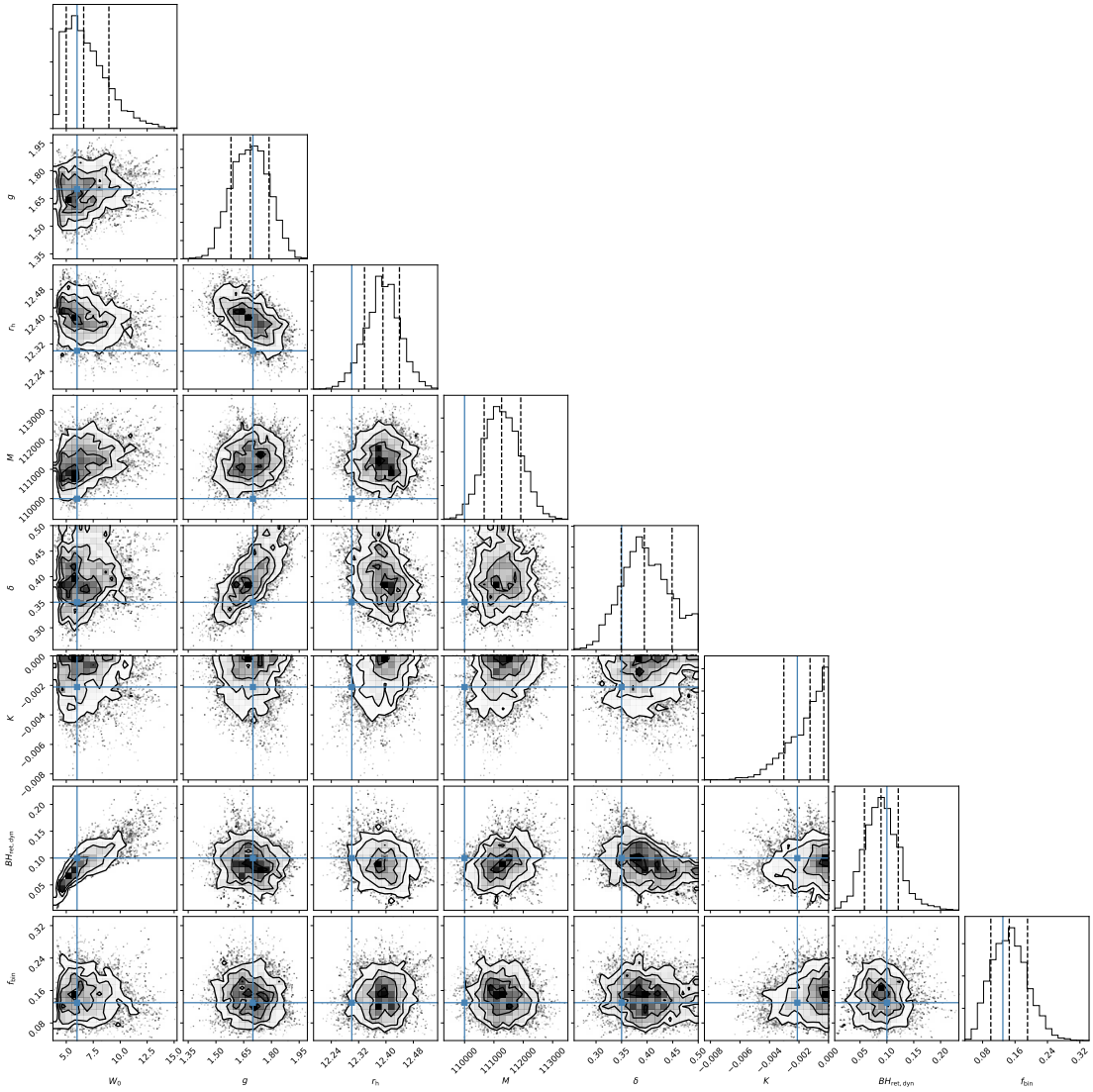

Figure 4.19: Marginalised posterior probability distribution and 2d-projections of the posterior probability distribution of the fitting parameters of a mock data set which was evolved for $6\,\mathrm{Gyr}$ using pre-mass segregation ejection, but fit on with the assumption of only using post mass segregation ejection. The black dashed line represent the 16th, 50th and 84th percentiles and the blue solid lines the true value used to create the mock data. As can be seen, are all but two parameters recovered within 1σ: Both g and r_h are overestimated but still within 2σ.

Table 4.4: Best fit results from my modelling of NGC 6101.

Parameter	Value
W_0	$6.7^{+0.1}_{-0.1}$
g	$1.98^{+0.02}_{-0.03}$
r_h	$17.6^{+0.2}_{-0.2}\,\mathrm{pc}$
M	$171389^{+1403}_{-1211}\,\mathrm{M}_\odot$
δ	$0.23^{+0.01}_{-0.01}$
K	$-0.055^{+0.001}_{-0.001}\,\mathrm{Gyr}^{-1}$
$f_\mathrm{BH,dyn}$	$0.02^{+0.01}_{-0.01}$
f_bin	$0.16^{+0.05}_{-0.05}$

to post- mass segregation ejection happens at $6\,\mathrm{Gyr}$. This represents the extreme case of a cluster which for half of its lifetime was not mass segregated, and then I perform an MCMC fit using only post mass segregation ejection. As can be seen in Fig. 4.19, where I have plotted the posteriori distribution of the fit, the different values are sufficiently recovered. Only the value for half-mass radius and total cluster mass are both overestimated, but still within 2σ. Most importantly, the value for the dynamical BH retention is well reproduced. Therefore I can safely neglect the pre-segregation ejection without having to apprehend a significant impact on the recovered values.

4.5.4 Results

Having proven my method in a manifold of tests, I finally applied it on the observed data: in Tab. 4.4, I present the best fit values for the individual parameters together with their uncertainties; and in Fig. 4.20, I present the posteriori distribution of the fit.

In Fig. 4.21, I present the number density profile as computed from the *HST* data together with the prediction from the best fit model. Some random divergences are apparent and the best-fit model cannot reproduce the central bin for two of the mass bins, but the fit reproduces the observed data nevertheless quite well. The same can be said for the observed *Gaia* data as depicted in Fig. 4.22, where again the observed data and the prediction are compared.

As discussed in the previous section, for the comparison of the *MUSE* data with the best-fit prediction, I compare in Fig. 4.23 the velocity dispersions, neglecting the effects of binaries: compared to the other observational data, the velocity dispersion seems to be under-predicted by the best fit model and only the outermost data point is in accordance with the prediction. One of the possible reasons could be that the binary fraction is too low. My best fit value, however, is in accordance with previously found values, which were determined using more accurate methods than here. There are some studies which found a radius-dependent binary fraction for NGC 6101 in the past (Sollima et al. 2007; Milone et al. 2012) which could explain the divergence, but the latest such study by Dalessandro et al. (2015) showed that there is no radial dependence, which is why I adopted a constant binary fraction here, too. In my mock tests, I also compared the best-fit predicted velocity dispersion to the velocity dispersion profile one obtains using equation (4.3.2) on the same mock data set, see Fig. 4.16, and have not encountered these problems. Apparently, in the data from the other observations, there is a stronger signal which leads my model to prefer lower velocity dispersions than observed in the *MUSE*

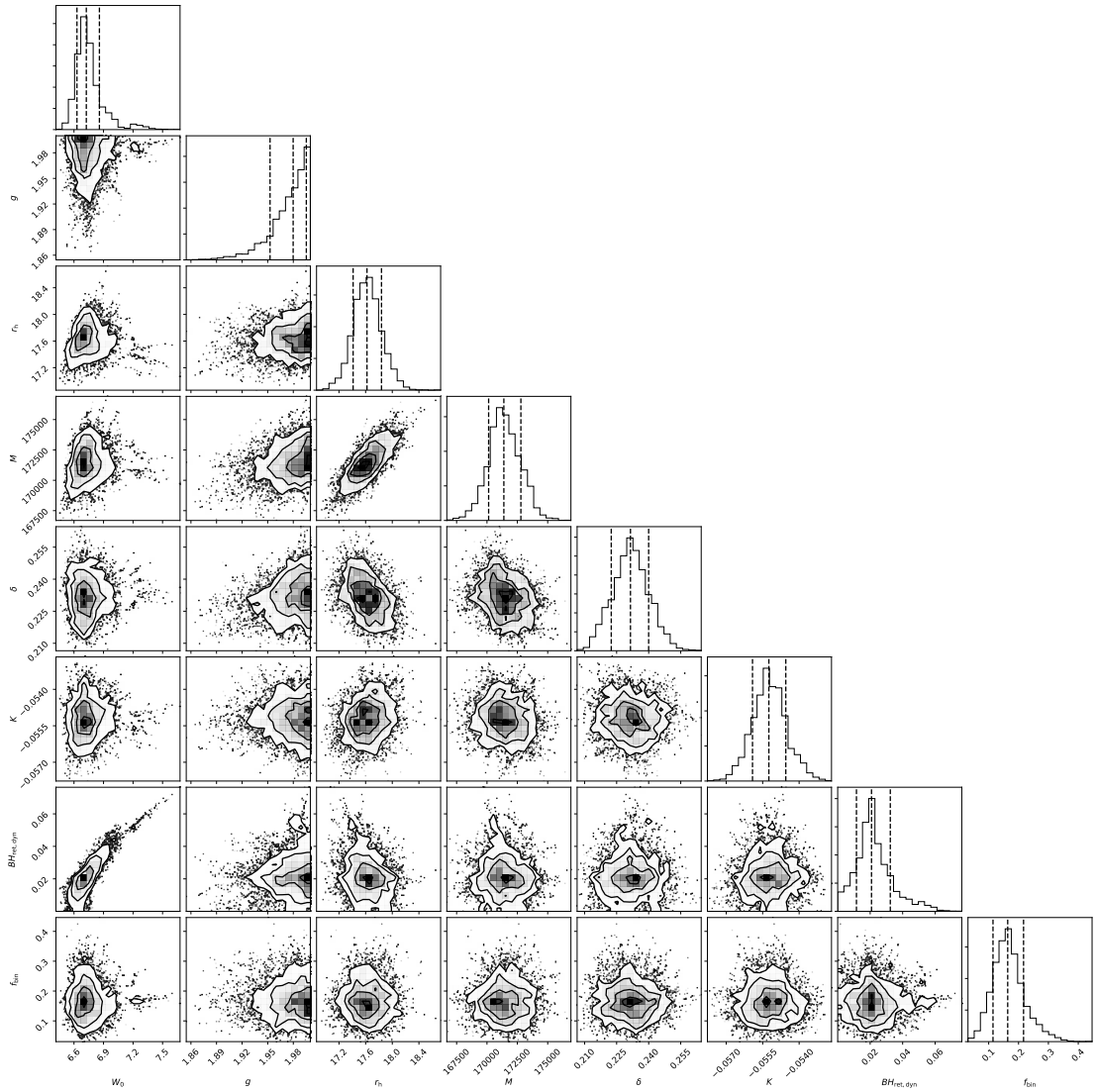

Figure 4.20: Marginalised posterior probability distribution and 2d-projections of the posterior probability distribution of the fitting parameters to the observed data. The black dashed line represent the 16th, 50th and 84th percentiles.

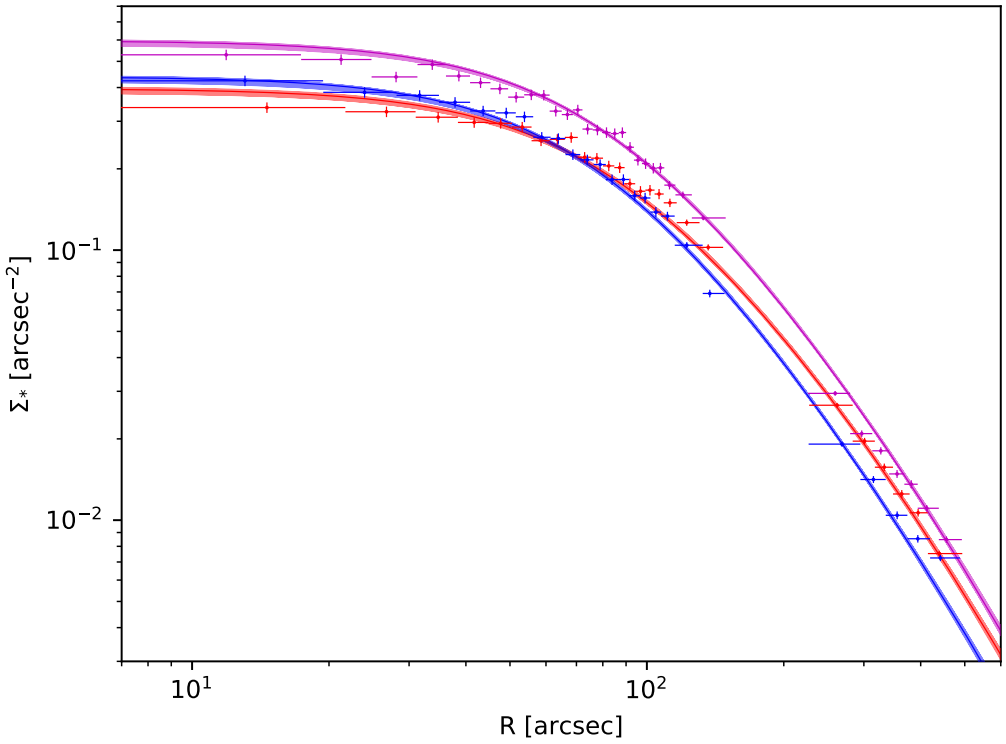

Figure 4.21: Comparison between the observed *HST* number density profiles (dots) and the best-fit modelling prediction (dark lines). The red lines/dots represent the 7th mass bin as listed in Tab. 4.2, the magenta lines/dots the 8th and the blue lines/dots the 9th. The x-bars for the mock *HST* data represent the radial range covered by that bin and the y-errorbar denote 1σ uncertainties. The thin lines represent the results from the walker positions at the last iteration. Note: For clarity I reduced the number of radial bins to 25 per mass bin and limited the x-range scale.

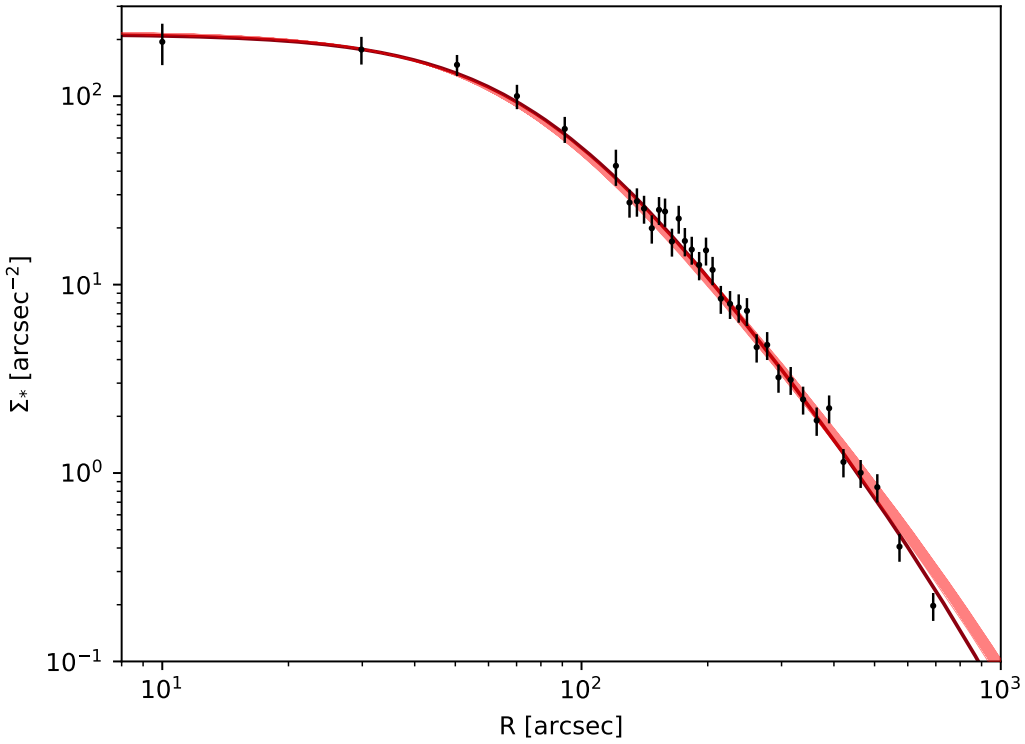

Figure 4.22: Comparison between the observed *Gaia* number density profiles (black dots) and the best-fit modelling prediction (dark red line) for a mock model with BHs. The thin red lines represent the results from the walker positions at the last iteration.

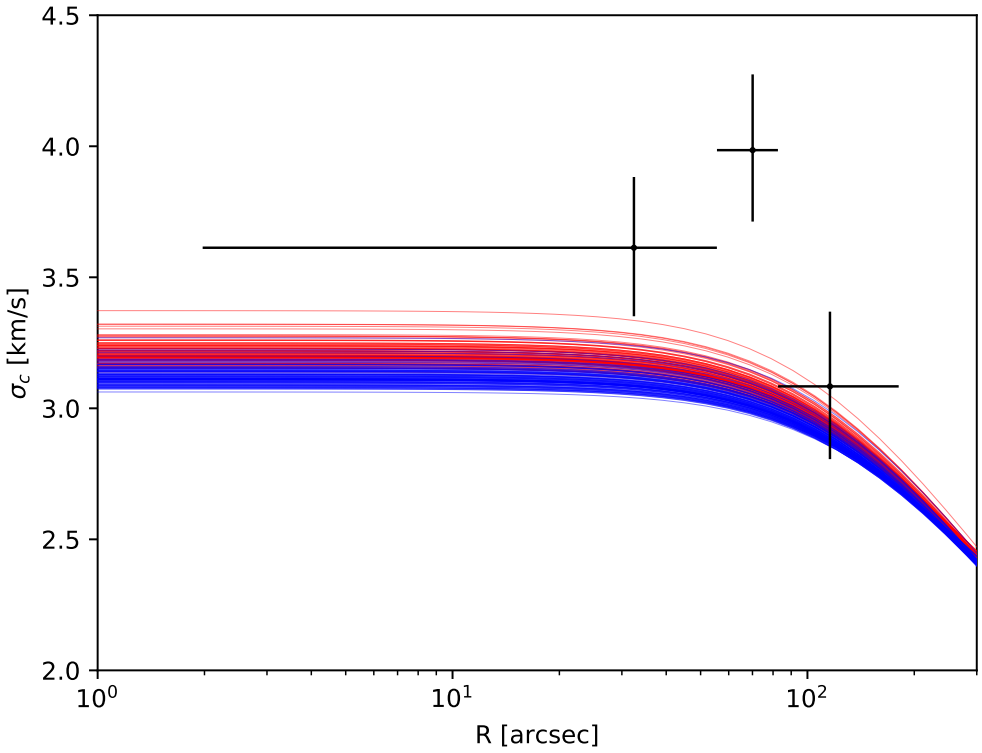

Figure 4.23: Comparison between the *MUSE* velocity dispersion profiles (black dots) as determined in Sec. 4.3.7 without applying any corrections for binaries, compared to best-fit modelling prediction (lines) where the velocity dispersion was convolved with the profiles due to binaries. The red lines represent the 8th mass bin as listed in Tab. 4.2, the blue lines the 9th. The x-bars for the *MUSE* data represent the radial range covered by that bin and the y-errorbar denote 1σ uncertainties. The thin lines represent the results from the walker positions at the last iteration.

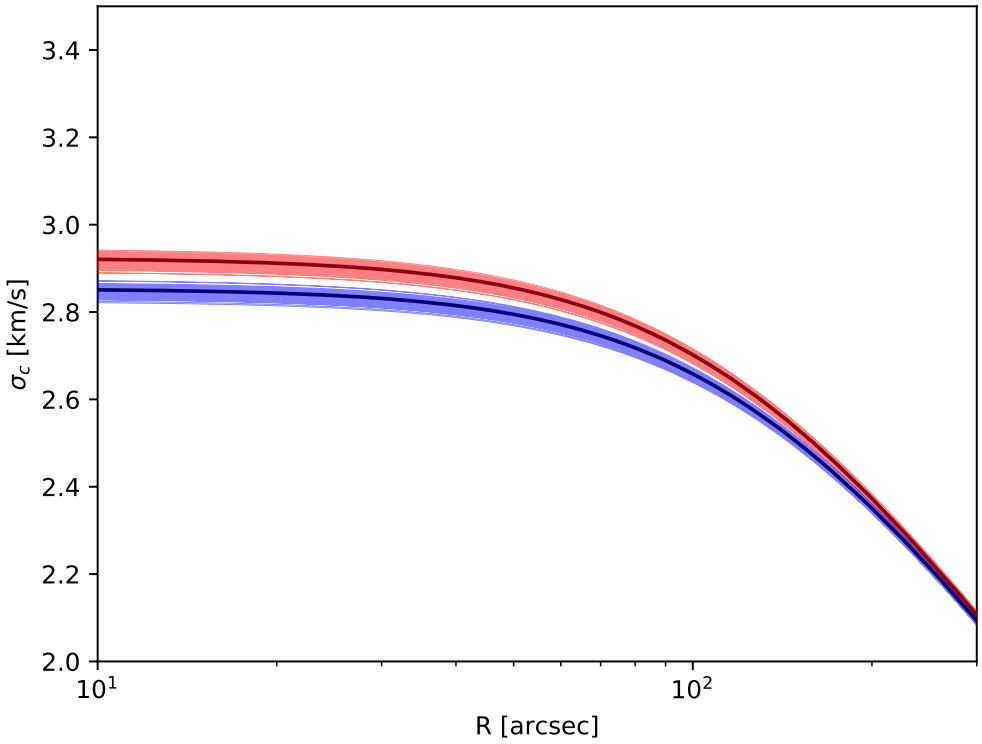

Figure 4.24: Predicted velocity dispersion profiles form the best-fit model to the observation data. The red lines represent the 8th mass bin as listed in Tab. 4.2, the blue lines/dots the 9th. The thin lines represent the results from the walker positions at the last iteration.

data. In Fig. 4.24, I additionally plot the predicted velocity dispersion profile from the best-fit model. Compared to the recovered values in Sec. 4.3.2, assuming a similar binary fraction, the values predicted by the model are also underestimating the observed velocity dispersion.

This under-prediction is therefore significant as the velocity dispersion is the key observation which enables to distinguish between a cluster with BHs and a cluster without (Mackey et al. 2008, and Chapter 3): an under-prediction of the velocity dispersion could therefore also lead to an under-prediction of the stellar-mass BH population.

For the best-fit value of the dynamical BH retention, I find $2^{+1}_{-1}\%$, which translates into a stellar mass BH population of 86^{+30}_{-23} BHs with a total BH mass of $291^{+144}_{-84}\,\mathrm{M}_\odot$ and a mean BH mass of $3.4^{+0.4}_{-0.1}\,\mathrm{M}_\odot$. While the posterior distribution of $f_{\mathrm{BH,dyn}}$ in Fig. 4.20 has a different shape than the one presented in Fig. 4.17 for a mock model without BHs, the case that the cluster has no BH left is within 2σ and can therefore not be fully excluded.

In Chapter 3 (Peuten et al. 2016), I presented a rough estimate for the possible BH population of NGC 6101 based on three N-body simulations. But the values recovered there cannot be compared to the values measured here, as several assumptions were made in the construction of these N-body models, which are most likely not fulfilled, such as the assumption that the cluster was always at its current position. However, I can compare my results to the ones from Askar et al. (2018): I find less BHs than they do and their total BH mass is almost six times larger than the one I recover. Only the mean BH mass agrees within uncertainties, although their mean mass is twice as heavy as the one I recover. Therefore, further studies are needed to explain the divergences between my results and theirs.

Next, I have a look at the best-fit values of the other parameters. First, the cluster mass, which is with $1.71^{+0.01}_{-0.01} \times 10^5\,\mathrm{M}_\odot$ higher than the one I estimated in Chapter 3, where I assumed a mass-to-light ratio of $\Upsilon_\mathrm{V} = 2.1\ \mathrm{M}_\odot/\,\mathrm{L}_\odot$. With the total cluster mass as recovered here and the observed luminosity of $L_\mathrm{V} = 5.7 \times 10^4$ (Harris 1996), I find that the true mass-to-light ratio of NGC 6101 is $\Upsilon_\mathrm{V} = 3.01^{+0.02}_{-0.02}\ \mathrm{M}_\odot/\,\mathrm{L}_\odot$. In my modelling, I find that $45.7 \pm 0.4\%$ of the total mass ($28.3 \pm 0.4\%$ in number) consist of remnants and therefore $54.3 \pm 0.4\%$ of the total mass ($71.7^{+0.4}_{-0.4}\%$ in number) consist of observable stars; apparently only half of the mass in NGC 6101 is luminous. This fact is also reflected in the next parameter, the half-mass radius, which is with $17.6^{+0.2}_{-0.2}\,\mathrm{pc}$ higher than the current value for the half-light radius of $12.3\,\mathrm{pc}$ (Dalessandro et al. 2015), which was calculated using a single mass King model.

Another interesting parameter is δ, which represents how mass segregated the cluster is: with a value of $0.23^{+0.01}_{-0.01}$, it is in accordance with the observationally found reduced mass segregation. It is lower than the values found for dynamically young N-body models with BH as studied in Chapter 2. But there, the stellar evolution was done before the actual dynamical evolution and therefore effects which could influence the mass segregation, such as mass loss due to stellar evolution, are missing. Therefore, the value presented there should be seen as guideline for the values one expects to find for the different dynamical cases.

For the binary fraction, my best fit value is $16^{+5}_{-5}\%$, which is comparable to the one determined with a simpler approach in Sec. 4.3.8, and as already discussed there, this result is comparable to the values recovered by other studies using different, more accurate, approaches. However, the under-prediction of the velocity dispersion could hint that the

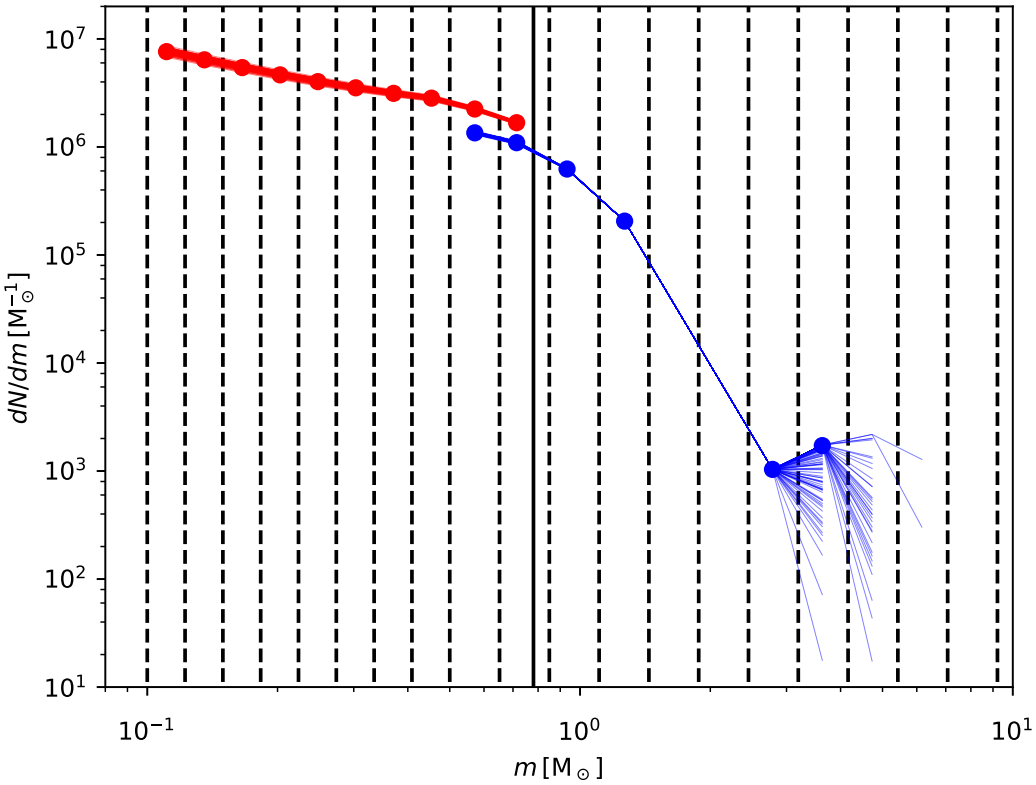

Figure 4.25: Global MF for the stars (red dots) and remnants (blue dots) as interfered from the best fit results. The black vertical dashed lines represent the mass bin borders and the black vertical solid line represents the current main-sequence turn off mass as estimate from the MF evolution code. The thin lines represent the results from the walker positions at the last iteration.

recovered value for the binary fraction could be too low.

For the central dimensionless concentration (W_0), I find a value of $6.7^{+0.1}_{-0.1}$ which is lower than the previously recovered value from the multimass fit in Chapter 3. However, this fit only uses the number density profile from NGC 6101 as presented in Dalessandro et al. (2015) as reference. This value is indicative of a low density cluster, as it is observed.

The best-fit value for the truncation parameter shows that the cluster is best fit by a Wilson (1975) model, which is also in accordance with the results of the previous multi-mass fit. In Chapter 2, I found in N-body models that during the evolution of a cluster, the truncation parameter value changes from $g \approx 2$, a Wilson (1975) model, to $g = 1$, a King (1966) model, before becoming $g \approx 0$, a Woolley (1954) model, due to tidal interactions at the cluster's border. The fact that the cluster is still described best by a Wilson (1975) model shows that NGC 6101 has not lost much stars due to tidal interaction, which at its current position and age is hard to explain unless the cluster was recently accreted (Mackey and Gilmore 2004).

Next, I have a look at the recovered MF: in Fig. 4.25, I plot the best-fit mass function as generated by my improved MF evolution. I also added the MF for each individual MCMC

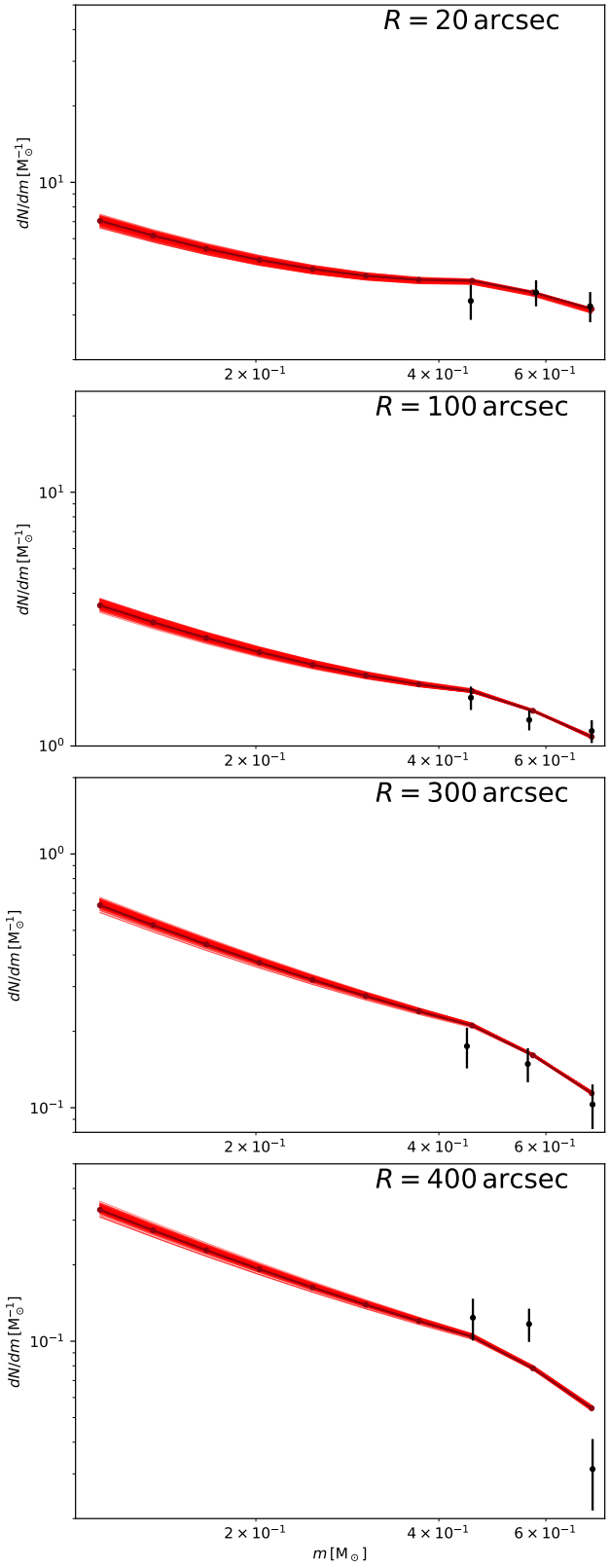

Figure 4.26: Comparison of the local MF of NGC 6101 determined from the *HST* data (black dots) with the best fit prediction from my model (red lines/dots) at four different radii: 20 arcsec, 100 arcsec, 300 arcsec and 400 arcsec. The thin lines represent the results from the walker positions at the last iteration.

walker in this plot: the greatest variations are seen in the MF of the BH population, which is no surprise given that there is no direct observation which can constrain them and I have left the retention fraction of BHs as a free parameter.

To study the radial dependence of the MF and with it the mass segregation, I plot in Fig. 4.26 the best-fit mass function and the observed mass function for the cluster at four different radii: for this, I cut the *HST* data in concentric circles with a width of one arcsec, at 20 arcsec, 100 arcsec, 300 arcsec, and at 400 arcsec, and then I determine the local MF, using the same mass cuts as in my modelling. My best-fit model is able to reproduce the observed MF in the two more central radial bins, while in the outer bins, divergences between model and observations are apparent. When I compare the MF as calculated from the *HST* data, I see that there is a change with radius as the heaviest observed stars are more abundant in the innermost radial bins than in the outermost bins when compared to the other lower mass bins.

In this study, I did not look directly into the analysis of an IMBH as source of NGC 6101's uncommon properties: in the discussion in Sec. 3.5, I showed that the expected velocity profile for a cluster with an IMBH is not too different from a cluster without mass segregation other than in the inner 10 arcsec where it steeply rises to a value of around $5.1\,\mathrm{km\,s^{-1}}$ in the centre. In the inner 10 arcsec, I have measured 23 velocities for which I calculated the observed velocity dispersion using equation (4.3.3), assuming the previously found cluster velocity and binary fraction to be $4.4^{+1.5}_{-1.3}\,\mathrm{km\,s^{-1}}$. Due to the large uncertainties, I can neither fully disprove nor prove the existence of an IMBH, but it is generally assumed that an IMBH would form a binary with another cluster member, preferentially with a BH, which would then be quite effective in ejecting other cluster members (Gill et al. 2008). Therefore, if an IMBH were present, one would expect to find no stellar mass BH population in the cluster. As I do find at least a few BHs, and given that the search for IMBHs using observational (Tremou et al. 2018a) or dynamical methods (Zocchi et al. 2018; Gieles et al. 2018) is currently inconclusive, I prefer the interpretation that there is no IMBH in NGC 6101.

As already discussed in Sec. 4.5.3, the method presented here is not able to distinguish between initial BH ejection and dynamical BH ejection. Given the relative low recovered value for the BH retention of $0.02^{+0.01}_{-0.01}$, it is even impossible to make any prediction how the measured BH retention could be divided up between the two contributions. If the dynamical BH retention were as high as 50%, as found in the N-body modelling of NGC 6101 in Chapter 3, then the initial BH retention would be as low as 4%. This value is lower than the recently published value of 20% for GCs by Pavlík et al. (2018) and should therefore be treated with care.

4.6 Conclusion

Analysing eight hours of MUSE observations, I measured NGC 6101 velocity to $364.3 \pm 0.16\,\mathrm{km\,s^{-1}}$, in accordance with previous findings. In order to shed light on the current discussion about the dynamical state of NGC 6101 (i.e. whether the cluster really is not mass segregated and what the cause for it is), and in order to test the prediction made in Chapter 3 (Peuten et al. 2016) that a stellar mass BH population could be the reason for it, I performed detailed modelling of NGC 6101. For this analysis, I used multimass models as provided by the LIMEPY dynamical models (Gieles and Zocchi 2015), improved MF

modelling from Balbinot and Gieles (2018) and statistical binary treatment from Cottaar et al. (2012). Besides the *MUSE* data, I used all available *HST* data as well as the recently released *Gaia* data to find the model parameters which describe the observations best.

Doing extensive testing, I showed that this method can indeed be used to determine any remaining stellar mass BH populations in GCs. Applying this method to the observation of NGC 6101, I can verify the suggestion I made in Chaper 3 that the cluster's odd properties can be explained by the cluster having a stellar mass BH population. In my modelling, I find a BH population of 86^{+30}_{-23} stellar mass BHs, with a total mass of $291^{+144}_{-84}\,\mathrm{M}_\odot$ and an average BH mass of $3.4^{+0.5}_{-0.1}\,\mathrm{M}_\odot$. Furthermore, I find the total cluster mass to be $1.71^{+0.01}_{-0.01}\times10^5\,\mathrm{M}_\odot$ and therefore heavier than anticipated. Also the half-mass radius is with $17.6^{+0.2}_{-0.2}\,\mathrm{pc}$ larger than previously estimated half-light radius. The best-fit value for the mass segregation parameter δ can reproduce the observationally found reduced mass segregation in NGC 6101. The finding that the cluster's truncation parameter $g = 1.98^{+0.02}_{-0.03}$ further supports the fact that NGC 6101 is an accreted cluster, as at the given position, the tidal effect should have had a stronger effect, which should have lowered the value of the truncation parameter significantly.

The fly in the ointment is that my best-fit model is underpredicting the observed velocity dispersion from my *MUSE* data. This is significant as the velocity dispersion is the key observation to determine the mass in BHs (Mackey et al. 2008, and Chapter 3). Underpredicting it could lead to an underprediction of the stellar mass BH population in NGC 6101. Additionally, the best-fit value for the dynamically retained fraction of the BH population is only 2σ away from a solution of a cluster without BHs. Therefore, further observations are needed to verify the result with the required accuracy.

Besides NGC 6101, Askar et al. (2018) list 28 other Milky Way GCs where they suspect a stellar-mass BH population. For two of them, NGC 3201 and NGC 6656, Kamann et al. (2018) presented high quality *MUSE* velocity measurements, with more *MUSE* observations of Milky Way GCs being currently processed. With an improved version of the modelling presented here, one cannot only test these two GCs for their BH population, but also all Milky Way GCs where sufficient data is available. Not only can the individual GC's BH population be determined, but it can also be used to study which GC properties have which effect on their BH population or which possible reason there could be if no BH population is left. Such a study could shed light on why most dwarf galaxy GCs and only some Milky Way GCs show typical signs of BH populations (Mackey and Gilmore 2004; Mackey et al. 2008) while others do not. Furthermore, these studies could help to locate those GCs where BH-BH merges are most likely to occur and which are therefore good targets for searches of gravitational wave events.

Chapter 5

Conclusions

In this conclusion, I want to focus on the most important results, their implications and their possible future influence, but also on questions that arose as a result of this thesis work.

With the continuous introduction of improved observations and especially methods to correct atmospheric turbulence, the quality of observations of globular clusters is increasing steadily, making high quality observations comparable to space-based instruments soon the norm. Furthermore, with instruments such as the *MUSE* integral field unit (IFU) and the *Gaia* satellite, we can measure the velocities of a large selection of globular cluster stars. With all these high quality data at hand, observers need models to better analyse and understand globular clusters. For many years, the standard approach was to use different versions of the single mass lower isothermal models, such as the renowned King (1966) models. But with high quality observations being able to observe the faintest and therefore lightest globular cluster stars, the single mass models cannot reproduce effects such as mass segregation or the different densities and velocities of stars with different masses. Already, Da Costa and Freeman (1976) faced problems with single-mass models, which is why they extended these otherwise successful models by adding a mass function. These models are now known as anisotropic lowered isothermal multimass models or multimass models, and despite their success in many observational studies, there were still some aspects and assumptions made in the construction of these models which have never been validated. In Chapter 2, I showed that a set of N-body simulations is well reproduced by anisotropic lowered isothermal multimass models, such as those provided by the LIMEPY software (Gieles and Zocchi 2015), and I showed that the assumptions made in the construction of the models are justified.

One of the main drawbacks when using multimass models is the selection of the right mass function, which traditionally is a mixture between realism and convenience (Meylan and Heggie 1997). In Chapter 2, the true mass function was already known, and therefore, I performed tests to select the best approach for the mass function for my comparison. In observations, this is a problem, as not all stars can be observed, since the remnants are mostly non-luminous. To counter this problem, in Chapter 4, I use the mass function evolution code as presented in Balbinot and Gieles (2018) and I added the evolution of black holes to it as well as including a metallicity dependent initial-final mass relation for remnants and a higher precision numerical solver. This approach can be used by any observer who wants to use multimass models to study observations or to quickly

generate mass functions for theoretical studies. Due to its sub-second runtime, it is ideal for any fitting approach where thousands of repeated calculations are needed, such as MCMC modelling. The possible applications are various and my hope is that it will be used by many astronomers studying all aspects of cluster evolution, and not only for the application in multimass models.

The modelling approach I present in Chapter 4 - multimass models together with the mass evolution code - has the ability to become the swiss army knife for globular cluster modelling: as I showed in numerous tests, the model is not only able to recover the general cluster properties such as the total cluster mass or the half-mass radius, but it is also able to discover a stellar mass black hole population if there is one in the cluster. In these tests, I am only using mock observations which recreate the actual observations currently available for NGC 6101, to show the real world performance of the approach.

The most important result from Chapter 3 is that in N-body models, stellar mass black hole populations can reduce mass segregation. Thus the observed lack of mass segregation of NGC 6101 is an indication for a stellar mass black hole population in its core. In the N-body models from Chapter 2, the same behaviour is also found. Bianchini et al. (2016) showed that there is a limiting mass below which the stars are not in equipartition. For clusters with black holes, I find that this limiting mass is above most observable stars. Therefore, these observed stars have a smaller spread in the velocity dispersion, which is the reason for the reduced mass segregation in the observable stars in clusters with black holes. Using a similar approach, Alessandrini et al. (2016) almost concurrently presented the same result for set different of N-body models.

I also considered alternative theories which could explain the current observations of NGC 6101: An intermediate mass black holes in NGC 6101 centre would be able to reproduce both observations (Gill et al. 2008), while binaries could explain the inflated core (Vesperini and Chernoff 1994; Giersz and Heggie 2011) and would produce a cusp in the density and velocity dispersion profiles. In order to find an observable quantity to distinguish the different proposed explanations, I created multimass models based on N-body models recreating the different proposed explanations: first of all, I find that multimass models are able to recreate the observed lack of mass segregation when black holes are present, and secondly, I found that with a measurement of the cluster's velocity dispersion, one should be able to distinguish between the proposed explanations.

With *MUSE* observations of NGC 6101 at hand, in Chapter 4, I present the reduction and extraction of the velocities of 1108 stars. From these, I measured the cluster velocity to be $364.3 \pm 0.16\,\mathrm{km\,s^{-1}}$ in accordance with the previous measured value of $364.3 \pm 1.9\mathrm{km/s}$ (Geisler et al. 1995). As I have only one epoch of data available and therefore cannot detect binaries, I have to include the statistical binary treatment approach presented in Cottaar et al. (2012) into my modelling. With this extended model applied to the available observations, I find that approximately $2 \pm 1\%$ of the initial black hole population is still in the cluster, which means that there are still 86^{+30}_{-23} stellar mass black holes, with a total mass of $291^{+144}_{-84}\,\mathrm{M}_{\odot}$, in NGC 6101. I could therefore show that indeed NGC 6101's properties such as the reduced mass segregation or the inflated profiles are due to the stellar mass black hole population. However, I must note that the result is only 2σ away from having no black holes left in the cluster. Therefore, further observations and studies are needed to verify the result with the required accuracy. Especially one or several further epochs of stellar velocity measurements with the *MUSE* instrument would

improve the results significantly, as there is a strong relation between the velocity dispersion and the cluster's black hole population. This would not only increase the number of measurements, but would also aid in locating those stars which are in a binary configurations and whose data should therefore be removed from the analysis. This would further eliminate the need for a statical approach for the binary treatment in my modelling.

The question raised by the findings in Chapter 3 and Chapter 4 is why some globular clusters do have a stellar mass black hole population while others do not. Especially as the more prominent signs, such as an inflated profile, are mostly observed in dwarf galaxy globular clusters (Merritt et al. 2004; Mackey et al. 2008) or Milky Way globular clusters assumed to be accreted from one, such as NGC 6101 (Geisler et al. 1995; Martin et al. 2004; Mackey and Gilmore 2004; Sohn et al. 2018). Assuming that the initial mass function (although, see Geha et al. 2013) and the black hole natal kick distribution are the same in dwarf galaxy globular clusters, my findings indicate that the observed difference could come from the host galaxy environment: in dwarf galaxies, globular clusters form with lower densities (Elmegreen 2008), which in turn implies they have a longer half-mass relaxation times, which, following Breen and Heggie (2013a) findings, accounts for a lower dynamical black hole ejection compared to globular clusters created with higher densities. One of the implications from this is that the black hole natal kicks must be so low that all globular clusters retain a large fraction of their black holes; the Milky Way globular clusters just eject them quicker than the dwarf galaxy globular clusters. But comparable studies of other globular clusters are needed to prove these assumptions, especially as with my current results I cannot make any justified prediction for the initial kick retention.

Of the 29 listed Milky Way globular clusters where Askar et al. (2018) suspect a stellar mass black hole population, there are two, namely NGC 3201 and NGC 6656, for which Kamann et al. (2018) presented high quality multi-epoch *MUSE* velocity measurements. These are therefore ideal candidates for follow-up modelling approaches, which could use the version of my approach without the statistical binary treatment. But also other globular clusters where no black hole population is suspected and where sufficient observations are available, such as the other 23 globular clusters in Kamann et al. (2018), should be targets of such modelling approaches. As I showed in my tests, the models are able to also recover the important cluster properties with good accuracy. Having a catalogue of results from such a modelling approach of a significant portion of the Milky Way globular clusters would not only help to better classify them, but also helps to find out which globular cluster properties have which effect on their black hole population or which possible reason there could be when no black holes are left. Such a study could shed light on why most dwarf galaxy globular cluster and only some Milky Way globular clusters show typical signs of black hole population (Mackey and Gilmore 2004; Mackey et al. 2008) while others do not. Furthermore, these studies could help to locate those globular clusters where black hole - black hole merges are most likely to occur and which are therefore good targets for searches of gravitational wave events.

With my current approach, I am able to discover the current properties of the Milky Way globular clusters, but I already started work on trying to unravel their initial conditions: for this, I started incorporating my improved mass function evolution code into the fast star cluster evolution code EMACSS (Evolve Me A Cluster of StarS) presented in Alexander et al. (2014). Using Hénon's findings (Hénon 1961, 1965) that in a state of

balanced evolution, the flow of energy within a cluster is independent of the actual energy source in the core, EMACSS calculates the evolution of some of a cluster's main properties. The idea is to let EMACSS evolve the cluster's properties as well as its mass function concurrently, and then use the resulting values to create a multimass model which is then used to compare to the current observations of a globular cluster. This would be the next obvious extension to my modelling approach and could therefore not only reveal the current properties, but could also give us hints about the initial conditions of the Milky Way globular clusters and the Milky Way itself.

Although producing good results, my modelling approach has still room for improvements and there are still many open questions concerning multimass models that I could only touch on briefly. One of them concerns the mass segregation parameter δ for which I found an indication for a relation between it and the cluster black hole population: as long as there are some black holes left in the cluster, they reduce the mass segregation and the best fit value of δ stays around 0.35. In the N-body model $N1$, which has initially retained all of its black holes, in Chapter 2, there seems to be an interesting relation between δ and the Spitzer stability parameter S (Spitzer 1969) of the black hole population of the form:

$$\delta \approx 0.35 + 0.15 \times \exp\left(-S\right) \tag{5.0.1}$$

where S is defined as (Fregeau et al. 2002)

$$S \equiv \left(\frac{M_{\rm BH}}{M_{\rm Cl}}\right)\left(\frac{m_{\rm BH}}{m_{\rm Cl}}\right)^{3/2} \tag{5.0.2}$$

where $M_{\rm Cl}$ and $m_{\rm C}$ are the total mass of the cluster and the mean mass of the stars excluding the black holes and $M_{\rm BH}$ and $m_{\rm BH}$ is the total mass and mean mass of the black holes. For values of S below 0.16 the black hole subsystem is considered "Spitzer stable" and for values above it is considered "Spitzer unstable" (Fregeau et al. 2002). Unfortunately, this relation is not reproduced in the other two N-body simulations with black holes in Chapter 2, which could be due to the fact that both of them lose their black hole population within the first few Gyrs. Apparently, there are other dependencies relating to the two quantities, which we are not aware of yet. Understanding this relation could help to find a better handle to estimate black hole populations in globular clusters and could therefore further aid in modelling globular clusters. This is an interesting aspect to study in the future to improve the modelling approach.

Another interesting relation found in studying the multimass models as provided by LIMEPY is that the truncation parameter g evolves, as tides are acting at the cluster's border. This was also found for single mass models by Zocchi et al. (2016). This evolution of g can therefore explain why different clusters are fit by different models better (McLaughlin and van der Marel 2005). Just recently, Dr Thomas de Boer started applying these improved LIMEPY models on the number density profiles from *Gaia* of all Milky Way globular clusters. The results could help test and see whether this trend is reproduced by the observations. Therefore g, could be an indicator whether a cluster is still dynamically expanding towards filling the Roche volume (Carballo-Bello et al. 2012) or whether it is shrinking again until dissolution (Hénon 1961; Gieles et al. 2011).

An aspect of the *limepy* models I studied in Chapter 2 but did not look at in the following chapters of this thesis is radial anisotropy: in my studies, I find that the LIMEPY

models are able to recreate radial anisotropy when the N-body model is radially anisotropic. Furthermore, I find that the cluster's anisotropy radius is indeed mass-dependent, and that over time the mass bin with the highest amount of radial anisotropy evolves from the lighter stars to the heavier stars. This can be explained by the fact that the stars which are kicked out of the cluster centre reach the halo on radial orbits and can therefore escape the cluster more efficiently, as they have positive velocity when reaching the cluster boundary (Lynden-Bell and Wood 1968; Spitzer and Shull 1975), explaining the depletion of the low-mass population of stars with radial orbits. In the construction of the radial anisotropy multimass models by Gunn and Griffin (1979), it was assumed that mass dependence effects should be negligible, which for my N-body models and for some of the models studied by Sollima et al. (2015) is not the case. A possible starting point for further studies would be to study radial anisotropy in other N-body models to see if the trends found for $r_{\mathrm{a},j}$ and η in Chapter 2 are universal and whether they are reproduced in real observations.

In Chapter 2 and in Chapter 3, I am using N-body simulations to create cluster models for different analyses, and in both of them, I find that the mean mass profile is independent of the remnant retention fraction. When analysing the behaviour of the relative mean mass profile, i.e the mean mass in radial bins divided by the global mean mass, I find that it is the same for the four N-body models in Chapter 2 (see Fig. 2.4), and for the three N-body models in Chapter 4 (see Fig. 3.3). Only in the core regions, I see a divergence between the models with black holes and the models without black holes. As the cluster evolves, I find that the relative mean mass profile becomes flatter. in the N-body models of Chapter 2, this is not as strong as in the N-body models of Chapter 3: this is due to the fact that for the N-body models of Chapter 2 the stellar evolution was done before the dynamical evolution. For single mass systems, it has been found that their evolution becomes self-similar (Hénon 1961, 1965) and it has been shown that the evolution of mass and radii for multimass systems is comparable to them, just faster (Lee and Goodman 1995; Gieles et al. 2010). For N-body models, Giersz and Heggie (1996, 1997) showed that after some time, the mean mass evolution in Lagrangian shells comes to halt. Currently, I am not aware of a theory providing an explanation for this attractor solution of $\bar{m}\,(r)$, but there is the possibility of using this relation as prior when comparing multimass models to observational data. But for this, one would first need to check whether this behaviour is found universally in all N-body simulations or whether any other conditions need to be met.

When scientists talk about the impact of their work, they mainly consider their scientific impact, but there is also the impact on the public perception. For astronomy, this impact is especially important: compared to other science where there is a more or less direct industrial application and therefore funding comes from companies hoping to make a profit. In astronomy, most funding comes from official agencies. One example would be the European Research Council, which gave my supervisor the opportunity to fund my PhD thesis. In a democracy, those who control these funds are in the end accountable to the general population. It is therefore indispensable to also inform the public about our results and findings, be it in the form of outreach events, presentations or articles aimed at the general audience. Publishing a press release[1] along the publication of the results from

[1] See `https://www.surrey.ac.uk/mediacentre/press/2018/new-research-reveals-hundreds-undiscovered-black-holes`

Chapter 3, I was first stunned by the interest of the media as well as by their variety of interpretation of my work. In subsequent interviews and conversations, at outreach events and presentations, I found that there is indeed a general interest in my field of research. Not everyone saw the importance why we have to study them now and with the current expenditure, but nevertheless they show genuine interest. Research in astronomy indeed touches mankind oldest question about our origin and our place within the universe. I hope that with this PhD thesis, I could not only make a scientific impact by presenting this improved approach to analyse globular clusters and to determine their black hole population, but also that it could make an impact on the public perception, so that others can also profit by engaging in a PhD in astronomy, and to make their own impact.

Bibliography

Aarseth, S. J. (1963). Dynamical evolution of clusters of galaxies, I. *MNRAS*, 126:223.

Aarseth, S. J. (1999). From NBODY1 to NBODY6: The Growth of an Industry. *Publications of the Astronomical Society of the Pacific*, 111:1333–1346.

Aarseth, S. J. (2003). *Gravitational N-Body Simulations*. Cambridge University Press.

Aarseth, S. J. (2012). Mergers and ejections of black holes in globular clusters. *MNRAS*, 422:841–848.

Abbott, B. P., Abbott, R., Abbott, T. D., Abernathy, M. R., Acernese, F., Ackley, K., Adams, C., Adams, T., Addesso, P., Adhikari, R. X., and et al. (2016a). Astrophysical Implications of the Binary Black-hole Merger GW150914. *ApJ*, 818:L22.

Abbott, B. P., Abbott, R., Abbott, T. D., Abernathy, M. R., Acernese, F., Ackley, K., Adams, C., Adams, T., Addesso, P., Adhikari, R. X., and et al. (2016b). GW151226: Observation of Gravitational Waves from a 22-Solar-Mass Binary Black Hole Coalescence. *Physical Review Letters*, 116(24):241103.

Abbott, B. P., Abbott, R., Abbott, T. D., Abernathy, M. R., Acernese, F., Ackley, K., Adams, C., Adams, T., Addesso, P., Adhikari, R. X., and et al. (2016c). Improved Analysis of GW150914 Using a Fully Spin-Precessing Waveform Model. *Physical Review X*, 6(4):041014.

Abbott, B. P., Abbott, R., Abbott, T. D., Abernathy, M. R., Acernese, F., Ackley, K., Adams, C., Adams, T., Addesso, P., Adhikari, R. X., and et al. (2016d). Observation of Gravitational Waves from a Binary Black Hole Merger. *Physical Review Letters*, 116(6):061102.

Abbott, B. P., Abbott, R., Abbott, T. D., Acernese, F., Ackley, K., Adams, C., Adams, T., Addesso, P., Adhikari, R. X., Adya, V. B., and et al. (2017a). GW170104: Observation of a 50-Solar-Mass Binary Black Hole Coalescence at Redshift 0.2. *Physical Review Letters*, 118(22):221101.

Abbott, B. P., Abbott, R., Abbott, T. D., Acernese, F., Ackley, K., Adams, C., Adams, T., Addesso, P., Adhikari, R. X., Adya, V. B., and et al. (2017b). GW170608: Observation of a 19 Solar-mass Binary Black Hole Coalescence. *ApJ*, 851:L35.

Abbott, B. P., Abbott, R., Abbott, T. D., Acernese, F., Ackley, K., Adams, C., Adams, T., Addesso, P., Adhikari, R. X., Adya, V. B., and et al. (2017c). GW170814: A Three-Detector Observation of Gravitational Waves from a Binary Black Hole Coalescence. *Physical Review Letters*, 119(14):141101.

Abbott, B. P., Abbott, R., Abbott, T. D., Acernese, F., Ackley, K., Adams, C., Adams, T., Addesso, P., Adhikari, R. X., Adya, V. B., and et al. (2017d). GW170817: Observation of Gravitational Waves from a Binary Neutron Star Inspiral. *Physical Review Letters*, 119(16):161101.

Ahmad, A. and Cohen, L. (1973). A numerical integration scheme for the N-body gravitational problem. *Journal of Computational Physics*, 12:389–402.

Alessandrini, E., Lanzoni, B., Ferraro, F. R., Miocchi, P., and Vesperini, E. (2016). Investigating the Mass Segregation Process in Globular Clusters with Blue Straggler Stars: The Impact of Dark Remnants. *ApJ*, 833:252.

Alexander, P. E. R., Gieles, M., Lamers, H. J. G. L. M., and Baumgardt, H. (2014). A prescription and fast code for the long-term evolution of star clusters - III. Unequal masses and stellar evolution. *MNRAS*, 442:1265–1285.

Anderson, J., Sarajedini, A., Bedin, L. R., King, I. R., Piotto, G., Reid, I. N., Siegel, M., Majewski, S. R., Paust, N. E. Q., Aparicio, A., Milone, A. P., Chaboyer, B., and Rosenberg, A. (2008). The Acs Survey of Globular Clusters. V. Generating a Comprehensive Star Catalog for each Cluster. *AJ*, 135:2055–2073.

Antonucci, R. (1993). Unified models for active galactic nuclei and quasars. *ARA&A*, 31:473–521.

Arca Sedda, M., Askar, A., and Giersz, M. (2018). MOCCA-Survey Database - I. Unravelling black hole subsystems in globular clusters. *MNRAS*, 479:4652–4664.

Arenou, F., Luri, X., Babusiaux, C., Fabricius, C., Helmi, A., Muraveva, T., Robin, A. C., Spoto, F., Vallenari, A., Antoja, T., Cantat-Gaudin, T., Jordi, C., Leclerc, N., Reylé, C., Romero-Gómez, M., Shih, I., Soria, S., Barache, C., Bossini, D., Bragaglia, A., Breddels, M. A., Fabrizio, M., Lambert, S., Marrese, P. M., Massari, D., Moitinho, A., Robichon, N., Ruiz-Dern, L., Sordo, R., Veljanoski, J., Di Matteo, P., Eyer, L., Jasniewicz, G., Pancino, E., Soubiran, C., Spagna, A., Tanga, P., Turon, C., and Zurbach, C. (2018). Gaia Data Release 2: Catalogue validation. *ArXiv e-prints*.

Ashman, K. M. and Zepf, S. E. (1992). The formation of globular clusters in merging and interacting galaxies. *ApJ*, 384:50–61.

Askar, A., Arca Sedda, M., and Giersz, M. (2018). MOCCA-SURVEY Database I: Galactic Globular Clusters Harbouring a Black Hole Subsystem. *ArXiv e-prints*.

Bacon, R., Vernet, J., Borisova, E., Bouché, N., Brinchmann, J., Carollo, M., Carton, D., Caruana, J., Cerda, S., Contini, T., Franx, M., Girard, M., Guerou, A., Haddad, N., Hau, G., Herenz, C., Herrera, J. C., Husemann, B., Husser, T.-O., Jarno, A., Kamann, S., Krajnovic, D., Lilly, S., Mainieri, V., Martinsson, T., Palsa, R., Patricio, V., Pécontal,

A., Pello, R., Piqueras, L., Richard, J., Sandin, C., Schroetter, I., Selman, F., Shirazi, M., Smette, A., Soto, K., Streicher, O., Urrutia, T., Weilbacher, P., Wisotzki, L., and Zins, G. (2014). MUSE Commissioning. *The Messenger*, 157:13–16.

Bahramian, A., Heinke, C. O., Tudor, V., Miller- Jones, J. C. A., Bogdanov, S., Maccarone, T. J., Knigge, C., Sivakoff, G. R., Chomiuk, L., Strader, J., Garcia, J. A., and Kallman, T. (2017). The ultracompact nature of the black hole candidate X-ray binary 47 Tuc X9. *MNRAS*, 467:2199–2216.

Balbinot, E. and Gieles, M. (2018). The devil is in the tails: the role of globular cluster mass evolution on stream properties. *MNRAS*, 474:2479–2492.

Banerjee, S. (2018). Stellar-mass black holes in young massive and open stellar clusters and their role in gravitational-wave generation - II. *MNRAS*, 473:909–926.

Barnard, R. and Kolb, U. (2009). A second black hole candidate in a M31 globular cluster is identified with XMM-Newton. *MNRAS*, 397:L92–L95.

Barnard, R., Stiele, H., Hatzidimitriou, D., Kong, A. K. H., Williams, B. F., Pietsch, W., Kolb, U. C., Haberl, F., and Sala, G. (2008). New XMM-Newton Analysis of Three Bright X-Ray Sources in M31 Globular Clusters, Including a New Black Hole Candidate. *ApJ*, 689:1215–1221.

Bastian, N. and Lardo, C. (2017). Multiple Stellar Populations in Globular Clusters. *ArXiv e-prints*, page arXiv:1712.01286.

Baumgardt, H. (2001). Scaling of N-body calculations. *MNRAS*, 325:1323–1331.

Baumgardt, H. (2017). N -body modelling of globular clusters: masses, mass-to-light ratios and intermediate-mass black holes. *MNRAS*, 464:2174–2202.

Baumgardt, H., Côté, P., Hilker, M., Rejkuba, M., Mieske, S., Djorgovski, S. G., and Stetson, P. (2010). Limits on the dark matter content of globular clusters. In de Grijs, R. and Lépine, J. R. D., editors, *IAU Symposium*, volume 266 of *IAU Symposium*, pages 365–365.

Baumgardt, H., De Marchi, G., and Kroupa, P. (2008). Evidence for Primordial Mass Segregation in Globular Clusters. *ApJ*, 685:247–253.

Baumgardt, H. and Makino, J. (2003). Dynamical evolution of star clusters in tidal fields. *MNRAS*, 340:227–246.

Baumgardt, H. and Mieske, S. (2008). High mass-to-light ratios of ultra-compact dwarf galaxies - evidence for dark matter? *MNRAS*, 391:942–948.

Baumgardt, H. and Sollima, A. (2017). The global mass functions of 35 Galactic globular clusters - II. Clues on the initial mass function and black hole retention fraction. *MNRAS*, 472:744–750.

Beccari, G., Dalessandro, E., Lanzoni, B., Ferraro, F. R., Bellazzini, M., and Sollima, A. (2015). Deep Multi-telescope Photometry of NGC 5466. II. The Radial Behavior of the Mass Function Slope. *ApJ*, 814:144.

Beccari, G., Pasquato, M., De Marchi, G., Dalessandro, E., Trenti, M., and Gill, M. (2010). The Dynamical State of the Globular Cluster M10 (NGC 6254). *ApJ*, 713:194–204.

Bedin, L. R., Piotto, G., Anderson, J., Cassisi, S., King, I. R., Momany, Y., and Carraro, G. (2004). ω Centauri: The Population Puzzle Goes Deeper. *ApJ*, 605:L125–L128.

Bekki, K. and Freeman, K. C. (2003). Formation of ω Centauri from an ancient nucleated dwarf galaxy in the young Galactic disc. *MNRAS*, 346:L11–L15.

Belczynski, K., Bulik, T., Fryer, C. L., Ruiter, A., Valsecchi, F., Vink, J. S., and Hurley, J. R. (2010). On the Maximum Mass of Stellar Black Holes. *ApJ*, 714:1217–1226.

Belczynski, K., Holz, D. E., Bulik, T., and O'Shaughnessy, R. (2016). The first gravitational-wave source from the isolated evolution of two stars in the 40-100 solar mass range. *Nature*, 534:512–515.

Belczynski, K., Kalogera, V., and Bulik, T. (2002). A Comprehensive Study of Binary Compact Objects as Gravitational Wave Sources: Evolutionary Channels, Rates, and Physical Properties. *ApJ*, 572:407–431.

Belczynski, K., Kalogera, V., Rasio, F. A., Taam, R. E., Zezas, A., Bulik, T., Maccarone, T. J., and Ivanova, N. (2008). Compact Object Modeling with the StarTrack Population Synthesis Code. *ApJS*, 174:223–260.

Benacquista, M. J. and Downing, J. M. B. (2013). Relativistic Binaries in Globular Clusters. *Living Reviews in Relativity*, 16:4.

Bernoulli, J. (1742). *Opera omnia : tum antea sparsim edita, quam hactenus inedita*, volume 1. Lausannae ; Genevae : Sumptibus Marci Michaelis Bousquet & Sociorum.

Bianchini, P., van de Ven, G., Norris, M. A., Schinnerer, E., and Varri, A. L. (2016). A novel look at energy equipartition in globular clusters. *MNRAS*, 458:3644–3654.

Binney, J. and McMillan, P. (2011). Models of our Galaxy - II. *MNRAS*, 413:1889–1898.

Binney, J. and Tremaine, S. (1987). *Galactic dynamics*. Princeton, NJ, Princeton University Press, 1987, 747 p.

Bonaca, A., Geha, M., Küpper, A. H. W., Diemand, J., Johnston, K. V., and Hogg, D. W. (2014). Milky Way Mass and Potential Recovery Using Tidal Streams in a Realistic Halo. *ApJ*, 795:94.

Breen, P. G. and Heggie, D. C. (2013a). Dynamical evolution of black hole subsystems in idealized star clusters. *MNRAS*, 432:2779–2797.

Breen, P. G. and Heggie, D. C. (2013b). On black hole subsystems in idealized nuclear star clusters. *MNRAS*, 436:584–589.

Bruns, H. (1887). Über die integrale des vielkörper-problems. *Acta Math.*, 11:25–96.

Bruzual, A. G. (2010). Star clusters as simple stellar populations. *Philosophical Transactions of the Royal Society of London Series A*, 368:783–799.

Carballo-Bello, J. A., Gieles, M., Sollima, A., Koposov, S., Martínez-Delgado, D., and Peñarrubia, J. (2012). Outer density profiles of 19 Galactic globular clusters from deep and wide-field imaging. *MNRAS*, 419:14–28.

Carretta, E., Bragaglia, A., Gratton, R., D'Orazi, V., and Lucatello, S. (2009). Intrinsic iron spread and a new metallicity scale for globular clusters. *A&A*, 508:695–706.

Chatterjee, S., Rasio, F. A., Sills, A., and Glebbeek, E. (2013). Stellar Collisions and Blue Straggler Stars in Dense Globular Clusters. *ApJ*, 777:106.

Chatterjee, S., Rodriguez, C. L., and Rasio, F. A. (2017). Binary Black Holes in Dense Star Clusters: Exploring the Theoretical Uncertainties. *ApJ*, 834:68.

Chernoff, D. F. and Weinberg, M. D. (1990). Evolution of globular clusters in the Galaxy. *ApJ*, 351:121–156.

Choi, J., Dotter, A., Conroy, C., Cantiello, M., Paxton, B., and Johnson, B. D. (2016). Mesa Isochrones and Stellar Tracks (MIST). I. Solar-scaled Models. *ApJ*, 823:102.

Chomiuk, L., Strader, J., Maccarone, T. J., Miller-Jones, J. C. A., Heinke, C., Noyola, E., Seth, A. C., and Ransom, S. (2013). A Radio-selected Black Hole X-Ray Binary Candidate in the Milky Way Globular Cluster M62. *ApJ*, 777:69.

Claydon, I., Gieles, M., and Zocchi, A. (2017). The properties of energetically unbound stars in stellar clusters. *MNRAS*, 466:3937–3950.

Clough, S. A., Iacono, M. J., and Moncet, J.-L. (1992). Line-by-Line Calculations of Atmospheric Fluxes and Cooling Rates: Application to Water Vapor. *J. Geophys. Res.*, 97:15.

Clough, S. A., Shephard, M. W., Mlawer, E. J., Delamere, J. S., Iacono, M. J., Cady-Pereira, K., Boukabara, S., and Brown, P. D. (2005). Atmospheric radiative transfer modeling: a summary of the AER codes. *J. Quant. Spectrosc. Radiative Transfer*, 91:233–244.

Cohn, H. (1980). Late core collapse in star clusters and the gravothermal instability. *ApJ*, 242:765–771.

Contenta, F., Balbinot, E., Petts, J. A., Read, J. I., Gieles, M., Collins, M. L. M., Peñarrubia, J., Delorme, M., and Gualandris, A. (2018). Probing dark matter with star clusters: a dark matter core in the ultra- faint dwarf Eridanus II. *MNRAS*, 476:3124–3136.

Côté, P., Marzke, R. O., and West, M. J. (1998). The Formation of Giant Elliptical Galaxies and Their Globular Cluster Systems. *ApJ*, 501:554–570.

Cottaar, M. and Hénault-Brunet, V. (2014). Binary-corrected velocity dispersions from single- and multi-epoch radial velocities: massive stars in R136 as a test case. *A&A*, 562:A20.

Cottaar, M., Meyer, M. R., and Parker, R. J. (2012). Characterizing a cluster's dynamic state using a single epoch of radial velocities. *A&A*, 547:A35.

Da Costa, G. S. and Freeman, K. C. (1976). The structure and mass function of the globular cluster M3. *ApJ*, 206:128–137.

Dalessandro, E., Ferraro, F. R., Massari, D., Lanzoni, B., Miocchi, P., and Beccari, G. (2015). No Evidence of Mass Segregation in the Low-mass Galactic Globular Cluster NGC 6101. *ApJ*, 810:40.

Davies, M. B. and Hansen, B. M. S. (1998). Neutron star retention and millisecond pulsar production in globular clusters. *MNRAS*, 301:15–24.

Davoust, E. (1977). Analytical models for spherical stellar systems. *A&A*, 61:391–396.

De Marco, O., Shara, M. M., Zurek, D., Ouellette, J. A., Lanz, T., Saffer, R. A., and Sepinsky, J. F. (2005). A Spectroscopic Analysis of Blue Stragglers, Horizontal Branch Stars, and Turnoff Stars in Four Globular Clusters. *ApJ*, 632:894–919.

Dejonghe, H. (1987). A completely analytical family of anisotropic Plummer models. *MNRAS*, 224:13–39.

Djorgovski, S. and King, I. R. (1986). A preliminary survey of collapsed cores in globular clusters. *ApJ*, 305:L61–L65.

Dolphin, A. E. (2000). WFPC2 Stellar Photometry with HSTPHOT. *PASP*, 112:1383–1396.

Dotter, A. (2016). MESA Isochrones and Stellar Tracks (MIST) 0: Methods for the Construction of Stellar Isochrones. *ApJS*, 222:8.

Dotter, A., Chaboyer, B., Jevremović, D., Baron, E., Ferguson, J. W., Sarajedini, A., and Anderson, J. (2007). The ACS Survey of Galactic Globular Clusters. II. Stellar Evolution Tracks, Isochrones, Luminosity Functions, and Synthetic Horizontal-Branch Models. *AJ*, 134:376–390.

Dotter, A., Chaboyer, B., Jevremović, D., Kostov, V., Baron, E., and Ferguson, J. W. (2008). The Dartmouth Stellar Evolution Database. *ApJS*, 178:89–101.

Dotter, A., Sarajedini, A., Anderson, J., Aparicio, A., Bedin, L. R., Chaboyer, B., Majewski, S., Marín-Franch, A., Milone, A., Paust, N., Piotto, G., Reid, I. N., Rosenberg, A., and Siegel, M. (2010). The ACS Survey of Galactic Globular Clusters. IX. Horizontal Branch Morphology and the Second Parameter Phenomenon. *ApJ*, 708:698–716.

Drukier, G. A. (1996a). On the Retention of Globular Cluster Neutron Stars. In Hut, P. and Makino, J., editors, *Dynamical Evolution of Star Clusters: Confrontation of Theory and Observations*, volume 174 of *IAU Symposium*, page 347.

Drukier, G. A. (1996b). Retention fractions for globular cluster neutron stars. *MNRAS*, 280:498–514.

Dunlop, J. (1828). A Catalogue of Nebulae and Clusters of Stars in the Southern Hemisphere, Observed at Paramatta in New South Wales. *Philosophical Transactions of the Royal Society of London Series I*, 118:113–151.

Eddington, A. S. (1915). The dynamics of a globular stellar system. *MNRAS*, 75:366–376.

Einstein, A. (1916). Näherungsweise Integration der Feldgleichungen der Gravitation. *Sitzungsberichte der Königlich Preußischen Akademie der Wissenschaften (Berlin), Seite 688-696.*

Elmegreen, B. G. (2008). Variations in Stellar Clustering with Environment: Dispersed Star Formation and the Origin of Faint Fuzzies. *ApJ*, 672:1006–1012.

Elmegreen, B. G. and Efremov, Y. N. (1997). A Universal Formation Mechanism for Open and Globular Clusters in Turbulent Gas. *ApJ*, 480:235–245.

Evans, D. W., Riello, M., De Angeli, F., Carrasco, J. M., Montegriffo, P., Fabricius, C., Jordi, C., Palaversa, L., Diener, C., Busso, G., Cacciari, C., and van Leeuwen, F. (2018). Gaia Data Release 2: Photometric content and validation. *ArXiv e-prints*.

Fiorentino, G., Lanzoni, B., Dalessandro, E., Ferraro, F. R., Bono, G., and Marconi, M. (2014). Blue Straggler Masses from Pulsation Properties. I. The Case of NGC 6541. *ApJ*, 783:34.

Foreman-Mackey, D., Hogg, D. W., Lang, D., and Goodman, J. (2013). emcee: The MCMC Hammer. *PASP*, 125:306–312.

Freeman, K. and Bland-Hawthorn, J. (2002). The New Galaxy: Signatures of Its Formation. *Annual Review of Astronomy and Astrophysics*, 40:487–537.

Freeman, K. C. (1993). Globular Clusters and Nucleated Dwarf Ellipticals. In *The Globular Cluster-Galaxy Connection*, volume 48, page 608.

Fregeau, J. M., Joshi, K. J., Portegies Zwart, S. F., and Rasio, F. A. (2002). Mass Segregation in Globular Clusters. *ApJ*, 570:171–183.

Friel, E. D. (1995). The Old Open Clusters Of The Milky Way. *Annual Review of Astronomy and Astrophysics*, 33:381–414.

Fryer, C. L., Belczynski, K., Wiktorowicz, G., Dominik, M., Kalogera, V., and Holz, D. E. (2012). Compact Remnant Mass Function: Dependence on the Explosion Mechanism and Metallicity. *ApJ*, 749:91.

Fryer, C. L. and Kalogera, V. (2001). Theoretical Black Hole Mass Distributions. *ApJ*, 554:548–560.

Fukushige, T. and Heggie, D. C. (2000). The time-scale of escape from star clusters. *MNRAS*, 318:753–761.

Gaia Collaboration, Brown, A. G. A., Vallenari, A., Prusti, T., de Bruijne, J. H. J., Mignard, F., Drimmel, R., Babusiaux, C., Bailer-Jones, C. A. L., Bastian, U., and et al. (2016a). Gaia Data Release 1. Summary of the astrometric, photometric, and survey properties. *A&A*, 595:A2.

Gaia Collaboration, Helmi, A., van Leeuwen, F., McMillan, P. J., Massari, D., Antoja, T., Robin, A., Lindegren, L., Bastian, U., and co-authors, . (2018). Gaia Data Release 2: Kinematics of globular clusters and dwarf galaxies around the Milky Way. *ArXiv e-prints*.

Gaia Collaboration, Prusti, T., de Bruijne, J. H. J., Brown, A. G. A., Vallenari, A., Babusiaux, C., Bailer-Jones, C. A. L., Bastian, U., Biermann, M., Evans, D. W., and et al. (2016b). The Gaia mission. *A&A*, 595:A1.

Gaia Collaboration, Prusti, T., de Bruijne, J. H. J., Brown, A. G. A., Vallenari, A., Babusiaux, C., Bailer-Jones, C. A. L., Bastian, U., Biermann, M., Evans, D. W., and et al. (2016c). The Gaia mission. *A&A*, 595:A1.

Geha, M., Brown, T. M., Tumlinson, J., Kalirai, J. S., Simon, J. D., Kirby, E. N., VandenBerg, D. A., Muñoz, R. R., Avila, R. J., Guhathakurta, P., and Ferguson, H. C. (2013). The Stellar Initial Mass Function of Ultra-faint Dwarf Galaxies: Evidence for IMF Variations with Galactic Environment. *ApJ*, 771:29.

Geisler, D., Piatti, A. E., Claria, J. J., and Minniti, D. (1995). Lower metallicity of the Galactic globular cluster system: Calcium triplet spectroscopy of metal-poor globular cluster giants. *AJ*, 109:605–617.

Gieles, M., Balbinot, E., Yaaqib, R. I. S. M., Hénault-Brunet, V., Zocchi, A., Peuten, M., and Jonker, P. G. (2018). Mass models of NGC 6624 without an intermediate-mass black hole. *MNRAS*, 473:4832–4839.

Gieles, M., Baumgardt, H., Heggie, D. C., and Lamers, H. J. G. L. M. (2010). On the mass-radius relation of hot stellar systems. *MNRAS*, 408:L16–L20.

Gieles, M., Heggie, D. C., and Zhao, H. (2011). The life cycle of star clusters in a tidal field. *MNRAS*, 413:2509–2524.

Gieles, M. and Zocchi, A. (2015). A family of lowered isothermal models. *MNRAS*, 454:576–592.

Giersz, M. and Heggie, D. C. (1994). Statistics of N-Body Simulations - Part One - Equal Masses Before Core Collapse. *MNRAS*, 268:257.

Giersz, M. and Heggie, D. C. (1996). Statistics of N-body simulations - III. Unequal masses. *MNRAS*, 279:1037–1056.

Giersz, M. and Heggie, D. C. (1997). Statistics of N-body simulations - IV. Unequal masses with a tidal field. *MNRAS*, 286:709–731.

Giersz, M. and Heggie, D. C. (2011). Monte Carlo simulations of star clusters - VII. The globular cluster 47 Tuc. *MNRAS*, 410:2698–2713.

Giersz, M., Heggie, D. C., Hurley, J. R., and Hypki, A. (2013). MOCCA code for star cluster simulations - II. Comparison with N-body simulations. *MNRAS*, 431:2184–2199.

Giesers, B., Dreizler, S., Husser, T.-O., Kamann, S., Anglada Escudé, G., Brinchmann, J., Carollo, C. M., Roth, M. M., Weilbacher, P. M., and Wisotzki, L. (2018). A detached stellar-mass black hole candidate in the globular cluster NGC 3201. *MNRAS*, 475:L15–L19.

Gill, M., Trenti, M., Miller, M. C., van der Marel, R., Hamilton, D., and Stiavelli, M. (2008). Intermediate-Mass Black Hole Induced Quenching of Mass Segregation in Star Clusters. *ApJ*, 686:303–309.

Gilliland, R. L., Bono, G., Edmonds, P. D., Caputo, F., Cassisi, S., Petro, L. D., Saha, A., and Shara, M. M. (1998). Oscillating Blue Stragglers in the Core of 47 Tucanae. *ApJ*, 507:818–845.

Goerdt, T., Moore, B., Read, J. I., Stadel, J., and Zemp, M. (2006). Does the Fornax dwarf spheroidal have a central cusp or core? *MNRAS*, 368:1073–1077.

Goldsbury, R., Richer, H. B., Anderson, J., Dotter, A., Sarajedini, A., and Woodley, K. (2010). The ACS Survey of Galactic Globular Clusters. X. New Determinations of Centers for 65 Clusters. *AJ*, 140:1830–1837.

Gomez-Leyton, Y. J. and Velazquez, L. (2014). Truncated γ-exponential models for tidal stellar systems. *Journal of Statistical Mechanics: Theory and Experiment*, 4:6.

Goodman, J. and Hut, P. (1989). Primordial binaries and globular cluster evolution. *Nature*, 339:40–42.

Goodman, J. and Weare, J. (2010). Ensemble samplers with affine invariance. *Communications in Applied Mathematics and Computational science*, 5:65–80.

Gratton, R., Sneden, C., and Carretta, E. (2004). Abundance Variations Within Globular Clusters. *ARA&A*, 42:385–440.

Gratton, R. G., Carretta, E., and Bragaglia, A. (2012). Multiple populations in globular clusters. Lessons learned from the Milky Way globular clusters. *A&ARv*, 20:50.

Gunn, J. E. and Griffin, R. F. (1979). Dynamical studies of globular clusters based on photoelectric radial velocities of individual stars. I - M3. *AJ*, 84:752–773.

Hansen, B. M. S. and Phinney, E. S. (1997). The pulsar kick velocity distribution. *MNRAS*, 291:569.

Harris, W. E. (1991). Globular cluster systems in galaxies beyond the Local Group. *ARA&A*, 29:543–579.

Harris, W. E. (1996). A Catalog of Parameters for Globular Clusters in the Milky Way. *AJ*, 112:1487.

Hawking, S. W. (1975). Particle creation by black holes. *Communications in Mathematical Physics*, 43:199–220.

Heggie, D. and Hut, P. (2003). *The Gravitational Million-Body Problem: A Multidisciplinary Approach to Star Cluster Dynamics*. Cambridge University Press.

Heggie, D. C. (1975). Binary evolution in stellar dynamics. *MNRAS*, 173:729–787.

Heggie, D. C. (2014). Towards an N-body model for the globular cluster M4. *MNRAS*, 445:3435–3443.

Heggie, D. C. and Giersz, M. (2008). Monte Carlo simulations of star clusters - V. The globular cluster M4. *MNRAS*, 389:1858–1870.

Heggie, D. C. and Giersz, M. (2014). MOCCA code for star cluster simulations - III. Stellar-mass black holes in the globular cluster M22. *MNRAS*, 439:2459–2467.

Heggie, D. C., Trenti, M., and Hut, P. (2006). Star clusters with primordial binaries - I. Dynamical evolution of isolated models. *MNRAS*, 368:677–689.

Hénon, M. (1959). L'amas isochrone: I. *Annales d'Astrophysique*, 22:126.

Hénon, M. (1961). Sur l'évolution dynamique des amas globulaires. *Annales d'Astrophysique*, 24:369.

Hénon, M. (1965). Sur l'évolution dynamique des amas globulaires. II. Amas isol&eacute. *Annales d'Astrophysique*, 28:62.

Henon, M. (1969). Rates of Escape from Isolated Clusters with an Arbitrary Mass Distribution. *A&A*, 2:151.

Hessels, J., Possenti, A., Bailes, M., Bassa, C., Freire, P. C. C., Lorimer, D. R., Lynch, R., Ransom, S. M., and Stairs, I. H. (2015). Pulsars in Globular Clusters with the SKA. *Advancing Astrophysics with the Square Kilometre Array (AASKA14)*, page 47.

Hessels, J. W. T., Ransom, S. M., Stairs, I. H., Freire, P. C. C., Kaspi, V. M., and Camilo, F. (2006). A Radio Pulsar Spinning at 716 Hz. *Science*, 311:1901–1904.

Holmberg, E. (1941). On the Clustering Tendencies among the Nebulae. II. a Study of Encounters Between Laboratory Models of Stellar Systems by a New Integration Procedure. *ApJ*, 94:385.

Hurley, J. R., Pols, O. R., Aarseth, S. J., and Tout, C. A. (2005). A complete N-body model of the old open cluster M67. *MNRAS*, 363:293–314.

Hurley, J. R., Pols, O. R., and Tout, C. A. (2000). Comprehensive analytic formulae for stellar evolution as a function of mass and metallicity. *MNRAS*, 315:543–569.

Hurley, J. R., Tout, C. A., and Pols, O. R. (2002). Evolution of binary stars and the effect of tides on binary populations. *MNRAS*, 329:897–928.

Husser, T.-O., Kamann, S., Dreizler, S., Wendt, M., Wulff, N., Bacon, R., Wisotzki, L., Brinchmann, J., Weilbacher, P. M., Roth, M. M., and Monreal-Ibero, A. (2016). MUSE crowded field 3D spectroscopy of over 12 000 stars in the globular cluster NGC 6397. I. The first comprehensive HRD of a globular cluster. *A&A*, 588:A148.

Husser, T.-O. and Ulbrich, K. (2014). Using a model for telluric absorption in full-spectrum fits. In *Astronomical Society of India Conference Series*, volume 11 of *Astronomical Society of India Conference Series*.

Husser, T.-O., Wende-von Berg, S., Dreizler, S., Homeier, D., Reiners, A., Barman, T., and Hauschildt, P. H. (2013). A new extensive library of PHOENIX stellar atmospheres and synthetic spectra. *A&A*, 553:A6.

Hut, P., McMillan, S., Goodman, J., Mateo, M., Phinney, E. S., Pryor, C., Richer, H. B., Verbunt, F., and Weinberg, M. (1992). Binaries in globular clusters. *PASP*, 104:981–1034.

Hut, P., Murphy, B. W., and Verbunt, F. (1991). The formation rate of low-mass X-ray binaries in globular clusters. *A&A*, 241:137–141.

Ibata, R., Nipoti, C., Sollima, A., Bellazzini, M., Chapman, S. C., and Dalessandro, E. (2013). Do globular clusters possess dark matter haloes? A case study in NGC 2419. *MNRAS*, 428:3648–3659.

Illingworth, G. and King, I. R. (1977). Dynamical models for M15 without a black hole. *ApJ*, 218:L109–L112.

Ivanova, N., Fregeau, J. M., and Rasio, F. A. (2005). Binary Evolution and Neutron Stars in Globular Clusters. In Rasio, F. A. and Stairs, I. H., editors, *Binary Radio Pulsars*, volume 328 of *Astronomical Society of the Pacific Conference Series*, page 231.

Ivanova, N., Heinke, C. O., and Rasio, F. (2008a). Neutron Stars in Globular Clusters. In Vesperini, E., Giersz, M., and Sills, A., editors, *Dynamical Evolution of Dense Stellar Systems*, volume 246 of *IAU Symposium*, pages 316–320.

Ivanova, N., Heinke, C. O., Rasio, F. A., Belczynski, K., and Fregeau, J. M. (2008b). Formation and evolution of compact binaries in globular clusters - II. Binaries with neutron stars. *MNRAS*, 386:553–576.

Jacobi, P. M. (1843). Sur l'élimination des noeuds dans le problème des trois corps. *Astronomische Nachrichten*, 20(6):81–98.

Janka, H.-T. (2013). Natal kicks of stellar mass black holes by asymmetric mass ejection in fallback supernovae. *MNRAS*, 434:1355–1361.

Johnston, K. V., Sigurdsson, S., and Hernquist, L. (1999). Measuring mass-loss rates from Galactic satellites. *MNRAS*, 302:771–789.

Kamann, S., Husser, T.-O., Brinchmann, J., Emsellem, E., Weilbacher, P. M., Wisotzki, L., Wendt, M., Krajnović, D., Roth, M. M., Bacon, R., and Dreizler, S. (2016). MUSE crowded field 3D spectroscopy of over 12 000 stars in the globular cluster NGC 6397.

II. Probing the internal dynamics and the presence of a central black hole. *A&A*, 588:A149.

Kamann, S., Husser, T.-O., Dreizler, S., Emsellem, E., Weilbacher, P. M., Martens, S., Bacon, R., den Brok, M., Giesers, B., Krajnović, D., Roth, M. M., Wendt, M., and Wisotzki, L. (2018). A stellar census in globular clusters with MUSE: The contribution of rotation to cluster dynamics studied with 200 000 stars. *MNRAS*, 473:5591–5616.

Kamann, S., Wisotzki, L., and Roth, M. M. (2013). Resolving stellar populations with crowded field 3D spectroscopy. *A&A*, 549:A71.

King, I. (1962). The structure of star clusters. I. an empirical density law. *AJ*, 67:471.

King, I. R. (1966). The structure of star clusters. III. Some simple dynamical models. *AJ*, 71:64.

King, I. R., Sosin, C., and Cool, A. M. (1995). Mass Segregation in the Globular Cluster NGC 6397. *ApJ*, 452:L33.

Kinman, T. D. (1959). Globular clusters, II. The spectral types of individual stars and of the integrated light. *MNRAS*, 119:538.

Knigge, C., Leigh, N., and Sills, A. (2009). A binary origin for 'blue stragglers' in globular clusters. *Nature*, 457:288–290.

Koleva, M., Prugniel, P., Bouchard, A., and Wu, Y. (2009). ULySS: a full spectrum fitting package. *A&A*, 501:1269–1279.

Koposov, S. E., Rix, H.-W., and Hogg, D. W. (2010). Constraining the Milky Way Potential with a Six-Dimensional Phase-Space Map of the GD-1 Stellar Stream. *ApJ*, 712:260–273.

Kroupa, P. (2001). On the variation of the initial mass function. *MNRAS*, 322:231–246.

Kruijssen, J. M. D. (2009). The evolution of the stellar mass function in star clusters. *A&A*, 507:1409–1423.

Kulkarni, S. R., Hut, P., and McMillan, S. J. (1993). Stellar black holes in globular clusters. *Nature*, 364:421–423.

Küpper, A. H. W., Kroupa, P., Baumgardt, H., and Heggie, D. C. (2010). Tidal tails of star clusters. *MNRAS*, 401:105–120.

Lamers, H. J. G. L. M., Baumgardt, H., and Gieles, M. (2013). The evolution of the global stellar mass function of star clusters: an analytic description. *MNRAS*, 433:1378–1388.

Lee, H. M. and Goodman, J. (1995). Influence of the stellar mass function of the evaporation rate of tidally limited postcollapse globular clusters. *ApJ*, 443:109–116.

Lee, H. M. and Ostriker, J. P. (1987). The evolution and final disintegration of spherical stellar systems in a steady galactic tidal field. *ApJ*, 322:123–132.

Lindegren, L., Hernandez, J., Bombrun, A., Klioner, S., Bastian, U., Ramos-Lerate, M., de Torres, A., Steidelmuller, H., Stephenson, C., Hobbs, D., Lammers, U., Biermann, M., Geyer, R., Hilger, T., Michalik, D., Stampa, U., McMillan, P. J., Castaneda, J., Clotet, M., Comoretto, G., Davidson, M., Fabricius, C., Gracia, G., Hambly, N. C., Hutton, A., Mora, A., Portell, J., van Leeuwen, F., Abbas, U., Abreu, A., Altmann, M., Andrei, A., Anglada, E., Balaguer-Nunez, L., Barache, C., Becciani, U., Bertone, S., Bianchi, L., Bouquillon, S., Bourda, G., Brusemeister, T., Bucciarelli, B., Busonero, D., Buzzi, R., Cancelliere, R., Carlucci, T., Charlot, P., Cheek, N., Crosta, M., Crowley, C., de Bruijne, J., de Felice, F., Drimmel, R., Esquej, P., Fienga, A., Fraile, E., Gai, M., Garralda, N., Gonzalez-Vidal, J. J., Guerra, R., Hauser, M., Hofmann, W., Holl, B., Jordan, S., Lattanzi, M. G., Lenhardt, H., Liao, S., Licata, E., Lister, T., Loffler, W., Marchant, J., Martin-Fleitas, J.-M., Messineo, R., Mignard, F., Morbidelli, R., Poggio, E., Riva, A., Rowell, N., Salguero, E., Sarasso, M., Sciacca, E., Siddiqui, H., Smart, R. L., Spagna, A., Steele, I., Taris, F., Torra, J., van Elteren, A., van Reeven, W., and Vecchiato, A. (2018). Gaia Data Release 2: The astrometric solution. *ArXiv e-prints*.

Lovisi, L., Mucciarelli, A., Lanzoni, B., Ferraro, F. R., Gratton, R., Dalessandro, E., and Contreras Ramos, R. (2012). Chemical and Kinematical Properties of Blue Straggler Stars and Horizontal Branch Stars in NGC 6397. *ApJ*, 754:91.

Lupton, R. H., Gunn, J. E., and Griffin, R. F. (1987). Dynamical studies of globular clusters based on photoelectric radial velocities of individual stars and on the observed mass function. II - M13. *AJ*, 93:1114–1136.

Lützgendorf, N., Baumgardt, H., and Kruijssen, J. M. D. (2013). N-body simulations of globular clusters in tidal fields: Effects of intermediate-mass black holes. *A&A*, 558:A117.

Lynden-Bell, D. and Eggleton, P. P. (1980). On the consequences of the gravothermal catastrophe. *MNRAS*, 191:483–498.

Lynden-Bell, D. and Wood, R. (1968). The gravo-thermal catastrophe in isothermal spheres and the onset of red-giant structure for stellar systems. *MNRAS*, 138:495.

Maccarone, T. J., Kundu, A., Zepf, S. E., and Rhode, K. L. (2007). A black hole in a globular cluster. *Nature*, 445:183–185.

Mackey, A. D. and Gilmore, G. F. (2004). Comparing the properties of local globular cluster systems: implications for the formation of the Galactic halo. *MNRAS*, 355:504–534.

Mackey, A. D., Wilkinson, M. I., Davies, M. B., and Gilmore, G. F. (2008). Black holes and core expansion in massive star clusters. *MNRAS*, 386:65–95.

Makino, J. (1991). Optimal Order and Time-Step Criterion for Aarseth-Type N-Body Integrators. *ApJ*, 369:200.

Makino, J. and Aarseth, S. J. (1992). On a Hermite Integrator with Ahmad-Cohen Scheme for Gravitational Many- Body Problems. *Publications of the Astronomical Society of Japan*, 44:141–151.

Mandel, I. (2016). Estimates of black hole natal kick velocities from observations of low-mass X-ray binaries. *MNRAS*, 456:578–581.

Marconi, G., Andreuzzi, G., Pulone, L., Cassisi, S., Testa, V., and Buonanno, R. (2001). Mass segregation of different populations inside the cluster NGC 6101. *A&A*, 380:478–489.

Marigo, P., Girardi, L., Bressan, A., Rosenfield, P., Aringer, B., Chen, Y., Dussin, M., Nanni, A., Pastorelli, G., Rodrigues, T. S., Trabucchi, M., Bladh, S., Dalcanton, J., Groenewegen, M. A. T., Montalbán, J., and Wood, P. R. (2017). A New Generation of PARSEC-COLIBRI Stellar Isochrones Including the TP-AGB Phase. *ApJ*, 835:77.

Marín-Franch, A., Aparicio, A., Piotto, G., Rosenberg, A., Chaboyer, B., Sarajedini, A., Siegel, M., Anderson, J., Bedin, L. R., Dotter, A., Hempel, M., King, I., Majewski, S., Milone, A. P., Paust, N., and Reid, I. N. (2009). The ACS Survey of Galactic Globular Clusters. VII. Relative Ages. *ApJ*, 694:1498–1516.

Martin, N. F., Ibata, R. A., Bellazzini, M., Irwin, M. J., Lewis, G. F., and Dehnen, W. (2004). A dwarf galaxy remnant in Canis Major: the fossil of an in-plane accretion on to the Milky Way. *MNRAS*, 348:12–23.

McLaughlin, D. E. (2003). Fitting Dynamical Models to Observations. In Piotto, G., Meylan, G., Djorgovski, S. G., and Riello, M., editors, *New Horizons in Globular Cluster Astronomy*, volume 296 of *Astronomical Society of the Pacific Conference Series*, page 101.

McLaughlin, D. E., Harris, W. E., and Hanes, D. A. (1994). The spatial structure of the M87 globular cluster system. *ApJ*, 422:486–507.

McLaughlin, D. E. and van der Marel, R. P. (2005). Resolved Massive Star Clusters in the Milky Way and Its Satellites: Brightness Profiles and a Catalog of Fundamental Parameters. *ApJS*, 161:304–360.

Merritt, D. (1981). Two-component stellar systems in thermal and dynamical equilibrium. *AJ*, 86:318–324.

Merritt, D., Piatek, S., Portegies Zwart, S., and Hemsendorf, M. (2004). Core Formation by a Population of Massive Remnants. *ApJ*, 608:L25–L28.

Meylan, G. (1987). Studies of dynamical properties of globular clusters. III - Anisotropy in Omega Centauri. *A&A*, 184:144–154.

Meylan, G. and Heggie, D. C. (1997). Internal dynamics of globular clusters. *A&ARv*, 8:1–143.

Meylan, G. and Mayor, M. (1991). Studies of dynamical properties of globular clusters. VI - The high-concentration cluster NGC 6397. *A&A*, 250:113–126.

Meylan, G., Mayor, M., Duquennoy, A., and Dubath, P. (1995). Central velocity dispersion in the globular cluster ω Centauri. *A&A*, 303:761.

Meza, A., Navarro, J. F., Abadi, M. G., and Steinmetz, M. (2005). Accretion relics in the solar neighbourhood: debris from ωCen's parent galaxy. *MNRAS*, 359:93–103.

Michie, R. W. (1963). On the distribution of high energy stars in spherical stellar systems. *MNRAS*, 125:127.

Mikkola, S. and Aarseth, S. J. (1990). A chain regularization method for the few-body problem. *Celestial Mechanics and Dynamical Astronomy*, 47:375–390.

Mikkola, S. and Aarseth, S. J. (1993). An Implementation of N-Body Chain Regularization. *Celestial Mechanics and Dynamical Astronomy*, 57:439–459.

Mikkola, S. and Aarseth, S. J. (1996). A Slow-down Treatment for Close Binaries. *Celestial Mechanics and Dynamical Astronomy*, 64:197–208.

Mikkola, S. and Aarseth, S. J. (1998). An efficient integration method for binaries in N-body simulations. *New Astron.*, 3:309–320.

Miller-Jones, J. C. A., Strader, J., Heinke, C. O., Maccarone, T. J., van den Berg, M., Knigge, C., Chomiuk, L., Noyola, E., Russell, T. D., Seth, A. C., and Sivakoff, G. R. (2015). Deep radio imaging of 47 Tuc identifies the peculiar X-ray source X9 as a new black hole candidate. *MNRAS*, 453:3918–3931.

Milone, A. P., Marino, A. F., Dotter, A., Norris, J. E., Jerjen, H., Piotto, G., Cassisi, S., Bedin, L. R., Recio Blanco, A., Sarajedini, A., Asplund, M., Monelli, M., and Aparicio, A. (2014). Global and Nonglobal Parameters of Horizontal-branch Morphology of Globular Clusters. *ApJ*, 785:21.

Milone, A. P., Piotto, G., Bedin, L. R., Aparicio, A., Anderson, J., Sarajedini, A., Marino, A. F., Moretti, A., Davies, M. B., Chaboyer, B., Dotter, A., Hempel, M., Marín-Franch, A., Majewski, S., Paust, N. E. Q., Reid, I. N., Rosenberg, A., and Siegel, M. (2012). The ACS survey of Galactic globular clusters. XII. Photometric binaries along the main sequence. *A&A*, 540:A16.

Minniti, D., Contreras Ramos, R., Alonso-García, J., Anguita, T., Catelan, M., Gran, F., Motta, V., Muro, G., Rojas, K., and Saito, R. K. (2015). VVV Survey Observations of a Microlensing Stellar Mass Black Hole Candidate in the Field of the Globular Cluster NGC 6553. *ApJ*, 810:L20.

Miocchi, P. (2006). Central energy equipartition in multimass models of globular clusters. *MNRAS*, 366:227–234.

Miocchi, P. (2007). The presence of intermediate-mass black holes in globular clusters and their connection with extreme horizontal branch stars. *MNRAS*, 381:103–116.

Monaco, L., Pancino, E., Ferraro, F. R., and Bellazzini, M. (2004). Wide-field photometry of the Galactic globular cluster M22. *MNRAS*, 349:1278–1290.

Morscher, M., Pattabiraman, B., Rodriguez, C., Rasio, F. A., and Umbreit, S. (2015). The Dynamical Evolution of Stellar Black Holes in Globular Clusters. *ApJ*, 800:9.

Morscher, M., Umbreit, S., Farr, W. M., and Rasio, F. A. (2013). Retention of Stellar-mass Black Holes in Globular Clusters. *ApJ*, 763:L15.

Newton, I. (1687). *Philosophiae Naturalis Principia Mathematica. Auctore Js. Newton*. Jussu Societatis Regiae ac Typis Josephi Streater.

Nitadori, K. and Aarseth, S. J. (2012). Accelerating NBODY6 with graphics processing units. *MNRAS*, 424:545–552.

Oort, J. H. and van Herk, G. (1959). Structure and dynamics of Messier 3. *Bull. Astron. Inst. Netherlands*, 14:299.

Oosterhoff, P. T. (1939). Some remarks on the variable stars in globular clusters. *The Observatory*, 62:104–109.

O'Shaughnessy, R., Gerosa, D., and Wysocki, D. (2017). Inferences about Supernova Physics from Gravitational-Wave Measurements: GW151226 Spin Misalignment as an Indicator of Strong Black-Hole Natal Kicks. *Phys. Rev. Lett.*, 119:011101.

Patruno, A., Portegies Zwart, S., Dewi, J., and Hopman, C. (2006). The ultraluminous X-ray source in M82: an intermediate-mass black hole with a giant companion. *MNRAS*, 370:L6–L9.

Paust, N. E. Q., Reid, I. N., Piotto, G., Aparicio, A., Anderson, J., Sarajedini, A., Bedin, L. R., Chaboyer, B., Dotter, A., Hempel, M., Majewski, S., Marín-Franch, A., Milone, A., Rosenberg, A., and Siegel, M. (2010). The ACS Survey of Galactic Globular Clusters. VIII. Effects of Environment on Globular Cluster Global Mass Functions. *AJ*, 139:476–491.

Pavlík, V., Jeřábková, T., Kroupa, P., and Baumgardt, H. (2018). The black hole retention fraction in star clusters. *ArXiv e-prints*, page arXiv:1806.05192.

Paxton, B., Bildsten, L., Dotter, A., Herwig, F., Lesaffre, P., and Timmes, F. (2011). Modules for Experiments in Stellar Astrophysics (MESA). *ApJS*, 192:3.

Paxton, B., Cantiello, M., Arras, P., Bildsten, L., Brown, E. F., Dotter, A., Mankovich, C., Montgomery, M. H., Stello, D., Timmes, F. X., and Townsend, R. (2013). Modules for Experiments in Stellar Astrophysics (MESA): Planets, Oscillations, Rotation, and Massive Stars. *ApJS*, 208:4.

Paxton, B., Marchant, P., Schwab, J., Bauer, E. B., Bildsten, L., Cantiello, M., Dessart, L., Farmer, R., Hu, H., Langer, N., Townsend, R. H. D., Townsley, D. M., and Timmes, F. X. (2015). Modules for Experiments in Stellar Astrophysics (MESA): Binaries, Pulsations, and Explosions. *ApJS*, 220:15.

Peuten, M., Zocchi, A., Gieles, M., Gualandris, A., and Hénault-Brunet, V. (2016). A stellar-mass black hole population in the globular cluster NGC 6101? *MNRAS*, 462:2333–2342.

Peuten, M., Zocchi, A., Gieles, M., and Hénault-Brunet, V. (2017). Testing lowered isothermal models with direct N-body simulations of globular clusters - II. Multimass models. *MNRAS*, 470:2736–2761.

Pfahl, E., Rappaport, S., and Podsiadlowski, P. (2002). A Comprehensive Study of Neutron Star Retention in Globular Clusters. *ApJ*, 573:283–305.

Piotto, G. (2010). Observational Evidence of Multiple Stellar Populations in Star Clusters. *Publication of Korean Astronomical Society*, 25:91–99.

Piotto, G. and Zoccali, M. (1999). HST luminosity functions of the globular clusters M10, M22, and M55. A comparison with other clusters. *A&A*, 345:485–498.

Plummer, H. C. (1911). On the problem of distribution in globular star clusters. *MNRAS*, 71:460–470.

Podsiadlowski, P., Pfahl, E., and Rappaport, S. (2005). Neutron-Star Birth Kicks. In Rasio, F. A. and Stairs, I. H., editors, *Binary Radio Pulsars*, volume 328 of *Astronomical Society of the Pacific Conference Series*, page 327.

Poincaré, H. (1892). *Les methodes nouvelles de la mecanique celeste*. Paris, Gauthier-Villars et fils, 1892-99.

Polyachenko, V. L. and Shukhman, I. G. (1981). General Models of Collisionless Spherically Symmetric Stellar Systems - a Stability Analysis. *Soviet Ast.*, 25:533.

Portegies Zwart, S. F. and McMillan, S. L. W. (2000). Black Hole Mergers in the Universe. *ApJ*, 528:L17–L20.

Portegies Zwart, S. F., McMillan, S. L. W., and Gieles, M. (2010). Young Massive Star Clusters. *Annual Review of Astronomy and Astrophysics*, 48:431–493.

Prince, T. A., Anderson, S. B., Kulkarni, S. R., and Wolszczan, A. (1991). Timing observations of the 8 hour binary pulsar 2127 + 11C in the globular cluster M15. *ApJ*, 374:L41–L44.

Pryor, C., Hartwick, F. D. A., McClure, R. D., Fletcher, J. M., and Kormendy, J. (1986). Dynamics of the globular cluster M2 (NGC 7089). *AJ*, 91:546–556.

Pryor, C. and Meylan, G. (1993). Velocity Dispersions for Galactic Globular Clusters. In Djorgovski, S. G. and Meylan, G., editors, *Structure and Dynamics of Globular Clusters*, volume 50 of *Astronomical Society of the Pacific Conference Series*, page 357.

Raghavan, D., McAlister, H. A., Henry, T. J., Latham, D. W., Marcy, G. W., Mason, B. D., Gies, D. R., White, R. J., and ten Brummelaar, T. A. (2010). A Survey of Stellar Families: Multiplicity of Solar-type Stars. *ApJS*, 190:1–42.

Rappenglück, M. (1997). The Pleiades in the "Salle des Taureaux", grotte de Lascaux. Does a rock picture in the cave of Lascaux show the open star cluster of the Pleiades at the Magdalénien era (ca 15.300 BC?". In *Astronomy and Culture*, pages 217–225.

Reggiani, M. and Meyer, M. R. (2013). Universality of the companion mass-ratio distribution. *A&A*, 553:A124.

Rejkuba, M. (2012). Globular cluster luminosity function as distance indicator. *Ap&SS*, 341:195–206.

Renaud, F., Agertz, O., and Gieles, M. (2017). The origin of the Milky Way globular clusters. *MNRAS*, 465:3622–3636.

Renzini, A. and Fusi Pecci, F. (1988). Tests of evolutionary sequences using color-magnitude diagrams of globular clusters. *Annual Review of Astronomy and Astrophysics*, 26:199–244.

Repetto, S., Davies, M. B., and Sigurdsson, S. (2012). Investigating stellar-mass black hole kicks. *MNRAS*, 425:2799–2809.

Repetto, S., Igoshev, A. P., and Nelemans, G. (2017). The Galactic distribution of X-ray binaries and its implications for compact object formation and natal kicks. *MNRAS*, 467:298–310.

Richer, H. B. and Fahlman, G. G. (1989). Star counts in the globular cluster M71. *ApJ*, 339:178–194.

Richer, H. B., Fahlman, G. G., Brewer, J., Davis, S., Kalirai, J., Stetson, P. B., Hansen, B. M. S., Rich, R. M., Ibata, R. A., Gibson, B. K., and Shara, M. (2004). Hubble Space Telescope Observations of the Main Sequence of M4. *AJ*, 127:2771–2792.

Richer, H. B., Goldsbury, R., Heyl, J., Hurley, J., Dotter, A., Kalirai, J. S., Woodley, K. A., Fahlman, G. G., Rich, R. M., and Shara, M. M. (2013). Comparing the White Dwarf Cooling Sequences in 47 Tuc and NGC 6397. *ApJ*, 778:104.

Rieder, S., Ishiyama, T., Langelaan, P., Makino, J., McMillan, S. L. W., and Portegies Zwart, S. (2013). Evolution of star clusters in a cosmological tidal field. *MNRAS*, 436:3695–3706.

Riello, M., De Angeli, F., Evans, D. W., Busso, G., Hambly, N. C., Davidson, M., Burgess, P. W., Montegriffo, P., Osborne, P. J., Kewley, A., Carrasco, J. M., Fabricius, C., Jordi, C., Cacciari, C., van Leeuwen, F., and Holland, G. (2018). Gaia Data Release 2: processing of the photometric data. *ArXiv e-prints*.

Roberts, T. P., Fabbiano, G., Luo, B., Kim, D. W., Strader, J., Middleton, M. J., Brodie, J. P., Fragos, T., Gallagher, J. S., Kalogera, V., King, A. R., and Zezas, A. (2012). A Variable Ultraluminous X-Ray Source in a Globular Cluster in NGC 4649. *ApJ*, 760:135.

Rodriguez, C. L., Chatterjee, S., and Rasio, F. A. (2016a). Binary black hole mergers from globular clusters: Masses, merger rates, and the impact of stellar evolution. *Phys. Rev. D*, 93(8):084029.

Rodriguez, C. L., Morscher, M., Wang, L., Chatterjee, S., Rasio, F. A., and Spurzem, R. (2016b). Million-body star cluster simulations: comparisons between Monte Carlo and direct N-body. *MNRAS*, 463:2109–2118.

Sánchez-Salcedo, F. J., Reyes-Iturbide, J., and Hernandez, X. (2006). An extensive study of dynamical friction in dwarf galaxies: the role of stars, dark matter, halo profiles and MOND. *MNRAS*, 370:1829–1840.

Sarajedini, A., Bedin, L. R., Chaboyer, B., Dotter, A., Siegel, M., Anderson, J., Aparicio, A., King, I., Majewski, S., Marín-Franch, A., Piotto, G., Reid, I. N., and Rosenberg, A. (2007). The ACS Survey of Galactic Globular Clusters. I. Overview and Clusters without Previous Hubble Space Telescope Photometry. *AJ*, 133:1658–1672.

Sarajedini, A. and Da Costa, G. S. (1991). CCD photometry of NGC 6101 - Another globular cluster with blue straggler stars. *AJ*, 102:628–641.

Shanahan, R. L. and Gieles, M. (2015). Biases in the inferred mass-to-light ratio of globular clusters: no need for variations in the stellar mass function. *MNRAS*, 448:L94–L98.

Shapley, H. (1918). Globular Clusters and the Structure of the Galactic System. *Publications of the Astronomical Society of the Pacific*, 30:42.

Shara, M. M., Saffer, R. A., and Livio, M. (1997). The First Direct Measurement of the Mass of a Blue Straggler in the Core of a Globular Cluster: BSS 19 in 47 Tucanae. *ApJ*, 489:L59–L62.

Sigurdsson, S. and Hernquist, L. (1993). Primordial black holes in globular clusters. *Nature*, 364:423–425.

Sigurdsson, S. and Phinney, E. S. (1993). Binary–Single Star Interactions in Globular Clusters. *ApJ*, 415:631.

Sigurdsson, S. and Phinney, E. S. (1995). Dynamics and Interactions of Binaries and Neutron Stars in Globular Clusters. *ApJS*, 99:609.

Sills, A., Glebbeek, E., Chatterjee, S., and Rasio, F. A. (2013). Mock Observations of Blue Stragglers in Globular Cluster Models. *ApJ*, 777:105.

Sippel, A. C. and Hurley, J. R. (2013). Multiple stellar-mass black holes in globular clusters: theoretical confirmation. *MNRAS*, 430:L30–L34.

Sohn, S. T., Watkins, L. L., Fardal, M. A., van der Marel, R. P., Deason, A. J., Besla, G., and Bellini, A. (2018). Absolute Hubble Space Telescope Proper Motion (HST-PROMO) of Distant Milky Way Globular Clusters: Galactocentric Space Velocities and the Milky Way Mass. *ApJ*, 862:52.

Sollima, A. and Baumgardt, H. (2017). The global mass functions of 35 Galactic globular clusters: I. Observational data and correlations with cluster parameters. *MNRAS*, 471:3668–3679.

Sollima, A., Baumgardt, H., Zocchi, A., Balbinot, E., Gieles, M., Hénault-Brunet, V., and Varri, A. L. (2015). Biases in the determination of dynamical parameters of star clusters: today and in the Gaia era. *MNRAS*, 451:2185–2197.

Sollima, A., Beccari, G., Ferraro, F. R., Fusi Pecci, F., and Sarajedini, A. (2007). The fraction of binary systems in the core of 13 low-density Galactic globular clusters. *MNRAS*, 380:781–791.

Sollima, A., Bellazzini, M., and Lee, J.-W. (2012). A Comparison between the Stellar and Dynamical Masses of Six Globular Clusters. *ApJ*, 755:156.

Sollima, A., Cignoni, M., Gratton, R. G., Tosi, M., Bragaglia, A., Lucatello, S., and Meurer, G. (2014). Resolved photometry of young massive clusters in the starburst galaxy NGC 4214. *MNRAS*, 437:1918–1929.

Sollima, A., Dalessandro, E., Beccari, G., and Pallanca, C. (2017). Testing multimass dynamical models of star clusters with real data: mass segregation in three Galactic globular clusters. *MNRAS*, 464:3871–3881.

Sollima, A., Lanzoni, B., Beccari, G., Ferraro, F. R., and Fusi Pecci, F. (2008). The correlation between blue straggler and binary fractions in the core of Galactic globular clusters. *A&A*, 481:701–704.

Sosin, C. (1997). Mass Segregation and Equipartition of Energy in Two Globular Clusters with Central Density Cusps. *AJ*, 114:1517.

Spitzer, Lyman, J. (1969). Equipartition and the Formation of Compact Nuclei in Spherical Stellar Systems. *ApJ*, 158:L139.

Spitzer, L. (1987). *Dynamical evolution of globular clusters*. Princeton, N.J. : Princeton University Press, c1987.

Spitzer, Jr., L. and Hart, M. H. (1971). Random Gravitational Encounters and the Evolution of Spherical Systems. I. Method. *ApJ*, 164:399.

Spitzer, Jr., L. and Shull, J. M. (1975). Random gravitational encounters and the evolution of spherical systems. VII - Systems with several mass groups. *ApJ*, 201:773–782.

Spurzem, R. (1999). Direct N-body Simulations. *Journal of Computational and Applied Mathematics*, 109:407–432.

Stiefel, E. and Kustaanheimo, P. (1965). Perturbation theory of kepler motion based on spinor regularization. *Journal für die reine und angewandte Mathematik*, 218:204–219.

Strader, J., Chomiuk, L., Maccarone, T. J., Miller-Jones, J. C. A., and Seth, A. C. (2012). Two stellar-mass black holes in the globular cluster M22. *Nature*, 490:71–73.

Sundman, K. F. (1913). Mémoire sur le problème des trois corps. *Acta Math.*, 36:105–179.

Takahashi, K. and Lee, H. M. (2000). Evolution of multimass globular clusters in the Galactic tidal field with the effects of velocity anisotropy. *MNRAS*, 316:671–683.

Takahashi, K. and Portegies Zwart, S. F. (2000). The Evolution of Globular Clusters in the Galaxy. *ApJ*, 535:759–775.

Tremou, E., Strader, J., Chomiuk, L., Shishkovsky, L., Maccarone, T. J., Miller- Jones, J. C. A., Tudor, V., Heinke, C. O., Sivakoff, G. R., Seth, A. C., and Noyola, E. (2018a). The MAVERIC Survey: Still No Evidence for Accreting Intermediate-mass Black Holes in Globular Clusters. *ApJ*, 862:16.

Tremou, E., Strader, J., Chomiuk, L., Shishkovsky, L., Maccarone, T. J., Miller-Jones, J. C. A., Tudor, V., Heinke, C. O., Sivakoff, G. R., Seth, A. C., and Noyola, E. (2018b). The MAVERIC Survey: Still No Evidence for Accreting Intermediate-mass Black Holes in Globular Clusters. *ArXiv e-prints*.

Trenti, M., Heggie, D. C., and Hut, P. (2007). Star clusters with primordial binaries - II. Dynamical evolution of models in a tidal field. *MNRAS*, 374:344–356.

Trenti, M. and van der Marel, R. (2013). No energy equipartition in globular clusters. *MNRAS*, 435:3272–3282.

Trenti, M., Vesperini, E., and Pasquato, M. (2010). Tidal Disruption, Global Mass Function, and Structural Parameter Evolution in Star Clusters. *ApJ*, 708:1598–1610.

Urry, C. M. and Padovani, P. (1995). Unified Schemes for Radio-Loud Active Galactic Nuclei. *PASP*, 107:803.

Šuvakov, M. and Dmitrašinović, V. (2013). Three Classes of Newtonian Three-Body Planar Periodic Orbits. *Physical Review Letters*, 110(11):114301.

van Albada, T. S. and Baker, N. (1973). On the Two Oosterhoff Groups of Globular Clusters. *ApJ*, 185:477–498.

van de Ven, G., van den Bosch, R. C. E., Verolme, E. K., and de Zeeuw, P. T. (2006). The dynamical distance and intrinsic structure of the globular cluster ω Centauri. *A&A*, 445:513–543.

Vesperini, E. and Chernoff, D. F. (1994). The Range of Core Size of Postcollapse Clusters Supported by Primordial Binaries. *ApJ*, 431:231.

von Hoerner, S. (1960). Die numerische Integration des n-Körper-Problemes für Sternhaufen. I. *Z. Astrophys.*, 50:184–214.

von Hoerner, S. (1963). Die numerische Integration des n-Körper-Problems für Sternhaufen, II. *Zeitschrift fur Astrophysik*, 57:47–82.

Wang, L., Spurzem, R., Aarseth, S., Giersz, M., Askar, A., Berczik, P., Naab, T., Schadow, R., and Kouwenhoven, M. B. N. (2016). The DRAGON simulations: globular cluster evolution with a million stars. *MNRAS*, 458:1450–1465.

Wang, L., Spurzem, R., Aarseth, S., Nitadori, K., Berczik, P., Kouwenhoven, M. B. N., and Naab, T. (2015). NBODY6++GPU: ready for the gravitational million-body problem. *MNRAS*, 450:4070–4080.

Wang, Q.-D. (1991). The global solution of the n-body problem. *Celestial Mechanics and Dynamical Astronomy*, 50:73–88.

Webb, J. J., Leigh, N., Sills, A., Harris, W. E., and Hurley, J. R. (2014). The effect of orbital eccentricity on the dynamical evolution of star clusters. *MNRAS*, 442:1569–1577.

Webb, J. J., Leigh, N. W. C., Singh, A., Ford, K. E. S., McKernan, B., and Bellovary, J. (2018). The evolution of kicked stellar-mass black holes in star cluster environments. *MNRAS*, 474:3835–3846.

Webb, J. J., Vesperini, E., Dalessandro, E., Beccari, G., Ferraro, F. R., and Lanzoni, B. (2017). Modelling the observed stellar mass function and its radial variation in galactic globular clusters. *MNRAS*, 471:3845–3855.

Weilbacher, P. M., Streicher, O., Urrutia, T., Pécontal-Rousset, A., Jarno, A., and Bacon, R. (2014). The MUSE Data Reduction Pipeline: Status after Preliminary Acceptance Europe. In Manset, N. and Forshay, P., editors, *Astronomical Data Analysis Software and Systems XXIII*, volume 485 of *Astronomical Society of the Pacific Conference Series*, page 451.

Wilson, C. P. (1975). Dynamical models of elliptical galaxies. *AJ*, 80:175–187.

Woolley, R. V. D. R. (1954). A study of the equilibrium of globular clusters. *MNRAS*, 114:191.

Zinn, R. (1985). The Globular Cluster System of the Galaxy. IV. The Halo and Disk Subsystems. *ApJ*, 293:424.

Zocchi, A., Gieles, M., and Hénault-Brunet, V. (2018). The effect of stellar-mass black holes on the central kinematics of ω Cen: a cautionary tale for IMBH interpretations. *MNRAS*.

Zocchi, A., Gieles, M., Hénault-Brunet, V., and Varri, A. L. (2016). Testing lowered isothermal models with direct N-body simulations of globular clusters. *MNRAS*, 462:696–714.

Zonoozi, A. H., Haghi, H., Kroupa, P., Küpper, A. H. W., and Baumgardt, H. (2017). Direct N-body simulations of globular clusters - III. Palomar 4 on an eccentric orbit. *MNRAS*, 467:758–767.

Zonoozi, A. H., Küpper, A. H. W., Baumgardt, H., Haghi, H., Kroupa, P., and Hilker, M. (2011). Direct N-body simulations of globular clusters - I. Palomar 14. *MNRAS*, 411:1989–2001.

Appendix A

Algorithm for the stellar mass function in discrete mass bins

A.1 Background

Here I describe the algorithm that evolves the stellar mass function, when approximated by discrete mass bins for stars and stellar remnants. The goal is to obtain both the average mass of objects in each bin, m_j, as well as the total bin masses, M_j, which can be used as input for the multimass dynamical models used in my modelling. This algorithm presented here is based on the one presented in Balbinot and Gieles (2018) but with various changes and improvements added, which is why I present here the full description of it.[1]

This part combines work done by Prof. Mark Gieles, Dr. Eduardo Balbinot and by myself. While one cannot make a clear division in who accounts for which part of this appendix, one can generally say that functional description was mostly done by Prof. Mark Gieles, the white dwarf evolution mostly by Dr.Eduardo Balbinot and the black hole evolution mostly by myself.

We need to find a discretized approximation to the stellar mass function $f_{\rm s}(m,t)$, which gives the number of stars in the range $m, m+{\rm d}m$ at time t. We consider the evolution of $f_{\rm s}$ as the result of stellar evolution and escape of stars, including the preferential escape of low-mass stars as the result of equipartition. In time, stars are turned into stellar remnants and we include a description for the growth of the remnants mass function $f_{\rm r}$, as well as the escape of remnants. Various analytic models exist that provide time-dependent expressions for $f_{\rm s}$ (Henon 1969; Kruijssen 2009; Lamers et al. 2013). Because we envision a coupling of this MF evolution code with the fast cluster evolution model EMACSS (Alexander et al. 2014), we here present a model based on time derivatives of both quantities. We here describe expressions for the rate of change of the properties of the mass bins, which can be used to solve m_j and M_j with the use of an ODE solver.

[1]The MF code presented here can be downloaded from `https://github.com/balbinot/ssptools`

A.2 Definitions

We describe the content of each stellar mass bin by the number of stars in bin j, $N_{\mathrm{s},j}$, and a power-law slope α_j. We approximate each bin by a power-law segment $f_j(m) = A_j\, m^{\alpha_j}$. For convenience, we introduce a function

$$P_k = P(k, \alpha_j, m_{j1}, m_{j2}) = \int_{m_{j1}}^{m_{j2}} m^{\alpha_j+k-1} \mathrm{d}m, \tag{A.2.1}$$

$$= \begin{cases} \dfrac{m_{j2}^{\alpha_j+k} - m_{j1}^{\alpha_j+k}}{\alpha_j + k}, & \alpha_j + k \neq 0 \\ \ln\left(\dfrac{m_{j2}}{m_{j1}}\right), & \alpha_j + k = 0. \end{cases} \tag{A.2.2}$$

Here m_{j1} and m_{j2} are the low-mass and high-mass edge of bin j, respectively. In this power-law approximation, we can find the mass of the bin $M_{\mathrm{s},j}$ and the mean mass $m_{\mathrm{s},j}$ from $N_{\mathrm{s},j}$, α_j and the function P_k. We first find $A_j = N_{\mathrm{s},j}/P_1$, and use this to find $M_{\mathrm{s},j} = A_j P_2$. Then $m_{\mathrm{s},j} = M_{\mathrm{s},j}/N_{\mathrm{s},j}$. Because of the way we solve for the change in the mass function as the result of stellar evolution and escape, expressing the bins in terms of number and power-law slope is preferred. As will become clear in Sec. A.3, for the remnant mass bins it is better to express the bin properties in terms of the number of remnants in the bin, $N_{\mathrm{r},j}$, and the mass of the bin, $M_{\mathrm{r},j}$.

A.3 Stellar evolution

At $t = 0$, the values for $N_{\mathrm{s},j}$ and α_j are found from the stellar initial mass function (IMF) and the definition of the bin edges. We approximate the main sequence life time as a function of initial mass as

$$t_{\mathrm{ms}}(m) = a_0 \exp\left(a_1 m^{a_2}\right). \tag{A.3.1}$$

The $[\mathrm{Fe/H}]$ dependent values of the coefficients a_0, a_1 and a_2 where derived from interpolated Darthmouth models (Dotter et al. 2007, 2008) and are listed in Tab. A.1. This function can be inverted to find the turn-off mass m_{to} as a function of time t. This is needed to find the rate of change of the stellar mass bin in which m_{to} falls. From conservation of number we find:

$$\dot{N}_{\mathrm{s},j}^{\mathrm{sev}}(m_{\mathrm{to}}) = -\left.\frac{\mathrm{d}N}{\mathrm{d}m}\right|_{m_{\mathrm{to}}} \left|\frac{\mathrm{d}m_{\mathrm{to}}}{\mathrm{d}t}\right| \tag{A.3.2}$$

Here we use $N_{\mathrm{s},j}$ and α_j to find $\mathrm{d}N/\mathrm{d}m$ at m_{to} and $\mathrm{d}m_{\mathrm{to}}/\mathrm{d}t$ is found from equation (A.3.1).

We adopt an initial-final mass relation which uses different polynomials to cover the different possible outcomes:

$$\frac{m_{\mathrm{r}}}{\mathrm{M}_\odot} = \begin{cases} \sum_{j=0}^{10} b_j m_i^j, & m_i < m_{\mathrm{WD,max}}\ (\mathrm{WD}), \\ 1.4, & m_{\mathrm{WD,max}} \leq m_i < m_{\mathrm{BH,min}}\ (\mathrm{NS}), \\ \sum_{j=0}^{1} c_j m_i^j, & m_{\mathrm{BH,min}} \leq m_i < m_{\mathrm{BH,a}}\ (\mathrm{BH}), \\ \sum_{j=0}^{1} d_j m_i^j, & m_{\mathrm{BH,a}} \leq m_i < m_{\mathrm{BH,b}}\ (\mathrm{BH}), \\ \sum_{j=0}^{6} e_j m_i^j, & m_{\mathrm{BH,b}} \leq m_i\ (\mathrm{BH}) \end{cases} \tag{A.3.3}$$

where m_i is the initial star mass, $m_{\rm r}$ the final remnant mass, b_j, c_j, d_j and e_j are the different constants of the individual polynomial functions (see discussion below), $m_{\rm WD,max}$ is the maximal mass of a star that turns into a WD at the end of its lifetime, $m_{\rm BH,min}$ is the minimal mass a star needs to turn into a BH, and $m_{\rm BH,a}$ and $m_{\rm BH,b}$ are two masses at which the different initial-final mass relations for BHs change functional form. The values of b_j and $m_{\rm WD,max}$ were determined from fitting polynomials to the initial-final mass relation from the MIST 2018 models (Dotter 2016; Choi et al. 2016; Paxton et al. 2011, 2013, 2015) for seven different values of $[{\rm Fe/H}]$. In Tab. A.2 and Tab. A.4, we list the $[{\rm Fe/H}]$ dependent value for $m_{\rm WD,max}$ and b_j, respectively. To get the values of those constants for a given [Fe/H], we use the values from the tables which have the closest value of $[{\rm Fe/H}]$. In Fig. A.1, we show our approximation for the initial to final mass relation derived from the MIST 2018 models.We regard every star which is too heavy to become a WD and too light to be a BH as a NS; and we simply assume the final mass of that NS to be $1.4\,{\rm M}_\odot$. For the initial-final mass relation for BHs, we used as reference the stellar evolution code as used in NBODY6 (Aarseth 2003), which is an improved version of the SSE code from Hurley et al. (2000) and which includes, among others, the improved description for remnant mass calculation from Belczynski et al. (2008). We found that the initial-final mass relation for BHs is best approximated by three polynomials. In Tab. A.5, we list the best-fit $[{\rm Fe/H}]$-dependent values for the coefficient c_j, d_j and e_j of the three polynomials. The initial stellar mass value, where the transition between the different polynomial occur, is also $[{\rm Fe/H}]$-dependent and the values are listed in Tab. A.3. The lowest value is also the minimal mass required for a star to turn into a BH. Compared to WDs, we found for BHs that for $[{\rm Fe/H}]$-values between the listed ones we can linearly interpolate and still get reasonable predictions as can be seen in Fig. A.2 where we plotted the initial-final mass relation for different values of $[{\rm Fe/H}]$ for BH-forming stars.

We then find the remnant bin in which $m_{\rm r}$ falls, and the rate of change of $N_{{\rm r},j}$ and $M_{{\rm r},j}$ of that bin are

$$\dot{N}^{\rm sev}_{{\rm r},j}(m_{\rm r}) = -\dot{N}^{\rm sev}_{{\rm s},j}(m_{\rm to}) f_{\rm ret}, \tag{A.3.4}$$

$$\dot{M}^{\rm sev}_{{\rm r},j}(m_{\rm r}) = -m_{\rm r}\dot{N}^{\rm sev}_{{\rm s},j}(m_{\rm to}) f_{\rm ret}, \tag{A.3.5}$$

where $\dot{N}^{\rm sev}_{{\rm s},j}$ is given by equation (A.3.2) and $f_{\rm ret}$ is the retention fraction of the remnants. For WDs, we set this always equal to unity, while for NS and BH one can vary their retention fraction to mimic the loss of those objects as the result of natal kicks.

A.4 Escape

For the escape rate of stars, we assume that the rate of change of the mass function goes as

$$\dot{f}(m) = -Bf(m)h(m) \tag{A.4.1}$$

In the pre-balanced evolution phase, there is no preferred mass for escape, i.e. the MF does not change shape and $h(m) = 1$. In the balanced evolution phase, low-mass stars are lost at a faster rate than high-mass stars, causing the MF to become flatter. Following

Balbinot & Gieles, we use $h(m)$

$$h(m) = \begin{cases} 1 - \left(\frac{m}{m_{\rm d}}\right)^{1/2}, & m < m_{\rm d} \\ 0, & m > m_{\rm d} \end{cases} \tag{A.4.2}$$

where $m_{\rm d}$ is the depletion mass (Lamers et al. 2013). The constant B is found from demanding that the total escape rate $\dot{N}$ equals the sum of the escape rates of each bin

$$\dot{N} = \int_{m_{\rm lo}}^{m_{\rm up}} \dot{f}\,{\rm d}m, \tag{A.4.3}$$

$$= -B \sum_j I_j \tag{A.4.4}$$

where $m_{\rm lo}$ is the lowest mass of the MF and I_j is the integration over $f(m)h(m)$ in each mass bin

$$I_j = N_j \left(1 - m_{\rm d}^{-1/2} \frac{P_{3/2}}{P_1}\right). \tag{A.4.5}$$

The rate of change of α_j is zero if $h = 1$ and for low-mass star depletion it is found from the values of $\dot{f}$ at the bin edges with the use of equation (A.4.1)

$$\dot{\alpha}_{j,{\rm s}} = \frac{B}{\ln(m_{j2}/m_{j1})} \left[\left(\frac{m_{j1}}{m_{\rm d}}\right)^{1/2} - \left(\frac{m_{j2}}{m_{\rm d}}\right)^{1/2}\right] \tag{A.4.6}$$

For the remnants we do not keep track of the power-law slopes, hence we can not exactly compute ratio $P_{3/2}/P_1 = \langle m_{\rm r}^{1/2} \rangle$. We approximate $\langle m_{\rm r}^{1/2} \rangle \simeq m_{{\rm r},j}^{1/2}$. We find for $m_{j2}/m_{j1} = 2$, the accuracy of this approximation is less than 0.5% and for $m_{j2}/m_{j1} = 20$ its less than 10% for all values of α. With this approximation of I_j for the remnants, the total contribution to $\dot{N}$ of escape from stars and remnants can be found and applied to the MF of stars and remnants.

For the remnants we need to find the rate of change of $M_{{\rm r},j}$, which can be done by realizing that the total mass-loss rate is $\dot{M} = \int_{m_{\rm lo}}^{m_{\rm up}} m\dot{f}{\rm d}m$, and introducing a similar integral as before

$$J_j = M_j \left(1 - m_{\rm d}^{-1/2} \frac{P_{5/2}}{P_2}\right) \tag{A.4.7}$$

such that

$$\dot{M}_j = -BJ_j, \tag{A.4.8}$$

where B is the same as before. For the remnants we again approximate $P_{5/2}/P_2 \simeq m_{{\rm r},j}^{1/2}$.

Breen and Heggie (2013a,b) described in their work how BHs get ejected from a star cluster through interactions with each other in the central core region. To mimic this additional ejection processes, our prescription removes a user defined BH number fraction from the MF at the end of the integration process. Following the results from Morscher et al. (2015) that the heaviest BHs get ejected first, we remove the BHs starting from the bin with the highest mean mass going to the lower ones, until the given number fraction is removed or no BHs are left.

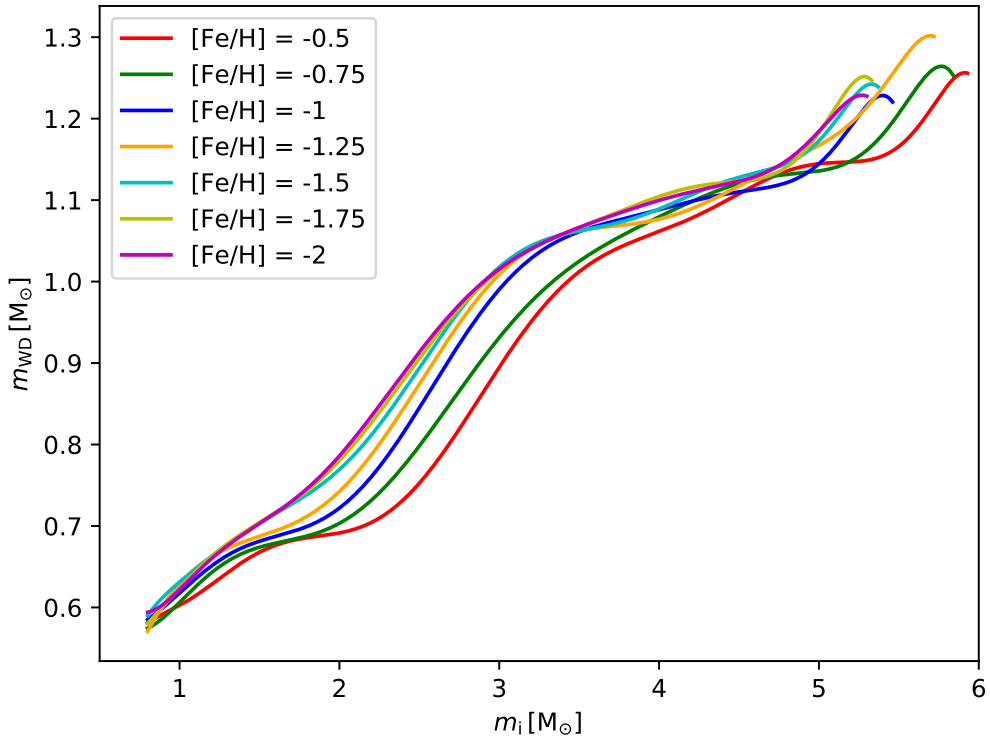

Figure A.1: Initial-final mass relation for stars that become WDs for different values of [Fe/H].

A.5 Sampling a discrete version of the MF

The MF created with this approach is a binned one, which is ideal as multimass models such as the one used in LIMEPY needed them binned. But when sampling mock data for method tests this can result in spurious positive results when the MF bins in the test model line up with the MF bins in the mock sample which can even be the case when the number of mass bins differ between them. To be able to perform proper tests and to better mimic observational data, one has to create a continues MF out of the binned one.

With the description for the observable stars this is rather simple as for each stellar mass bin the total mass as well as the slope of the mass function is given, from which masses can randomly sample as:

$$m_j = \left[x N_j \frac{(\alpha_j + 1)}{A_j} - m_{j1}^{\alpha_j + 1} \right]^{1/(\alpha_j + 1)}, \tag{A.5.1}$$

where x is a random number between zero and one, m_{j1}, N_j and α_j are the low-mass border, the total number of stars and the power-law slope in mass bin j, respectively. And A_j is calculated as discussed in Sec. A.2.

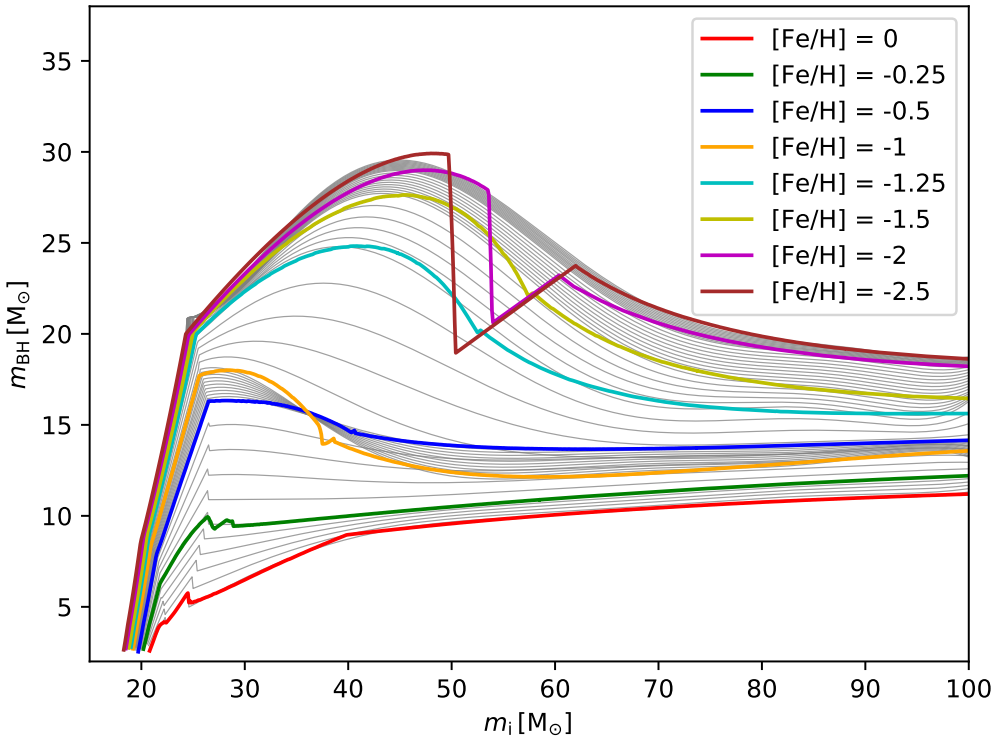

Figure A.2: Initial-final mass relation for stars that become BHs: In color the relation as predicted from the NBODY6 stellar evolution code for different values of $[\mathrm{Fe/H}]$. In gray the prediction from our approach for values of $[\mathrm{Fe/H}]$ from 0 to -2.5 in steps of 0.05.

Table A.1: Coefficients of equation (A.3.1) derived from interpolated Darthmouth models.

[Fe/H]	a_0	a_1	a_2
-2.5	0.27	9.9	-0.35
-2.4	0.26	9.9	-0.34
-2.3	0.25	9.9	-0.34
-2.2	0.24	10.0	-0.34
-2.1	0.23	10.0	-0.34
-2	0.22	10.1	-0.34
-1.9	0.21	10.1	-0.33
-1.8	0.20	10.2	-0.33
-1.7	0.20	10.2	-0.33
-1.6	0.20	10.2	-0.33
-1.5	0.20	10.2	-0.33
-1.4	0.19	10.2	-0.33
-1.3	0.19	10.3	-0.33
-1.2	0.19	10.3	-0.33
-1.1	0.19	10.3	-0.33
-1	0.19	10.3	-0.33
-0.9	0.18	10.4	-0.33
-0.8	0.17	10.5	-0.33
-0.7	0.17	10.5	-0.33
-0.6	0.17	10.6	-0.33

Table A.2: [Fe/H] dependent maximal mass of a star that turns into a WD at the end of its lifetime derived from the MIST 2018 models.

[Fe/H]	$m_{\mathrm{WD,max}}$ $\mathrm{M}_\odot$
-2	5.32
-1.75	5.35
-1.5	5.38
-1.25	5.73
-1	5.47
-0.75	5.85
-0.5	5.94

Table A.3: $[\mathrm{Fe/H}]$ dependent masses where the transitions between the three different prescriptions for the initial-final mass relation for the BH happens. This first mass is the minimal mass a star needs to turn into a BH at the end of its lifetime.

$[\mathrm{Fe/H}]$	$m_{\mathrm{BH,min}}$ $\mathrm{M}_\odot$	$m_{\mathrm{BH,a}}$ $\mathrm{M}_\odot$	$m_{\mathrm{BH,b}}$ $\mathrm{M}_\odot$
-2.5	18.3	20	24.4
-2	18.5	20.3	24.6
-1.5	18.8	20.7	25.1
-1.25	19	20.8	25.4
-1	19.2	20.9	25.7
-0.5	19.7	21.6	26.6
-0.25	20.2	21.8	26.5
0	20.8	22.3	24.6

Table A.4: Coefficients for the calculation of the final WD mass as derived from the MIST 2018 models.

[Fe/H]	b_0	b_1	b_2	b_3	b_4	b_5	b_6	b_7	b_8	b_9	b_{10}
-2	3.8	-14.4	25.6	-23.9	12.8	-3.9	0.55	0.019	-0.019	2.6×10^{-3}	-1.2×10^{-4}
-1.75	0.18	2.8	-9.5	16.7	-16.9	10.4	-4.0	0.98	-0.15	1.2×10^{-2}	-4.5×10^{-4}
-1.5	-4.8	27.3	-60.2	75.6	-59.1	30.1	-10.1	2.2	-0.30	2.3×10^{-2}	-7.9×10^{-4}
-1.25	-1.0	6.9	-14.2	18.4	-15.4	8.4	-2.9	0.66	-0.091	7.1×10^{-3}	-2.3×10^{-4}
-1	-0.61	7.7	-21.5	32.3	-28.8	16.1	-5.7	1.3	-0.18	1.5×10^{-2}	-5.0×10^{-4}
-0.75	1.8	-4.5	4.7	0.44	-4.5	3.8	-1.6	0.41	-0.060	4.9×10^{-3}	-1.7×10^{-4}
-0.5	-4.2	24.5	-53.4	64.5	-47.7	22.5	-6.9	1.4	-0.17	1.2×10^{-2}	-3.7×10^{-4}

Table A.5: Coefficients for the three polynomials used to calculate the final BH mass.

[Fe/H]	c_0	c_1	d_0	d_1	e_0	e_1	e_2	e_3	e_4	e_5	e_6
-2.5	-63	3.6	-44	2.6	218	-26	1.3	-3.0×10^{-2}	3.7×10^{-4}	-2.3×10^{-6}	5.8×10^{-9}
-2	-63	3.5	-43	2.6	255	-30	1.4	-3.4×10^{-2}	4.2×10^{-4}	-2.7×10^{-6}	6.7×10^{-9}
-1.5	-64	3.5	-43	2.5	271	-32	1.6	-3.8×10^{-2}	4.8×10^{-4}	-3.1×10^{-6}	7.8×10^{-9}
-1.25	-64	3.5	-42	2.4	138	-18	0.98	-2.6×10^{-2}	3.5×10^{-4}	-2.4×10^{-6}	6.4×10^{-9}
-1	-59	3.2	-34	2.0	-145	19	-0.90	2.1×10^{-2}	-2.5×10^{-4}	1.6×10^{-6}	-4.1×10^{-9}
-0.5	-57	3.0	-28	1.7	-76	11	-0.47	1.1×10^{-2}	-1.3×10^{-4}	7.8×10^{-7}	-2.0×10^{-9}
-0.25	-43	2.3	-11	0.81	26	-1.8	0.077	-1.6×10^{-3}	1.9×10^{-5}	-1.2×10^{-7}	2.9×10^{-10}
0	-22	1.2	-13	0.78	13	-2.0	0.13	-3.6×10^{-3}	4.9×10^{-5}	-3.3×10^{-7}	9.0×10^{-10}

Appendix B

N-body data and MCMC results for Chapter 2

Table B.1: Properties of the snapshots from the N-body model N1 with 100% initial BH and NS retention. I list the age in units of the initial half-mass relaxation time, the total bound mass in $\mathrm{M}_\odot$, the half-mass radius in pc, the number of BHs in the cluster, the number of NSs in the cluster and the Jacobi radius r_J in pc calculated as in Section 2.3.2. For the bound mass and the number of BHs and NSs, I also give the percentage relative to the initial values in brackets.

Age	M_CL	Half-Mass radius	Number of BHs	Number of NSs	r_J
$\tau_{\mathrm{rh},0}$	$\mathrm{M}_\odot$	pc			pc
0	37353 (100%)	2.06	121 (100%)	632 (100%)	30.12
2.4	30408 (81%)	5.03	119 (56%)	551 (87%)	27.98
4.9	25737 (69%)	6.03	85 (40%)	518 (82%)	26.51
7.3	22077 (59%)	6.56	59 (28%)	503 (80%)	25.24
9.7	19109 (51%)	6.58	55 (26%)	490 (78%)	24.08
12.1	15827 (42%)	6.54	43 (20%)	474 (75%)	22.68
14.6	12618 (34%)	6.27	35 (17%)	461 (73%)	21.10
17.0	9434 (25%)	5.71	26 (12%)	439 (69%)	19.22
19.4	6602 (18%)	4.98	18 (8.5%)	416 (66%)	17.11
21.9	4094 (11%)	4.09	12 (5.7%)	368 (58%)	14.62
24.3	2046 (5.5%)	2.92	6 (2.8%)	301 (48%)	11.68
26.7	497 (1.3%)	1.58	0 (0.0%)	149 (24%)	7.52

Table B.2: Properties of the snapshots from the N-body model N0.3 with 33% initial BH and NS retention. I list the age in units of the initial half-mass relaxation time, the total bound mass in $\mathrm{M}_\odot$, the half-mass radius in pc, the number of BHs in the cluster, the number of NSs in the cluster and the Jacobi radius r_J in pc calculated as in Section 2.3.2. For the bound mass and the number of BHs and NSs, I also give the percentage relative to the initial values in brackets.

Age	M_CL	Half-Mass radius	Number of BHs	Number of NSs	r_J
$\tau_{\mathrm{rh},0}$	$\mathrm{M}_\odot$	pc			pc
0	34404 (100%)	2.06	66 (100%)	211 (100%)	29.33
2.3	31131 (90%)	3.07	22 (33%)	199 (94%)	28.14
4.7	29061 (84%)	3.13	8 (12%)	189 (90%)	27.50
7.0	26824 (78%)	3.12	1 (1.5%)	179 (85%)	26.78
9.4	24151 (70%)	3.27	0 (0%)	150 (71%)	25.88
11.7	21002 (61%)	3.57	0 (0%)	119 (56%)	24.72
14.1	17922 (52%)	3.57	0 (0%)	94 (45%)	23.45
16.4	14861 (43%)	3.61	0 (0%)	75 (36%)	22.06
18.8	11785 (34%)	3.43	0 (0%)	59 (28%)	20.45
21.1	8808 (26%)	3.28	0 (0%)	46 (22%)	18.59
23.5	6077 (18%)	2.88	0 (0%)	37 (18%)	16.49
25.8	3651 (11%)	2.61	0 (0%)	26 (12%)	13.99
28.1	1489 (4.3%)	1.89	0 (0%)	15 (7.1%)	10.53
30.5	268 (0.8%)	1.08	0 (0%)	7 (3.3%)	6.06

Table B.3: Properties of the snapshots from the N-body model N0.1 with 10% initial BH and NS retention. I list the age in units of the initial half-mass relaxation time, the total bound mass in $\mathrm{M}_\odot$, the half-mass radius in pc, the number of BHs in the cluster, the number of NSs in the cluster and the Jacobi radius r_J in pc calculated as in Section 2.3.2. For the bound mass and the number of BHs and NSs, I also give the percentage relative to the initial values in brackets.

Age $\tau_{\mathrm{rh},0}$	M_CL $\mathrm{M}_\odot$	Half-Mass radius pc	Number of BHs	Number of NSs	r_J pc
0	33476 (100%)	2.04	22 (100%)	56 (100%)	29.06
2.3	31156 (93%)	2.46	5 (23%)	54 (96%)	28.15
4.7	28719 (86%)	2.76	0 (0%)	50 (89%)	27.41
7.0	25388 (76%)	3.27	0 (0%)	24 (43%)	26.33
9.4	22112 (66%)	3.52	0 (0%)	19 (34%)	25.16
11.7	18956 (57%)	3.60	0 (0%)	12 (21%)	23.91
14.1	15809 (47%)	3.65	0 (0%)	7 (13%)	22.53
16.4	12625 (38%)	3.52	0 (0%)	5 (8.9%)	20.94
18.7	9772 (29%)	3.42	0 (0%)	3 (5.4%)	19.26
21.1	6926 (21%)	3.11	0 (0%)	1 (1.8%)	17.23
23.4	4373 (13%)	2.75	0 (0%)	0 (0%)	14.85
25.8	2172 (6.5%)	2.29	0 (0%)	0 (0%)	11.89
28.1	6780 (2.0%)	1.48	0 (0%)	0 (0%)	8.19

Table B.4: Properties of the snapshots from the N-body model N0 with no initial BH and NS retention. I list the age in units of the initial half-mass relaxation time, the total bound mass in $\mathrm{M}_\odot$, the half-mass radius in pc and the Jacobi radius r_J in pc calculated as in Section 2.3.2. For the bound mass I also give the percentage relative to the initial value in brackets.

Age $\tau_{\mathrm{rh},0}$	M_Cl $\mathrm{M}_\odot$	Half-Mass radius pc	r_J pc
0	33042 (100%)	2.04	28.93
2.3	30886 (93%)	2.26	28.07
4.7	27539 (83%)	2.93	27.03
7.0	24261 (73%)	3.25	25.93
9.3	21223 (64%)	3.46	24.80
11.7	18167 (55%)	3.53	23.56
14.0	15053 (46%)	3.56	22.15
16.3	12026 (36%)	3.47	20.58
18.7	9183 (28%)	3.18	18.84
21.0	6367 (19%)	2.89	16.75
23.3	3955 (12%)	2.55	14.33
25.7	1951 (5.9%)	2.12	11.42
28.0	455 (1.4%)	1.06	7.18

Table B.5: Mass bins of the different snapshots of N-body model N1. I list the age in units of the initial half-mass relaxation time and for each mass bin the total mass M_j and the mean mass m_j in units of $\mathrm{M}_\odot$. There are a total of 11 mass bins: five for the MSs, one for the ESs, three for the WDs and one each for the NS and BHs.

Age	MS1		MS2		MS3		MS4		MS5		ES		WD1		WD2		WD3		NS		BH	
	M_j	m_j	M_j	m_j	M_j	m_j	M_j	m_j	M_j	m_j	M_j	m_j	M_j	m_j	M_j	m_j	M_j	m_j	M_j	m_j	M_j	m_j
$\tau_{\mathrm{rh},0}$	$\mathrm{M}_\odot$	$\mathrm{M}_\odot$	$\mathrm{M}_\odot$	$\mathrm{M}_\odot$	$\mathrm{M}_\odot$	$\mathrm{M}_\odot$	$\mathrm{M}_\odot$	$\mathrm{M}_\odot$	$\mathrm{M}_\odot$	$\mathrm{M}_\odot$	$\mathrm{M}_\odot$	$\mathrm{M}_\odot$	$\mathrm{M}_\odot$	$\mathrm{M}_\odot$	$\mathrm{M}_\odot$	$\mathrm{M}_\odot$	$\mathrm{M}_\odot$	$\mathrm{M}_\odot$	$\mathrm{M}_\odot$	$\mathrm{M}_\odot$	$\mathrm{M}_\odot$	$\mathrm{M}_\odot$
2.4	2498	0.13	3288	0.2	4792	0.32	6155	0.5	3630	0.72	185	0.82	3650	0.6	2346	0.78	1521	1.08	841	1.53	1504	12.6
4.9	2024	0.13	2702	0.2	4004	0.32	5287	0.5	3194	0.72	164	0.82	3152	0.6	2075	0.78	1391	1.08	789	1.52	955	11.2
7.3	1626	0.13	2182	0.2	3354	0.32	4572	0.5	2878	0.72	152	0.82	2775	0.6	1877	0.78	1299	1.09	766	1.52	596	10.1
9.7	1252	0.13	1722	0.2	2773	0.32	3943	0.5	2585	0.72	138	0.82	2475	0.6	1704	0.78	1230	1.09	748	1.53	538	9.79
12.1	892	0.13	1280	0.2	2149	0.32	3283	0.5	2235	0.72	118	0.82	2104	0.6	1507	0.78	1154	1.09	725	1.53	379	8.81
14.6	568	0.13	874	0.2	1543	0.32	2549	0.5	1894	0.72	104	0.83	1728	0.6	1317	0.79	1055	1.09	706	1.53	280	7.99
17.0	317	0.13	528	0.2	987	0.32	1818	0.51	1519	0.72	82	0.83	1299	0.6	1060	0.79	957	1.1	675	1.54	192	7.38
19.4	144	0.13	269	0.2	544	0.33	1172	0.51	1119	0.72	62	0.83	881	0.6	817	0.79	831	1.1	642	1.54	119	6.63
21.9	47.5	0.13	98	0.2	230	0.33	611	0.51	728	0.73	41.4	0.83	496	0.61	541	0.79	647	1.11	574	1.56	80	6.68
24.3	8.99	0.13	22.7	0.21	63	0.33	213	0.52	325	0.73	15.7	0.83	204	0.61	272	0.8	418	1.13	474	1.57	30.7	5.11
26.7	0.12	0.12	0.24	0.24	4.52	0.35	14.4	0.53	50	0.74	2.51	0.84	15.4	0.62	47.2	0.81	119	1.18	243	1.63	0	0

Table B.6: Mass bins of the different snapshots of N-body model N0.3. I list the age in units of the initial half-mass relaxation time and for each mass bin the total mass M_j and the mean mass m_j in units of $\mathrm{M}_\odot$. There are a total of 11 mass bins: five for the MSs, one for the ESs, three for the WDs and one each for the NS and BHs.

Age	MS1		MS2		MS3		MS4		MS5		ES		WD1		WD2		WD3		NS		BH	
	M_j	m_j	M_j	m_j	M_j	m_j	M_j	m_j	M_j	m_j	M_j	m_j	M_j	m_j	M_j	m_j	M_j	m_j	M_j	m_j	M_j	m_j
$\tau_{\mathrm{rh},0}$	$\mathrm{M}_\odot$	$\mathrm{M}_\odot$	$\mathrm{M}_\odot$	$\mathrm{M}_\odot$	$\mathrm{M}_\odot$	$\mathrm{M}_\odot$	$\mathrm{M}_\odot$	$\mathrm{M}_\odot$	$\mathrm{M}_\odot$	$\mathrm{M}_\odot$	$\mathrm{M}_\odot$	$\mathrm{M}_\odot$	$\mathrm{M}_\odot$	$\mathrm{M}_\odot$	$\mathrm{M}_\odot$	$\mathrm{M}_\odot$	$\mathrm{M}_\odot$	$\mathrm{M}_\odot$	$\mathrm{M}_\odot$	$\mathrm{M}_\odot$	$\mathrm{M}_\odot$	$\mathrm{M}_\odot$
2.3	2746	0.13	3609	0.2	5268	0.32	6732	0.5	3935	0.72	200	0.81	3975	0.6	2516	0.78	1622	1.08	302	1.52	224	10.2
4.7	2465	0.13	3276	0.2	4845	0.32	6340	0.5	3783	0.72	196	0.82	3805	0.6	2423	0.78	1588	1.08	285	1.51	53	6.62
7.0	2113	0.13	2869	0.2	4365	0.32	5889	0.5	3637	0.72	184	0.82	3603	0.6	3603	0.78	1546	1.08	269	1.50	6.31	6.31
9.3	1731	0.13	2386	0.2	3783	0.32	5356	0.5	3457	0.72	179	0.82	3329	0.6	2235	0.78	1478	1.08	218	1.45	0	0
11.7	1337	0.13	1782	0.2	3118	0.32	4691	0.5	3205	0.72	164	0.82	3005	0.6	2087	0.78	1354	1.07	168	1.41	0	0
14.0	964	0.13	1406	0.2	2471	0.32	4003	0.5	2941	0.72	155	0.82	2675	0.6	1933	0.78	1244	1.06	130	1.38	0	0
16.3	635	0.13	990	0.2	1861	0.32	3308	0.5	2636	0.72	143	0.82	2274	0.61	1772	0.79	1140	1.05	102	1.36	0	0
18.7	385	0.13	622	0.2	1274	0.32	2595	0.51	2263	0.72	126	0.82	1859	0.61	1559	0.79	1024	1.05	80	1.35	0	0
21.0	189	0.13	341	0.2	779	0.33	1862	0.51	1847	0.73	104	0.82	1390	0.61	1329	0.79	904	1.04	61	1.34	0	0
23.3	74	0.13	144	0.2	404	0.33	1169	0.52	1394	0.73	83	0.82	949	0.61	1055	0.8	756	1.04	49.1	1.33	0	0
25.7	19.1	0.13	45.8	0.2	144	0.33	587	0.52	892	0.73	55	0.81	533	0.61	729	0.8	612	1.04	43.4	1.32	0	0
28.0	2.92	0.13	5.93	0.2	21.5	0.35	148	0.53	367	0.74	20.7	0.83	161	0.61	349	0.81	393	1.04	19.7	1.31	0	0
30.3	0.17	0.17	0.39	0.39	0	0	6.1	0.55	38.5	0.74	3.32	0.83	8.71	0.62	69	0.85	133	1.06	9.18	1.31	0	0

Table B.7: Mass bins of the different snapshots of N-body model N0.1. I list the age in units of the initial half-mass relaxation time and for each mass bin the total mass M_j and the mean mass m_j in units of $\mathrm{M}_\odot$. There are a total of 11 mass bins: five for the MSs, one for the ESs, three for the WDs and one each for the NS and BHs.

Age	MS1		MS2		MS3		MS4		MS5		ES		WD1		WD2		WD3		NS		BH	
	M_j	m_j	M_j	m_j	M_j	m_j	M_j	m_j	M_j	m_j	M_j	m_j	M_j	m_j	M_j	m_j	M_j	m_j	M_j	m_j	M_j	m_j
$\tau_{\mathrm{rh},0}$	$\mathrm{M}_\odot$	$\mathrm{M}_\odot$	$\mathrm{M}_\odot$	$\mathrm{M}_\odot$	$\mathrm{M}_\odot$	$\mathrm{M}_\odot$	$\mathrm{M}_\odot$	$\mathrm{M}_\odot$	$\mathrm{M}_\odot$	$\mathrm{M}_\odot$	$\mathrm{M}_\odot$	$\mathrm{M}_\odot$	$\mathrm{M}_\odot$	$\mathrm{M}_\odot$	$\mathrm{M}_\odot$	$\mathrm{M}_\odot$	$\mathrm{M}_\odot$	$\mathrm{M}_\odot$	$\mathrm{M}_\odot$	$\mathrm{M}_\odot$	$\mathrm{M}_\odot$	$\mathrm{M}_\odot$
2.3	2779	0.13	3658	0.2	5338	0.32	6844	0.5	3976	0.72	204	0.81	4039	0.6	2538	0.78	1644	1.08	82	1.52	53	10.6
4.7	2394	0.13	3220	0.2	4800	0.32	6374	0.5	3801	0.72	200	0.82	3827	0.6	2451	0.78	1577	1.08	75	1.50	0	0
7.0	1954	0.13	2683	0.2	4103	0.32	5703	0.5	3560	0.72	186	0.81	3515	0.6	2317	0.78	1334	1.06	33	1.36	0	0
9.4	1516	0.13	2142	0.2	3405	0.32	5015	0.5	3290	0.72	180	0.82	3183	0.6	2171	0.78	1185	1.05	26	1.35	0	0
11.7	1131	0.13	1652	0.2	2757	0.32	4323	0.5	3011	0.72	168	0.82	2824	0.6	2009	0.78	1065	1.04	16.3	1.36	0	0
14.1	776	0.13	1207	0.2	2121	0.32	3606	0.5	2706	0.72	158	0.82	2455	0.6	1838	0.78	935	1.03	9.26	1.33	0	0
16.4	480	0.13	787	0.2	1504	0.32	2845	0.51	2345	0.72	147	0.82	2064	0.61	1635	0.79	811	1.02	6.51	1.3	0	0
18.7	262	0.13	456	0.2	971	0.32	2148	0.51	2025	0.73	130	0.82	1651	0.61	1414	0.79	711	1.01	3.91	1.3	0	0
21.1	107	0.13	227	0.2	528	0.33	1411	0.51	1600	0.73	113	0.82	1179	0.61	1169	0.79	592	1.01	1.3	1.3	0	0
23.4	33.4	0.13	81	0.2	227	0.33	745	0.52	1121	0.73	89	0.82	724	0.61	871	0.79	481	1.0	0	0	0	0
25.8	5.55	0.13	14.1	0.2	57	0.33	291	0.53	596	0.74	55	0.83	305	0.61	511	0.8	337	1.01	0	0	0	0
28.1	0.14	0.14	0.48	0.24	3.68	0.33	53	0.55	196	0.75	21.6	0.83	57	0.61	192	0.82	155	1.01	0	0	0	0

Table B.8: Mass bins of the different snapshots of N-body model N0. I list the age in units of the initial half-mass relaxation time and for each mass bin the total mass M_j and the mean mass m_j in units of $\mathrm{M}_\odot$. There are a total of 9 mass bins: five for the MSs, one for the ESs and three for the WDs.

Age	MS1		MS2		MS3		MS4		MS5		ES		WD1		WD2		WD3	
	M_j	m_j	M_j	m_j	M_j	m_j	M_j	m_j	M_j	m_j	M_j	m_j	M_j	m_j	M_j	m_j	M_j	m_j
$\tau_{\mathrm{rh},0}$	$\mathrm{M}_\odot$	$\mathrm{M}_\odot$	$\mathrm{M}_\odot$	$\mathrm{M}_\odot$	$\mathrm{M}_\odot$	$\mathrm{M}_\odot$	$\mathrm{M}_\odot$	$\mathrm{M}_\odot$	$\mathrm{M}_\odot$	$\mathrm{M}_\odot$	$\mathrm{M}_\odot$	$\mathrm{M}_\odot$	$\mathrm{M}_\odot$	$\mathrm{M}_\odot$	$\mathrm{M}_\odot$	$\mathrm{M}_\odot$	$\mathrm{M}_\odot$	$\mathrm{M}_\odot$
2.3	2743	0.13	3613	0.2	5300	0.32	6817	0.5	3987	0.72	210	0.82	4016	0.6	2541	0.78	1659	1.08
4.7	2285	0.13	3091	0.2	4614	0.32	6174	0.5	3742	0.72	197	0.81	3703	0.6	2378	0.78	1356	1.06
7.0	1847	0.13	2543	0.2	3944	0.32	5515	0.5	3489	0.72	185	0.81	3385	0.6	2218	0.78	1135	1.04
9.4	1450	0.13	2055	0.2	3292	0.32	4874	0.5	3236	0.72	174	0.81	3074	0.6	2081	0.78	987	1.03
11.7	1071	0.13	1589	0.2	2665	0.32	4210	0.5	2984	0.72	159	0.81	2708	0.6	1917	0.78	867	1.02
14.1	730	0.13	1147	0.2	2053	0.32	3495	0.51	2667	0.72	140	0.81	2329	0.6	1747	0.78	745	1.01
16.4	453	0.13	747	0.2	1466	0.32	2763	0.51	2336	0.72	123	0.82	1945	0.61	1557	0.78	636	1.0
18.8	236	0.13	432	0.2	935	0.32	2045	0.51	1961	0.73	107	0.82	1550	0.61	1362	0.79	555	0.99
21.1	98	0.13	196	0.2	506	0.33	1316	0.51	1518	0.73	87	0.82	1098	0.61	1086	0.79	463	0.99
23.5	26.7	0.13	68	0.2	213	0.33	707	0.52	1045	0.73	66	0.82	681	0.61	795	0.79	353	0.98
25.8	4.32	0.13	13	0.21	52	0.34	248	0.53	578	0.74	43	0.83	287	0.61	473	0.8	252	0.98
28.1	0.11	0.11	0.61	0.2	2.31	0.33	25.4	0.54	139	0.76	10.9	0.84	29	0.62	138	0.82	111	0.98

Table B.9: Results from the MCMC fitting process for the snapshots from the N-body model N1 with initial 100% BH and NS retention. I list here the age of each snapshot in units of the initial half-mass relaxation time, the total cluster mass in $\mathrm{M}_\odot$, the half-mass radius in pc, the dimensionless central concentration for the global mean mass, the central mean mass, and the ES stars, the truncation parameter g, the mass segregation parameter δ, the anisotropy radius for the global mean mass and the central mean mass in pc, the anisotropy parameter η and the truncation radius r_t in pc. All parameters except the dimensionless central concentration for the global mean mass, and the ES stars, the anisotropy radius for the global mean mass and the truncation radius r_t, are fitting parameters; the other values were obtained from the multimass models of the 10 last walker positions of each MCMC chain. The median of the marginalized posterior distribution of each parameter is used to estimate its best-fitting value and the 16th and 84th percentiles as proxy for the 1σ uncertainties.

Age	M_Cl	r_h	W_0	$W_{0,\mathrm{CMM}}$	$W_{0,\mathrm{ES}}$	g	δ	r_a	$r_{\mathrm{a,CMM}}$	η	r_t
$\tau_{\mathrm{rh},0}$	$\mathrm{M}_\odot$	pc						pc	pc		pc
2.4	30455^{+14}_{-14}	$5.11^{+0.02}_{-0.02}$	$1.7^{+0.1}_{-0.1}$	$16.9^{+0.4}_{-0.4}$	$2.8^{+0.1}_{-0.1}$	$1.43^{+0.02}_{-0.02}$	$0.350^{+0.009}_{-0.008}$	$4.3^{+0.15}_{-0.2}$	$7.5^{+0.7}_{-0.6}$	$0.17^{+0.02}_{-0.02}$	$31.2^{+0.2}_{-0.2}$
4.9	25790^{+13}_{-12}	$6.13^{+0.02}_{-0.02}$	$1.8^{+0.1}_{-0.1}$	$20.4^{+0.2}_{-0.2}$	$3.3^{+0.03}_{-0.2}$	$1.25^{+0.02}_{-0.02}$	$0.368^{+0.008}_{-0.008}$	$8.4^{+0.41}_{-0.4}$	$3.6^{+0.4}_{-0.4}$	$-0.26^{+0.04}_{-0.03}$	$28.37^{+0.1}_{-0.09}$
7.3	22140^{+11}_{-11}	$6.59^{+0.02}_{-0.02}$	$2.40^{+0.07}_{-0.07}$	$23.6^{+0.7}_{-1.0}$	$4.1^{+0.1}_{-0.1}$	$1.05^{+0.01}_{-0.01}$	$0.362^{+0.005}_{-0.005}$	$20^{+2.6}_{-2.3}$	$6.2^{+0.8}_{-0.9}$	$-0.39^{+0.06}_{-0.06}$	$26.73^{+0.06}_{-0.06}$
9.7	$19175^{+9.3}_{-9.9}$	$6.61^{+0.01}_{-0.02}$	$2.68^{+0.07}_{-0.08}$	$18^{+1.2}_{-1.2}$	$4.3^{+0.08}_{-0.10}$	$0.91^{+0.01}_{-0.01}$	$0.331^{+0.007}_{-0.007}$	$61^{+\infty}_{-31}$	29^{+4770}_{-17}	$-0.4^{+0.2}_{-3.6}$	$25.56^{+0.05}_{-0.05}$
12.1	$15878^{+8.5}_{-9.1}$	$6.51^{+0.02}_{-0.02}$	$2.74^{+0.06}_{-0.06}$	$20^{+1.2}_{-1.5}$	$4.4^{+0.08}_{-0.08}$	$0.8^{+0.02}_{-0.01}$	$0.360^{+0.006}_{-0.007}$	$102^{+\infty}_{-43}$	39^{+208}_{-18}	$-0.4^{+0.2}_{-0.3}$	$23.96^{+0.09}_{-0.05}$
14.6	$12659^{+7.7}_{-8.2}$	$6.23^{+0.02}_{-0.02}$	$2.85^{+0.06}_{-0.06}$	$19^{+1.6}_{-1.2}$	$4.4^{+0.08}_{-0.08}$	$0.72^{+0.02}_{-0.02}$	$0.377^{+0.007}_{-0.007}$	...	4416^{+2814}_{-2895}	-4^{+4}_{-4}	$22.39^{+0.06}_{-0.04}$
17.0	$9464^{+6.8}_{-7.3}$	$5.64^{+0.02}_{-0.02}$	$3.09^{+0.07}_{-0.06}$	$20^{+1.3}_{-1.2}$	$4.6^{+0.08}_{-0.08}$	$0.64^{+0.02}_{-0.02}$	$0.390^{+0.007}_{-0.007}$	...	3740^{+2365}_{-2428}	-4^{+4}_{-4}	$20.27^{+0.07}_{-0.05}$
19.4	$6623^{+6.2}_{-6.9}$	$4.96^{+0.03}_{-0.03}$	$3.20^{+0.08}_{-0.09}$	$18^{+2.9}_{-1.7}$	$4.4^{+0.1}_{-0.1}$	$0.64^{+0.02}_{-0.02}$	$0.42^{+0.01}_{-0.01}$	...	1017^{+2149}_{-741}	-4^{+4}_{-4}	$18.23^{+0.07}_{-0.05}$
21.9	$4107^{+5.0}_{-5.7}$	$4.03^{+0.04}_{-0.04}$	$3.5^{+0.13}_{-0.13}$	$17^{+3.0}_{-2.1}$	$4.3^{+0.1}_{-0.1}$	$0.71^{+0.04}_{-0.04}$	$0.42^{+0.02}_{-0.02}$	...	3041^{+1843}_{-1941}	-4^{+4}_{-4}	$15.9^{+0.3}_{-0.2}$
24.3	$2050^{+4.2}_{-5.0}$	$2.92^{+0.04}_{-0.04}$	$4.3^{+0.04}_{-0.23}$	$23^{+4.0}_{-5.4}$	$4.5^{+0.4}_{-0.2}$	$0.7^{+0.04}_{-0.04}$	$0.50^{+0.02}_{-0.03}$	...	874^{+600}_{-576}	-4^{+4}_{-4}	$12.9^{+0.1}_{-0.1}$
26.7	$495^{+2.7}_{-3.9}$	$1.7^{+0.08}_{-0.1}$	$5^{+1.1}_{-1.2}$	$8.9^{+1.0}_{-0.7}$	$2.7^{+1.2}_{-1.1}$	$0.7^{+0.2}_{-0.1}$	$0.9^{+0.4}_{-0.3}$	72^{+266}_{-54}	21^{+12}_{-11}	-4^{+4}_{-4}	$8.7^{+0.4}_{-0.2}$

Table B.10: Results from the MCMC fitting process for the snapshots from the N-body model N0.3 with initial 33% BH and NS retention. I list here the age of each snapshot in units of the initial half-mass relaxation time, the total cluster mass in $\mathrm{M}_\odot$, the half-mass radius in pc, the dimensionless central concentration for the global mean mass, the central mean mass, and the ES stars, the truncation parameter g, the mass segregation parameter δ, the anisotropy radius for the global mean mass and the central mean mass in pc, the anisotropy parameter η and the truncation radius r_t in pc. All parameters except the dimensionless central concentration for the global mean mass, and the ES stars, the anisotropy radius for the global mean mass and the truncation radius r_t, are fitting parameters; the other values were obtained from the multimass models of the 10 last walker positions of each MCMC chain. The median of the marginalized posterior distribution of each parameter is used to estimate its best-fitting value and the 16th and 84th percentiles as proxy for the 1σ uncertainties.

Age	M_Cl	r_h	W_0	$W_{0,\mathrm{CMM}}$	$W_{0,\mathrm{ES}}$	g	δ	r_a	$r_{\mathrm{a,CMM}}$	η	r_t
$\tau_{\mathrm{rh},0}$	$\mathrm{M}_\odot$	pc						pc	pc		pc
2.3	31166^{+13}_{-14}	$3.14^{+0.01}_{-0.01}$	$4.22^{+0.06}_{-0.06}$	$47.8^{+0.2}_{-0.7}$	$7.76^{+0.07}_{-0.08}$	$1.52^{+0.02}_{-0.02}$	$0.370^{+0.003}_{-0.003}$	$5.9^{+0.2}_{-0.1}$	$25.0^{+2.6}_{-2.8}$	$0.44^{+0.03}_{-0.02}$	$32.0^{+0.4}_{-0.4}$
4.7	29103^{+14}_{-13}	$3.18^{+0.01}_{-0.01}$	$4.65^{+0.02}_{-0.03}$	$13.26^{+0.05}_{-0.05}$	$8.30^{+0.02}_{-0.03}$	$1.22^{+0.01}_{-0.01}$	$0.356^{+0.002}_{-0.001}$	$7.8^{+0.1}_{-0.1}$	$13.0^{+0.3}_{-0.3}$	$0.35^{+0.02}_{-0.02}$	$28.6^{+0.1}_{-0.2}$
7.0	26860^{+14}_{-13}	$3.13^{+0.01}_{-0.01}$	$4.69^{+0.04}_{-0.04}$	$11.23^{+0.04}_{-0.04}$	$9.03^{+0.04}_{-0.04}$	$1.11^{+0.01}_{-0.01}$	$0.414^{+0.003}_{-0.003}$	$6.7^{+0.2}_{-0.2}$	$6.5^{+0.3}_{-0.3}$	$-0.03^{+0.03}_{-0.04}$	$27.55^{+0.1}_{-0.1}$
9.3	24196^{+12}_{-12}	$3.38^{+0.01}_{-0.01}$	$5.38^{+0.08}_{-0.08}$	$13.5^{+0.1}_{-0.1}$	$10.75^{+0.08}_{-0.07}$	$1.102^{+0.009}_{-0.009}$	$0.458^{+0.006}_{-0.006}$	$6.3^{+0.2}_{-0.2}$	$4.0^{+0.2}_{-0.2}$	$-0.45^{+0.05}_{-0.04}$	$26.8^{+0.1}_{-0.1}$
11.7	21047^{+11}_{-11}	$3.64^{+0.01}_{-0.01}$	$5.67^{+0.1}_{-0.09}$	$13.8^{+0.2}_{-0.2}$	$10.97^{+0.08}_{-0.09}$	$1.03^{+0.01}_{-0.01}$	$0.460^{+0.009}_{-0.009}$	$7.5^{+0.3}_{-0.2}$	$4.0^{+0.3}_{-0.2}$	$-0.67^{+0.05}_{-0.05}$	$25.56^{+0.09}_{-0.09}$
14.0	17972^{+9}_{-10}	$3.68^{+0.009}_{-0.01}$	$5.7^{+0.1}_{-0.1}$	$13.9^{+0.2}_{-0.3}$	$11.0^{+0.1}_{-0.1}$	$0.97^{+0.01}_{-0.01}$	$0.49^{+0.01}_{-0.01}$	$7.9^{+0.3}_{-0.3}$	$3.8^{+0.3}_{-0.3}$	$-0.81^{+0.06}_{-0.06}$	$24.34^{+0.09}_{-0.08}$
16.3	14905^{+9}_{-9}	$3.60^{+0.008}_{-0.01}$	$5.5^{+0.1}_{-0.09}$	$12.0^{+0.1}_{-0.1}$	$10.10^{+0.07}_{-0.07}$	$0.89^{+0.01}_{-0.01}$	$0.50^{+0.01}_{-0.01}$	$9.6^{+0.6}_{-0.5}$	$4.5^{+0.2}_{-0.2}$	$-0.97^{+0.08}_{-0.07}$	$22.92^{+0.07}_{-0.07}$
18.7	11820^{+8}_{-9}	$3.47^{+0.01}_{-0.01}$	$6.1^{+0.1}_{-0.1}$	$11.9^{+0.2}_{-0.2}$	$10.16^{+0.08}_{-0.09}$	$0.85^{+0.01}_{-0.01}$	$0.48^{+0.01}_{-0.01}$	$10.4^{+0.9}_{-0.7}$	$4.7^{+0.3}_{-0.3}$	$-1.1^{+0.1}_{-0.1}$	$21.33^{+0.08}_{-0.07}$
21.0	8832^{+7}_{-8}	$3.32^{+0.02}_{-0.04}$	$6.0^{+0.1}_{-0.1}$	$11.6^{+0.2}_{-0.2}$	$9.7^{+0.1}_{-0.1}$	$0.82^{+0.03}_{-0.02}$	$0.53^{+0.02}_{-0.02}$	12^{+2}_{-1}	$6.0^{+0.6}_{-0.5}$	$-1.2^{+0.2}_{-0.2}$	$19.6^{+0.2}_{-0.1}$
23.3	6089^{+7}_{-8}	$2.94^{+0.02}_{-0.02}$	$6.7^{+0.2}_{-0.2}$	$11.2^{+0.2}_{-0.2}$	$9.4^{+0.1}_{-0.1}$	$0.8^{+0.03}_{-0.03}$	$0.51^{+0.02}_{-0.02}$	14^{+4}_{-2}	$5.7^{+0.9}_{-0.7}$	$-1.8^{+0.4}_{-0.4}$	$17.3^{+0.2}_{-0.2}$
25.7	3658^{+6}_{-6}	$2.57^{+0.02}_{-0.03}$	$7.3^{+0.2}_{-0.2}$	$10.9^{+0.2}_{-0.2}$	$9.1^{+0.2}_{-0.2}$	$0.75^{+0.03}_{-0.03}$	$0.48^{+0.03}_{-0.03}$	14^{+7}_{-4}	$5.5^{+1.4}_{-0.8}$	$-2.3^{+0.6}_{-0.8}$	$14.91^{+0.1}_{-0.1}$
28.0	1494^{+3}_{-4}	$1.92^{+0.04}_{-0.04}$	$6.4^{+0.3}_{-0.3}$	$9.4^{+0.4}_{-0.3}$	$7.4^{+0.2}_{-0.2}$	$0.76^{+0.05}_{-0.05}$	$0.65^{+0.07}_{-0.07}$	2621^{+8346}_{-1921}	1034^{+696}_{-689}	$-4.^{+4.1}_{-4.1}$	$11.6^{+0.2}_{-0.2}$
30.3	268^{+2}_{-3}	$1.10^{+0.06}_{-0.06}$	$7.1^{+0.4}_{-0.6}$	$8.4^{+0.7}_{-0.5}$	$4.7^{+1.0}_{-1.1}$	$0.6^{+0.2}_{-0.1}$	$0.6^{+0.2}_{-0.2}$	1140^{+1444}_{-782}	737^{+504}_{-497}	$-4.^{+4.1}_{-4.1}$	$6.5^{+0.5}_{-0.2}$

Table B.11: Results from the MCMC fitting process for the snapshots from the N-body model N0.1 with initial 10% BH and NS retention. I list here the age of each snapshot in units of the initial half-mass relaxation time, the total cluster mass in $\mathrm{M}_\odot$, the half-mass radius in pc, the dimensionless central concentration for the global mean mass, the central mean mass, and the ES stars, the truncation parameter g, the mass segregation parameter δ, the anisotropy radius for the global mean mass and the central mean mass in pc, the anisotropy parameter η and the truncation radius r_t in pc. All parameters except the dimensionless central concentration for the global mean mass, and the ES stars, the anisotropy radius for the global mean mass and the truncation radius r_t, are fitting parameters; the other values were obtained from the multimass models of the 10 last walker positions of each MCMC chain. The median of the marginalized posterior distribution of each parameter is used to estimate its best-fitting value and the 16th and 84th percentiles as proxy for the 1σ uncertainties.

Age	M_Cl	r_h	W_0	$W_{0,\mathrm{CMM}}$	$W_{0,\mathrm{ES}}$	g	δ	r_a	$r_{\mathrm{a,CMM}}$	η	r_t
$\tau_{\mathrm{rh},0}$	$\mathrm{M}_\odot$	pc						pc	pc		pc
2.3	31177^{+15}_{-15}	$2.51^{+0.01}_{-0.01}$	$5.41^{+0.04}_{-0.03}$	$16.2^{+0.2}_{-0.1}$	$8.84^{+0.03}_{-0.03}$	$1.47^{+0.01}_{-0.01}$	$0.295^{+0.002}_{-0.002}$	$11.7^{+0.3}_{-0.4}$	41^{+1}_{-1}	$0.67^{+0.02}_{-0.02}$	$31.1^{+0.3}_{-0.2}$
4.7	28763^{+14}_{-14}	$2.82^{+0.01}_{-0.01}$	$6.18^{+0.07}_{-0.06}$	$12.9^{+0.1}_{-0.1}$	$11.56^{+0.05}_{-0.05}$	$1.30^{+0.01}_{-0.01}$	$0.387^{+0.006}_{-0.006}$	$4.33^{+0.07}_{-0.08}$	$4.6^{+0.2}_{-0.2}$	$0.05^{+0.02}_{-0.02}$	$30.1^{+0.2}_{-0.2}$
7.0	25430^{+11}_{-12}	$3.36^{+0.01}_{-0.02}$	$5.62^{+0.09}_{-0.08}$	$12.7^{+0.1}_{-0.1}$	$11.46^{+0.08}_{-0.07}$	$1.12^{+0.01}_{-0.01}$	$0.453^{+0.008}_{-0.007}$	$5.4^{+0.1}_{-0.1}$	$4.9^{+0.2}_{-0.2}$	$-0.11^{+0.03}_{-0.03}$	$27.7^{+0.1}_{-0.1}$
9.4	22153^{+11}_{-12}	$3.56^{+0.01}_{-0.01}$	$5.9^{+0.1}_{-0.1}$	$12.9^{+0.1}_{-0.1}$	$11.60^{+0.09}_{-0.08}$	$1.04^{+0.01}_{-0.01}$	$0.46^{+0.01}_{-0.01}$	$6.6^{+0.2}_{-0.2}$	$4.5^{+0.2}_{-0.2}$	$-0.45^{+0.05}_{-0.05}$	$26.2^{+0.1}_{-0.1}$
11.7	18998^{+10}_{-10}	$3.67^{+0.01}_{-0.01}$	$5.8^{+0.1}_{-0.1}$	$12.2^{+0.1}_{-0.1}$	$11.22^{+0.08}_{-0.07}$	$0.94^{+0.01}_{-0.01}$	$0.46^{+0.01}_{-0.01}$	$8.0^{+0.3}_{-0.3}$	$4.6^{+0.2}_{-0.2}$	$-0.68^{+0.05}_{-0.06}$	$24.76^{+0.08}_{-0.08}$
14.1	15846^{+9}_{-10}	$3.69^{+0.02}_{-0.02}$	$6.1^{+0.1}_{-0.1}$	$11.7^{+0.1}_{-0.1}$	$11.00^{+0.08}_{-0.07}$	$0.85^{+0.01}_{-0.01}$	$0.46^{+0.01}_{-0.01}$	$8.7^{+0.4}_{-0.4}$	$4.4^{+0.2}_{-0.2}$	$-0.97^{+0.08}_{-0.07}$	$23.40^{+0.06}_{-0.1}$
16.4	12658^{+8}_{-8}	$3.58^{+0.02}_{-0.02}$	$6.1^{+0.1}_{-0.2}$	$11.8^{+0.2}_{-0.2}$	$10.96^{+0.1}_{-0.09}$	$0.84^{+0.01}_{-0.01}$	$0.50^{+0.02}_{-0.02}$	$9.3^{+0.6}_{-0.5}$	$4.5^{+0.3}_{-0.3}$	$-1.1^{+0.1}_{-0.1}$	$21.90^{+0.09}_{-0.08}$
18.7	9799^{+8}_{-8}	$3.45^{+0.02}_{-0.01}$	$6.8^{+0.2}_{-0.2}$	$12.1^{+0.2}_{-0.2}$	$11.1^{+0.1}_{-0.1}$	$0.80^{+0.01}_{-0.01}$	$0.49^{+0.02}_{-0.02}$	$10.1^{+0.9}_{-0.7}$	$4.5^{+0.4}_{-0.3}$	$-1.4^{+0.1}_{-0.2}$	$20.2^{+0.1}_{-0.1}$
21.1	6945^{+7}_{-8}	$3.06^{+0.03}_{-0.03}$	$6.8^{+0.2}_{-0.2}$	$11.1^{+0.2}_{-0.2}$	$10.4^{+0.1}_{-0.1}$	$0.84^{+0.02}_{-0.02}$	$0.53^{+0.02}_{-0.02}$	14^{+3}_{-2}	$6.6^{+0.8}_{-0.7}$	$-1.7^{+0.3}_{-0.4}$	$18.5^{+0.2}_{-0.1}$
23.4	4384^{+6}_{-7}	$2.77^{+0.03}_{-0.03}$	$7.4^{+0.2}_{-0.1}$	$10.8^{+0.2}_{-0.2}$	$10.1^{+0.1}_{-0.1}$	$0.80^{+0.03}_{-0.02}$	$0.53^{+0.03}_{-0.03}$	1594^{+8138}_{-1418}	504^{+491}_{-471}	$-4.^{+4}_{-4}$	$15.9^{+0.2}_{-0.2}$
25.8	2177^{+4}_{-5}	$2.29^{+0.05}_{-0.05}$	$8.2^{+0.3}_{-0.2}$	$10.7^{+0.3}_{-0.3}$	$9.9^{+0.2}_{-0.2}$	$0.79^{+0.05}_{-0.04}$	$0.49^{+0.05}_{-0.05}$	1099^{+2822}_{-772}	466^{+305}_{-304}	$-4.^{+4}_{-4}$	$13.2^{+0.2}_{-0.2}$
28.1	681^{+2}_{-3}	$1.42^{+0.04}_{-0.06}$	$7.5^{+0.3}_{-0.3}$	$8.6^{+0.3}_{-0.3}$	$8.0^{+0.2}_{-0.2}$	$0.68^{+0.09}_{-0.06}$	$0.5^{+0.1}_{-0.1}$	1338^{+1719}_{-874}	858^{+589}_{-584}	$-4.^{+4}_{-4}$	$9.2^{+0.3}_{-0.2}$

Table B.12: Results from the MCMC fitting process for the snapshots from the N-body model N0 with no initial BH and NS retention. I list here the age of each snapshot in units of the initial half-mass relaxation time, the total cluster mass in $\mathrm{M}_\odot$, the half-mass radius in pc, the dimensionless central concentration for the global mean mass, the central mean mass, and the ES stars, the truncation parameter g, the mass segregation parameter δ, the anisotropy radius for the global mean mass and the central mean mass in pc, the anisotropy parameter η and the truncation radius r_t in pc. All parameters except the dimensionless central concentration for the global mean mass, and the ES stars, the anisotropy radius for the global mean mass and the truncation radius r_t, are fitting parameters; the other values were obtained from the multimass models of the 10 last walker positions of each MCMC chain. The median of the marginalized posterior distribution of each parameter is used to estimate its best-fitting value and the 16th and 84th percentiles as proxy for the 1σ uncertainties.

Age	M_Cl	r_h	W_0	$W_{0,\mathrm{CMM}}$	$W_{0,\mathrm{ES}}$	g	δ	r_a	$r_{\mathrm{a,CMM}}$	η	r_t
$\tau_{\mathrm{rh},0}$	$\mathrm{M}_\odot$	pc						pc	pc		pc
2.3	30921^{+13}_{-15}	$2.30^{+0.01}_{-0.01}$	$5.65^{+0.07}_{-0.07}$	$11.9^{+0.1}_{-0.1}$	$11.29^{+0.05}_{-0.05}$	$1.57^{+0.01}_{-0.01}$	$0.415^{+0.007}_{-0.007}$	$4.7^{+0.1}_{-0.1}$	$7.0^{+0.4}_{-0.3}$	$0.45^{+0.02}_{-0.02}$	$33.0^{+0.3}_{-0.2}$
4.7	27575^{+13}_{-13}	$3.01^{+0.01}_{-0.01}$	$5.9^{+0.1}_{-0.1}$	$13.1^{+0.1}_{-0.1}$	$12.09^{+0.08}_{-0.08}$	$1.28^{+0.01}_{-0.02}$	$0.439^{+0.008}_{-0.008}$	$4.60^{+0.08}_{-0.09}$	$5.4^{+0.3}_{-0.3}$	$0.17^{+0.02}_{-0.02}$	$29.4^{+0.1}_{-0.3}$
7.0	24303^{+12}_{-13}	$3.32^{+0.01}_{-0.01}$	$5.7^{+0.1}_{-0.1}$	$12.8^{+0.1}_{-0.1}$	$11.93^{+0.08}_{-0.07}$	$1.16^{+0.01}_{-0.01}$	$0.466^{+0.009}_{-0.009}$	$5.8^{+0.2}_{-0.2}$	$5.1^{+0.3}_{-0.2}$	$-0.14^{+0.04}_{-0.04}$	$27.12^{+0.09}_{-0.07}$
9.4	21266^{+11}_{-11}	$3.55^{+0.01}_{-0.02}$	$6.1^{+0.1}_{-0.1}$	$13.1^{+0.1}_{-0.1}$	$12.17^{+0.1}_{-0.09}$	$1.08^{+0.01}_{-0.01}$	$0.47^{+0.01}_{-0.01}$	$7.4^{+0.3}_{-0.3}$	$4.8^{+0.3}_{-0.2}$	$-0.51^{+0.05}_{-0.05}$	$25.74^{+0.09}_{-0.1}$
11.7	18207^{+10}_{-10}	$3.59^{+0.01}_{-0.02}$	$6.2^{+0.1}_{-0.1}$	$12.7^{+0.2}_{-0.2}$	$11.93^{+0.09}_{-0.1}$	$0.99^{+0.01}_{-0.01}$	$0.47^{+0.01}_{-0.01}$	$8.1^{+0.4}_{-0.3}$	$4.6^{+0.3}_{-0.3}$	$-0.75^{+0.06}_{-0.07}$	$24.28^{+0.09}_{-0.08}$
14.1	15089^{+9}_{-9}	$3.65^{+0.01}_{-0.01}$	$6.6^{+0.2}_{-0.2}$	$13.3^{+0.2}_{-0.2}$	$12.3^{+0.1}_{-0.1}$	$0.94^{+0.01}_{-0.01}$	$0.48^{+0.01}_{-0.01}$	$9.0^{+0.5}_{-0.4}$	$4.5^{+0.3}_{-0.3}$	$-0.95^{+0.08}_{-0.08}$	$23.05^{+0.07}_{-0.1}$
16.4	12058^{+8}_{-9}	$3.50^{+0.01}_{-0.01}$	$7.0^{+0.2}_{-0.1}$	$12.3^{+0.1}_{-0.1}$	$11.86^{+0.09}_{-0.1}$	$0.86^{+0.01}_{-0.01}$	$0.45^{+0.02}_{-0.02}$	$9.7^{+0.8}_{-0.6}$	$4.4^{+0.2}_{-0.2}$	$-1.3^{+0.1}_{-0.1}$	$21.40^{+0.07}_{-0.06}$
18.8	9209^{+7}_{-8}	$3.22^{+0.02}_{-0.02}$	$6.4^{+0.1}_{-0.1}$	$11.0^{+0.2}_{-0.2}$	$10.73^{+0.1}_{-0.09}$	$0.81^{+0.02}_{-0.02}$	$0.52^{+0.02}_{-0.02}$	11^{+1}_{-1}	$5.5^{+0.4}_{-0.4}$	$-1.4^{+0.2}_{-0.2}$	$19.62^{+0.1}_{-0.07}$
21.1	6384^{+6}_{-7}	$2.95^{+0.03}_{-0.03}$	$7.5^{+0.2}_{-0.2}$	$11.7^{+0.2}_{-0.2}$	$11.2^{+0.2}_{-0.1}$	$0.86^{+0.02}_{-0.03}$	$0.50^{+0.02}_{-0.02}$	12^{+2}_{-1}	$4.7^{+0.5}_{-0.4}$	$-2.0^{+0.3}_{-0.3}$	$17.8^{+0.2}_{-0.1}$
23.5	3966^{+5}_{-6}	$2.54^{+0.03}_{-0.03}$	$7.3^{+0.2}_{-0.2}$	$10.6^{+0.2}_{-0.2}$	$10.1^{+0.2}_{-0.1}$	$0.79^{+0.03}_{-0.03}$	$0.55^{+0.04}_{-0.04}$	16^{+11}_{-4}	7^{+2}_{-1}	$-2.5^{+0.7}_{-1.0}$	$15.2^{+0.2}_{-0.1}$
25.8	1955^{+4}_{-5}	$2.10^{+0.04}_{-0.04}$	$7.4^{+0.3}_{-0.3}$	$10.3^{+0.3}_{-0.3}$	$9.5^{+0.1}_{-0.2}$	$0.81^{+0.04}_{-0.04}$	$0.66^{+0.06}_{-0.06}$	1369^{+3098}_{-983}	592^{+390}_{-391}	-4^{+4}_{-4}	$12.6^{+0.3}_{-0.3}$
28.1	455^{+2}_{-3}	$1.01^{+0.04}_{-0.05}$	$7.6^{+0.3}_{-0.4}$	$8.7^{+0.4}_{-0.3}$	$8.2^{+0.3}_{-0.3}$	$1.0^{+0.1}_{-0.1}$	$0.6^{+0.2}_{-0.2}$	19^{+17}_{-10}	12^{+6}_{-6}	-4^{+4}_{-4}	$8.4^{+0.7}_{-0.5}$

Appendix C

Copyright and Permissions

Peuten et al. (2016) and Peuten et al. (2017) were published in Monthly Notices of the Royal Astronomical Society (MNRAS). These papers were published under the Oxford Journals Licence to publish (see `http://www.oxfordjournals.org/` for details). Under this licence, as the first author, I have the right to include these papers in full or in part in this thesis (see `https://academic.oup.com/journals/pages/authors/authors_faqs/online_licensing#three` for details)

Appendix D

Online Material

All links and other online resources of this PhD Thesis are available at

`http://phd.mpeuten.de`